STRUCTURE AND MAGNETIC PROPERTIES OF THIN PERMALLOY FILMS

by

Russel John Fairholme, B.Sc., A.R.C.S.

Thesis submitted to the University of London
for the degree of Doctor of Philosophy

Autumn 1969

Materials Section
Dept. of Electrical Engineering
Imperial College
London, S.W.7.

ABSTRACT

This work is mainly concerned with the magnetic properties of permalloy films which have differing crystallographic structures. The structure is altered by using different single-crystal substrates (NaCl, NaF or LiF) held at varying substrate temperatures.

In the first two chapters the magnetic behaviour of thin films is discussed and much of the previous work is reviewed. Chapter 3 deals with the magnetisation ripple in detail, comparing most of the theories on the subject.

All the experimental apparatus and procedures are discussed in chapter 4. A large part is concerned with the biased susceptibility apparatus and the theory behind it. This theory has been extended to include the cases of biaxial and combined anisotropies, the latter case being important for real single-crystal films.

Chapter 5 is concerned with the crystallographic structure of the films. The orientation of the film is observed in the electron microscope using diffraction patterns. As the substrate temperature is increased the films change from polycrystalline with a (100) texture to a (100) single crystal. In this transition several stages with spurious diffraction spots were observed which have been explained by twinning, double diffraction and an atomistic nucleation theory. NaF and LiF substrates produce better epitaxy for the same substrate temperature.

The effect of the substrate temperature on the uniaxial anisotropy field is discussed in chapter 6, as is the effect of the various

substrates on the biaxial anisotropy. The change in magnetic properties produced by using polished substrates has been completely explained using Harte's ripple theory.

In chapter 7 some experiments made on the loss mechanisms are discussed and explained in terms of a wall-motion model. The hysteresis loops of single-crystal films grown on NaF are shown to agree well with the Stoner-Wohlfarth model in chapter 8, contrary to previous observations.

ACKNOWLEDGEMENTS

I would like to express my sincere thanks to my supervisor, Dr. K. D. Leaver, for his continued encouragement and for many helpful discussions; also to Professor J. C. Anderson for making available the facilities of his department.

My thanks are due to all my contemporaries in the Materials Section, especially M. E. Jones for his help and advice with the photographs.

I am indebted to the Science Research Council for the provision of a Research Studentship during the three years in which this work was carried out.

Finally, I must thank my wife who interpreted and typed the manuscript.

CONTENTS

CHAPTER 1

Introduction and Historical Survey

1.1. Introduction

Thin films have considerable advantages in physical investigations due to the fact that the various properties measured are in two, rather than three, dimensions. However, due to their shape, surface effects are greatly exaggerated and may obscure the bulk properties under observation. Furthermore, the method of fabrication has a profound influence on the properties of the thin films: in particular the substrates on which they are deposited will affect the structural properties whilst the residual atmosphere, in which the film is prepared, can give rise to surface oxidation and inclusions whose influence may be difficult to assess. Thus there are many extrinsic properties of thin films which have been the subject of considerable study in the past decade.

There are several techniques currently available for the production of thin films (see for instance, pg. 11, ref. A.1). The films in this work were produced by thermal evaporation in high vacuum, so that all future discussions will refer mainly to evaporated films. As has been mentioned previously, the structure of the film is governed by the choice of substrate and its temperature during deposition, although the rate of deposition does seem to have some effect. Most metals can be produced in thin-film form having a structure varying from polycrystalline, with randomly oriented crystallites, to single crystal. (In thin film technology the term 'single crystal' means: well-oriented crystallites of

the order of several millimetres diameter, contrary to the bulk (and literal) meaning.) If an amorphous substrate is used, such as glass or carbon, then the metal overgrowth produced is generally polycrystalline with completely random orientation. For the production of single crystal films (an art known as epitaxy) an appropriately-cut single crystal substrate is used, the most common being the (100) cleavage plane of sodium chloride. This is held at an elevated temperature of about 300° or 400°C during deposition and for NiFe the film's (100) plane is parallel to the substrate and [001] direction of NiFe parallel to [001] direction of NaCl. At lower temperatures other orientations are present and at room temperature we have a polycrystalline ring diffraction pattern synonymous with a film randomly oriented in the plane of the substrate but with [001] NiFe parallel to [001] NaCl normal to the substrate.

Since there is a great need to understand the structure of thin films a large amount of effort has been put into understanding the nucleation and growth stages. The result of this is that growth can be divided into several distinct phases, the first being the nucleation of small islands (about 20 Å diameter) on the substrate consisting of several atoms. For most materials these islands nucleate at preferential energy sites, such as cleavage steps. The number increases exponentially during this nucleation stage until a saturation number of about $10^{11}/cm^2$ is reached. The nucleation stage is not very well understood but several theories showing quite good agreement with the saturation number have been propounded (H.1, H.2, L.1, W.1). The second phase consists of island growth in preference to further nucleation. The incident vapour atoms are absorbed directly into

the existing islands although a minority go towards the nucleation of new islands. In the cases of metals on non-metal substrates the islands grow in three dimensions so that the film cannot be considered as growing in layers of single atoms. Also at this stage for epitaxial films the islands generally have definite crystallographic sides (S.3). Then we have coalescence where some of the islands join up like drops of liquid so that the general picture is a decrease in the number of the islands while they are still increasing in size. In the early stages of coalescence in single crystal films, a certain amount of reorientation relative to the substrate occurs and at the coalescence of islands they lose their crystallographic form. However, if no more coalescence occurs the islands will eventually regain their crystallographic sides. Eventually, as coalescence proceeds, the islands join up to form a network. It is at these last two phases in the growth that all the defects such as dislocations and stacking faults occur (J.1). In the final stage, the holes are gradually filled in and the film becomes continuous, although it is far from being a parallel-sided slab, and surface structure, inherent in this mode of growth, will always be present. To achieve a parallel-sided film we need the film to become continuous at as low a thickness as possible, which requires the islands to grow in two dimensions rather than three. This is very difficult and occurs only for a few metals on metals (e.g. Au on Ag, P.1) which have low interfacial energy, between the substrate and the deposit (relative to the surface energy of the deposit on substrate). A result of the island coalescence method of growth is the large number of defects $\sim 10^{10}$ to

$10^{11}/cm^2$, usually dislocations and stacking faults. The effect these defects have on the film's magnetic properties is not fully understood.

Original work on magnetic films proceeded along two lines until about twenty years ago. The first, experimental, line consisted of rather simple measurements on thin films prepared by electrodeposition as far back as 1896 (L.2) although apparatus was not sufficiently refined then to measure, accurately, properties of about 10^{-4}gm of material. It was not until 1951 that Crittenden et al (C.1) designed a very sensitive loop plotter which enabled hysteresis loops of thin films to be observed. Methods of preparation improved and two years later Crittenden and Hoffmann (C.2) published some work on nickel thin films prepared by evaporation in vacuo. His unfortunate choice of nickel prevented him from observing the uniaxial anisotropy which was present. In 1955 Blois (B.2) evaporated 80/20 NiFe films under a magnetic field and found that there was a minimum energy position for the magnetisation when it lay parallel, or antiparallel, to the direction of the field applied during deposition (this is uniaxial anisotropy). This discovery was of considerable importance to the computer industry, offering, as it does, a bistable device for memory storage applications.

The second independent line of research was a theoretical one. As far back as 1930, Frenkel and Dorfmann (F.1) calculated the size of particle for which it is energetically more favourable to be a single magnetic domain. They did this using the analogy of a collection of drops versus a liquid formulation, the lower energy state being the more stable. Later Kittel (K.1), using a more realistic approach, worked out

these critical sizes for plates, needles and particles. He derived a critical thickness for a lamina of about 5000 Å, although the calculation was rather limited in using Bloch walls and a uniaxial anisotropy perpendicular to the plate. However, it was probably one of the first calculations using 'micromagnetics'.

This fact, that a thin magnetic film (thickness < 5000 Å) should be a single domain, means that on application of an increasing reverse field the magnetisation should rotate until a critical field (H_k) is reached when the film will switch (see Chapter 2). This coherent spin rotation is an extremely fast process taking, typically, about one nanosecond. Thus a uniaxial, single domain film could be used as a binary store which would be one or two orders of magnitude faster than present-day stores. Further potential advantages are: they have a high packing density, could be cheaply produced and require low switching fields.

For these reasons a great deal of research has been carried out by the computer industry. The research may be divided into two main parts: that done by the computer industry, which is mainly concerned with the reversal mechanism and its departure from ideal behaviour; secondly, more basic research into the causes of the uniaxial anisotropy and the variation of the saturation magnetisation with thickness.

1.2. The Properties of Films

Films behave as single domains only under certain conditions and do not usually reverse by coherent spin rotation. Reversal in the easy direction (minimum energy direction) usually occurs by domains of reverse

magnetisation nucleating at one edge and moving across the film. This reduces the stray magnetostatic field produced by surface poles along the edge of the film. Processes involving domain wall movement are much slower than those associated with rotation so that the envisaged store would be slower than anticipated. Thus to a first approximation we can deal with thin films using the Stoner-Wohlfarth model (S.1) (Chapter 2) but as the torque on the magnetisation approaches zero, domains will be created. Taking a closer look at film behaviour near the critical switching fields we find that there are very noticeable departures from ideal behaviour. These departures can be qualitatively explained if one allows the magnetisation within a domain to vary sinusoidally along its length as shown in figure 3.1a. This 'magnetisation ripple' as it is called has been observed and although its origin is not very well understood, it is thought that the dispersion in the local uniaxial easy axes of the crystallites in the film makes a large contribution towards it. The theories explaining the effect of ripple on film behaviour will be dealt with more fully in Chapter 3. An important fact which emerges from these theories is that the angular amplitude of the ripple is field dependent. At certain fields ($> H_k$, the anisotropy field) as the film approaches the theoretical switching field, H_k, the magnetisation becomes locked (figure 1.1) so that it is held by the stray fields produced by the surface charges on the ripple walls. Thus the effective switching field is increased and higher fields are required to switch the film. We see, therefore, that ripple must be kept as small as possible in a store, and for this reason a great deal of research is concerned with

the origins of the magnetisation ripple. A further drawback to thin film stores is the phenomenon of wall creeping. No wall motion occurs in films when two d.c. fields are applied simultaneously in the easy and hard directions if the vectorial sum lies inside the critical curve for wall motion (figure 1.2). However, if an alternating field is applied in the hard direction then the walls tend to move very slowly at fields well inside the critical curve. This so-called wall creeping has been the subject of much research as, because of it, the pulsed stray fields from neighbouring storage elements could cause the stored information to change. In early experiments using unipolar hard axis fields, creep was not observed in films containing only Néel walls and was extremely pronounced for films with combined or intermediate walls. It would seem that wall creeping is related to Bloch line and 90° line motion.* Using bipolar hard axis fields, creep has been observed in very thin films containing Néel walls and is much faster than in thicker films. Hence creep may be assumed to be caused by some internal wall rearrangements as well as the motion and nucleation of Bloch and 90° lines.

Several ingenious models for this behaviour have recently been reviewed by Kayser (K.2) who concludes that none are capable of explaining all the observed effects, although all explain some of the effects. Creep may be overcome by using two identical films separated by a non-magnetic layer so that unipolar Néel walls in one film induce quasi-Néel walls in the other. The thickness of the non-magnetic layer is

---

* 90° lines are the border lines of different magnetisation directions in a domain wall.

important being up to 2000 Å for SiO. Using this and only unipolar pulses, creep may be eliminated (pg. 405, ref. A.1).

Domain Walls. Domains were first postulated by Weiss (W.2) to explain his observations in 1907. They were not observed until 1931 when Bitter (B.3), using a fine colloidal suspension of Fe_2O_3 in ethyl acetate, showed the existence of domains by the collection of colloid at their boundaries, where the localised magnetic fields are greatest. This pattern was analysed by Bloch (B.4) who postulated a mechanism, known as the Bloch wall, by which the spins could rotate from one domain to another. This is shown in figure 1.3a. For bulk materials the shape of the wall is governed mainly by the anisotropy energy and the exchange energy, (the magnetostatic energy caused by the surface poles in the wall being negligible). This is not the case for thin films, however, as was shown by Néel (N.1) who postulated that below a certain thickness it would be energetically more favourable for the magnetisation to rotate in the plane of the film (figure 1.3b). This type of wall will have volume poles in the domain walls and not surface poles as for Bloch walls. Therefore it follows that the changeover from Néel to Bloch walls can be expected when the film thickness is of the same order as the wall width.

With these two wall models many calculations (D.1, M.1, A2) have been performed on the wall energy and width as functions of film thickness; the main differences being the form of the magnetisation distribution through the wall. Bloch walls show good agreement between

most models and obey Aharoni's self-consistency criterion (A.3) well. The agreement in the case of Néel walls is poor and Aharoni concludes that all present-day models are unrealistic at the important thicknesses. More recent work by Suzuki et al (S.2) shows that there is good agreement between theory and experiment for the width of Néel walls and poor agreement for Bloch walls. It is clear that more work is required before we can completely understand how the rotations occur in domain walls.

One expects the transition from Néel to Bloch walls to be gradual rather than abrupt, since a Bloch wall of alternate rotations has a smaller magnetostatic energy (due to surface poles) than a unipolar Bloch wall. The rotation of the spins within a Bloch wall of alternate segments must occur by short Néel sections which grow in size while the Bloch segments decrease as the thickness decreases until we have alternate Néel walls separated by 90° lines. This method of change from Néel to Bloch walls is shown in figure 1.4 as proposed by Feldtkeller and Fuchs (F.2). The mixed walls have large stray fields around the Bloch lines separating the Néel segments and the formation of 'cross-ties' is energetically favoured. This intermediate form of wall was first observed by Huber et al (H.3) who also proposed the magnetisation distribution in figure 1.3c. The transition from Néel to Bloch walls was clearly demonstrated by Methfessel et al (M.2) using the Bitter technique on a wedge-shaped film. They found that walls with a high density of cross-ties appeared in permalloy films of about 900 Å thickness and as the thickness decreased the cross-tie density also decreased

until they disappeared at about 250 Å. These results are in reasonable agreement with Middlehoek's calculations (see figure 1.5a). Middlehoek (M.3) also calculated the dependence of wall energy on the angle of magnetisation each side of the wall and his results show which type of wall is stable under fixed conditions of thickness and wall angle (figure 1.5b).

The observation of domains and their boundaries has been reviewed in several books (C.2, C.3, P.2); consequently only a brief description of the available methods will be given.

(a) Colloid. This was originally used by Bitter as described above. It is essentially a static method and for use in dark field illumination it requires a good surface. This technique delineates the domain walls by an interaction with the stray field from the walls so that it is difficult to see Bloch walls. Further drawbacks are that if the colloid is incorrectly made it becomes acidic and attacks the sample as well as being very temperature sensitive. Many workers have tried to improve the resolution of the colloid and these methods have been reviewed by Garrood (G.1). The fine structure of domain walls may be observed by the method of Craik and Griffiths (C.5). Using a Celacol-stabilised colloid they formed a thin film on the surface of the sample by allowing the colloid to dry. After replicating it was viewed by transmission in the electron microscope. The resolution of this technique for high anisotropy materials can be as low as 300 Å, although it is generally quoted as better than 2000 Å (C.4).

(b) Magneto-optical Techniques. The most popular method is the Kerr effect where the plane of incident polarised beam is rotated by the magnetised surface, the amount of rotation depending on the direction of the magnetisation. Thus by using crossed polarisers we can make domains visible by contrast. The main advantages of this method of domain observations are: (i) the experimental arrangements are easier for films in difficult environments (high vacuum or extreme temperatures); (ii) edge effects can be eliminated by using small areas (down to about 1 micron with lasers) in the centre of the specimen; (iii) quantitative measurements (hysteresis loops) can easily be made as the light intensity is directly proportional to the magnetisation so no integrator is required. The two big disadvantages are that, first, the contrast is low, although this can be improved by 'blooming' the film with a dielectric layer, e.g. zinc sulphide (P.3). Secondly, the surface must be free from imperfections since these can produce contrast. This last disadvantage has largely been overcome by Green and Thomas (G.2) who have designed ~~an apparatus~~ a loop plotter which may be used for diffuse surfaces.

The second magneto-optical effect is the Faraday effect which is limited to transparent films less than about 1000 Å thick. This method relies upon the fact that the plane of polarisation is rotated when passing through a magnetic medium. The resolution of the Faraday effect is much higher than that of the Kerr effect and as a result of this magnetisation ripple can be observed and the magnetisation directions accurately determined.

Both these optical methods allow dynamic observations of domains and were first used on thin films by Fowler and Fryer (F.3). Since then much work has been carried out on optimising the theoretical and experimental conditions (see for example, Lissberger, L.4) and a review of present-day techniques has recently been produced by Lambeck (L.3).

(c) Electron Microscopy. The most popular and powerful technique for thin films and foils at the moment is Lorentz microscopy where the film is observed in transmission in an ordinary electron microscope which is deliberately defocussed. A second in-focus method, known as the Foucault mode, is occasionally used where a knife edge is used to obliterate one of the split diffraction spots caused by a domain wall. The internal fields (with magnetic induction = $\underline{B}$) in the film deflect the electrons (moving with velocity $\underline{v}$) by means of the Lorentz force $e(\underline{v} \times \underline{B})$ as they pass through and produce amplitude contrast at magnetic discontinuities. As in the Faraday effect the magnetisation direction is known exactly as it is perpendicular to the observed striations in the image.

This method has a very high resolution and was first used by Fuller, Hale and Rubinstein (F.4) to observe ripple. However, early calculations based on a geometrical optics approach have been shown by Wohlleben (W.3) to be unsatisfactory and wave optics must be used. This makes quantitative measurements difficult as they will depend on the defocussing distance and apparent source size. Nevertheless, complicated magnetisation distributions and fine magnetic structure can easily be observed and investigations on the interaction of imperfections and domain walls performed (J.2, W.4).

The obvious limitation to this method is that it can only be applied to thinner films but, recently, films of 2000 Å have been used in an ordinary 100 kv microscope (L.5). Another disadvantage is that the film has to be removed from the substrate. These disadvantages are overcome in the following two techniques. In mirror microscopy the electrons are reflected at equipotential surfaces very close to the specimen, produced by holding the specimen at a small negative voltage relative to the cathode. Thus the electrons travel very slowly and will be strongly affected by surface fields (both electric and magnetic). Domains were first observed in this mode by Mayer (M.4) and improved observations were made by Barnett and Nixon (B.5). This method does require very smooth surfaces or else surface features will be superimposed and indistinguishable. The second technique uses the scanning microscope. Here the secondary electrons emitted from the surface by the scanning electron probe produce the contrast. Using a new form of detector, Banbury and Nixon (B.6) have been able to distinguish between the magnetic and topographical contrasts. By suitably biasing the collector system one can eliminate magnetic contrast completely or distinguish between surface domains and internal domains. Thus perfection of the surface is not a special requirement, although with both of these methods the resolution at the moment is low, typically about 10 microns.

A recent review of developments in Lorentz microscopy has been published by Cohen (C.6).

Magnetic Anisotropy. Many important magnetic properties of films are governed by the relative sizes and directions of the anisotropies present in them. They are complicated by the fact that usually several different anisotropies are present which cannot simply be added vectorially. Below are listed some of the possible anisotropies and their causes.

(i) Shape Anisotropy: When a ferromagnetic body is uniformly magnetised, the surface poles created produce a demagnetising field proportional to the magnetisation, i.e. $\underline{H}_D = -N\underline{M}$ where N is the demagnetising factor. Now an ellipsoidal body is the only one which, when uniformly magnetised produces a uniform demagnetising field, so that this shape is the only one for which the concept of the demagnetising factor, N, is strictly applicable. However, for simplified mathematics the demagnetising field is often approximated to $-N\underline{M}$. For instance, a thin film can be approximated to a long, extremely thin elliptical cylinder. For an elliptical cylinder with semi-axes a and b, magnetised along one of these axes then $N_a = 4\pi a/(a+b)$ and $N_b = 4\pi b/(a+b)$. Therefore for a film whose width 2W is much larger than its thickness, 2L, we have $N_W \simeq 4\pi$ and $N_L \simeq 4\pi L/W$. The size of the demagnetising field perpendicular to the film is $4\pi M \simeq 10^4$ oe for 80/20 NiFe (and $N_L M \sim 10^{-1}$ oe in the film plane) which is sufficient to keep $\underline{M}$ in the film plane since other anisotropies in the film plane are typically ~ 10 oe. In fact most thin films have $\underline{M}$ confined to the plane and are said to have a shape anisotropy constant of $2\pi M^2$ the hard direction being normal to the film. An exception to this is Manganese Bismuthide which, when grown epitaxially, has a very high magneto-crystalline anisotropy energy

of $\sim 10^7$ erg/cc when magnetised in the plane compared with a shape anisotropy energy when magnetised normal to the plane of $\sim 2 \times 10^5$ erg/cc. Thus $\underline{M}$ prefers to lie normal to the surface.

(ii) Magneto-crystalline Anisotropy: It has long been known that the electron orbits in a crystal lattice have a strongly directional character and are virtually unaffected by applied magnetic fields. However, the electron spin is influenced by the applied field but since it is also coupled to the orbital motion of the electron it will be affected by orbital, and therefore crystal, symmetry. Thus we expect preferred directions for the magnetisation relative to the crystal lattice. This magnetocrystalline anisotropy energy has the following form for a cubic crystal:

$$E_{cub} = K_1 \sum_{i \neq j} \alpha_i^2 \alpha_j^2 \quad + \quad K_2 \alpha_1^2 \alpha_2^2 \alpha_3^2$$

where α_1 α_2 α_3 are the direction cosines of $\underline{M}$ relative to the crystal axes and K_1, K_2 are the first and second order anisotropy constants. For a (100) single crystal thin film $\underline{M}$ is confined to the (100) plane and the anisotropy energy density reduces to $E_k = K_1 \sin^2 2\theta$ which is a biaxial anisotropy. Measurements of magnetocrystalline anisotropy constants for epitaxial thin films are usually in fair agreement with bulk data, deviations being attributed to strain in the film produced by the misfit between film and substrate and/or differential thermal expansion.

(iii) Magnetoelastic Anisotropy: When a ferromagnetic body is magnetised the magnetic forces between atoms cause a slight change in the dimensions of the crystal lattice. This phenomenon is called magnetostriction.

Conversely, when a crystal lattice is strained there is a change in the energy of magnetisation. It is generally thought that these magnetic interactions occur by means of the spin-orbit coupling so that magneto-crystalline anisotropy and magnetostriction should be closely connected. In fact Kittel (K.3) showed that for a cubic crystal one adds a term $\frac{9}{4}\left[(C_{11} - C_{12})\lambda_{100}^2 - 2C_{44}\lambda_{111}^2\right]$ to the expression for the magneto-crystalline anisotropy. C_{11} C_{12} C_{44} are elastic moduli and λ_{100} λ_{111} the magnetostriction constants in the [100] and [111] directions. For a system of random crystallites a uniform stress S produces an energy of $\frac{3}{2}\lambda_s S \sin^2\theta$ where λ_s is the saturation magnetostriction and θ is the angle between $\underline{M}$ and the stress. As films are generally highly stressed there will be a magnetoelastic anisotropy. Attempts have been made to overcome this by using zero magnetostriction compositions where $\lambda_s = 0$, e.g. 81% Ni 19% Fe. For these compositions λ_{100} and λ_{111} are not separately zero and so we still have local variations in anisotropy which in turn will contribute to the ripple. The strain in the film will vary, depending on compositional fluctuations, substrate temperature and deposition rate variations so that the magnetoelastic anisotropy will have local fluctuations. This is probably one of the major causes of ripple and could be related directly to crystal structure and defect density in the film. Comprehensive reviews on magnetostriction have been compiled by Lee (L.6) and Birss (B.7).

(iv) Induced Anisotropy: Although a great deal of work has been initiated on this subject since its discovery, its origins are still rather obscure. It is usual to have a saturating magnetic field applied

during film production, which, although not essential, aligns the magnetisation, and hence the induced easy axis, into a particular direction. A uniaxial anisotropy can be described by an energy of the form $E = K_u \sin^2\theta$ where θ is the angle between $\underline{M}$ and the easy direction. K_u can be unambiguously measured by means of torque curves (taken in saturation fields); low-field methods are sometimes dubious as they can be masked by other effects. The magnitude of K_u is greatly influenced by: composition, substrate temperature and any subsequent annealing. It appears to be almost independent of deposition rate, film thickness and deposition pressure. Much work has been performed on most of the Ni-Fe-Co systems and the work up to 1964 has been comprehensively reviewed by Prutton (P.2). More recent reviews by Slonczewski (S.4), Wilts and Humphrey (W.5) have helped to clarify a few more points.

There are two well-established mechanisms for the origin of the uniaxial anisotropy. The first is the constraint mechanism which is based on the fact that at a temperature T a film, free of the substrate, will contain a strain which to first order is $\lambda(T)$ where λ is a suitably-averaged magnetostriction constant. As the film is cooled, a critical temperature (T_1) is reached where the film is constrained to the substrate and at this point a stress = $Y\lambda(T_1)$ is exerted on the film by the substrate (Y = Young's modulus). If the film is measured at T_m then there will be a uniaxial anisotropy with $K_u = \frac{3}{2} S \lambda(T_m) = \frac{3}{2} Y \lambda(T_1)\lambda(T_m)$ (I.1). Robinson (R.1) used the averaged saturation magnetisation λ_s which gave values which were generally too small. West (W.6) modified this by averaging the single crystal magnetoelastic energy over a random

collection of crystallites. For a polycrystalline film of material with cubic symmetry West found:

$$K_u = \frac{9}{10}\left[(c_{11} - c_{12})\,\lambda_{100}(T_1)\,\lambda_{100}(T_m) + 3c_{44}\,\lambda_{111}(T_1)\,\lambda_{111}(T_m)\right]$$

The agreement between experiment and this formula is quite good and measurements of K_u versus substrate temperature for Ni are in very good agreement with West's theory. The scatter of previous results and some deviations have been explained by the incomplete adherence of the film to the substrate. This will be influenced by the preparation conditions (W.6) and governs the constraint temperature.

The second mechanism, proposed by Néel (N.2) is that of directional pair ordering which is already well established in bulk NiFe alloys. It is based on the idea that an atom pair can have different energies depending on its orientation relative to the lattice. If the film is annealed, or deposited at a high substrate temperature, the atom pairs can migrate to minimum energy positions in which they remain fixed as the film is cooled, causing a magnetic anisotropy. Various approaches have been made to evaluate the dependence of the uniaxial anisotropy constant on the substrate or annealing temperature and on the film composition. The composition dependence is strictly only valid for very dilute alloys and shows good agreement for the Ni-rich NiFe alloy system (R.1). The temperature dependence is determined by the approach but the various forms differ only slightly (T.1, N.2, S.4). However, combinations of these two mechanisms do not explain completely the induced anisotropy in films and several other mechanisms have been proposed. Experimental evidence both for and against them has been produced and

only vague conclusions can be drawn. Those drawn by Wilts and Humphrey in a recent review (W.5) are that gas inclusions have a negligible effect and that the directional ordering of vacancies, foreign atoms, etc. may produce appreciable components in the induced anisotropy. An important method by which the contributions to the anisotropy may be separated and perhaps identified is by determining the spectrum of the annealing activation energies as done by Smith et al (S.5). Here the specimen is annealed with a hard direction field in vacuo immediately after the evaporation and the anisotropy constant continually monitored. The activation energies are determined assuming that the anisotropy field, H_k, $= \sum_j H_{kj}\left[2\exp.(-\frac{t}{\tau_j}) - 1\right]$ where τ_j is the j^{th} process relaxation time having an activation energy E_j given by $\tau_j = \tau_{jo}\exp.(E_j/kT_a)$. Much further careful work is needed in order to confirm these effects as annealing often introduces extraneous effects such as oxidation or even fundamental film structure changes.

(v) Perpendicular Anisotropy: It is found in certain conditions that the anisotropy $K_\perp$ normal to the film plane is not just the shape anisotropy $2\pi M^2$ but contains an extra structural term $K_\perp^s$ which can be negative causing $\underline{M}$ to rise from the plane. This can only be measured easily by torque magnetometry. If there is an isotropic strain in the film plane then a perpendicular anisotropy $= \frac{3}{2}\lambda S$ will be produced, which will be strongly dependent on substrate temperature (via S) and composition (via λ). Epitaxial Ni films on NaCl have clearly demonstrated this mechanism as on relieving the strain $K_\perp$ reverts back to $2\pi M^2$. However, the fact that $K_\perp^s$ has been found to be finite for zero

magnetostrictive composition films has caused another mechanism to be proposed. This is that columnar growth, caused by slow deposition rates, poor pressure or oblique incidence, can produce $K_{\perp}^{S}$ by means of the shape anisotropy of the columns. Of course, in epitaxial films the magnetocrystalline anisotropy will contribute to $K_{\perp}$. A consequence of large $K_{\perp}$ is the appearance of stripe domains which have been observed in 80/20 NiFe by Lo and Hanson (L.7).

(vi) Anisotropies introduced by special evaporation conditions: There are three possibilities, viz: (a) oblique incidence anisotropy, caused by oblique evaporation, as its name suggests. Large anisotropies of either sign may be produced (due to shape anisotropy of chain or column growths); (b) biaxial anisotropy produced by unidirectional scratching of substrate prior to evaporation; (c) unidirectional anisotropy caused by the exchange interaction of a ferromagnet and antiferromagnet in close contact (e.g. Ni-NiO, NiFe-NiFeMn) produced by either oxidation or film contamination.

We can conclude that apart from the M-induced uniaxial anisotropy most of the anisotropies in thin films are fairly-well understood.

The Saturation Magnetisation. Ferromagnetism is caused by exchange interactions between neighbouring spins, thus in very thin films having two surfaces in close proximity, the number of neighbours is reduced and this interaction will diminish. Therefore one should observe a considerable decrease in the saturation magnetisation and Curie temperature compared with bulk values below a certain thickness. This thickness will be reached when the ratio of surface atoms to interior

atoms becomes appreciable. There have been two main theoretical approaches to this problem which have recently been reviewed by Corciovei (C.7). First the Molecular Field theory (proposed by Weiss (W.2) and explained by Heisenberg (H.4) as due to interactions between unpaired spins in neighbouring atoms' d-shells) and secondly the Spin-wave theory (an approximation used by Bloch (B.8)). The Molecular Field theory has been modified by Valenta (V.1) and more generally by Corciovei (C.8) to account for thin films, although due to a slow convergence in the spin partition function these only apply accurately to high temperatures. On the other hand, the Spin-wave theory as formulated by Glass, Klein and Smith (G.3, K.4) and modified by Döring (D.2) is valid for low temperatures, where spin-wave interactions may be assumed negligible as the number of reversed spins is small. These advances have produced reasonable agreement between the two theories. However, more recently the Green's function method has been applied and has the advantage of being valid over the complete temperature range although the mathematics involved is extremely difficult (C.9).

Great care must be taken when comparing experimental and theoretical variations in M_s versus T as oxidation has a large effect on M_s and also very large fields must be used to ensure that very thin films are saturated. These two reasons account for the large divergence between earlier data and the more modern experiments.

Neugebauer (N.3) observed superparamagnetic behaviour of Ni films with thicknesses < 27 Å but more recently Gradmann et al (G.4) have found that films remain ferromagnetic down to 2.5 atomic layers. The

reason for this discrepancy seems to be that Neugebauer's films consisted of islands of the order of 50 - 100 Å across and behaved as superparamagnetic particles (B.9). However, Gradmann's results (from both structural and magnetic observations) indicate that his films are coherent single crystals down to 2.5 layers. His results showed good agreement with both Spin-wave and Green function theories apart from the variation of the magnetisation with applied field. The films of 48/52 NiFe prepared in between single crystal Cu films showed M_s to be independent of field up to 5000 oe which was contrary to the theories. Films below 2.5 layers had anomalous behaviour which could be explained by assuming very large surface anisotropies (~.2 - .3 erg/cc) causing M to lie perpendicular to the film. The effect of the bounding Cu films on the exchange interactions of the film surface are as yet unknown and if calculations are made then they may provide answers to a few of his discrepancies.

1.3. The Aim of the Present Work

Ripple and dispersion in the anisotropy, together with the property of creep mentioned earlier, are of considerable importance as limitations on the applications of thin magnetic films. Furthermore, it will be clear from the foregoing that many factors contribute to these phenomena, several being only vaguely understood. The present work was undertaken in an attempt to achieve a better understanding of some of these factors, particularly the origin and causes of magnetisation ripple.

Preliminary work was concerned with the effect of crystallite orientation on the magnetic properties but the degree of orientation was found to be rather a difficult quantity to measure. Later work was carried out using different substrates and substrate preparations, to observe their associated effects on the magnetic properties.

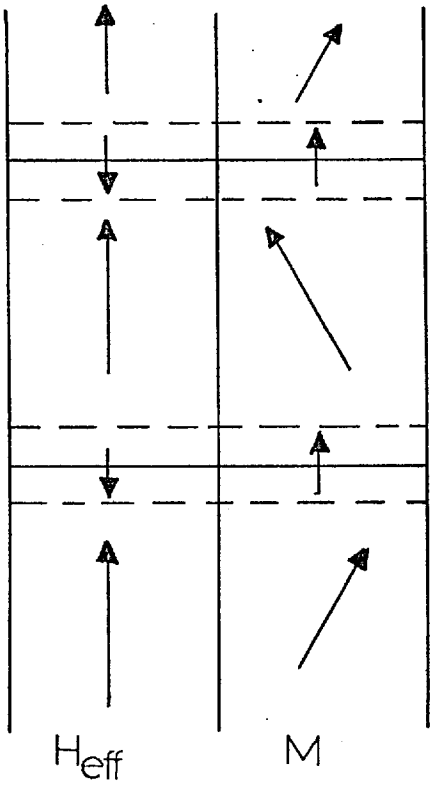

Figure 1.1 Diagramatic representation of 'locking'

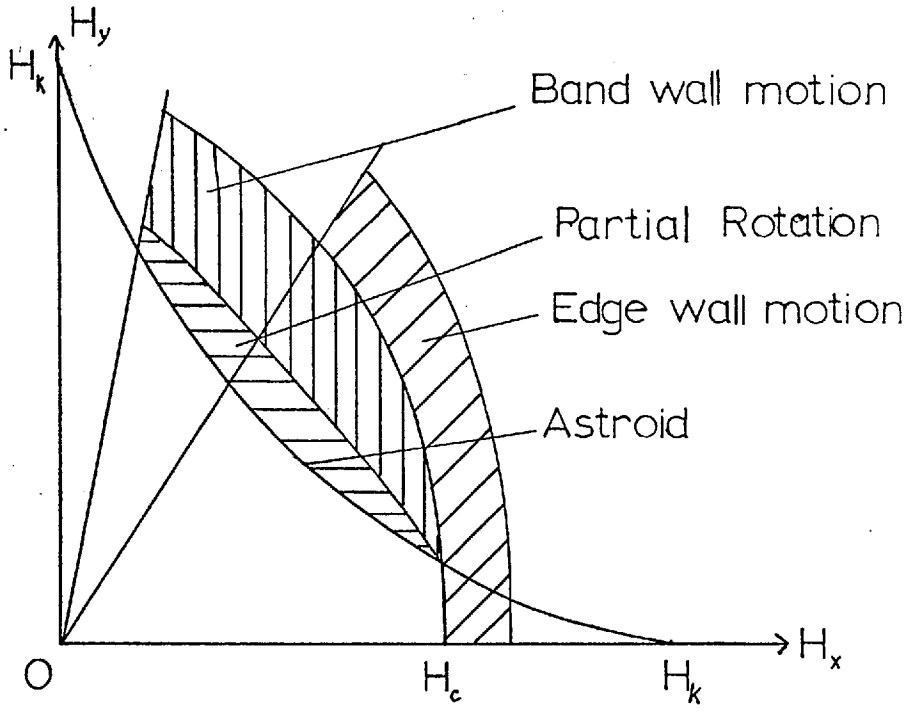

Figure 1.2 Critical fields for rotation and wall motion (M.7)

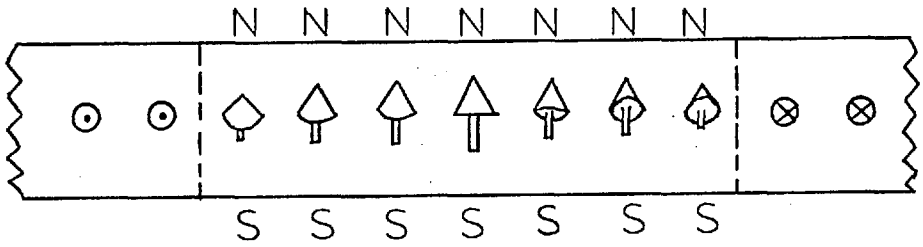

(a)

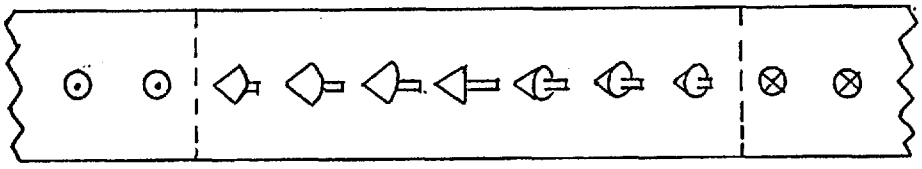

(b)

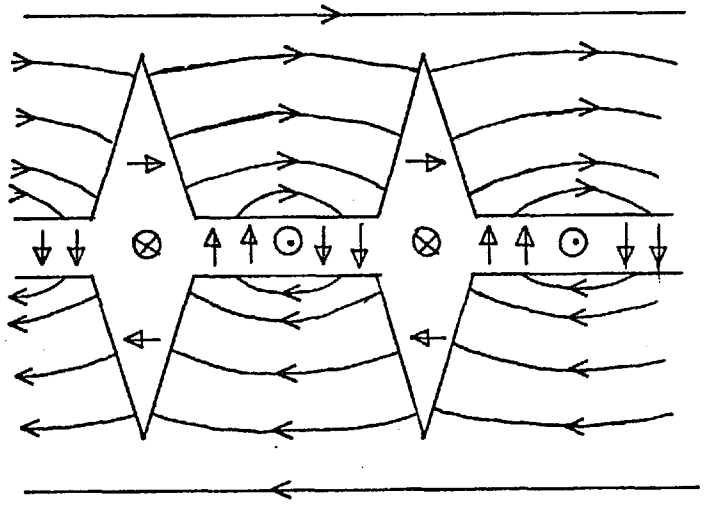

(c)

Figure 1.3 (a) Section of a Bloch wall
(b) Section of a Néel wall
(c) Plan of a cross-tie wall

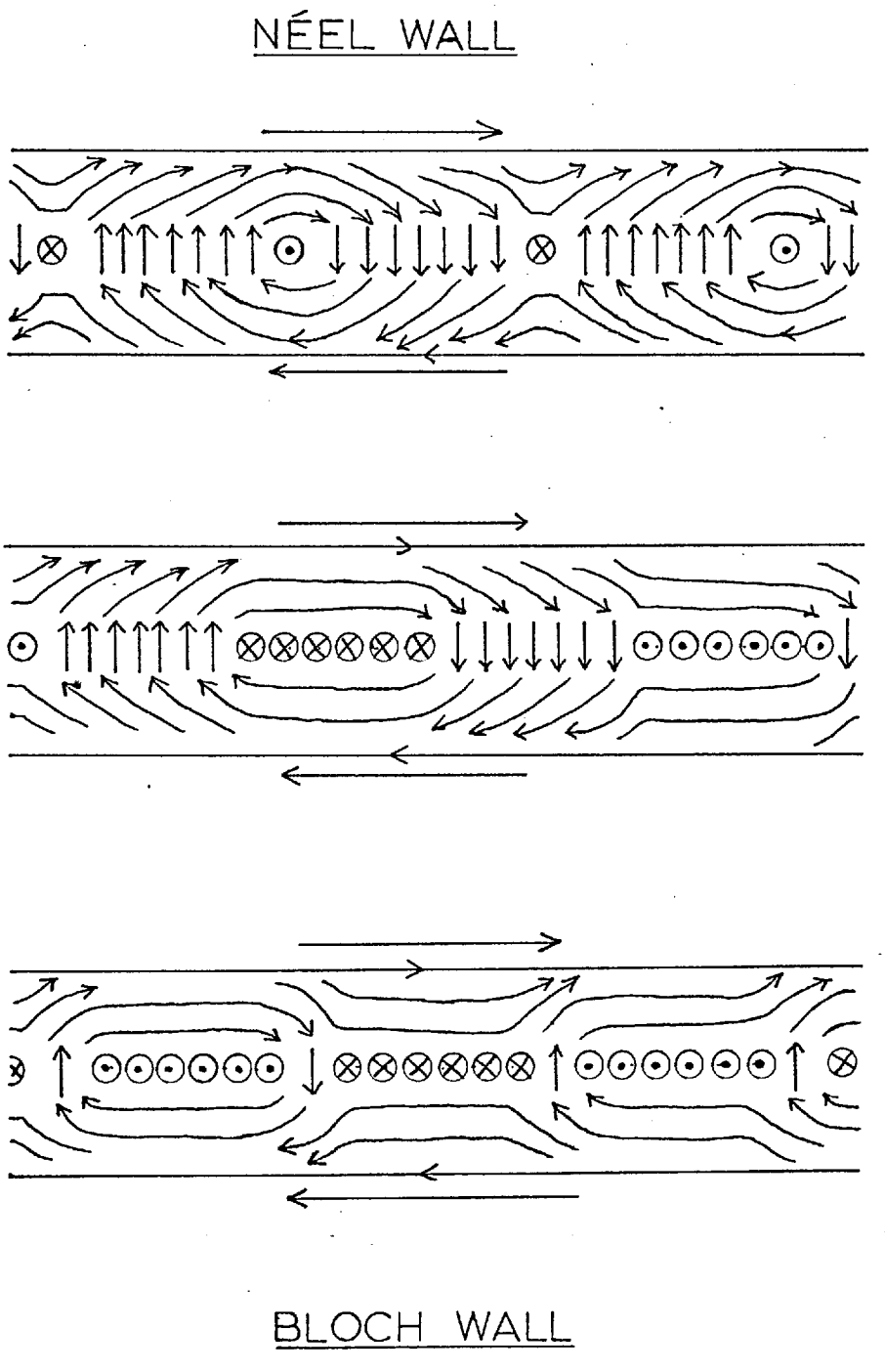

Figure 1.4 Plan diagrams of the transition from a Néel wall to a Bloch wall with increasing thickness (F.2)

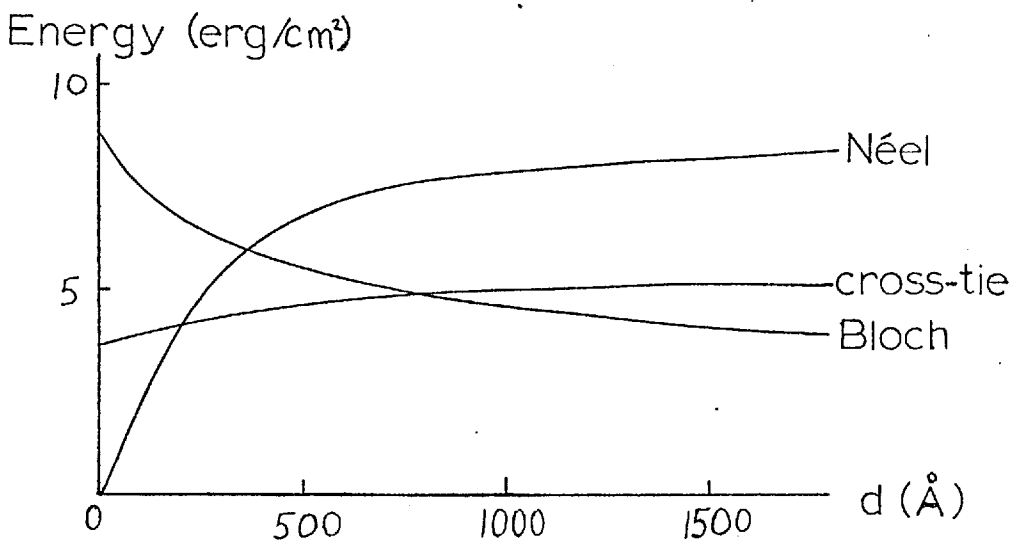

Figure 1.5.a Surface energy densities of various walls as a function of film thickness (M.3)

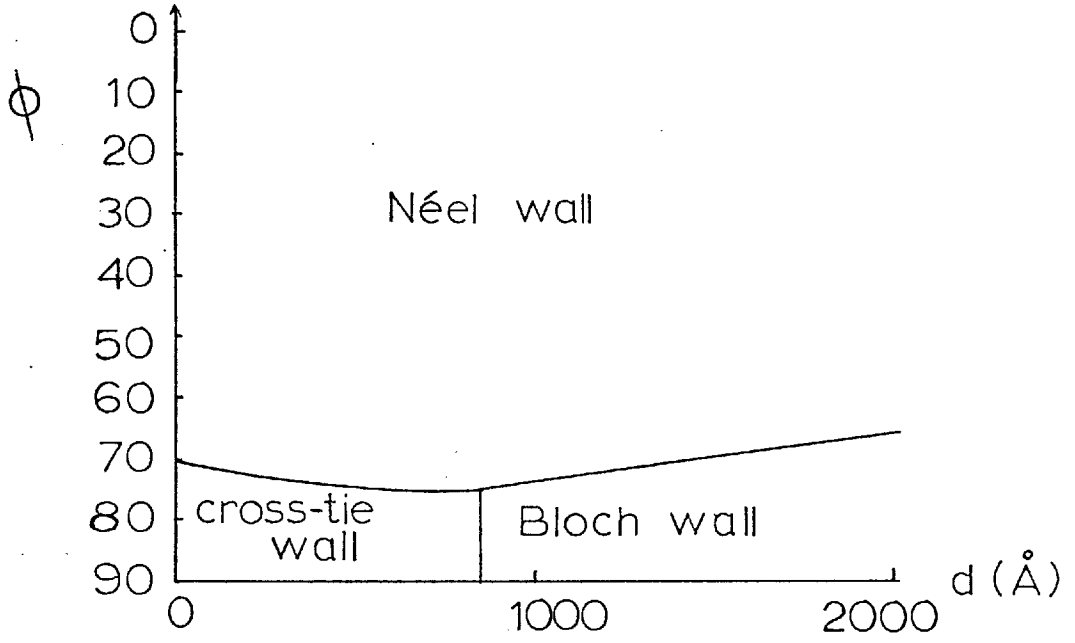

Figure 1.5.b Diagram showing which type of wall is stable for a given thickness (d) and angle (ϕ) between the magnetisation outside the wall and the hard direction (M.3)

CHAPTER 2

The Reversal Behaviour of Films

In this chapter we will consider in some detail the reversal mechanisms in thin films to see how well they fit the theoretical model of Stoner and Wohlfarth (S.1). This model will also be extended to include the cases of a film with biaxial anisotropy and a single crystal film, which will in general possess both biaxial and uniaxial anisotropy.

2.1. Theoretical Model for the Reversal of Uniaxial Films

Polycrystalline ferromagnetic films prepared in a magnetic field possess a uniaxial anisotropy (B.2) and following Stoner and Wohlfarth's model, originally proposed to explain the B-H loops of bulk uniaxial materials, fairly good agreement has been obtained for thin films. Stoner and Wohlfarth's model (hereafter abbreviated to S-W) assumes that the film can only be a single domain (following Kittel, K.1) and that reversal occurs by coherent spin rotation. This means that the exchange coupling is strong enough to keep all the spins parallel so that they rotate together on applying a magnetic field.

For a field, H_a, applied at an angle α to the uniaxial easy direction (figure 3.2) the total magnetic free energy density may be written as:

$$E_T = K_u \sin^2\theta - M_s H_a \cos(\theta - \alpha)$$

where θ is the angle between the saturation magnetisation, M_s, and the easy direction. (K_u is the uniaxial anisotropy constant.) The stable positions of the magnetisation at any particular field are given by

minima in the total magnetic free energy density. These are given by:

$$\frac{\partial E_T}{\partial \theta} = 0 \qquad \text{and} \qquad \frac{\partial^2 E_T}{\partial \theta^2} < 0.$$

In most magnetic text books detailed behaviour with the applied field in the uniaxial easy and hard directions is considered so only a brief summary will be given here. For the applied field in the easy direction ($\alpha = 0$), two stable states ($\theta = 0, \pi$) are derived, these becoming unstable (when the second derivative of E_T with respect to θ equals zero) when $H_a = \pm \frac{2K_u}{M_s}$. This field is known as the anisotropy field H_k.

The hysteresis loops may be obtained by plotting the component of magnetisation parallel to the applied field (for the 'aligned' loops) and perpendicular to the applied field (for the 'crossed' loops) against the applied field. The aligned loops in the easy and hard directions are shown in figure 2.1.

From these loops we can deduce two general ideas: (i) In the easy direction for certain fields there are two possible magnetisation states, and which state the magnetisation is in will depend on its magnetic history; (ii) Where there is more than one stable state the magnetisation can switch from one state to the other at a certain critical field. At this field the initial state begins to go unstable ($\partial^2 E_T / \partial \theta^2 = 0$).

If we write the general energy density in terms of the field components in the hard (y) and easy (x) directions, we will have:

$$E = - M_s H_x \cos\theta \; - M_s H_y \sin\theta \; + K_u \sin^2\theta .$$

Solving this using the conditions $\frac{\partial E}{\partial \theta} = \frac{\partial^2 E}{\partial \theta 2} = 0$, we have

$$H_x = \frac{2K_u}{M_s} \cos^3\theta \qquad \text{and} \qquad H_y = -\frac{2K_u}{M_s} \sin^3\theta ,$$

or, eliminating θ,

$$(H_x)^{\frac{2}{3}} + (H_y)^{\frac{2}{3}} = (2K_u/M_s)^{\frac{2}{3}} = (H_k)^{\frac{2}{3}} \qquad .. \quad .. \quad .. \quad .. \quad .. \quad (2.1)$$

If we use the reduced field notation, i.e. $h_x = \frac{H_x}{H_k}$, this simplifies further to:

$$h_x^{\frac{2}{3}} + h_y^{\frac{2}{3}} = 1 \qquad .. \quad .. \quad .. \quad .. \quad .. \quad .. \quad .. \quad .. \quad (2.1a)$$

This is the equation of a hypercycloid with four cusps (commonly called an astroid), and is shown in figure 2.2a, which represents the locus of critical fields. Outside there only occur irreversible changes in the magnetisation, whereas inside all the changes are completely reversible.

The astroid has one very important property, i.e. its tangents represent stationary points in the energy, $\frac{\partial E}{\partial \theta} = 0$, so if a tangent is drawn to the curve from the tip of the resultant applied field vector, this will be the direction of the magnetisation. Care must be taken when the field vector lies inside the astroid as there are four possible tangents. Two of these tangents (H_2A and H_2B in figure 2.2a) will be energy minima as they are nearest to the easy axis and the other two will be maxima. Which of the two minima the magnetisation will be lying along depends upon whether, at zero field, M was lying in the $+H_x$ or $-H_x$ direction.

From this curve we can derive the hysteresis loop in any general direction. Referring to diagram 2.3a, as the field H_a is decreased from

saturation and then reversed
(the magnetisation goes through the positions M_1, M_2. The component of M parallel to H decreases until in the position M_3 a switch to M_4 occurs. Following the curve round we have the hysteresis loop shown in figure 2.3b. Thus the astroid saves a great deal of mathematics in determining the qualitative thin film behaviour.

2.2. Actual Behaviour

Although certain films (notably 80/20 NiFe) follow this model extremely well, none can be completely described by it.

The main discrepancies are that: (a) the coercive force in the easy direction is generally different from the predicted one of the anisotropy field (H_k); (b) the discontinuous jump in magnetisation direction actually consists of several jumps over a small range of fields; (c) the hard-direction loop opens slightly as the field is increased above H_k; (d) the observation of flux changes perpendicular to the applied field (the 'crossed' loops) enables the fraction of the total flux rotating to be determined. When the field is exactly along the easy or hard directions none is observed to be rotating, contrary to theoretical predictions.

The reason for these differences is that one of the basic assumptions, that the film remains a single domain, is not always valid.

This implies that with multidomain states we have the second possibility of reversal by domain-wall motion. In fact, reversal solely by coherent rotation has never been observed and reversal usually occurs partly by rotation and partly by domain-wall motion.

The reversal process can be conveniently divided into three categories determined by the direction of the applied field relative to the uniaxial easy axis.

2.2.1. Reversal with a Field Applied along the Easy Axis. As has previously been mentioned, the shape of the easy axis hysteresis loop in some films is in good qualitative agreement with the S-W model, but the coercivity is not equal to H_k. Another disagreement is that the reversal itself consists of a series of discreet irreversible jumps in the magnetisation rather than one abrupt switch (B.10). These two points seem to suggest that reversal occurs by wall motion rather than by rotation.

It was first pointed out by Shtrikman and Treves (S.6) that the demagnetising fields at sharp discontinuities in the magnetisation could be reduced if closure domains were formed. Therefore, at the edge of a film one might expect closure domains, but this would require domains magnetised in the hard direction, which would be energetically unfavourable. However, the demagnetising fields could be reduced by the formation of reverse spike domains and this is what actually happens. These reverse domains can exist in zero applied field so that when a reverse field is applied these domains will grow inwards from the edge and reverse the film.

If these edge domains are eliminated, as in the barrier films of Methfessel et al (M.5) then reversal occurs at the domain nucleating field or the field for domain-wall motion, whichever is the higher.

With edge domains present the reversal will depend on the field for domain-wall motion, which varies across the film. This is caused by inclusions and inhomogeneities producing localised energy barriers (pg. 285 of reference C.10). It is the wall moving from one energy barrier to the next which causes the Barkhausen jumps, and so for square-loop films we expect the coercive force to be approximately equal to the maximum wall-motion field. Thus we see that the squareness of the loop is not governed by the anisotropy as predicted by theory, but by the fact that reverse-edge domains are present at fields lower than H_c and by the number of inhomogeneities in the film which might pin the domain walls.

Evaluation of coercive force mechanisms is very difficult and many authors have proposed models. The contributions to the wall-motion coercive force fall into four possible groups: (a) dispersion of the anisotropy easy directions; (b) thickness variations due to surface roughness; (c) wall length changes; and (d) interactions with non-magnetic inclusions. Middlehoek (M.3) has calculated contributions from the first three and finds that the first two are the important ones and thickness variations are only appreciable for thick films containing Bloch walls. Non-magnetic inclusions can have an appreciable effect for high densities of inclusions and agreement between theory and experiment is fairly good (N.4, N.5).

We see, therefore, that the coercive force, H_c, determines the method of reversal in the easy direction. For H_c much less than H_k the reversal occurs by wall motion and is governed mainly by the anisotropy dispersion and the presence of edge domains.

For films with H_c larger than H_k (or equal to it) we expect the reversal to occur by rotation in agreement with theory. However, the behaviour is rather complicated and is dealt with in section 2.2.4.

2.2.2. Reversal with the Applied Field along the Hard Axis. The discrepancies with this field configuration are that no flux is observed in the easy direction during reversal and that the hysteresis loop opens at and above the saturating fields. Both these discrepancies are caused by the presence in the film of magnetisation ripple, which is probably due to local strains and differing crystallite orientations causing variations in the local anisotropy from point to point.

As will be shown later (equation 3.6 or table 3.3) the amplitude of the ripple is field dependent, therefore as the field is decreased from saturation towards H_k the ripple amplitude increases, so that although the average magnetisation will have no torque acting on it the local magnetisation, which varies periodically, will have a torque on it. Thus, instead of the magnetisation rotating round to an easy axis as the field is decreased, we find that it splits up into bands of oppositely-magnetised sections, which accounts for the lack of flux measured in the easy direction. The width of these bands, or 180° domains, is governed mainly by the ripple wavelength, and since the ripple depends on the anisotropy dispersion, so the films having lower dispersion will have widely-spaced domains in the final multidomain state. Incidentally, this phenomenon is known as 'hard-axis fallback' and provides an accurate method of finding the hard axis (i.e. evenly-

spaced domain walls) and also provides a method of measuring the anisotropy dispersion (M.3).

The aligned loops always possess some degree of hysteresis unless the magnitude of the peak a.c. field is less than $2H_k$, in which case the film can behave as a single domain, since the magnetisation lies within the astroid. If the film is saturated we do observe hysteresis, and the reason for this lies in the hard-axis fall-back mentioned above. After saturation the film can possess many domains and it is the presence of these domains which causes the hysteresis losses. As the saturating field is decreased the ripple amplitude increases until small-angle Néel walls are formed (F.5). These contain surface poles and if they are sufficiently close together (small ripple wavelength and high dispersion) they cause stray fields which 'lock' the ripple, thus preventing further rotation except in irreversible jumps, so that reversal will occur by ripple reorientation, which involves hysteresis (F.6).

Thus films with lower dispersion have smaller stray fields from the more widely-spaced Néel walls and so show less hysteresis, as expected.

2.2.3. Intermediate Directions. When a field is applied in an intermediate direction the magnetisation should, ideally, rotate until a critical field (when the tip of the field vector touches the S-W astroid) is reached and an irreversible switch occurs. In practice, the rotation to approximately the critical field is observed, then domains are formed and reversal is usually completed by wall motion. There appear to be three

distinct methods by which reversal occurs, governed mainly by the anisotropy dispersion in the film. Models have been proposed (P.4, M.6, M.7, S.7, S.8) to explain these mechanisms but relationships between the wall angle and the applied field direction do not agree very well for any model. The three models will be briefly described; a fuller account can be found in Prutton's book (P.2).

For very low dispersion the low stray field model (P.4) is thought to be applicable. In this, rotation occurs to the critical field when elongated domains are nucleated at an edge and grow across the film in bands. The angle of the wall bisects the magnetisation direction, reducing the stray field to zero.

Films with high dispersion reverse by partial rotation (M.6). Because of its large dispersion, a film of this type will have enhanced ripple so that when the average magnetisation is rotated to the critical field some of the ripple will pass this point and switch, again forming elongated domains. However, in this case the wall angle does not bisect the magnetisation directions, which are a compromise between the easy axis and the applied field. The stray fields which arise from this determine whether further rotation occurs by the domains' moving parallel to each other or by a new domain parallel to the easy axis being nucleated and moving across the film.

The final model, which seems to apply to intermediate dispersion, is comprised of a mixture (S.8). The large stray fields at the film edge nucleate domains as in the first model, but the wall direction is governed by the stray field and the easy direction, and in general does

not bisect the magnetisation direction. The resulting labyrinth walls have very complex fields associated with them, the coupling between the walls is unknown and many approximations have to be made in Smith's calculations (S.7).

The various types of wall motion which occur for a film under different switching angles is graphically demonstrated by Middlehoek (M.7) for a film showing partial rotation.

2.2.4. Behaviour in Anomalous Films. Due to the method of fabrication, the difficulty of reproducibility has been one of the drawbacks of thin films. Because of this, a great deal of work has been concerned with the anomalous behaviour of some films. This behaviour is brought about by using low evaporation rates, poor vacuum, high substrate temperatures and by evaporating onto agglomerated metal underlayers.

There are three distinct types of anomalous films depending on the amount of anisotropy dispersion they possess.

First, there are high coercivity films including the inverted films (K.5) already mentioned. These have a coercive force of the order of, or greater than, H_k, and one would expect that they might switch by coherent rotation as wall motion requires a higher field. However, even inverted films switch by wall motion and the explanation, due to Smith et al (S.9), is as follows: As the field in the easy direction is decreased from saturation the dispersion, being large, causes the formation of low-angle Néel walls or ripple walls. The ripple amplitude increases as the field is increased in the opposite direction until it

becomes locked by the stray field from the Néel walls. Reversal is completed by reverse domains nucleating at the edge and moving across the film.

The next type of film is termed 'rotatable initial susceptibility' (RIS) film. The reason for this is that an easy axis can apparently be induced in any direction by means of a high field. Cohen (C.11) has subdivided RIS films into two types: type I have a large signal in a small drive hysteresis loop perpendicular to a previously-applied high a.c. field and have no signal parallel to it; for type II films the converse is true. The explanation of this behaviour is that after the high a.c. field has been applied the type I film magnetisation remains in this direction, which acts as an easy axis. Type II films, possessing higher dispersion, are left in a locked state on removal of the a.c. field and so no signal is observed perpendicular to the magnetisation, but a signal is observed parallel to it since the magnetisation can rotate towards the induced easy axis within each domain.

The last type of film is the 'mottled' film which possesses low remanance as well as RIS (which still has high remanance). The name comes from the appearance of the Bitter patterns first observed by Huber et al (H.5), whose interpretations are based on an easy axis perpendicular to the film. This effect only occurs in films above a certain thickness and for Ni-rich alloys having negative magnetostriction. This, together with the fact that the film loses its mottled appearance on being released from the substrate, suggests that its cause is inhomogeneous strains via magnetostriction.

Two similar qualitative models have been proposed (C.11, F.7) which explain the behaviour of these types of film, but there is still doubt as to whether these models apply.

The first model, due to Cohen, suggests that the film contains some high anisotropy centres, the density of which governs how poor the film is.

The model due to Flanders et al (F.7) suggests that the film behaviour depends on the volume fraction and the distribution of anisotropies of randomly oriented material present in the film.

The causes of these 'centres' are not very clear. Cohen, in his paper, puts forward strong evidence for inhomogeneous strains being the cause, but work by Wilts and others (W.7, P.5, L.8) points to the fact that RIS behaviour and rotatable anisotropy are caused solely by oxidation as this has been shown to occur for non-magnetostrictive alloys. However, the fact that Wilts is unable to produce mottled films by his oxidation-reduction method does indicate that inhomogeneous strains play an important part in the formation of these films.

It seems that the presence of NiO has an effect on the film either by uniaxial exchange coupling or by a constraint mechanism (B.11) which produces RIS behaviour. This surface layer of NiO might prevent the magnetisation from tipping out of the film plane and so 'mottled' films are not allowed to form. In the absence of oxidation the large isotropic strain in the film plane may produce an easy axis perpendicular to the plane and so the magnetisation will no longer be planar, causing mottled films. (This is strongly supported by the observation of stripe domains in films with large perpendicular anisotropies (L.7).)

2.3. Reversal in Biaxial Films

Cubic crystals have a magnetocrystalline anisotropy energy density:

$$E_k = K_1 (\gamma_1^2\gamma_2^2 + \gamma_2^2\gamma_3^2 + \gamma_3^2\gamma_1^2) + K_2 \gamma_1^2\gamma_2^2\gamma_3^2$$

where γ_1, γ_2, γ_3 are the direction cosines of the magnetisation relative to the cube edges and K_1, K_2 are the first and second order magnetocrystalline anisotropy constants. Due to the large demagnetising factor normal to a thin film, $\gamma_3 = 0$ when the film plane is (001) and the anisotropy energy density reduces to $E_k = \frac{1}{4}K_1 \sin^2 2\theta$, where θ is the angle which the magnetisation makes with the easy axis in the film plane.

Proceeding as we did for the uniaxial case, we have the total magnetic free energy density:

$$E = \tfrac{1}{4}K_1 \sin^2 2\theta - M_s H_a \cos (\theta - \alpha) \quad .. \quad .. \quad .. \quad .. \quad (2.2)$$

Now E becomes unstable when $\frac{\partial^2 E}{\partial \theta^2} = \frac{\partial E}{\partial \theta} = 0$ which gives:

$$M_s H_a \sin (\theta - \alpha) + \frac{K_1}{2} \sin 4\theta = 0 \quad .. \quad .. \quad .. \quad .. \quad (2.3)$$

and $$M_s H_a \cos (\theta - \alpha) + 2K_1 \cos 4\theta = 0 \quad .. \quad .. \quad .. \quad .. \quad (2.4)$$

or in terms of the reduced field components $h_x = \frac{M_s H_a}{2K_1} \cos\alpha$, $h_y = \frac{M_s H_a}{2K_1} \sin\alpha$, equations (2.3) and (2.4) become:

$$h_y - h_x \tan\theta = \frac{\sin 4\theta}{4 \cos\theta} \quad .. \quad .. \quad .. \quad .. \quad .. \quad .. \quad (2.3a)$$

$$h_x + h_y \tan\theta = - \frac{\cos 4\theta}{\cos\theta} \quad .. \quad .. \quad .. \quad .. \quad .. \quad .. \quad (2.4a)$$

In the easy direction ($\theta = 0$) gives $h_x = -1$, $h_y = 0$, therefore an irreversible magnetisation change occurs in the easy direction when $h = -1$ or $H_a = - \frac{2K_1}{M_s} = -H_1$, the biaxial anisotropy field. A closer

examination reveals that the film's behaviour in the biaxial easy axis is very similar to the uniaxial case with the replacement of H_k by H_1.

The hard direction is more difficult and generally requires numerical solutions for the discontinuities. However, we can easily visualise what is happening by using the biaxial 'astroid', derived in a similar manner to the uniaxial case.

From equations (2.3a) and (2.4a) we have:

$$\left.\begin{aligned} h_x &= -\cos\theta\cos 4\theta - \tfrac{1}{4}\sin\theta\sin 4\theta \quad .. \quad .. \quad .. \\ h_y &= -\sin\theta\cos 4\theta + \tfrac{1}{4}\cos\theta\sin 4\theta \quad .. \quad .. \quad .. \end{aligned}\right\} \quad (2.5)$$

This, with θ as the variable parameter, represents the locus of fields at which irreversible magnetisation changes can occur. The eight-cusped hypercycloid is shown in figure 2.2b and the ringed tips represent the easy axes, which will be [110] for 80/20 NiFe. Using the property of the astroid for determining the direction of the magnetisation at any known field, we are able to observe what changes occur in the magnetisation for various fields and so produce hysteresis loops.

As has previously been mentioned, the easy axis loop is square, as in the uniaxial case. However, for the hard direction the loop is open and switching occurs between adjacent easy axes. This is best explained by referring to diagram 2.2b. As the field is increased in the hard direction the magnetisation, assumed to be originally lying along the easy axis 'OB', moves around the arm 'BE' of the curve until it is parallel to the applied field. The corresponding component of the magnetisation parallel to the applied field is plotted on the 'aligned' hysteresis loop and the perpendicular component gives the 'crossed' hysteresis loop.

On decreasing the field the magnetisation rotates back around the arm 'EB' and after reversal to position M_1 whereupon, as the field is further increased, the magnetisation will switch to a new arm of the curve, 'AD'. This process is now repeated about -H in the same way.

By similar methods the hysteresis loops at other angles have been derived and are displayed in figure 2.4. Note that at certain intermediate angles there are double jumps corresponding to intermediate states, which have been omitted by Edel'man (E.1) working on similar calculations.

2.4. Reversal Behaviour of Single Crystal Films

It is difficult to compare theory and experiment for the biaxial case as most films possess a uniaxial component in the anisotropy and only in very careful experiments can $\frac{H_k}{H_1}$ be reduced below about 5%. The presence of the uniaxial component not only alters the switching fields but also eliminates real easy (hard) axes except where the deposition field is so arranged that it produces an easy (hard) axis parallel to either of the biaxial easy or hard axes. We must now calculate the curves for magnetisation discontinuities for a real single crystal film containing mixed anisotropies.

The magnetic free energy will depend on both the relative size and orientation of the anisotropies, so consider the general case shown overleaf. For this configuration the total magnetic free energy is:

$$E = - H_a M_s \cos(\alpha - \theta) + \tfrac{1}{4}K_1 \sin^2 2(\theta + \beta) + K_u \sin^2\theta \quad .. \quad (2.6)$$

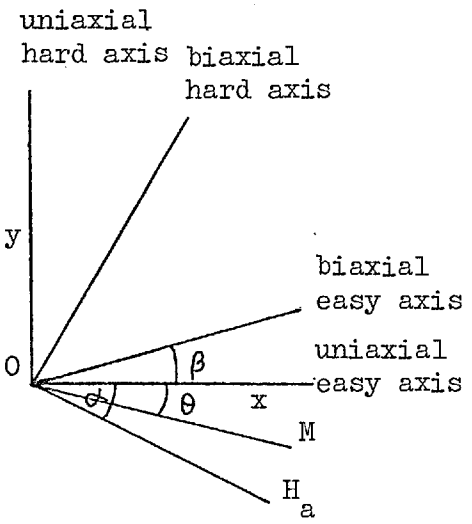

where β is the orientation of the biaxial easy axis relative to the uniaxial easy axis, the other terms having their usual meaning (see Glossary A.1).

The switching fields (the locus of which is given by the astroid), which are solutions of $\frac{\partial E}{\partial \theta} = \frac{\partial^2 E}{\partial \theta 2} = 0$, cannot be obtained easily except for special cases. The policy adopted here is to calculate, numerically, the curves for $\frac{\partial E}{\partial \theta} = \frac{\partial^2 E}{\partial \theta^2} = 0$ for specific cases and from these we can determine the interesting field directions.

Writing equation 2.6 in terms of the reduced field components $h_x = \frac{H_a \cos\alpha}{H_k}$ and $h_y = \frac{H_a \sin\alpha}{H_k}$ we have:

$$\frac{E}{2K_u} = -h_x \cos\theta - h_y \sin\theta + \tfrac{1}{8}\left(\frac{K_1}{K_u}\right) \sin^2 2(\theta + \beta) + \tfrac{1}{2}\sin^2\theta \qquad (2.6a)$$

(i) $\frac{\partial E}{\partial \theta} = 0$ and (ii) $\frac{\partial^2 E}{\partial \theta^2} = 0$ give the following equations:

$$\text{(i)}\quad h_y \cos\theta - h_x \sin\theta = \tfrac{1}{4} b_1 \sin 4(\theta + \beta) + \tfrac{1}{2}\sin 2\theta \qquad (2.7)$$

$$\text{(ii)}\quad -h_y \sin\theta - h_x \cos\theta = b_1 \cos 4(\theta + \beta) + \cos 2\theta \qquad (2.8)$$

where b_1 is the ratio of the anisotropies (K_1/K_u).

From these two equations (2.7) and (2.8) the components of the critical applied fields, h_x and h_y are given by:

$$\left.\begin{aligned} h_x &= -\cos\theta\cos 2\theta - \tfrac{1}{2}\sin 2\theta\sin\theta - b_1\left[\cos 4(\theta+\beta)\cos\theta + \tfrac{1}{4}\sin 4(\theta+\beta)\sin\theta\right] \\ &\text{and} \\ h_y &= -\sin\theta\cos 2\theta + \tfrac{1}{2}\sin 2\theta\cos\theta - b_1\left[\cos 4(\theta+\beta)\sin\theta - \tfrac{1}{4}\sin 4(\theta+\beta)\cos\theta\right] \end{aligned}\right\} \qquad (2.9)$$

We see that the critical curve, again in parametric form, depends on the relative orientation of the anisotropies, β, and on their relative magnitudes, b_1. Only the special case under study is considered here. For 80/20 NiFe, or Ni concentrations higher than 75%, K_1 is negative so that the easy direction in the single crystal film will be [110] (reduced from [111] by demagnetising effects). As the applied field during deposition is parallel to the [100] directions then the angle between the two easy axes will be 45°. The factors governing the relative magnitudes of the anisotropies are the crystallite orientation and the substrate temperature. The two are very closely related and go hand-in-hand, for as the substrate temperature is increased the orientation gets better, so K_1 increases while the uniaxial component decreases (see Chapter 6). Thus for completeness the switching curve is plotted for a range of anisotropies, $b_1 = 0.5$ to 3.0 and $\beta = 45^\circ$ (see figure 2.5). For other relative orientations the reader is referred to work by Pugh (P.6) and Torok et al (T.2) but as will be shown later the separate anisotropies cannot easily be evaluated using the ~~biaxial~~ biased susceptibility apparatus unless $\beta = 45^\circ$.

From the curves shown in figure 2.5 we can see that the easy axis is not at 45° to the biaxial hard axis but varies with the ratio of anisotropies. The method of finding the easy axis is the same as finding the hard axis, which is to maximise both h_x and h_y simultaneously. From equation (2.9) with $\beta = 45^\circ$, $\frac{\partial h_x}{\partial \theta} = 0$ or $\frac{\partial h_y}{\partial \theta} = 0$ gives:

$$\sin 2\theta \cos\theta - \frac{5b_1}{2} \sin 4\theta \cos\theta = 0 \qquad .. \quad .. \quad .. \quad .. \quad (2.10)$$

which has the solutions, $\sin\theta = 0$, $\cos\theta = 0$ and $\cos 2\theta = \frac{1}{5b_1}$. The first two solutions represent the biaxial hard axes. The combined easy axis is at an angle $\theta = \frac{1}{2}\cos^{-1}\frac{1}{5b_1}$ to the uniaxial easy axis which in general is not 45°. Furthermore, the magnetisation will not be parallel to the applied field along one of these easy directions since the tangents to the easy axis cusps do not pass through the origin.

As in the pure biaxial case we may observe the two possible jumps in the hysteresis loop as the magnetisation switches into an intermediate state. Once again, due to their complexity, the hysteresis loops have to be numerically calculated. A series of loops at various field directions is shown for the ratio of anisotropies = 9 (figure 8.2). Since the combined easy direction depends on the ratio of anisotropies, one expects the angles at which these double jumps occur to depend on the anisotropies also. This is in fact the case as is shown in Chapter 8 where the hysteresis loops of a good single-crystal film are compared with the theoretical ones.

In this comparison good agreement is shown for the 'aligned' loops but the 'crossed' loops, although not measured here, disagree in the hard direction in the same manner as they did for uniaxial films. This is to be expected as the effects of dispersion are enhanced due to the close proximity of the easy axes (only about 45° from the hard axes). Reversal by wall motion in single crystal films has not been as intensively studied as in other films, although much work has been done on the observation of domain configurations, mainly by Lorentz Microscopy.

There are three main reasons for this:

(a) It is difficult to produce good single crystal films;

(b) The interpretation of their switching behaviour is far more difficult than the uniaxial case due to the added complication of the biaxial anisotropy;

(c) Very few Bitter patterns have been observed because the film is released (if prepared on sodium chloride), when the colloid is placed on it. Furthermore, most single crystal substrates possess many small cleavage steps on their faces which make observations by the Kerr effect and in dark field illumination very difficult.

It has been shown that only 90° and a few 180° domain walls are present in good single crystal films (S.10, T.3). During demagnetisation the renowned checker-board pattern is observed and no cross-tie walls have been observed although the 180° walls do possess some fine structure (S.11). Since the easy axes are only about 45° away from the hard axes the formation of domains should occur very easily and one would expect wall motion and partial rotation to be responsible for most reversals. As has previously been mentioned, the anisotropy dispersion will be of great importance in the hard direction. It is for these two reasons that very little work has been published on the use of single crystal films in computers, as outlined by Pugh (P.6).

The dispersion may be measured using a similar method to Middlehoek (M.3) and Crowther (C.12), by observing the transverse hysteresis loop around the biaxial easy and hard directions.

As can be seen from the above, the reversal behaviour of single crystal films is far more complicated than that of uniaxial films and as a consequence very little work has been done on single crystal films, even though the better alignment of the crystallites reduces angular dispersion and so should reduce the ripple amplitude.

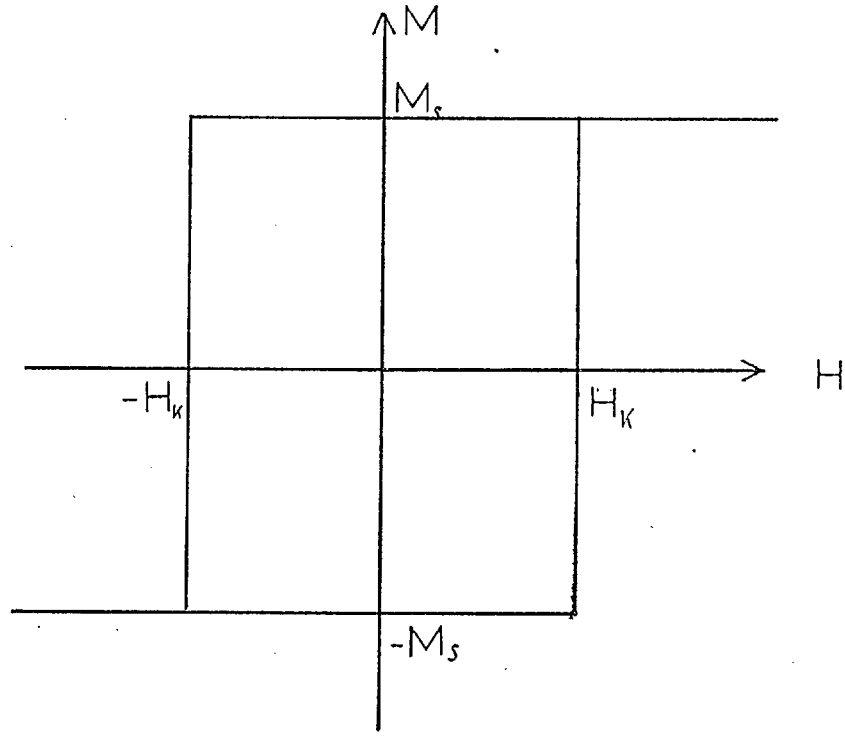

(a) easy direction

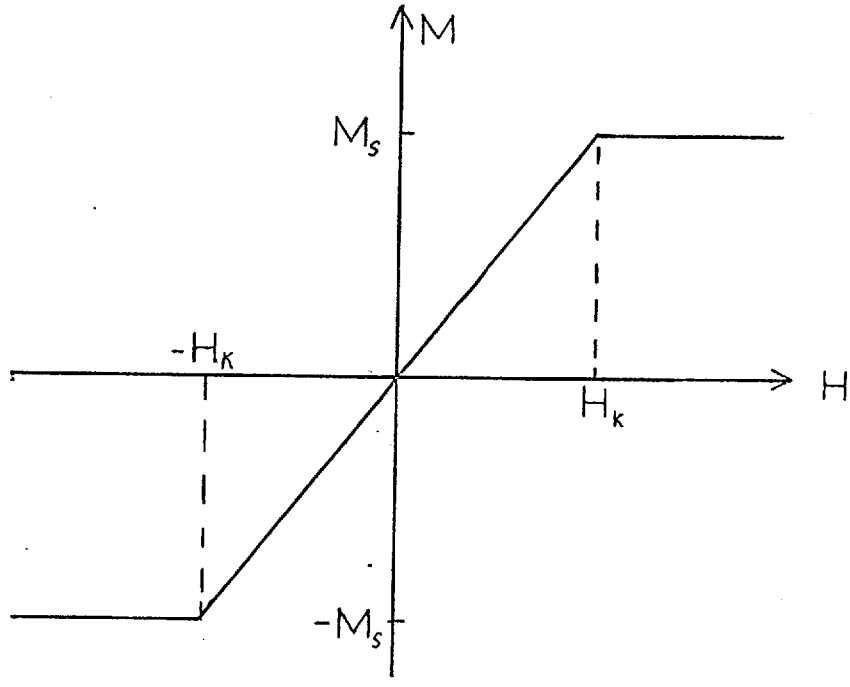

(b) hard direction

Figure 2.1 Calculated hysteresis loops for a uniaxial film

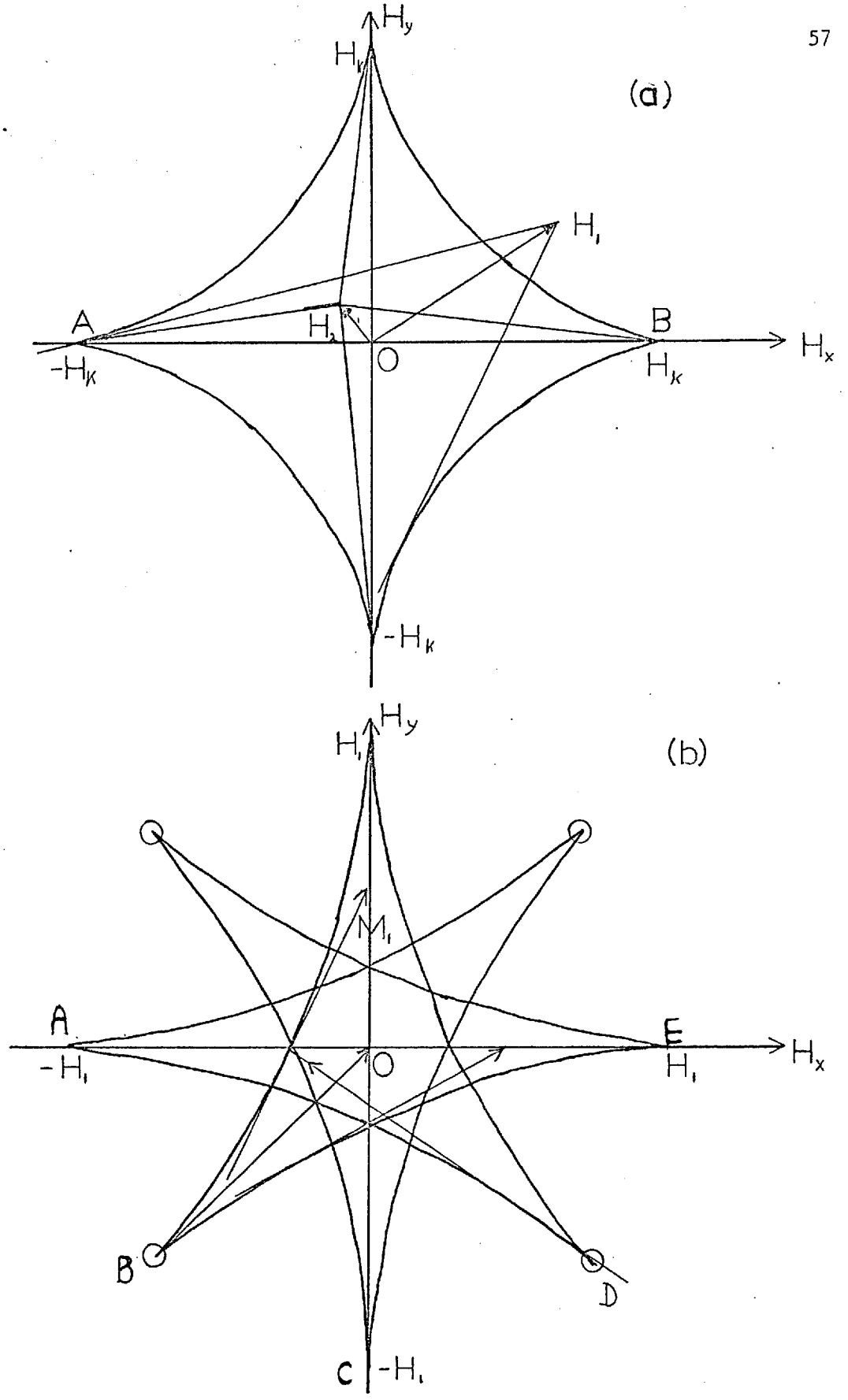

Figure 2.2 Theoretical switching curves for (a) uniaxial and (b) biaxial anisotropy

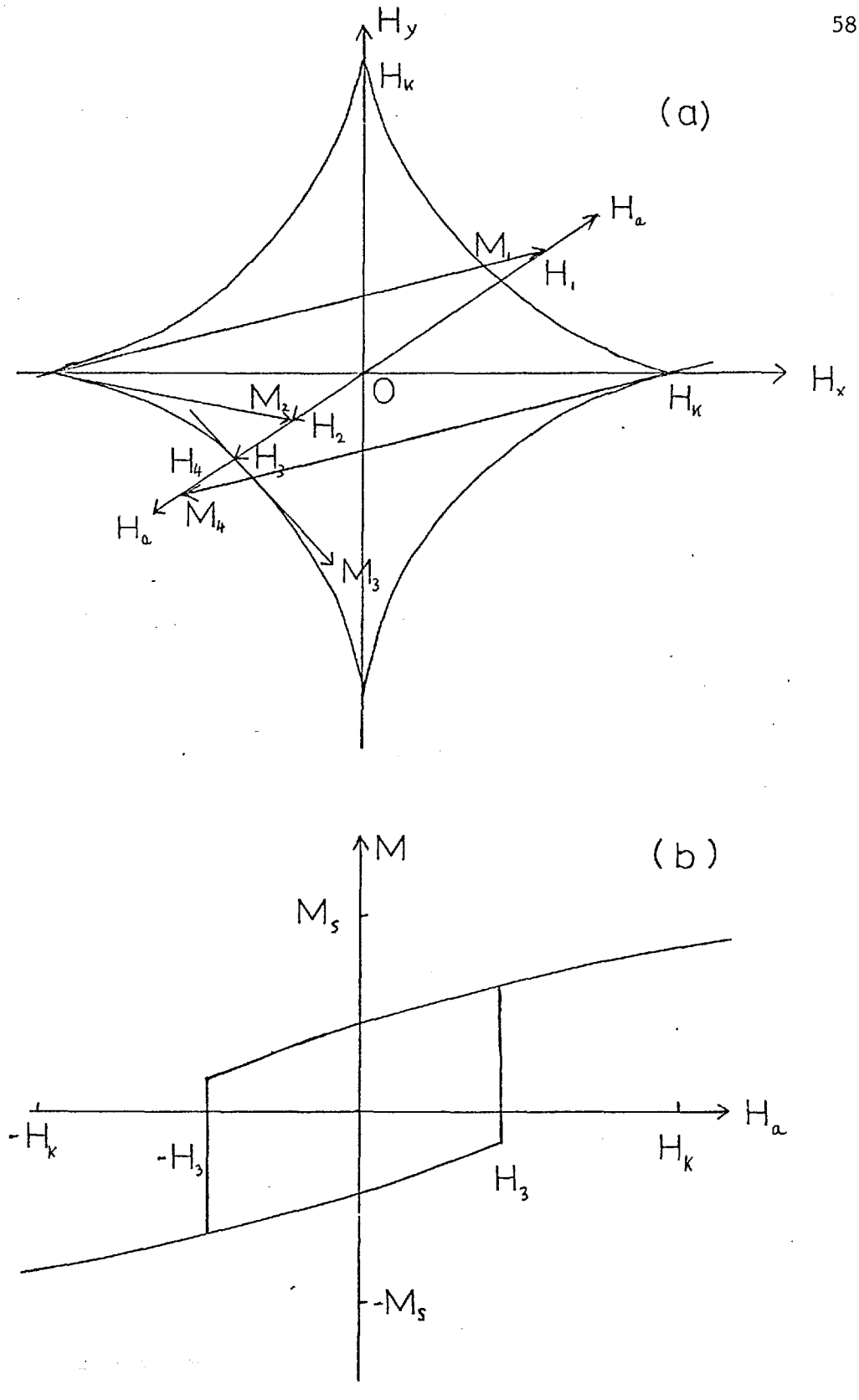

Figure 2.3 Determination of a hysteresis loop at an intermediate angle using the astroid

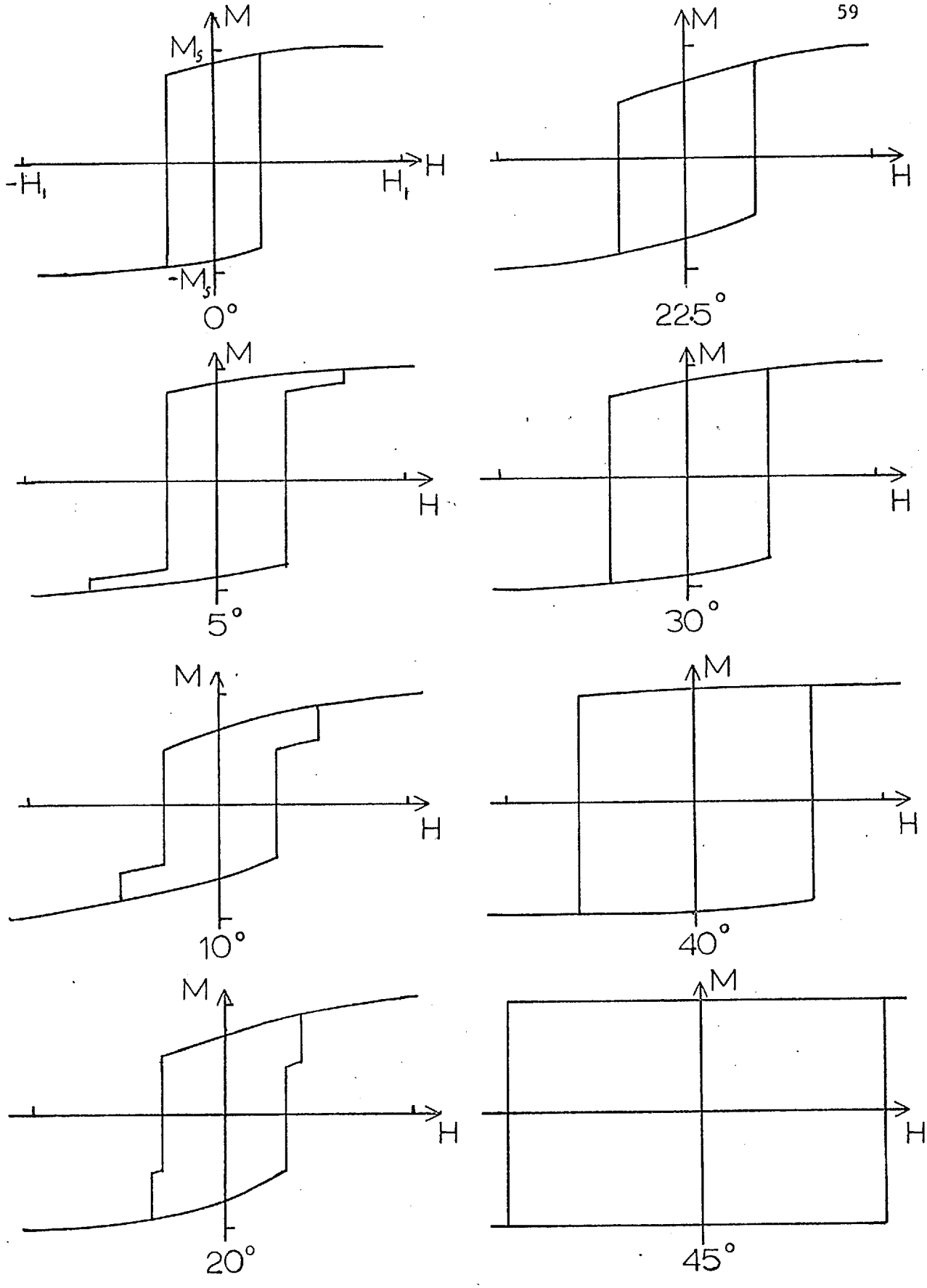

Figure 2.4 Series of theoretical hysteresis loops at various angles for pure biaxial anisotropy

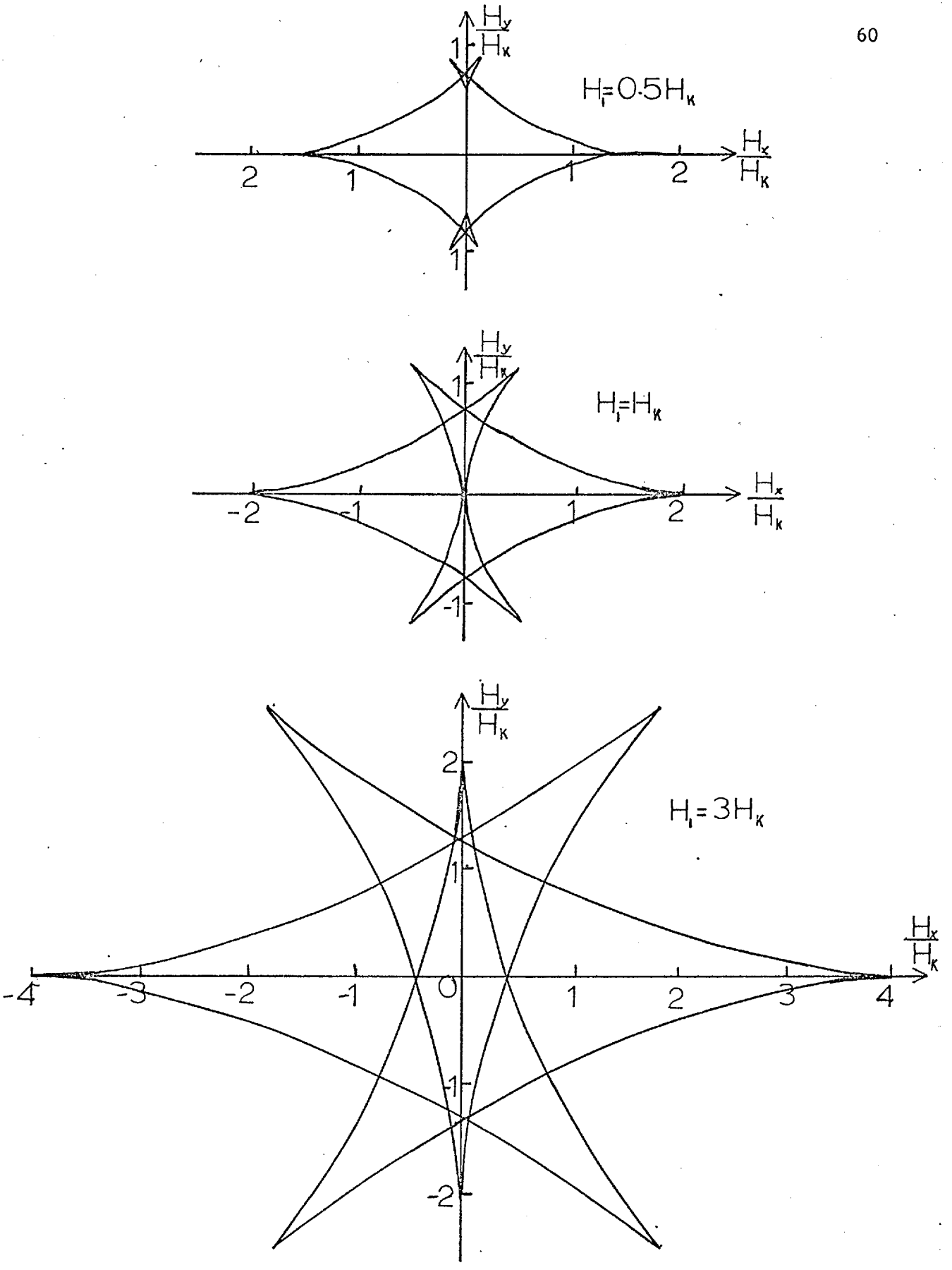

Figure 2.5 Theoretical switching curves for various combinations of uniaxial and biaxial anisotropies

CHAPTER 3

Magnetisation Ripple

As has been mentioned in the previous chapters, magnetisation ripple is one of the serious drawbacks of thin film stores. In this chapter the theoretical models will be analysed in greater detail and a brief comparison of theoretical predictions and experimental results will be made.

3.1. Introduction

It is now well established that the magnetisation varies periodically, in direction, in a real film since its discovery by Fuller et al (F.4). The scale of this magnetisation ripple is typically 1^{o} amplitude and 1 micron wavelength so that only Lorentz microscopy or high-resolution magneto-optic effects (usually the Faraday effect (L.3)) can be used to observe this effect directly. Most of the experimental work determining ripple wavelengths and amplitudes has involved a geometrical optics interpretation which makes the results doubtful, since it is known that unless special precautions are taken only wave optical treatments can be used (W.3). Thus great care must be taken when comparing theoretical results with values obtained from Lorentz microscopy. In more recent work, by Suzuki and Wilts (S.2) for example, care has been taken to reduce the apparent source size so that the error involved in using geometrical optics is minimised.

From the striations observed in Lorentz micrographs there are two possible magnetisation configurations, the transverse and longitudinal ripple, as shown in figure 3.1. Both these configurations have the same exchange and anisotropy energies but in the transverse ripple the induced pole distribution is different producing larger stray ~~magnetisation turns through sharper angles producing a higher value for~~ fields ~~div. M~~ and hence a higher magnetostatic energy.

Since actual observation of ripple is limited to Lorentz microscopy or the Faraday effect, work has been concentrated on macroscopic variables which have been related directly by various theories to film parameters. The most popular macroscopic variable is the incorrectly-termed 'angular dispersion' α_{90}. This is defined in the following way: if a field greater than H_k is applied at an angle α_{90} to the hard axis and then reduced to zero, the remanence in the easy direction is 90% of the saturation magnetisation. Thus the angle α_{90} is an index of the magnetisation dispersion and not necessarily a measure of the angular dispersion of the easy directions. The quantitative correlation between α_{90} and the ripple amplitude is complicated and has not been formulated as yet.

It has recently been shown that α_{90} is not necessarily related to the small-scale ripple since large-scale random fluctuations of the magnetisation are usually present. The origin of this dispersion is completely unknown and has a profound effect on α_{90}. Fujii et al (F.8) have shown that average values of α_{90} over the whole film are several times larger than values taken over small areas (100-micron squares). Furthermore, these local values were consistent over the whole film.

Previous results incorporating α_{90} values measured over the whole film must be regarded as rather dubious unless attempts have been made to eliminate this large-scale dispersion.

A great deal of work has been concerned with the origins of the magnetisation ripple. The theories show that the ripple can be explained by local random anisotropies possibly associated with the randomly-oriented crystallites in the film. Most attempts have been made to distinguish between the magnetocrystalline anisotropy and strain magnetostriction contributions to the random anisotropies. The method usually employed is to study the variation of α_{90} with composition and substrate temperature. A brief description of some of the more reliable experiments is given in section 3.5; for more comprehensive details reference to the reviews by Leaver (L.9) and Cohen (C.13) should be made.

The first quantitative ripple theory was derived by Middlehoek (M.3) who, assuming a sinusoidal variation in the magnetisation, calculated the relative magnitudes of the exchange, magnetostatic and anisotropic interactions and their effects on the ripple amplitude. This approach was extended by Feldtkeller (F.6a) to evaluate the ripple field, enabling him to explain the biased susceptibility curves.

A more realistic approach was made by Rother (R.2) and Hoffmann (H.6) as described in section 3.3.1. The original theories have been reviewed by Joenk (J.3). Since then Hoffmann (H.7) has extended his theory to higher approximations incorporating non-linear interactions. Harte (H.8) has also developed a rigorous theory assuming an arbitrary origin of the local anisotropy. This theory is extremely general but is

rather difficult to use for deriving many of the measurable quantities easily accessible from Hoffmann's theory.

A totally different approach has been evolved by Torok (T.2, T.4) which, although it is based on some rather arbitrary assumptions, simplifies the mathematics and produces an easily-understood model.

These two approaches will be dealt with in greater detail in the following sections.

3.2. The Anisotropy Dispersion Model

This theory is a non-rigorous model designed essentially to explain ripple-dependent properties rather than ripple itself (C.12). It is based on the postulate that the film consists of a series of non-interacting regions. These regions are assumed to have a uniaxial anisotropy and easy axis which differ slightly from adjacent regions in magnitude and direction respectively. The Stoner-Wohlfarth astroid is applied to each region tilted according to the local easy direction. The biggest drawback with this approach is that the interactions between these regions are neglected.

Torok (T.4) has produced a similar type of model which approximates these interactions. These regions or 'protodomains' are based on Hoffmann's original approximations, i.e. that the magnetisation is strongly coupled over a small volume determined by the coupling lengths parallel and perpendicular to the ripple. The magnetisation is then approximately uniform in these protodomains. The protodomains are assumed to have an anisotropy consisting of a uniform uniaxial anisotropy

with a randomly-oriented biaxial anisotropy superimposed. These biaxial anisotropies are postulated as originating from the strong coupling between regions with different uniaxial anisotropies, as well as the magnetocrystalline anisotropy of the crystallites. (Other possible sources suggested by Torok were coupling between holes, scratches, film edge and the adjacent regions of the film.) In their calculation of the anisotropy of two coupled regions, Torok et al (T.2) neglected completely the effects of an applied field on the system and argued that the local biaxial constant is directly related to the local anisotropy. This interaction has been treated more rigorously by Yelon (Y.2) who finds that the effective biaxial anisotropy constant for the two regions with the same anisotropy constant K_u is given by: $\frac{K_u^2}{2E_c + \underline{M}.\underline{H}}$ where E_c is a coupling constant. This term is field independent for low fields and/or strong coupling but is still proportional to K_u^2. Taking this to a higher approximation there appears a quadriaxial term together with an additional biaxial term which both decrease as H^{-3} at high fields.

Thus we see that to treat interacting regions as having complex anisotropy is just a first approximation limited to strongly-coupled regions in low fields.

The anisotropy dispersion model incorporates this additional biaxial anisotropy by using complex switching curves as described in chapter 2.

One serious limitation of Torok's theory is that the interactions between locked domains are neglected, which confines this theory to the same field regions as Hoffmann's linear theory.

A discrepancy arising between the micromagnetic theory and the model of Torok et al is in the calculation of α_{90}. This term is defined in terms of the dispersion of the local anisotropy field (H_b). δH_b is defined so that 90% of the film has a local anisotropy field, H_b, within δH_b of the average value of H_b of the film, $\bar{H}_b$. Then, according to Crowther (C.12) (2 or 4)$\alpha_{90} = \sin^{-1} \delta H_b/\bar{H}_b$, the 2(4) referring to uniaxial (biaxial) perturbations. It has been shown by Oredson and Torok (O.1) that ignoring stress and composition effects, then δH_b = constant x K_1, where K_1 is the anisotropy constant of a crystallite. (The effective anisotropy of a protodomain containing N crystallites is then $N^{-\frac{1}{2}}K_1$.) From this, for small angular dispersions we have α_{90} = constant x $\frac{K_1}{\bar{H}_b}$ or for a uniaxial film $\bar{H}_b = H_k$ so $K_u \propto_{90} \propto K_1$.

For strongly-coupled regions Torok determines the local biaxial anisotropy constant as directly related to K, the local uniaxial anisotropy constant, so deriving the relation: $K_u \propto_{90} \propto K$ .. .. (3.1.)

However, if the more rigorous treatment of Yelon is used we have: $K_u \propto_{90} \propto K^2$ in agreement with Hoffmann.

The general conclusions concerning this theory seem to be that, although it explains many ripple-affected properties, there are several limitations incurred during the development of this particular model.

3.3. Micromagnetic Model

This type of treatment represents a fairly rigorous attempt at describing the magnetisation variations, based on the principle that the minimum energy state is the stablest state. Even with this rigorous

treatment several assumptions have to be made but most are shown by a self-consistency argument to be justified. The basic assumption, common to all theories, is that the magnetisation is parallel to the film surface due to the large demagnetising field perpendicular to the film. In this theory the parameter causing the ripple is a local anisotropy in each randomly-oriented crystallite. (In Harte's theory the local anisotropy is uniform within a generalised region governed by the size of the inhomogeneity causing the ripple.) This local anisotropy is superimposed on the overall uniaxial anisotropy which is uniform in both magnitude and direction. It has been shown by Roth (R.3) that there is a variation in direction of the induced anisotropy on the same scale as the crystallites. Hoffmann (H.9) overcomes this by defining the local anisotropy as the cause of the inhomogeneous part of the anisotropy energy.

One further simplifying assumption is that the film possesses no overall magnetostrictive effects, although local stresses do contribute to the local anisotropy.

The magnetisation direction will be affected by these local anisotropy perturbations but abrupt changes will be prevented by exchange and magnetostatic interactions. The equilibrium direction of the local magnetisation will be given by the position for a minimum in the total energy as in the Stoner-Wohlfarth calculation. The components of the total energy are as follows:

(a) applied field energy E_H

(b) uniaxial anisotropy energy E_{K_u}

(c) local anisotropy energy E_k

(d) exchange energy E_{ex}

(e) magnetostatic energy E_m.

The first two terms are the two terms appearing in the single-domain model, while the other three arise from the fact that the magnetisation direction is not constant.

Referring to the co-ordinate system in figure 3.2 we have for the various energy densities:

(a) Applied field $e_H = -\underline{H}_a . \underline{M} = - H_a M \cos (\alpha - \Phi)$

(b) Uniaxial anisotropy $e_{K_u} = K_u \sin^2 \Phi$

(c) Local anisotropy $e_k = Kf(\Phi, x, y)$

This is the local anisotropy energy over a region where K is constant, f being some general trigonometric function.

(d) Exchange energy $e_{ex} = A (\text{grad}. \Phi)^2$

This term arises from the coupling between electron spins, being a minimum when the spins are parallel (for a ferromagnet). This can be regarded as a 'stiffness' term as it prevents abrupt changes in $\underline{M}$. A is the exchange constant.

(e) Magnetostatic or stray-field energy $e_m = -\frac{1}{2} \underline{H}_s . \underline{M}$.

The stray field terminology avoids confusion with the magnetostatic energy of the applied field. The energy arises from the interactions of the magnetisation with the stray fields or demagnetising fields caused by the fluctuations in M inducing internal magnetic poles. All the mathematical difficulties in the micromagnetic approach stem from this term and usually simplifying approximations are made.

It is from this point, the evaluation of the total energy, that all micromagnetic approaches start. We will now consider in detail the

two basic methods due to Hoffmann and Harte with some of their basic results.

3.3.1. Hoffmann's Theory. This has recently been extended and was reviewed by Hoffmann (H.9) in 1968. Most of his results are taken from this paper and reference to his original work is only made for actual calculations omitted from the review.

Hoffmann's approach is to minimise the total energy of the film using the variational integral,

$$\delta\int_V (e_H + e_{K_u} + e_{ex} + e_k + e_m)\, dx\, dy\, dz = 0 \quad .. \quad .. \quad .. \qquad (3.2)$$

where V is the volume of the film. The energies are expressed in terms of the local magnetisation deviation $\phi(\underline{r})$ so that the magnetisation direction at any point $\underline{\Phi}(\underline{r})$ is given by:

$$\underline{\Phi}(\underline{r}) = \phi_o + \phi(\underline{r}) \qquad .. \quad .. \quad .. \quad .. \quad .. \quad .. \qquad (3.3)$$

where ϕ_o is the average magnetisation direction.

The trigonometric function $f(\underline{\Phi},x,y)$ is expanded in a Taylor series about the point $\underline{\Phi} = \phi_o$ and cut off at the second power since ϕ is generally quite small, so:

$$e_k = Kf(\phi_o,x,y) + K\phi\frac{\partial}{\partial\phi}f(\phi_o,x,y) + K\phi^2\frac{\partial^2}{\partial\phi^2}f(\phi_o,x,y)$$

Hoffmann then evaluates the derivatives of f in terms of a position-dependent variable, σ, lying between 0 and 1. The stray field is evaluated as being the gradient of the magnetic potential, U, which is given by the volume integral:

$$U = \iiint_V -\frac{\text{div } \underline{M}}{\underline{r}}\, dV$$

By approximating this integration using a curtailed Taylor expansion of $\underline{M}$ about the point $\underline{r}$, the stray-field energy e_m is derived in terms of ϕ and the two 'magnetostatic' constants c_x and c_y. These constants define a small volume surrounding the point $\underline{r}$ within which the stray field is large enough to affect the magnetisation.

The Euler equation resulting from the variational equation $\delta \int e_{tot} dV = 0$ is given as:

$$\left\{ -\frac{\partial^2 \phi}{\partial x^2} - \left(\frac{2A + M_s^2 c_y}{2A} \right) \frac{\partial^2 \phi}{\partial y^2} + \frac{K}{2A} \frac{\partial f(\underline{r})}{\partial \phi} \right\} + \left\{ \frac{K_u h(\alpha)}{A} - \frac{M_s^2 c_x}{2A} \left[\phi \frac{\partial^2 \phi}{\partial x^2} + \left(\frac{\partial \phi}{\partial x} \right)^2 \right] \right\} \phi = -Q \quad (3.4)$$

where Q is a structure-dependent quantity (zero for hysteresis-free film) given by $Q = \frac{K}{K_u} \sqrt{\left(\frac{\partial f}{\partial \phi} \right)^2}$

$h(\alpha)$ is the Stoner-Wohlfarth field = $\frac{1}{2K_u} \frac{\partial^2}{\partial \phi^2} (e_H + e_{K_u})$.

Integrating this equation enables the magnetostatic constants to be determined. As mentioned previously, these constants give the effective volume over which the stray field is significant and are often referred to as the longitudinal (c_x) and transverse (c_y) coupling lengths. Hoffmann derives the expression:

$$c_x = 4D \sqrt{\frac{A}{K_u h(\alpha)}} \ , \ c_y = 4c_x \ .$$

The transverse stray field causes a coupling of the spins perpendicular to the mean direction with an effective exchange constant $M_s^2 c_y$. From equation 3.4 we see that the transverse stray field depends solely on the second derivative of ϕ with respect to y, i.e. a linear term, whereas the longitudinal stray field (exchange constant $M_s^2 c_x$) depends on both the first and second derivatives of ϕ and is a non-linear effect.

Hoffmann's linear theory is applicable when the longitudinal stray field is neglected in equation 3.4. It is this approximation which determines the limit of validity of the linear theory.

Integrating equation 3.4. a second time enables the dispersion to be determined in terms of a modified Bessel function. Hence, knowing the distribution of local anisotropies in the film the dispersion at any point in the film can be calculated.

Due to the involvement of a modified Bessel function in the dispersion it can be shown that only the local anisotropies within an ellipse centred about $\underline{r}$ contribute to the dispersion at $\underline{r}$. These coupling ellipses have a ratio of major to minor axis of about 30 for a permalloy film, which is in good agreement with Lorentz micrographs. The wavelength of the ripple (λ) is directly related to the minor axis of the ellipse and so

$$\lambda = 2\pi\sqrt{\frac{A}{K_u h(\alpha)}} \qquad (3.5)$$

This long-range wavelength will not be the only wavelength visible in the electron microscope but it should be the dominant wavelength visible at different out-of-focus distances.

The magnetisation dispersion, δ, defined quantitatively as the root mean square of ϕ over the whole film, can be determined for randomly-oriented local anisotropies as:

$$\delta = \sqrt{\overline{\phi^2}} = \frac{0.17\ S}{D^{\frac{1}{2}} M^{\frac{1}{2}} \left[A K_u h(\alpha) \right]^{\frac{3}{8}}} \qquad (3.6)$$

where S is the structure factor $= \frac{Kd}{\sqrt{n}}\sigma$, d being the crystallite size, n the number of crystallite layers in the film and σ the standard deviation of the distribution of the perturbing anisotropies ($\frac{1}{6} \leq \sigma \leq \frac{1}{\sqrt{2}}$).

Typical values of δ are of the order of 1^{o} and measurements by Suzuki and Wilts (S.12) are in fair agreement with predicted values of δ and λ.

The linear theory is strictly only applicable at high fields since as the astroid is approached the ripple becomes less stable due to the action of the longitudinal stray field. The form of this stray field is determined in Hoffmann's non-linear approach. Due to the non-linearity of equation 3.4 with the longitudinal stray field present the integration is impossible and Hoffmann (H.7) overcame this be defining an effective field, h_{eff}, from the second variational derivative of the energy, i.e. $\delta^2 \int e_{tot} dV = 0$, in the same way as for the single domain, i.e. $\frac{1}{2K_u} \frac{d^2 E_{tot}}{d\phi^2}$.

This field, dependent on position, consists of three parts, (a) the Stoner-Wohlfarth field, $h(\alpha)$; (b) an effective demagnetising or stray field; (c) an effective field due to local anisotropies. Its form is given by:

$$h_{eff} = h(\alpha) - \frac{M_s^2 c_x}{K_u}\left(\phi \frac{\partial^2 \phi}{\partial x^2} + \tfrac{1}{2}\left(\frac{\partial \phi}{\partial x}\right)^2\right) + \frac{K}{2K_u}\frac{\partial^2 f}{\partial \phi^2} \quad .. \quad .. \quad (3.7)$$

The two stray-field components in the second term are parallel and antiparallel to M causing stability and instability respectively. The condition for stability is:

$$h(\alpha) > \frac{M_s^2 c_x}{2K_u}\left(\frac{\partial \phi}{\partial x}\right)^2$$

since the last term is negligible. The limit of stability occurs at a field, h_b, known as the blocking field, given by:

$$h_b = \frac{1}{AK_u}\left[\frac{(2D)^{\frac{1}{2}} M d^2 K^2}{16\pi n}\right]^{4/5} .. \quad .. \quad .. \quad .. \quad .. \quad .. \quad .. \quad (3.8)$$

The physical interpretation of this is as follows: consider the film saturated along the hard axis, as the field $h(\alpha)$ is reduced then the wavelength and amplitude of the ripple increase as do the stray fields in h_{eff}. When the blocking field is reached the ripple becomes unstable and should switch; however, this is not the case since we have considered the ripple as being free, i.e. able to arrange itself into a minimum-energy state. When the longitudinal stray field becomes appreciable, i.e. as $h(\alpha)$ approaches the astroid, the ripple is not free. This results in the production of low-angle ripple walls which eventually lead to the domain splitting observed in zero field. The domain splitting will be determined by the blocking field (H.17) and the domain width, b, equal to half the ripple wavelength at the blocking field is given by:

$$b = \pi A \left[\frac{16\pi n}{(2D)^{\frac{1}{2}} M d^2 K^2} \right]^{2/5} \qquad (3.9)$$

The blocking field can occur in directions away from the hard axis, provided that the coercive field is high enough, and Hoffmann (H.7) has calculated the form of the blocking curve (see for example figure 7.3). One expects this blocking field to vary throughout the film due to the non-uniformity. It can be shown that whatever the distribution of h_b the film will always be in a blocked state before reaching the S-W astroid, assuming wall-motion effects are negligible.

Another ripple-sensitive variable with which experimental comparisons can be made is the susceptibility. It has been shown (section 4.3.2) that the transverse susceptibility for a uniaxial film is given by:

$$\chi_t = \frac{M_s}{H_k \, h(\alpha)} \qquad (3.10)$$

This is in good agreement at high fields but near the astroid ripple effects cause a large deviation between S-W theory and experiment. Hoffmann (H.10) pointed out that one needs to replace $h(\alpha)$ by h_{eff} to obtain χ_t near the astroid. $\chi_t = \frac{M_s}{H_k\, h_{eff}}$ .. .. .. (3.11)

This prevents the susceptibility from reaching infinite values.

The incremental susceptibility, χ_i', is extremely ripple sensitive, since the ideal case with M and H parallel predicts a zero χ_i' so that any contribution to χ_i' must come from ripple effects. Applying the linear theory we derive:

$$\chi_i' = \frac{M}{H_k} \frac{\overline{\phi^2}}{h(\alpha)} \propto h(\alpha)^{-7/4} \quad .. \quad .. \quad .. \quad .. \quad .. \quad .. \quad (3.12)$$

which provides an accurate test of the linear ripple theory.

Hoffmann has also derived the angular dispersion α_{90} using his linear ripple theory (H.11), obtaining:

$$\alpha_{90} = \frac{3d^2}{16\pi AK_u} \frac{K^2}{h_b} \quad .. \quad .. \quad .. \quad .. \quad .. \quad .. \quad .. \quad (3.13)$$

Rotational hysteresis has been explained using this linear ripple theory (H.14). This is caused by the presence of ripple hysteresis (as observed by Feldtkeller (F.6a)) since as the applied-field direction is changed the coupling region will change and so there will be a random perturbation energy superimposed on the smooth anisotropy energy. This perturbation causes small energy barriers and hence ripple hysteresis.

Recently, Brown (B.13) has shown that Hoffmann's linear theory is unreliable for applications in which the long-range effects of the local disturbances on the magnetisation are critical. This is due to the form

of the transverse magnetostatic field and, in particular, the approximation used for c_y. The true transverse magnetostatic field for long-range disturbances behaves like a dipole field, whereas Hoffmann's field decays exponentially. However, for most linear ripple theory problems these long-range effects will be negligible and Hoffmann's values give fairly accurate results. A possible case where these long-range effects cannot be ignored would be in films with inclusions where the local anisotropy could be much higher than the average value.

3.3.2. Harte's Theory. This theory (H.8) is a more general approach than Hoffmann's and is more able to treat the magnetostatic energy although the physical interpretation is more abstruse. Harte is therefore able to treat non-linear effects easily but produces r.m.s. values directly rather than the form of the local ripple behaviour.

The basic assumption is that the local anisotropy, K, is caused by some general inhomogeneity of scale R. To evaluate the ripple quantities various limiting cases have to be considered, these cases depending on the size of R compared with certain coupling lengths.

The magnetisation direction $\underline{\Phi}(\underline{r})$ is expressed in a Fourier series:

$$\underline{\Phi}(\underline{r}) = \sum_{k\neq 0} \phi_k \, e^{i\underline{k}.\underline{r}} \qquad (3.14)$$

where $\underline{k}$ is a wave vector $= \pi\left(\frac{N_x}{L_x}, \frac{N_y}{L_y}, 0\right)$; N_x, N_y being integers and L_x and L_y the film's dimensions. It is necessary to find all the ϕ_k's, corresponding to the various ripple wavelengths, and so Harte calculated the total torque expanded about the equilibrium ϕ_o and Fourier analysed it.

The equilibrium position is obtained when these torques balance and by considering the zero order, when $\phi_k = 0$ for all $k \neq 0$ the S-W field $h(\alpha)$ is obtained. The first-order effective field is obtained using the zero-order value for ϕ_o in the general torque equation:

$$\left(H^k_{eff}\right)_1 = H(\alpha) + \frac{2A}{M} k^2 + 4\pi M_s \tilde{\chi}_{\underline{k}} \sin^2(\psi_k - \phi_o) \quad .. \quad .. \quad (3.15)$$

where $\tilde{\chi}_{\underline{k}}$ is a magnetostatic function of $\underline{k}$ and $\psi_{\underline{k}}$ is the azimuth of $\underline{k}$.

The dispersion, to first order, is given by $(\phi_k)_1 = \frac{P_{\underline{k}}}{(H^k_{eff})_1}$, where $P_{\underline{k}}$ is the coefficient in the Fourier expansion of the trigonometric functions describing the randomly-oriented local anisotropies.

The formula for the effective field contains an isotropic term from the exchange interactions and a transverse magnetostatic field (3rd term) in agreement with Hoffmann's linear theory.

To obtain higher-order solutions a similar type of solution is assumed, i.e. $H^k_{eff} = (H^k_{eff})_1 + V_k$ where V_k is a non-linear field, and the dispersion $\phi_{\underline{k}} = \frac{P_k}{H^k_{eff}}$. After substituting these into the torque equation and taking an ensemble average, an integral equation for $V_{\underline{k}}$ is obtained. Harte showed that $V_{\underline{k}}$ could be approximated by V_o for k values below a critical wave number ($\sim$ 1/thickness of film) and by V_∞ for k values greater than this critical value. This is a good approximation provided that negligible contributions were made to V_o and V_∞ by wave numbers around the critical value. Even the integrals for V_o and V_∞ proved to be complicated and could only be calculated numerically. However, by considering several limiting cases values could be obtained for the effective field and the dispersion.

These limiting cases depend on the relative size of R, the inhomogeneity scale, and the film thickness, D, to the coupling lengths R_e and R_m. R_e is the exchange coupling length given by $R_e = \sqrt{\frac{2A}{MH_{eff}}}$ (3.16a) while the magnetostatic coupling length $R_m = \frac{2\pi M_s D}{H_{eff}}$ .. .. (3.16b) This determines whether the interactions are exchange or magnetostatic or both. In table 3.1 the various limiting cases are calculated together with the coupling lengths (longitudinal R_l and transverse R_t).

Table 3.1

Inhomogeneity	Conditions	Interactions	Longitudinal coherence length, R_l	Transverse coherence length, R_t
Fine Scale	$R, D \ll R_e$	Exchange and magnetostatic	$\pi\sqrt{\frac{2A}{M_s H_{eff}}}$	$\frac{(2\pi^2)^{\frac{3}{4}}(M_s A)^{\frac{1}{4}} D^{\frac{1}{2}}}{H_{eff}^{-\frac{3}{4}}}$
Coarse Scale	$D, R_e \ll R \ll R_m$	Magnetostatic	πR	$\pi\left(\frac{2\pi M_s RD}{H_{eff}}\right)^{\frac{1}{2}}$
Macroscopic	$R \gg R_m$	None	πR	πR

Harte evaluates these for both the thin and thick film cases but we will only consider the thin film case. For the fine-scale inhomogeneity the coherence lengths, R_l and R_t, are almost identical with the coupling lengths derived by Hoffmann. In fact, all the properties derived by Harte for the linear, fine-scale inhomogeneity case are identical with Hoffmann's, apart from averaging constants.

V_o and V_∞ have been derived for each of the limiting cases, enabling the effective fields to be determined and hence the magnetisation

dispersion. Each case considered has its own 'intrinsic non-linear field' Ω which is just a normalising constant. The general form of the exact solution for the effective field is:

$$H_{eff} = H(\alpha) + \Omega\left(\frac{\Omega}{H_{eff}}\right)^n \quad .. \quad .. \quad .. \quad .. \quad .. \quad .. \quad (3.17a)$$

where n is a fraction determined by the case under consideration. The non-linear case is derived for applied fields $H(\alpha)$ much smaller than the non-linear field Ω and is given by: $H_{eff} = H(\alpha) + \Omega$ .. (3.17b)

Harte makes an intermediate approximation, termed the quasi-linear approximation, which gives fairly reasonable results over a wide field range. In this approximation the applied field is assumed much larger than the ripple field so that: $H_{eff} = H(\alpha) + \Omega\left(\frac{\Omega}{H(\alpha)}\right)^n$ .. (3.18)

The various fields for the quasi-linear and non-linear approximations are shown in table 3.2 for the various limiting cases, together with the associated magnetisation dispersion (table 3.3). The graphs of these effective fields as a function of the applied field for the fine and coarse scale inhomogeneities are shown in figure 6.11.

Table 3.2

Inhomogeneity	Ripple Field $H_{eff} - H(\alpha)$			Intrinsic Non-linear Field, Ω
	Exact	Quasi-linear	Non-linear	
Fine Scale	$\Omega_f^{5/4} H_{eff}^{-1/4}$	$\Omega_f^{5/4} H(\alpha)^{-1/4}$	Ω_f	$0.56 \frac{(RK)^{8/5} D^{2/5}}{A M^{1/5}}$
Coarse Scale	$\Omega_c^{5/2} H_{eff}^{-3/2}$	$\Omega_c^{5/2} H(\alpha)^{-3/2}$	Ω_c	$1.14 \left(\frac{K^4 D}{M^3 R}\right)^{1/5}$

Table 3.3

Inhomogeneity	Magnetisation Dispersion		
	Exact	Quasi-linear	Non-linear
Fine Scale	$\left(\frac{0.04A}{D^2M^3}\right)^{\frac{1}{4}} \Omega_f^{\frac{5}{8}} H_{eff}^{-\frac{3}{8}}$	$0.14 \frac{KRD^{\frac{1}{4}}}{M^{\frac{7}{8}}A^{\frac{3}{8}}} H(\alpha)^{-\frac{3}{8}}$	$0.26\left(\frac{RK}{DM^2}\right)^{2/5}$
Coarse Scale	$\left(\frac{0.07R}{DM}\right)^{\frac{1}{2}} \Omega_c^{5/4} H_{eff}^{-\frac{3}{4}}$	$0.27\ K\left(\frac{R}{DM^5}\right)^{\frac{1}{4}} H(\alpha)^{-\frac{3}{4}}$	"

The only measurable quantity which can be easily derived from this theory is the transverse susceptibility χ_t, but as yet very little work has been done to apply this theory to experimental observations.

3.4. Further Theoretical Treatments

The earlier treatments, notably by Middlehoek (M.3) assumed a sinusoidal variation in the anisotropy dispersion, together with the same variation in the magnetisation but with a different amplitude. Middlehoek considered the total energy of both longitudinal and transverse ripple to calculate the lowest energy configuration. He also determined the ripple amplitude in both cases.

For the longitudinal ripple, if the easy direction is given by $\theta = \theta_o \sin \frac{2\pi x}{\lambda}$ and the magnetisation direction given by $\Phi = \theta_1 \sin \frac{2\pi x}{\lambda}$ then the ripple amplitude, θ_1, for longitudinal ripple is given by:

$$\theta_o = \left(\frac{H}{H_k} \pm 1\right) \theta_1 + \frac{\pi^2 M_s^2 D}{2K_u \lambda} \theta_1^3 \quad .. \quad .. \quad .. \quad .. \qquad (3.19)$$

the positive (negative) sign referring to the applied field in the average easy (hard) direction. θ_1 must be small and $H > H_k$.

From this we can see that the method due to Crowther (C.12) used for measuring the easy direction ~~amplitude~~ dispersion actually measures the amplitude of the magnetisation ripple. The difficulty in measuring θ_o, together with the assumption of sinusoidal variations, prevents wide applications of this formula.

A more realistic approach was then made by Rother (R.4) based again on the easy-direction dispersion origin for the ripple. This treatment was far more refined than Middlehoek's. His original results emphasised the strong coupling in the transverse ripple, the ripple amplitude being proportional to the square of the crystallite size and the wavelength dependent only on the crystallite size. Results of Baltz and Doyle (B.12) showed quite good agreement of the short-wave ripple wavelength with Rother's prediction of $\lambda = 4d$. However, λ levelled off above crystallite diameters of 2000 $\mathring{A}$, when it became equal to the long-range wavelength of Hoffmann. Rother (R.4) then revised his theory incorporating magnetostatic interactions from the beginning. Assuming a Gaussian distribution of easy axes, he derived a relation for the average ripple amplitude in agreement with Hoffmann (apart from the numerical coefficient). He predicted the wavelength $\lambda = 4d$ again but this reached a limiting value, almost identical with Hoffmann's long-wave ripple wavelength. The one serious drawback with Rother's theory is that the predicted domain-splitting width is over an order of magnitude smaller than experimental values. Since this theory has not been extended to the non-linear case it has been used infrequently although it is explained fairly thoroughly in the review by Joenk (J.3).

Another simplified approach has been made by Feldtkeller (F.6a, F.9) who again assumed a sinusoidal variation in the magnetisation to explain the discrepancies in the susceptibility. The anisotropy was assumed constant and the stray field resulting from the divergence of the magnetisation was calculated. By evaluating the total torque on the magnetisation an effective field can be derived:

$$H_{eff} = H_a \pm H_k + M_s \frac{\theta^2 Df}{\lambda} \quad .. \quad .. \quad .. \quad .. \quad .. \quad .. \quad (3.20)$$

f is a numerically-calculated integral depending on $\frac{\lambda}{D}$. For $\frac{\lambda}{D}$ between 10 and ∞ f lies between 1 and $\frac{\pi}{2}$ and is often taken as unity for convenience.

With the ripple field, $\frac{M_s \theta^2 Df}{\lambda}$, Feldtkeller was able to explain the transverse susceptibility curves, and in a further paper (F.6b) explained the imaginary susceptibility in terms of ripple hysteresis.

3.5. Experimental Evidence Concerning Ripple

As mentioned previously, this has recently been critically reviewed by Leaver (L.9) and so only a brief description of some of the more important and reliable work will be given. There are two basic approaches to this problem, the first being concerned with the cause of the ripple (i.e. the random anisotropy) and the second with testing the theories.

The cause of the ripple is investigated in two possible ways, the first and most powerful being the direct observation of the ripple by Lorentz microscopy, varying the materials and methods of production of the films. The other way is to vary evaporation properties again (such as composition and substrate temperature) and use a macroscopic variable,

such as α_{90} or the susceptibility. This latter method necessarily incorporates the various theories and forms part of theory-testing experimental work. These two methods can be combined by measuring the field dependence of the ripple amplitude and wavelength by Lorentz microscopy.

3.5.1. The Origin of the Random Anisotropy. We must first consider the proposed possible origins of the local anisotropy and the supporting evidence.

Two effects which probably contribute to the major part of the local anisotropy are the magnetocrystalline anisotropy of each crystallite and magnetoelastic effects correlating the stresses in the film with the anisotropies produced, via magnetostriction. Roth (R.3) has shown that a variation in the direction of the induced anisotropy, caused by pair ordering and stress effects within each crystallite, can give rise to a random anisotropy greater than the magnetocrystalline anisotropy. This is probably undetectable in the nickel-iron alloys since the effect is small there. Other contributions to the local anisotropy having a scale not equal to the crystallite size are composition inhomogeneities, film imperfections (holes and inclusions) and surface roughness.

The surface roughness model due to Torok and Oredson (T.5) has an inhomogeneity scale of the order of the crystallite size, but the local anisotropy in films on polished substrates has a scale of the size of the scratch inhomogeneity (Chapter 6).

If more than one of these contributory effects is in operation the method of combining the various anisotropies and the effect on the ripple will depend on the scales of their inhomogeneities. If the two

sources of anisotropy have widely different inhomogeneity sizes then the effects on the ripple may be considered separately (H.8). When the two sizes are about the same the resultant anisotropy is often taken as the r.m.s. value of the constituents. However, recently Doyle and Finnegan (D.3) have shown that the simple r.m.s. value is not the correct one for combining the magnetocrystalline and stress-induced anisotropies. They show that the resulting anisotropy for a uniform isotropic stress, σ, and an applied tension producing an anisotropic strain e, is given by:

$$K = \left[(K_1 + B_s e + \frac{3\sigma}{8}(\lambda_{100} - \lambda_{111}))^2 + \frac{63}{64}(\lambda_{100} - \lambda_{111})^2\sigma^2\right]^{\frac{1}{2}} \quad (3.21)$$

where $B_s = B_1 - B_2$, B_1 and B_2 are the magnetoelastic coupling coefficients and λ_{100}, λ_{111} are the magnetostriction constants in the [100] and [111] directions. The form of the local anisotropy as determined by Doyle and Finnegan has been used to explain the discrepancies observed by Uchiyama et al (U.1) in the temperature and compositional dependence of their measurements of $\alpha_{90}K_u$ against the theoretical predictions of Hoffmann.

The methods used for determining the contributory anisotropy effects are basically the observation of a variable (either by Lorentz microscopy or macroscopic measurements) as a function of composition or substrate temperature. The compositional variation changes the magnetocrystalline anisotropy, K_1, and the stress effects also change, but only slightly. On the other hand, the variation of substrate temperature changes the stress effects without changing the magnetocrystalline anisotropy. Both methods of determining the magnetic variables suffer from drawbacks; Lorentz microscopy has complicated wave-optical effects whereas macroscopic measurements include the long-range random magnetisation

fluctuations which may not be related to the ripple. This restricts the number of reliable experiments on which these comparisons can be made.

Lorentz microscopy measurements can still be used qualitatively but only in the work of Suzuki and Wilts (S.12) has care been taken to minimise wave-optical effects. The results they obtain indicate a minimum in the ripple amplitude at about 73% Ni, 27% Fe and a composition-independent wavelength in agreement with Baltz (B.14). This points to the origin of K being the magnetocrystalline anisotropy, which is to be expected since most constraints will be removed when the film leaves the substrate. The actual values agreed with Hoffmann's calculated values within 20%.

Tsukahara (T.6) has shown that surface roughness, produced by chemically polishing sheet material, caused ripple to appear in 75% NiFe. However, electrolytic polishing caused no ripple and the thickness contrast observed with the chemical polishing was absent. This indicates that the surface roughness produced by chemical polishing makes a contribution to the local random anisotropy.

The most reliable macroscopic measurements on α_{90} have been made by Uchiyama et al (U.1). They found that the product $\alpha_{90}K_u$ was not proportional to the square of the product of Kd (d = crystallite size) but depended directly on K. K was assumed to arise from the magneto-crystalline anisotropy and a non-uniform anisotropic stress, K being the r.m.s. value of these two contributions. There are three criticisms of this work. The first two, pointed out by Doyle (D.3) are that if

these anisotropic stresses exist then the resultant anisotropy is given by expression 3.21, not the intuitive r.m.s. value; secondly, the assumption that the stress is independent of composition is dubious since, from table 6.4, certain temperatures produce permalloy films with tensile stresses in, whereas nickel films possess compressive stresses; thirdly, the anisotropy due to the isotropic stress in the film has been neglected. This will be important where $\lambda_s \simeq 0$ since the anisotropic stress vanishes at this point.

More recently Fujii et al (F.10) have re-examined their α_{90} measurements and determined the structure constant, $S \propto Kd$, from the transverse susceptibility measurements and found very good agreement with Hoffmann's theory, i.e. $K_u \alpha_{90} \propto S^2$. It would appear, therefore, that the previous discrepancy lay in the wrong evaluation of the local anisotropy constant.

Macroscopic evidence for the surface roughness of local anisotropy has been put forward by Fisher and Haber (F.11) who measured the variation of α_{90} as a function of surface roughness. This was done by measuring α_{90} over the whole film as a function of grain diameter as measured from replicas in the electron microscope. They found a linear dependence of α_{90} on the grain density but the grain sizes used in this experiment were about 3 to 15 microns in diameter which is well outside the range for polycrystalline films. A second important point was that by extrapolation for infinite grain size there was a definite dispersion indicating that surface roughness was only one contributory cause.

3.5.2. Direct Comparison between Experiment and Ripple Theory. Very few field-dependent measurements of the ripple amplitude and wavelength have been

made using Lorentz microscopy since the effective field at the area under observation may be affected by nearby domain walls, stray fields of lenses, etc. This could possibly explain some of the peculiarities observed by Tsukahara (T.6) in her field dependence of the ripple wavelength. However, Hoffmann (H.12) has shown that the field dependence of the longitudinal coupling length was in good agreement with theory.

As regards macroscopic measurements, the theory has been fairly successfully applied to the α_{90} measurements as described previously. The susceptibility measurements taken in conditions obeying Hoffmann's theory show good agreement. Most experimentors (the author included) have been concerned with the variation of the field for peak susceptibility (H_p) above the anisotropy field (H_k) with the local anisotropy. This can be done by applying stresses to the film (D.3, L.10). Leaver et al (L.10) attempted to correlate ($H_p - H_k$) with K_1 and $\lambda_{100} - \lambda_{111}$ resulting in only a general trend. Doyle and Finnegan (D.3), although unable to explain the large, actual changes in ($H_p - H_k$), did show that values of ($H_p - H_k$) relative to ($H_p - H_k$) at zero strain varied linearly with the strain to the correct, predicted, power of $^8/_3$, implying that the strain or coupling constant in each crystallite is larger than measured.

For the field dependence of the transverse susceptibility good agreement with Hoffmann's theory was obtained by Fujii et al (F.10) on small film areas, but poor agreement was obtained by Leaver, Prutton and West (L.10) who fitted the curves at the peak susceptibility (H_p). Maksymowicz (M.8) obtained slightly better agreement by fitting the

susceptibility at $2H_p$, but it is still rather poor. There appear to be two reasons for these last two disagreements: firstly, the susceptibility of the whole film will incorporate the long-range dispersion discovered by Fujii et al (F.8) and secondly, the method of fitting is possibly beyond the limits of the linear theory.

Small-area measurements of the incremental susceptibility performed by Leaver (L.11) show good agreement with Hoffmann's theory in skew-free regions, but for films with skew this relation was not obeyed. These regions did behave as predicted by Harte's theory for inhomogeneity sizes corresponding to coarse and macroscopic scales.

Further experiments regarding ripple hysteresis have been made to explain the cause of the loss component (or imaginary susceptibility). Harte et al (H.13) showed that the field dependence of the quadrature flux (imaginary susceptibility) was the same for any magnetisation direction so long as the field used was the component of applied field parallel to the magnetisation, as predicted by ripple theory. This also showed that the imaginary susceptibility is caused by the ripple, as suggested by Feldtkeller (F.6a).

Another discrepancy between experiment and the S-W theory is the rotational-hysteresis-field curve. The S-W model predicts that rotational hysteresis occurs only for fields in the range $\frac{1}{2}H_k < H < H_k$, however these curves do in fact possess a high field tail. This has been qualitatively explained by Hoffmann (H.14) using a ripple hysteresis theory. The explanation is based on his linear theory and needs to be extended to incorporate the non-linear effects at the blocking field before good quantitative agreement is expected.

3.6. Conclusions

From the preceding section we see that the number of reliable experiments with which quantitative comparisons can be made with the theories is very few. Reliable results can only be made from macroscopic variables when measured over a skew-free region or a very small area, $<0.1\ mm^2$. Lorentz micrographs must be made only when the wave-optical effects have been minimised. With these precautions more experiments are required on the origins of the local anisotropy.

The linear theory has been fairly-well proven and is now widely accepted, provided that it is not applied outside the limits of the theory.

Hoffmann's non-linear theory is still in its early stages and very little work has been done to quantitatively support the theory. This theory requires extensions incorporating a distribution of blocking fields and then reasonable comparisons of properties, such as domain-splitting width and α_{90}, can be made near the astroid.

Harte's theory in its general form must be adapted to provide equations for macroscopic measurables other than magnetisation dispersion and transverse susceptibility.

The experimental evidence supporting Torok's theory seems rather scarce and this model has difficulty in explaining certain susceptibility phenomena, locking and inverted films, so is generally regarded as an approximation with many severe limitations.

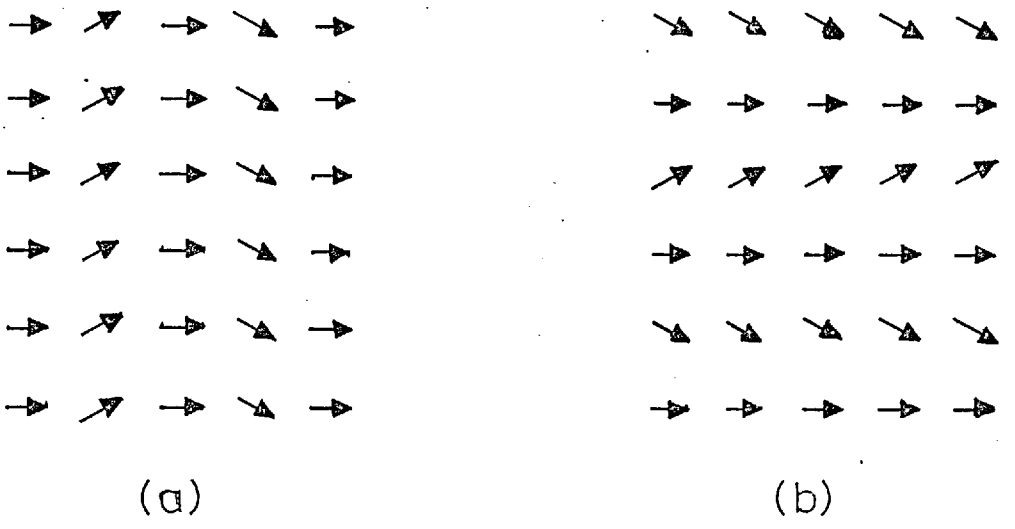

Figure 3.1 (a) Longitudinal ripple and (b) Transverse ripple

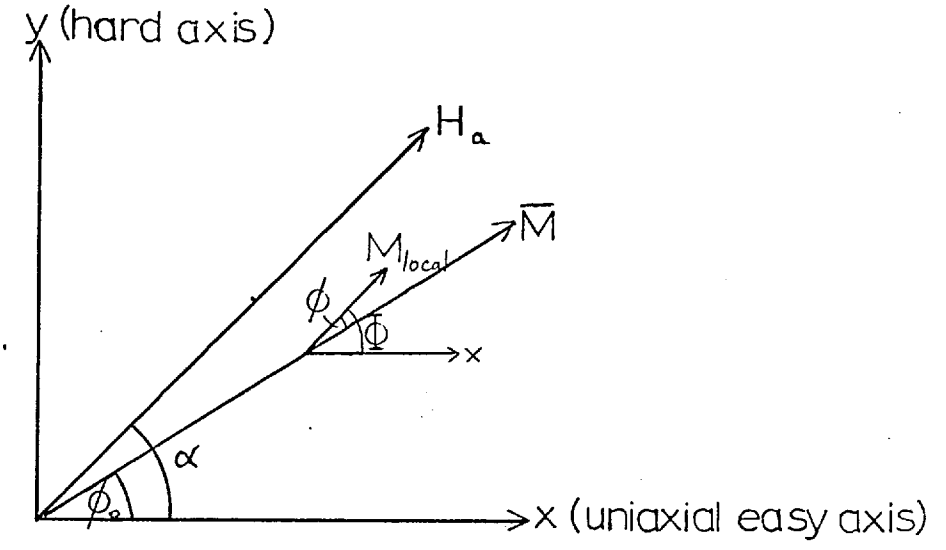

Figure 3.2 Field and magnetisation directions for micromagnetic theory

CHAPTER 4

The Experimental Methods

In this chapter the experimental apparatus and methods used in this work are discussed. As well as the measuring systems, the theories behind them and the method of film fabrication are described.

4.1. The Production of Magnetic Films by Vacuum Evaporation

Section 4.1. deals with the method by which the variously-orientated films were grown on different types of single-crystal substrates, some prepared in different ways, followed by a brief description of the methods by which the film thicknesses and compositions were determined.

4.1.1. The Vacuum System. A six-inch vacuum system, using an oil diffusion pump and cold trap, was constructed as shown in figure 4.1. The water-cooled chevron baffle prevented backstreaming of diffusion-pump oil vapour into the chamber which could be very troublesome when using an electron bombardment source (section 4.1.3). The bell jar could be isolated by the high-vacuum butterfly valve, thus giving access to the source and substrate without turning off the diffusion pump. Contamination of the source and substrate by hydrocarbons was kept low by heating them immediately before, and usually during, deposition. The base pressure attainable with this system was 2×10^{-8} torr (1 torr $\equiv$ 1 mm Hg), after pumping overnight. The pressure during evaporation (which will be the pressure referred to in future) depended on the

length of pumping and consequently on the amount of degassing. It was always in the range 4×10^{-7} torr to 2×10^{-6} torr.

It is popularly quoted that at these pressures there is a monolayer of gas deposited per second. This fact is obtained by using the formula $J = 3.51 \times 10^{22} P(MT)^{-\frac{1}{2}}$, J being the arrival flux of atoms of molecular weight M, T the absolute temperature of the gas and P the pressure (torr). This formula, derived from the kinetic theory of gases, assumes that the sticking coefficient is unity, i.e. none of the adsorbed atoms (or adatoms) are re-evaporated from the substrate. The average lifetime of adatoms on the surface is $\tau_s = 10^{-13} \exp \frac{503.3\ Q_a}{T_s}$ (F.12), where Q_a is the adsorption energy of an atom on the substrate in kilocal/mole and T_s is the substrate temperature. These times are usually extremely short for deposits on insulators and so the number of atoms per unit area on the substrate at any time is given by:

$$n = 3.51 \times 10^{9}\ (MT)^{-\frac{1}{2}} P \exp \frac{503.3\ Q_a}{T_s}\ .$$

Taking typical values of $Q_a = 10$ kilocal/mole, M = 20, and $P = 10^{-6}$ torr it is found that for room temperature $n = 9 \times 10^{8}$ and for the epitaxial temperature (300°C) $n = 9 \times 10^{4}$. Assuming that the area of substrate occupied by a gas atom is 10 $(\text{A}^{\circ})^2$ then for a 1 cm^2 substrate the area covered per unit time is 9×10^{5} $(\text{A}^{\circ})^2$ at the elevated temperature and the contamination during the bake-out is $< 10^{-4}$%. At room temperature the contamination would be about 0.3% for the same period.

Thus we see that there is negligible contamination of the substrate at elevated temperatures by the residual atmosphere unless there is a

stronger, physical or chemical, attraction. Furthermore, the quantity of adsorbed gas in the film will be negligible unless the film has an affinity for any of the gases in the surrounding atmosphere.

The amount of volatile gas was kept to a minimum by using viton gaskets or indium seals in all the high-vacuum parts of the system. The evaporation chamber is also shown in figure 4.1. An off-centre base plate had to be used to allow the vertically-mounted electron bombardment source to be located as near the centre as possible, as a result of which the pumping speed was reduced by about 50%.

During each evaporation three circular films were prepared. They were supported by glass microscope slips which had 1-cm diameter holes in the centre and a small hole at the side which enabled the temperature to be monitored and also provided a specimen for the electron microscope. The three specimens, an inch apart, were nearly 8" from the source so that the variation of the angle of incidence across each specimen was negligible. The two side films were deposited at an angle of incidence of 8°. (The effect of this on the anisotropy is very small, however, see S.13.) The shutter was operated by melting through a nickel fuse wire, (which was carefully shielded from the substrate), allowing the shutter to swing open.

A d.c. magnetic field of 36 oe was normally applied during the evaporation and also while the film cooled. It was produced by two large coils held near the Helmholtz position and parallel to any field from the substrate heater. The variation in direction of the field over a film was less than 0.1° and its magnitude constant to within ½%.

4.1.2. The Substrate Temperature. The substrates were radiantly heated by six parallel tantalum wires connected in series about 1" above the substrates. There was no direct heating from underneath the substrates, apart from source radiation and reflected heat from the shutter, so there might have been a temperature gradient across the substrate. These gradients were kept constant and fairly small by allowing the substrates to reach a steady-state condition before evaporation.

The substrate temperature was monitored using a 40-gauge chromel-alumel thermocouple in physical contact with the front face of the substrate and the glass mask. One side of the thermocouple was earthed to prevent the ionised vapour beam from affecting the true thermocouple voltage. Since this temperature was not the actual temperature it was calibrated using the series of compounds shown in table 4.1. These were placed on the substrate's back surface and the calibration curve shown in figure 4.2 was obtained. It should be noted that the measured sublimation point of NaCl ($\sim 420^{\circ}C$) agrees well with the curve.

Table 4.1

Compound	In	$AgNO_3$	$NaNO_2$	$NaNO_3$	$KClO_3$
Melting Point ($^{\circ}C$)	156	212	271	307	368

When the various substrates were calibrated by this method they all registered the same temperature within the large experimental error involved. If the compounds do not melt by direct adsorption of the radiation, it can be surmised that the substrate is being heated by

conduction from the mask and supports rather than by radiation. This idea is supported by the similarity in the thermal conductivities of the different substrate materials in table 4.2. (see over). If the substrates are only heated by absorption of wavelengths outside their transmission range and including the small percentage not transmitted in this range, then it would take a long time for the substrate to reach the high temperatures used. Furthermore, the LiF should get much hotter than the NaCl but, in actual fact, they both reach approximately the same temperature. The presence of inclusions in the substrate may increase the absorption but from these results it would appear that the main increase in temperature is due to conduction from the mask and supports.

4.1.3. The Method of Evaporation. There are many methods of heating the evaporant, the one used here being a Planer-Unvala electron bombardment source (manufactured by G. V. Planer Ltd.). It is so designed that the electrons emitted from the filament can be focussed onto the ingot by the electric field from the cage which is held at -6 or -7 kilovolts. The central, earthed stem is made of stainless steel with a copper hearth brazed on top to prevent any nickel alloying with the steel. This stem is water cooled, thus preventing any contamination of the ingot by the copper and, if the thermal contact is very good, the base of the ingot remains cold and evaporation occurs only from the top of the ingot. This method, however, requires a great deal of input power and transfers any local inhomogeneity in an alloy ingot to the film. If the thermal

Table 4.2

	NaCl	NaF	LiF
Transmission range (μ)	0.2 - 15	0.19 - 12	0.11 - 6
Absorption coefficient at: 4μ	<0.01	0.02	0.03
10μ	0.1	0.7	30
% transmittance 2μ	94	94	94
Energy transmitted by a tungsten filament at 2000°K at the end of each substrate's transmission range expressed as a percentage of its maximum, assuming Planck's radiation law applies	0.25%	0.6%	6%
Thermal conductivity at room temperature (10^{-3} cal/sec.cm °C)	15	22	25
Thermal expansion coeff at room temperature (10^{-6}/°C)	44	36	37
Melting point (°C)	801	980	870
Solubility at room temperature in gm per 100 gm of water	35.7	4.22	0.27
Density at room temperature in gm/cc	2.2	2.8	2.6

References: J.4 and A.4

contact is reduced the whole ingot melts into a ball and vigorous agitation in it is observed. Although the temperature gradient across the ingot is lowered, its base still remains solid, ensuring negligible contamination from the hearth. The ingot was supplied in the form of a ½" diameter rod from New Metals and Chemicals Ltd. The composition was confirmed as 80.15% Ni and 19.85% Fe by chemical analysis and was constant within 0.2% down the whole rod. Each ingot was used for about six or seven evaporations and then disposed of as its composition had changed to about 81.9% Ni. This is the result of fractionation; iron, having a lower vapour pressure than nickel at any temperature, evaporates more readily. Consequently, the film composition was usually up to 2% more nickel rich than the ingot.

Several modifications were carried out on the source to improve its performance. As supplied, this source had a drawback in that many flash-overs occurred during an evaporation. This was very inconvenient as the 10 kv power supply (manufactured by E. M. Wareham Ltd.) had good regulation and so tripped every time a flash-over occurred. By disconnecting the trip and putting a 2 kΩ limiting resistor in series with the source, the surge for a short circuit was limited to 3½ amps. The pressure reading was also drastically affected by the large number of ions produced by the flash-overs. In fact, monitoring the pressure during an evaporation was virtually impossible. These flash-overs were mainly caused by metallic deposits on the central quartz insulator, thus allowing 'tracking' across its surface. In addition, gas inclusions in the ingot and on the source assembly produced some ionisation.

The flash-overs were minimised by a thorough outgassing procedure and by preventing a continuous path of deposit on the insulator. This latter problem was overcome by placing two small quartz rings around the central stem, thus preventing the formation of a continuous path by any deposit. The outgassing could have been carried out by isolating the filament from the cage and putting a positive voltage on the cage, causing the electrons from the filament to outgas the cage. This was not very successful since the gun design limited this positive voltage to 500 volts and hence the power to only 30 watts for outgassing, before the insulation broke down. This meant that the source had to be run for a long time. ~~quite a while~~. The method eventually used for outgassing was to run the filament at full current for about 1 - 2 hours prior to evaporation with the water supply turned off. This enabled the stem and cage to outgas. The ingot was outgassed by running the source at 4 kV for about ten minutes before evaporating. With these alterations no flash-overs were observed until after several evaporations. The quartz insulators were cleaned in a 50:50 mixture of HF and HNO_3 after about ten evaporations.

There are several distinct advantages of this method of evaporation, but there are also some disadvantages whose effects had to be minimised. The main advantage of this source is that there is no contamination from the source material (crucibles, etc.) since the hearth, being water cooled, remains well below its melting temperature. This source may also be used for materials which alloy with normal source refractories, as the hearth can be made from almost any metal. It may also be used

for evaporating refractory materials or difficult materials such as tungsten, platinum etc. A side effect from this source, which in the present case is a considerable advantage, is that the epitaxy is improved. Films have better orientations when evaporated from an electron bombardment source, all other conditions being identical. It has been shown (S.14, C.14) that the improved epitaxy is due to the electron bombardment of the substrate during film formation, the reason for this not being very clear.

One possible drawback stems from this last advantage and is connected with possible film damage from this bombardment. This is a difficult question to answer but in experiments with a d.c. magnetic field applied during evaporation the electron bombardment, although greatly reduced, was found to be still finite and the films so produced had dislocation densities of the order of $5 \times 10^{10}/cm^3$, which is typically the number for films produced using other sources. Furthermore, the number of microtwins in the electron diffraction pattern is greatly reduced (C.14), thus confirming the fact that with a field of 36 oe present the electron bombardment does not seem to have any appreciable effect on the defect density.

The second disadvantage of this source is again connected with the electron bombardment of the substrate. In any kinetic vacuum system there will be some hydrocarbon vapours in the residual gas and during evaporation the associated electron bombardment will polymerize any hydrocarbons which condense on the substrate. This contamination will build up linearly with the time of bombardment as in the electron

microscope and is virtually independent of the accelerating voltage above 80 volts (E.2). The two ways in which this contamination may be reduced are, first to prevent condensation onto the substrate, which may be achieved by heating it above about 250^{o}C (E.3); secondly, the number of hydrocarbons in the residual gas may be decreased. To do this, all sources of these vapours must be eliminated, such as grease, certain rubber gaskets (E.3); the provision of a cold trap above the diffusion pump will prevent the intake of backing-pump and diffusion-pump oil vapour; finally, all metal surfaces near the substrate should be chemically cleaned and baked before being put in the vacuum system. With all these precautions the contamination rate will be negligible.

The final disadvantage of the electron gun is that, for the electron emission currents required, an appreciable amount of the filament is evaporated. This can be overcome by a careful choice of filament material and also be shielding the substrate from direct evaporation. Of the three possible materials, tungsten, molybdenum and tantalum, the latter gives the highest emission for the same temperature, closely followed by molybdenum and then tungsten (S.15). Tungsten is ruled out as it reacts with residual water vapour to form the volatile WO_2 and is also difficult to work because it is so brittle. Molybdenum and tantalum both evaporate at similar rates but since the resistivity of tantalum is three times that of molybdenum (B.15) the latter was used as it suited the available power supply. The substrate can be shielded from the filament directly but evaporation onto the ingot and reflection from hot surfaces are difficult to eliminate. However,

with this system the amount of filament evaporated onto the substrate was undetectable.

The procedure for an evaporation was as follows:

(i) the substrate was placed into the vacuum system immediately after being cleaved, etc. and the system was left pumping at about 5×10^{-8} torr overnight;

(ii) the substrate was then baked at between 400° and 420°C for between 1 and 1½ hours, at the same time as the electron gun was being outgassed;

(iii) the substrate temperature was altered to the required level and left to stabilise for 30 minutes;

(iv) the electron gun water supply was turned on and the source run at -4 kV and about 60 - 80 watts to outgas the ingot. At this power the ingot was almost white hot and no noticeable evaporation was taking place. The gun was then focussed by maximising the ratemeter current (see section 4.1.4.). This was stopped when the pressure had dropped again (after about 5 - 10 minutes);

(v) the magnetic field was switched on and the voltage on the gun was then increased to -6 or -7 kV and the filament current altered until the correct rate was attained, the gun's focus being checked before the shutter was opened by melting through the fuse wire supporting it;

(vi) the evaporation usually lasted for about 5 minutes at a rate of $2 \pm .5$ $\overset{\circ}{\text{A}}$/sec before the gun and substrate heater were switched off;

(vii) the films were allowed to cool down to room temperature in the magnetic field before being removed for magnetic measurements.

4.1.4. Other Film Parameters. Many of the magnetic properties depend on the film thickness, composition and occasionally on the rate of deposition. In this section the methods by which these parameters were measured are discussed.

The thickness was measured indirectly using the third film grown on a glass substrate. This was coated with about 1000 Å of aluminium (using a high rate of deposition to obtain a good reflecting surface) and the thickness measured using a Varian Interferometer. This instrument is based on the principle that the multiple-beam interference pattern will show a step at the film edge, the thickness of the film governing the size of this step (T.6). By taking about ten different readings the average error in thickness was usually about 40 Å.

The thickness of films grown on the single-crystal substrate could not be measured directly as the surface is covered with many cleavage steps (section 4.2.1.) which are indistinguishable from the film edge in the interferometer (see figure 4.3a). However, for the polished substrates these steps were absent, but here the scratches interfere with the pattern (see figure 4.3b).

A check was made to compare the thicknesses of films grown on NaCl and glass in the same evaporation, using the electron probe (see below). It was found that for these thicknesses ($\sim$ 800 Å) the difference in thickness was within the experimental errors of about 10 - 15%.

The compositions were determined by the Analytical Services Laboratory at Imperial College. Both the nickel and iron contents were determined simultaneously by means of electron probe microanalysis.

This method was first used by Castaing and Descamps (C.15) and involves the bombardment of the specimens by electrons with energies of about 25 keV. The intensities of the two characteristic X-radiations produced (from the nickel and iron contents) were measured. These counts, taken over a scan of about 150 microns length, were compared with nickel and iron standards. The composition was determined from these two values assuming the film only contains the two elements.

However, with the films produced, the compositions so determined were more iron rich than expected. When a polished sample from the ingot, prior to evaporation, was analysed by this method it was found to be 6 - 7% too iron rich. This ingot was then chemically analysed to 0.03% and used as the bulk standard. It seems that, due to the closeness of these elements (only two atomic numbers apart) and the spread in the X-ray intensity, there is some overlapping of the intensities. This means that the weaker component will contain some counts from the other. Using the pure elements as standards this will be emphasised in determining the compositions. The error will be greatly reduced by using a composition near the required one as a standard.

The film composition ranges from 80% NiFe for the first evaporation to about 83% NiFe for the final evaporation from one ingot. The error in these compositions is about 0.8%.

The relative film thicknesses could be obtained by directly comparing the relative total X-ray intensities. This provides only a very rough ratio of thicknesses since the measured intensity has to be corrected for (a) the presence of the substrate, (b) the finite thickness

of the film as there might not be 100% absorption, (c) the normalisation factor between film and bulk intensity. Hutchins (H.15) explores these corrections and derives a formula from which the thickness of any film may be determined after calibrating the instrument. From this article we see that the correction for (b) is a power series in the thickness and neglecting the correction for this we have a 19% error in the example Hutchins uses which will give an error of about 14% in the thickness. This leads to an error of up to 12% in the ratio of thicknesses depending on how close together the two thicknesses are. However, this method was used to obtain an indication of all the relative thicknesses.

The method of measuring the rate of deposition utilised the fact that the vapour beam was ionised. A crystal ratemeter could not be used as the ionised beam would damage the quartz crystal unless a large magnetic field was applied across the crystal during deposition. As this would have affected the direction and homogeneity of the deposition field it was not used.

The ratemeter consisted of a tantalum vane situated next to the substrates and well insulated from the apparatus. This vane was used to collect electrons and ions in the evaporation chamber, produced by ionisation of the residual gas or vapour beam, although a certain number arrive direct from the electron bombardment source. Initially, an electron current of about 20 microamps was collected during an evaporation, corresponding to an electron flux of the order of 1.5×10^{12} electrons per cm^2 per second. The current was measured by connecting an AVO

meter directly between the vane and earth. However, this method of measuring the rate proved to be rather inadequate since it was affected by the filament current (independent of the evaporation rate). If the input power, and therefore the evaporation rate, was changed by altering the voltage on the cage and keeping the filament current constant, the electron current gave a fairly reproducible value of the rate. This proved to be a rather insensitive and difficult method of keeping a constant rate and so it was discarded.

When a positive voltage was applied to the collector an ion current of between 10 and 20 microamps could be measured. With increasing voltage on the collector the electron current dropped until above about 4.6 kV a constant ion current was measured (with a cage voltage of -6 kV). The ion current was found to be independent of the pressure (at least within the range used) but it did vary with the cage voltage which had to be kept constant for each evaporation. The ratemeter was not calibrated since the same rate was required for each evaporation. However, keeping the voltage on the cage constant, the same ion current gave very similar evaporation rates and was found to be sensitive enough to enable accurate focussing of the source (by maximising the rate).

4.2. Substrate Preparation

Several types of substrates were used to improve the epitaxy and the magnetic properties. The first substrate used was single-crystal NaCl, which being the commonest proved difficult to handle due to its affinity for water. In order to try to improve the film properties

several treatments of the NaCl were used. Other substrates used were sodium fluoride and lithium fluoride, but no special treatments were necessary for these. The single-crystal NaCl and LiF were obtained from Harshaw Chemical Co. and the single-crystal NaF was kindly supplied by Dr. Stevenson of Aberdeen University.

4.2.1. Cleaved Substrates. All the single-crystal substrates used cleaved in the [100] directions and each was cleaved using a new, clean razor blade. Care had to be taken not to let the blade scratch the cleavage face after it had been struck. Even so, the faces were covered with many cleavage steps which, although not visible to the eye, can be shown after decoration, and using the electron microscope. This method, due to Bassett (B.1) involves evaporating a few Å of gold, or silver, onto the freshly-cleaved surface. Due to its high mobility the gold moves to preferential nucleation sites, resulting in the contours of the cleavage steps being visible in the electron microscope. In figure 4.4a is shown a typical example of the decoration of a cleaved NaCl crystal.

The substrates were cleaved immediately before pump down so that little moisture or dust could contaminate the surface.

Replicas of these surfaces showed little detail, apart from the cleavage steps which sometimes broke into minor cleavage steps (figure 4.4b) leaving loose pieces of NaCl on the surface. These were removed by brushing the surface lightly with a camel-hair brush before placing in the vacuum system.

The replicas were produced by shadowing with platinum at about 20° and a carbon support film evaporated, normally, on top. The platinum was evaporated by putting a small piece of platinum foil in the carbon arc and evaporating as for carbon.

4.2.2. Polished Substrates. In an attempt to remove the cleavage steps, which could have an effect on the magnetic properties of the film, polishing was tried in a similar manner to that reported by Heavens et al (H.16).

The procedure was to cleave the rocksalt and remove any gross cleavage steps by vigorous rubbing on wet filter paper for a short time. Further etching was prevented by immediately polishing on a dry filter paper. The substrate was then polished on a new Selvyt cloth, lubricated with a fine suspension of tin oxide in saturated brine. Before looking at the face the NaCl had to be polished on a dry Selvyt cloth to prevent the saturated brine from crystallising in the polished face. A final polish on a dry Selvyt cloth completed the procedure. However, films prepared on these substrates were found to contain a large number of tin-oxide particles from the polish. This was reduced by washing the substrate in isopropyl alcohol in between polishes.

Several other lubricants were tried without much success but better magnetic films were produced by using a solution of saturated brine containing ceric-oxide powder (e.g. table 6.6, anomalously high H_k values for polished films using tin oxide).

The platinum-carbon replica in figure 4.5a shows that the cleavage steps are replaced by random scratches of various sizes. The density

of scratches is very high, as can be seen from the low-magnification electron micrograph in figure 4.5b. Some of the polished substrates, when replicated, showed rectangular crystallites of NaCl on the surface (figure 4.5c). This was presumably due to either moisture attack from the atmosphere after polishing or incomplete drying at the end of polishing. Occasionally the replica showed a very bumpy, irregular surface (figure 4.5d) which is possibly due to isopropyl alcohol being left on the surface after polishing. However, with care these irregularities can be removed as is shown by figure (4.5a).

4.2.3. Etched Substrates. All the imperfections and dust on the surface may be removed by etching the sodium chloride in de-ionised water. This leaves the surface very bumpy on a microscopic scale and improves the epitaxy (the production of many nucleation sites, crystallographically situated) but the film is no longer planar. Thus, if the etching could be controlled it might be possible to improve the epitaxy and keep the film planar.

When the NaCl is placed in water the Coulomb force of attraction between the Na and Cl ions is reduced due to the high dielectric constant of water and the Na and Cl ions will go into solution until the water becomes saturated (from table 4.2. this requires just under 36 gm in 100 gm of water). Since the Coulomb force is directional the etching will also be directional and so a rough surface will be expected. An obvious way to reduce the etching is to put the substrate in a near-saturated brine solution. However, this has the disadvantage that the

brine crystallises on the substrate in rectangular crystallites similar to those in figure 4.5c.

The NaCl will only dissolve if equal amounts of Na and Cl ions are allowed to go into solution. If there are some Na or Cl ions already in the water then the rate of etching can be slowed down. This was achieved with a 50% mixture of hydrochloric acid and water. Both the H and Cl ions go into solution in the water and so reduce the rate of etching.

The drawback with this method was that after dipping the substrate in the mixture the solution on the substrate surface had a large surface tension energy and would not drain away easily. This was removed by spinning the substrate on a centrifuge for 15 - 20 minutes to enable a flat surface to form.

4.2.4. Microscope Slips. These were required for the control film from which the composition and thickness were determined. The method by which the 24-mm square slips were cleaned is described below. Being very fragile (only 0.15 mm thick) they had to be handled very carefully.

First they were washed with 'teepol', to remove any grease on the surface, and well rinsed before being transferred to an ultrasonic bath. They were left in this in a 4% solution of RBS 25 (an efficient and very pure detergent) for 30 - 40 minutes, then rinsed in distilled water in the bath for a further 5 minutes. Finally they were put in a recirculatory vapour degreaser, using isopropyl alcohol, for several hours. After cooling and drying they were placed in the evaporating plant.

4.3. Biased Susceptibility Apparatus

This section describes the apparatus with which most of the magnetic measurements were made and also the theory behind it for all types of films from polycrystalline to single crystal. The actual apparatus is shown in figure 4.6a and in block form in 4.6b.

4.3.1. Apparatus. This is based on the hysteresis loop plotter of Crittenden et al (C.1). It consists of two perpendicular sets of Helmholtz coils mounted vertically with a third 'pick-up' coil, much smaller than the others, mounted horizontally near the film's surface. An alternating current is fed into one of the pairs of coils from an Advance audio oscillator (type H1) coupled with a 50-watt power amplifier (manufactured by Vortexion Ltd.). A suitable capacitor is placed in series with the coils to form a resonant L,C (and R) circuit. This is necessary because at the frequency used (2 kc/s) the output voltage of the oscillator is small and as the coil's reactance is so high the current flowing would be small. A series resistor, R_1, is used to monitor the current going through the coil, by observing the voltage across it using an oscilloscope. The value of R_1 was about 1 ohm but the error in its actual size was overcome by measuring the a.c. field at the film surface directly, with a Hall probe gaussmeter, as a function of the voltage on the oscilloscope. (It should be mentioned that a lower frequency (250 c/s) had to be used since the Hall probe is limited to frequencies below about 300 c/s. However the resistor, being non-inductive, had the same reactance at both frequencies.)

In the hysteresis loop plotter the induced voltage in the pick-up coil, which is proportional to the rate of change of flux, is fed into an integrating amplifier and then into the Y input of an oscilloscope, the X-plates being connected to the a.c. field. The Y signal, the integrated induced voltage, will then be proportional to the flux or magnetic induction, B, of the film. The figure on the oscilloscope will then be a B-H hysteresis loop, assuming that both the X and Y signals are in phase. (Any small relative phase shift can cause a large distortion of the loop.)

The method used here differs from this, and was originally used by Torok et al (T.7) although his interpretation is rather dubious. A fuller description is given by Feldtkeller (F.9). The signal is not integrated but only amplified before being fed into an X-Y recorder as being proportional to $\frac{dB}{dt}$. The a.c. field used in this method is extremely small and in the second pair of coils a d.c. field or bias field is produced, so that the resulting effect is a bias field oscillating through a very small angle about its mean position. This bias field is applied to the X input of the recorder via the resistor R_2 and the current is measured using an AVO mark 8 in series with a stabilised, constant-current power supply. On the recorder, therefore, the rate of change of induction is plotted as a function of the bias field.

Connected in series with the pick-up coil is a similar coil which compensates for the signal induced in the pick-up coil by its mutual inductance with the a.c. field coils. This compensating coil is moved

in a non-uniform part of the a.c. field, well away from the film, until the air-flux signal is cancelled out. Oguey (0.2), in a comprehensive review on increasing the signal to noise ratio in the loop plotter, decided that this was the most satisfactory method of eliminating the air-flux signal, although this signal cannot always be completely compensated for. This was due to eddy currents in nearby metallic conductors which produce a relative phase shift in the signals induced in the two coils. To overcome this a conductor such as a piece of aluminium is moved about near the compensating coil in an inhomogeneous part of the field and together with the compensating coil can reduce the air-flux signal to a very low level. To increase the sensitivity of the system the pick-up coil was wound in a square figure of eight so that voltages induced in the arms would cancel while those induced in the centre near the film were added.

It is very difficult to eliminate noise with the hysteresis loop plotter since the integrator must be a wide-band amplifier which means that most of the noise will also be amplified. However, in this method the wide-band amplifier is not used since no integration is required. As only the component of the signal having the same frequency as the a.c. field is required, the use of a lock-in amplifier will eliminate a large amount of the noise. A reference signal of the same frequency and phase as the a.c. field was fed from the oscillator direct to the Brookdeal phase shifter (MS 320). This was connected to the lock-in amplifier (Brookdeal model FL 355) which compares the pick-up signal with the reference signal and amplifies that part of it having the

same frequency. The lock-in amplifier acts as a synchronous switch so that the d.c. output voltage will be proportional to that part of the input signal which is in phase with the reference signal. The induced signal was previously passed through a narrow-band amplifier having 3 db points at 1 and 3 kc/s which, in conjunction with the phase-sensitive detector, improves the signal to noise ratio tremendously and enables very small susceptibilities to be measured.

One further advantage which ought to be mentioned is that the phase shifter alters the reference signal phase relative to the pick-up voltage so that either the in-phase or out-of-phase component of the induced signal can be measured just by changing the reference signal phase by 90°. This means that both the real and imaginary parts of the susceptibility can be observed.

The choice of frequency is governed by two factors. The lower limit is governed by inductive pick-up from nearby mains cables and transformers. The upper frequency is limited by the lag of the magnetisation change behind the applied field, which introduces an effective phase shift, and stray capacitances also play an important part at high frequencies.

The film is supported by a rotatable circular perspex holder, thus enabling any co-planar orientation between the film and the bias field to be used.

There are several important points which must be carefully investigated as possible sources of error. They may be divided into two categories: (a) phase of signal and (b) amplitude of signal.

(a) Any slight phase shift between the pick-up voltage and the reference signal can have drastic effects on the signal magnitude, especially near the critical fields. The phase shift can come from two sources. The first causes a change in the zero susceptibility. If any surrounding metallic object is moved after the noise level is minimised the phase of the pick-up signal is altered and the noise level increases. The second cause of phase shift is instrumental. If we are measuring the real part of the susceptibility then we need the in-phase component and so an oscilloscope trace of the signal against the reference signal should be a straight line. However, this phase setting did not give the correct curves and it was found that there was a slight phase shift either in the lock in amplifier or the oscilloscope amplifiers. It was therefore decided to adjust the phase so that the susceptibility was a maximum with a bias field in the hard direction of $2H_k$. This method of adjusting the phase was found to be far more accurate for measuring the imaginary susceptibility since this should be zero for large fields where the S-W model is obeyed with a small peak at a field just below H_p where H_p is the field for the peak real susceptibility. The phase was thus adjusted so that $\chi_i = 0$ for $H > 2H_k$.

(b) The amplitude error is not very large for most films but can become significant. The output voltage is very dependent on the size of the a.c. field and any slight change in this field can cause a large variation in the susceptibility, especially near H_p. To ensure having as constant an a.c. field as possible, both the oscillator and

power amplifier were driven from an Advance constant voltage transformer (type CVN 750) which reduced input variations by a factor of 15. The oscilloscope used to measure the a.c. field was also run from this to avoid amplification changes. The actual size of the a.c. field may also affect both the real and imaginary susceptibilities. The real susceptibility varies with the a.c. field amplitude over a range of fields depending on the size of the dispersion (F.9), and the imaginary suceptibility varies appreciably with the a.c. field near the astroid. This is because of ripple hysteresis produced by the a.c. field. It will be dealt with in more detail in chapter 7.

The hard direction is found by maximising the susceptibility with a bias field of about $2H_k$ with respect to the direction of the applied field. One further important error is connected with the earth's field. At fields near the astroid the resultant torque on the film is nearly zero and then the earth's field can have a large effect so that it has to be cancelled. Alternatively, the coils can be arranged so that the earth's field is parallel to the bias field and the film is rotated within this system. When measuring in the hard and easy directions, the intercepts of the $\frac{1}{\chi}$ versus H graph should be $-H_k + H_e$ and $H_k + H_e$, thus evaluating both H_k and H_e. If the earth's field is not parallel to the bias field the two hard directions, with $\pm$ bias field, will appear not to be 180^o apart, or, the maximum susceptibility in the hard direction will be different for $\pm H_p$. In fact, this provides a very accurate method of aligning the coil system in the earth's field.

4.3.2. Theoretical Behaviour for Uniaxial Anisotropy. The evolution of this apparatus was by way of Torok et al (T.8) who still used an integrator together with the extra bias field, thus obtaining a series of biased hysteresis loops from which they determined the anisotropy dispersion. Torok's interpretation neglects interactions between domain walls and so must be rather suspect near the astroid. Feldtkeller (F.9) describes the apparatus briefly and discusses the behaviour of two uniaxial films and also the causes of any losses, which appear as an imaginary susceptibility.

In discussing the measurements it is most convenient to start with the ideal, Stoner-Wohlfarth film. Referring to the astroid in figure 4.7a the d.c. bias field, H_a, is in the easy direction with the a.c. 'tickle' field, $\hat{H}e^{iwt}$, along the hard axis. The resultant field, therefore, varies between the points A and B. The associated magnetisation directions, those lying nearest to the easy axis, are known to be between positions M_A and M_B at angles $\leqslant \left| \pm \delta_e \right|$ to the easy direction. These angles are quite small as $2\hat{H}$ is small compared with H_k, so that we can say:

$$\tan \delta_e = \frac{\hat{H}}{H_a + H_k} \simeq \delta_e \qquad \text{or} \qquad \delta_e e^{iwt} = \frac{\hat{H}e^{iwt}}{H_a + H_k} \quad .. \quad .. \quad (4.1.)$$

The induced voltage is $v = \frac{Nd\Phi}{dt}$ where N is the number of turns in the search coil (of area A) picking up a flux Φ. Now the compensating coil was adjusted so that no voltage was picked up with the specimen absent. The pick-up flux with the specimen in position will then be $\Phi_{\text{specimen}} - \Phi_{\text{displaced air}}$, therefore:

$$v = \frac{Nd}{dt}\left(\Phi_{sp} - \Phi_{air}\right) = \frac{NAd}{dt}\left(B_s - B_{air}\right) = \frac{NAd}{dt}\left(4\pi M\right),$$

since for air $\mu = 1$, i.e.

$$v = 4\pi NA\chi\frac{dH}{dt} = i4\pi\omega NA\hat{H}\chi e^{iwt} \quad .. \quad .. \quad .. \quad .. \quad (4.2.)$$

and so the induced voltage is proportional to the susceptibility, χ.

Now the susceptibility, $\chi = \frac{dM}{dH} = \frac{M_s\delta_e e^{iwt}}{\hat{H}e^{iwt}} = \frac{M_s}{H_a + H_k}$, using equation 4.1.

For the bias field in the hard direction the situation is shown in figure 4.7b. The difference for this case is that the magnetisation directions nearest to the easy axis are M_c and M_D where $\delta_h \simeq \frac{\hat{H}}{H_a - H_k}$ so that the signal $v \propto \frac{1}{H_a - H_k}$.

These calculations only apply for $H_a > H_k$ where M is nearly parallel to the applied field. For fields inside the astroid the field dependence of the signal is extremely complicated except for very small fields ($< H_k/10$) where the signal is linearly dependent on H_a^2. The signal should reduce to zero at $H_a = 0$, since M will be in the easy direction and so parallel to the a.c. field.

It is apparent, therefore, that the susceptibility at various d.c. bias fields should have the form $\chi \propto \frac{1}{H_a \pm H_k}$ depending on the direction of the applied field and the applicability of the S-W model. The shapes of these curves should be hyperbolae with infinite points at $H_a = \pm H_k$. Furthermore, the separation of the curves in the easy and hard directions should be $2H_k$, so by plotting $\frac{1}{\chi}$ versus H_a we should have two parallel straight lines with intercepts at H_k and $-H_k$.

4.3.3. Actual Behaviour of Uniaxial Films. In figure 4.8 are shown two such curves for a typical uniaxial film and the theoretical curves from the

S-W model. The agreement between theory and experiment in the hard direction is very good down to a field slightly greater than H_k when it drops below the theoretical curve, the peak susceptibility, χ_p, occurring at a field $H_p (> H_k)$. An idea of how closely the film obeys the S-W prediction can be obtained by measuring $H_p - H_k$ and χ_p / χ_o, χ_o being a normalising constant. (It is the susceptibility in an effective field of H_k, so that $\chi_o = \frac{M^2}{2K_u}$.)

The experimental curve tends to the theoretical one as $H_p - H_k \rightarrow 0$ and $\frac{\chi_p}{\chi_o} \rightarrow \infty$ and so $\frac{\chi_p}{\chi_o}$ and $\frac{H_p - H_k}{H_k}$ are critical measures of how near the film is to the Stoner-Wohlfarth model for a perfect film.

The discrepancy between theory and experiment in the hard direction can be explained as being due entirely to ripple effects. As the field is decreased from saturation, so the ripple amplitude increases according to equation 3.6. There will be no divergence from the theoretical curve if the ripple, which is being rotated slightly by the a.c. field, produces no hysteresis losses and acts as though it is completely free. Thus, as the ripple amplitude increases the stray field coupling will increase and cause the magnetisation ripple to become stiffer. Feldtkeller (F.9), using a simplified sinusoidal ripple with no hysteresis, finds that the susceptibility may be written as $\chi = \frac{M_s}{\pm H_a \pm H_k + \frac{M_s f D \theta^2}{\lambda}}$,

where θ is the ripple amplitude, λ its wavelength, D is the film thickness and f a numerically calculated definite integral. The susceptibility decreases, therefore, from the S-W prediction, the difference increasing as the amplitude, θ, increases. However, due to

the dispersion both in the anisotropy field magnitude and direction, which contributes to the ripple, certain regions will have a local anisotropy field $>H_k$ and so will try to switch at fields higher than H_k. The result of this dispersion is to allow some regions to switch before others, causing the film to split into narrow domains separated by small-angle Néel walls. The susceptibility will now continue to decrease as the field is decreased. The maximum imaginary susceptibility is not expected to occur at the field H_p since both ripple hysteresis and irreversible ripple wall motion contribute to the losses and these are greater the larger is the ripple amplitude. For fields decreasing below H_p the amplitude is greater and consequently the losses will be greater until the magnetisation rotation within the domains is prevented by stray fields from the walls. From figure 4.8 we see that the imaginary susceptibility has its maximum below H_p and this field varies with the a.c. field as described in chapter 7.

The agreement between theory and experiment in the easy direction is not as good. The film switches from one branch to the other at the coercive field H_c, usually $<H_k$. This process occurs simply by wall motion, edge domains nucleating and reversing the film by moving across. The film does obey the S-W model above H_c as can be seen from figure 4.8. The $\frac{1}{\chi}$ versus H_a curves are also parallel (figure 4.9) even though there are deviations from the ideal model. Different curves are observed for inverted films and they have been explained by Feldtkeller (F.9) in a similar manner to normal films.

4.3.4. Behaviour for Biaxial Anisotropy and Single Crystal Films. We can calculate the susceptibility-field relationships for biaxial anisotropy in a similar manner to the uniaxial case. The easy and hard directions will be almost identical with the uniaxial case but with H_1 replacing H_k. Because the biaxial easy axis is at 45° to the hard axis there will be a finite signal = $ie^{iwt} 4\pi NA\hat{H}\omega \frac{M_s}{\sqrt{2}\, H_1}$, with no field applied in the hard direction, since M will be at 45° to the a.c. field and not parallel to it.

As has previously been mentioned, Permalloy single crystal films nearly always have an appreciable uniaxial anisotropy superimposed on the magnetocrystalline anisotropy. In the case of NiFe on NaCl, where K_1 is negative, this mixture of anisotropies has the immediate effect of eliminating any easy-direction curve, unless two perpendicular bias fields are used. The curves in the two adjacent biaxial hard directions are very similar to the uniaxial films. It can easily be shown that the curves will be of the form $\chi \propto \frac{1}{H_a - H_1 \pm H_k}$, the positive (negative) sign being for the bias field in the uniaxial easy (hard) direction. When the inverse signal is plotted against the bias field there should be two parallel lines, separated by $2H_k$ and with intercepts of $H_1 \pm H_k$. Thus both the uniaxial and biaxial anisotropies can be evaluated at low fields.

In figures 4.10 and 4.11 are shown two typical curves. The agreement is good in both directions and the differences can be explained in exactly the same way as for the uniaxial hard direction.

Note again that the susceptibility in the hard directions is not zero at zero field. Referring to figure 4.12 the signal in zero field will be proportional to the angle δ. The signals in the two hard directions will be in the ratio $\frac{\delta a}{\delta b}$, where $\delta_a = \frac{2\hat{H}\sin\theta}{H_R}$ and $\delta_b = \frac{2\hat{H}\cos\theta}{H_R}$ where θ is the angle between M and the uniaxial hard axis, 'b'. The ratio of the two susceptibilities is therefore = tan θ. The angle θ is approximately the angle between the net easy axis and the uniaxial hard axis and from equation 2.10 this is given by $\cos 2\theta = \frac{1}{5b_1}$. Expanding $\cos 2\theta$ in terms of $\tan\theta$ gives $\tan^2\theta = \frac{5b_1 - 1}{5b_1 + 1}$ so that

$$\frac{\chi_a}{\chi_b} = \sqrt{\frac{5b_1 - 1}{5b_1 + 1}} = \left[\frac{5H_1 - H_k}{5H_1 + H_k}\right]^{\frac{1}{2}} \quad .. \quad .. \quad .. \quad .. \quad .. \quad (4.3.)$$

An interesting case arise when the biaxial anisotropy is present but is the smaller anisotropy component ($b_1 < 1$). The susceptibility curves are then rather different and are shown in figure 4.13a. The uniaxial hard direction is as predicted for the cases with $b_1 > 1$. The uniaxial easy direction should, according to the previous explanation, have a peak at $H_1 - H_k$ i.e. a negative applied field. However, as can be seen from figure 4.13a, the peak occurs at a positive applied field as for cases with $b_1 > 1$. This can be explained using the biaxial astroid shown in figure 4.13b. For a field in the uniaxial easy direction the magnetisation orientation which is energetically favourable will be M_1 on the arm $(H_k - H_1)$ rather than on the arm $(H_1 - H_k)$ as for the case with $b_1 > 1$. Thus the peak is expected at $H_k - H_1$ rather than $H_1 - H_k$.

The film shown in figure 4.13 has anisotropy fields H_1 = 2 oe and H_k = 3 oe. Thus the tips of the arms '$H_k - H_1$' and '$H_1 - H_k$' will be

very close so that the angle through which the magnetisation moves after the initial peak at $H_k - H_1$ is very small and remains virtually constant so that the susceptibility changes only slightly.

This example demonstrates the complexity of combined anisotropy behaviour and that the position of the maximum susceptibility field does not always give a correct indication of the ratio of the anisotropies present.

A second possibility which will now be discussed is the case where the uniaxial easy axis is induced parallel to the biaxial easy axis (i.e. $[1\bar{1}0]$). The analysis is very similar and the susceptibility curves in two adjacent biaxial easy axes (the uniaxial hard and easy directions) should have intercepts of $-H_1 \pm H_k$. However, there are two difficulties which occur for this case:

(a) Measurements are being taken in the biaxial easy direction so the curves will be cut off by wall motion at 'H_c' and the range of fields over which the susceptibility can thus be measured accurately is greatly reduced;

(b) It will be difficult to determine the exact easy directions since the average hard direction will be at an intermediate angle (depending on the relative anisotropies) to the easy axis and the method of determining the easy axis is not as sensitive as the determination of the hard axis. To find the easy axis the susceptibility is maximised in zero field, producing a typical error of up to 5^o compared with the $\frac{1}{2}^o$ error in determining the hard axis. This combination of anisotropies does allow the coercive forces to be measured.

The biaxial anisotropy was always fixed in direction relative to the crystal, but the uniaxial anisotropy depended on the relative direction of the deposition field to the crystal. Since this could not be lined up better than, say, 5^{o}, a small-angle approximation was performed to account for such a discrepancy.

Suppose the uniaxial easy axis lies at an angle $\beta = 45^{o} + \epsilon$ to the [110] direction, where ϵ is small, $\leq 2^{o}$. The general form for the angles (θ) at which switching vertices occur for the mixed anisotropy case is given by:

$$2 \sin 2\theta + 5b_1 \sin 4(\theta + \beta) = 0.$$

The switching vertices in the biaxial hard direction are given by $\sin 2\theta = 0$, for $\beta = 45^{o}$ and the 'easy' directions are given by $\cos 2\theta = \frac{1}{5b_1}$. Assume that the effect of a relative displacement of the anisotropies by ϵ causes a movement of the switching vertex by a small angle η, then proceeding as for equation 2.10:

$$2 \sin(2\eta + n\pi) = -5b_1 \sin(\pi + 2n\pi + 4\eta + 4\epsilon)$$

where n is a positive integer.

$$\therefore \quad (-1)^{n} 2 \sin 2\eta = +5b_1 \sin 4(\eta + \epsilon).$$

Using the small-angle approximations $\sin\eta = \eta$, $\cos\eta = 1$, we have

$$4\eta\left[(-1)^{n} - 5b_1\right] = 20b_1\epsilon$$

$$\text{or} \quad \eta = \frac{5b_1}{(-1)^{n} - 5b_1}\,\epsilon$$

It is therefore expected that the susceptibility maxima, i.e. the two 'biaxial hard' directions, will be separated by an angle

$$\Delta = 90 - \eta_{n=1} - \eta_{n=0} \qquad \text{or} \qquad \Delta = 90 - \left(\frac{10b_1\epsilon}{1 - 25b_1^{2}}\right).$$

This slight misorientation does not affect the size of the switching field but has the effect of slightly changing the shape of the curve at the switching vertices.

4.4. Torque Measurements

The susceptibility apparatus can measure the uniaxial and biaxial anisotropy fields for single-crystal films with certain known relative orientations. Certain polished films (section 6.5) had properties which suggested the presence of biaxial anisotropies in unknown directions and due to the complicated mathematics, analysis of the susceptibility curves is very difficult. The method used to determine a mixture of anisotropies of any relative orientation is torque magnetometry. This involves measuring the torque exerted on a film placed in a uniform magnetic field for various angles between the magnetisation and the applied field. The following gives a theoretical interpretation of the torque-anisotropy relationships used in torque magnetometry.

For a sample in a uniform field H_a at an angle α with the easy direction then the magnetic energy density, E, is given by:

$$E = - MH_a \cos(\alpha - \theta) + E_k(\theta) \qquad (4.4.)$$

where θ is the angle the magnetisation makes with the same easy axis and $E_k(\theta)$ the anisotropy energy density.

The torque on the sample, $L = \frac{\partial E}{\partial \alpha} = MH_a \sin(\alpha - \theta)$ and the condition for equilibrium is $\frac{\partial E}{\partial \theta} = 0$, which gives $MH_a \sin(\alpha - \theta) = \frac{\partial E_k}{\partial \theta}$, from equation 4.4. Thus the general torque equation is:

$$L = \frac{\partial E_k}{\partial \theta} \qquad (4.5.)$$

and knowing the general form of E_k, by Fourier analysis of the torque curves both the anisotropies and their relative orientations can be found.

4.4.1. Low-field Torque Curves. These were produced by adapting the susceptibility apparatus, previously described (4.3.1), after the method of Beam and Siegle (B.16). This involves applying a constant d.c. bias field (H_o) parallel to the small a.c. field ($\hat{H}$) which ensures that the film remains a single stable domain. The d.c. field perpendicular to this (H_a) is decreased from saturation until no flux change is observed (i.e. the pick-up signal is zero) and then the magnetisation will be parallel to the a.c. field. The torque on the magnetisation exerted by the external fields will then be MH_a, thus producing a torque equation: $MH_a = \frac{\partial E_k}{\partial \theta}$.

In the case of real films the field, H_a, is adjusted to find a minimum susceptibility, (non-zero because of dispersion and ripple). An important effect to be eliminated is that of rotational hysteresis, which will be very important at these low fields (only slightly greater than the anisotropy field). This is achieved by approaching the null point from saturation in the same direction every time.

The constant d.c. field was supplied by batteries as shown in the inset in figure 4.6b and could be varied from 7 to 22 oe. The inductance, L, was made very large at 2 kc/s but still keeping the resistance small so that the resonance of the a.c. field was hardly affected.

The anisotropy energy density for a uniaxial film is $E_k = K_u \sin^2\theta$ so that $\frac{\partial E_k}{\partial \theta} = K_u \sin 2\theta$, therefore:

$$MH_a = K_u \sin 2\theta \qquad \text{or} \qquad H_a = \frac{H_k}{2} \sin 2\theta \quad .. \quad .. \quad .. \quad (4.6.)$$

This curve gave a result for H_k which was in very good agreement with the susceptibility method, and its torque curve is shown in figure 4.14. The displaced centre is due to the effect of the earth's field. This film was one with small dispersion and large susceptibility ($\frac{\chi_p}{\chi_o} \simeq 6$). On the whole, for films with poor dispersion, the null point could not be detected very accurately and some points where the torque was small were almost impossible to determine with an error of less than 50 - 100%.

It was concluded that this technique was simple and useful for films with large signals and fairly low dispersion, but for other films only qualitative results could be extracted.

The sensitivity of this method depends on $\left[H_o \pm \hat{H}\right]^{-2}$ so the smaller the d.c. bias field, H_o, the greater the sensitivity. However, the minimum field must be kept above H_k and H_c or the film will be in a multidomain state. Thus it can be seen that this method will be very sensitive for films with low H_k and H_c, which are usually difficult to measure with the torque magnetometer. For films with higher anisotropies H_o has to be increased but the a.c. field also has to be increased to give larger signals, thus reducing the sensitivity appreciably. The drawback with this is that for higher dispersion films the variation in the resultant transverse field will cause large changes in ripple amplitude and so produce appreciable signals even though the magnetisation may be in the 'null' position. This means

that the determination of the null point with any accuracy near the eaxy axis is almost impossible as the sensitivity drops close to zero at these points for any film.

This method appears very useful for low-anisotropy, low-coercive-force films and the sensitivity may be increased sufficiently (by increasing the a.c. field) for higher anisotropy films to enable torque curves to be measured. However, for increasing dispersion the torque curves become rather erratic and no numerical values can be obtained from them.

4.4.2. High-field Torque Curves. In the previous section some of the drawbacks of the low-field torque measurements were outlined. The object of these measurements was to determine if any biaxial anisotropy was present in polished films which possessed a large degree of dispersion. It was obvious, therefore, that a torque magnetometer had to be used for these polished films.

The torque magnetometer used is described in more detail by Secemski (S.16), but it consists essentially of a quartz holder suspended by a fine strip of phospher-bronze from a torsion head.

The sensitivity of the instrument could be varied by altering the length of the suspension. The film's reference position was measured by reflection of a small light beam from a mirror attached to the quartz holder onto a photocell, its reading being a maximum in the reference direction. The whole suspension was enclosed in a perspex tube and placed in between the poles of a four-inch electromagnet.

A constant field of 5000 oe was used and the torque was calibrated by measuring the period of a known moment of inertia in the absence of a field and assuming simple harmonic motion. The calibration of the suspension used was 1.54 erg/radian and 2π radians $\equiv$ 25 cm on the torsion head.

The instrumental errors were eliminated by measuring a torque curve with a blank NaCl substrate in the holder and subtracting this from the actual curve. The corrected curve was then Fourier analysed and the relevant anisotropies and orientations extracted.

The case under study consists of a general mixture of biaxial (K_1) and uniaxial (K_u) anisotropies at angles of γ_1 and γ_u to the reference direction. For the magnetisation at an angle θ to this direction the anisotropy energy density $E_k = \frac{1}{4} K_1 \sin^2 2(\theta - \gamma_1) + K_u \sin^2(\theta - \gamma_u)$

$$\therefore \text{ torque, } L = \frac{\partial E_k}{\partial(\theta - \gamma_u)} = \frac{\partial E_k}{\partial \theta} = \frac{K_1}{2} \sin 4(\theta - \gamma_1) + K_u \sin 2(\theta - \gamma_u)$$

$$\text{or} \quad L = (K_u \cos 2\gamma_u) \sin 2\theta + \frac{K_1}{2} \cos 4\gamma_1 \sin 4\theta$$

$$+ (-K_u \sin 2\gamma_u) \cos 2\theta + \frac{-K_1}{2} \sin 4\gamma_1 \cos 4\theta$$

$$= A_2 \sin 2\theta + A_4 \sin 4\theta + B_2 \cos 2\theta + B_4 \cos 4\theta$$

Thus from a Fourier analysis of this curve the uniaxial and biaxial anisotropy constants will be the moduli of A_2, B_2 and A_4, B_4 respectively and their relative orientations can be determined from the ratio of these coefficients.

If the film and the applied field are not co-planar or the film is very thick the fourth-order magnetocrystalline anisotropy constant, K_2,

must be taken into account, as well as demagnetising effects. Ignoring demagnetising effects the analysis for K_1, K_2 and K_3 has been performed by Aubert (A.5).

Details of the Fourier analysis used here are given in the appendix of reference S.16.

4.5. Kerr Effect Apparatus

The final piece of apparatus was used for the observation of the hysteresis loops of films prepared on single-crystal substrates. These single-crystal substrates presented a large problem since they produced non-specular reflection from cleavage steps and the microstructure of polished films. By using a small spot size these effects could be minimised and the effects of 'skew' (F.8) could also be eliminated. The longitudinal Kerr effect could not be enhanced by 'blooming' since the epitaxy would be affected. It is therefore necessary that a high-powered, coherent source be used, capable of being focussed to a small spot size. With these points in mind the following apparatus was used.

In figure 4.15 the main components are shown: an 8 mW continuous-wave, uniphase, He-Ne gas laser as the source and a R.C.A. photomultiplier with ten stages as the detector. The polariser and analyser consisted of Glan-Thompson prisms which had extinction coefficients greater than 10^6.

The first Glan-Thompson prism is arranged so that plane-polarised light with the plane of vibration parallel to the plane of incidence is focussed onto the film surface by the lenses A and B in figure 4.15.

The reflected beam will contain a component vibrating in a plane perpendicular to the plane of incidence if there is a component of magnetisation in both the plane of incidence and the film plane. The amplitude and phase of this perpendicular component will depend on the magnitude and direction of the magnetisation. The second Glan-Thompson prism is placed in front of the photomultiplier in an almost-crossed position with the analyser. The photomultiplier output, being proportional to the component of magnetisation in a fixed direction in the plane of incidence, is fed to the Y input of an oscilloscope, the X input being proportional to the a.c. field.

The size of the longitudinal Kerr effect depends on the angle of incidence, being a maximum for about 60°. However, this finite angle of incidence introduces elliptical polarisation since, due to the convergence of the beam onto the film surface, the angle of incidence will vary. This effect can be minimised by using a smaller angle of incidence, a smaller spot size and a lens with a smaller numerical aperture. In this apparatus the angle of incidence was 49°, the spot size was 0.8 mm^2 and the numerical aperture was 0.08.

The film was supported in the same holder as for the susceptibility measurements to enable the easy axis to be determined accurately prior to the observation of its hysteresis loop. This was necessary for some of the polished films which had nearly isotropic hysteresis loops.

Typical hysteresis loops from this apparatus are shown in figures 4.16a and 4.16b. The non-linearity in the saturation part of the loops was present even with the laser switched off and was assumed to be due

to mains pick-up by an earth loop between the oscilloscope and photomultiplier.

The a.c. field used was at 50 c/s for convenience and was supplied by a variac and transformer from the mains.

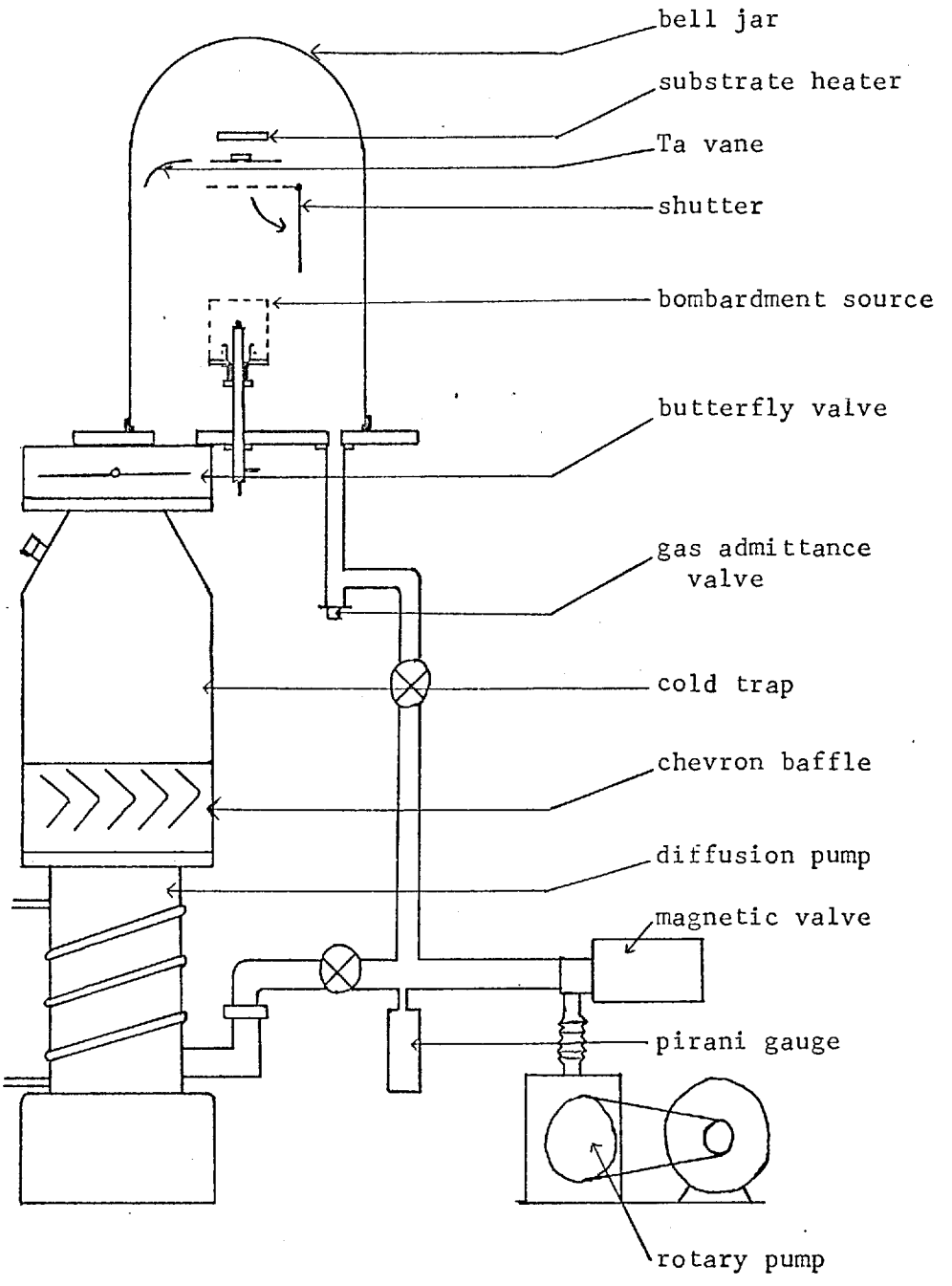

Figure 4.1 Schematic diagram of the vacuum system

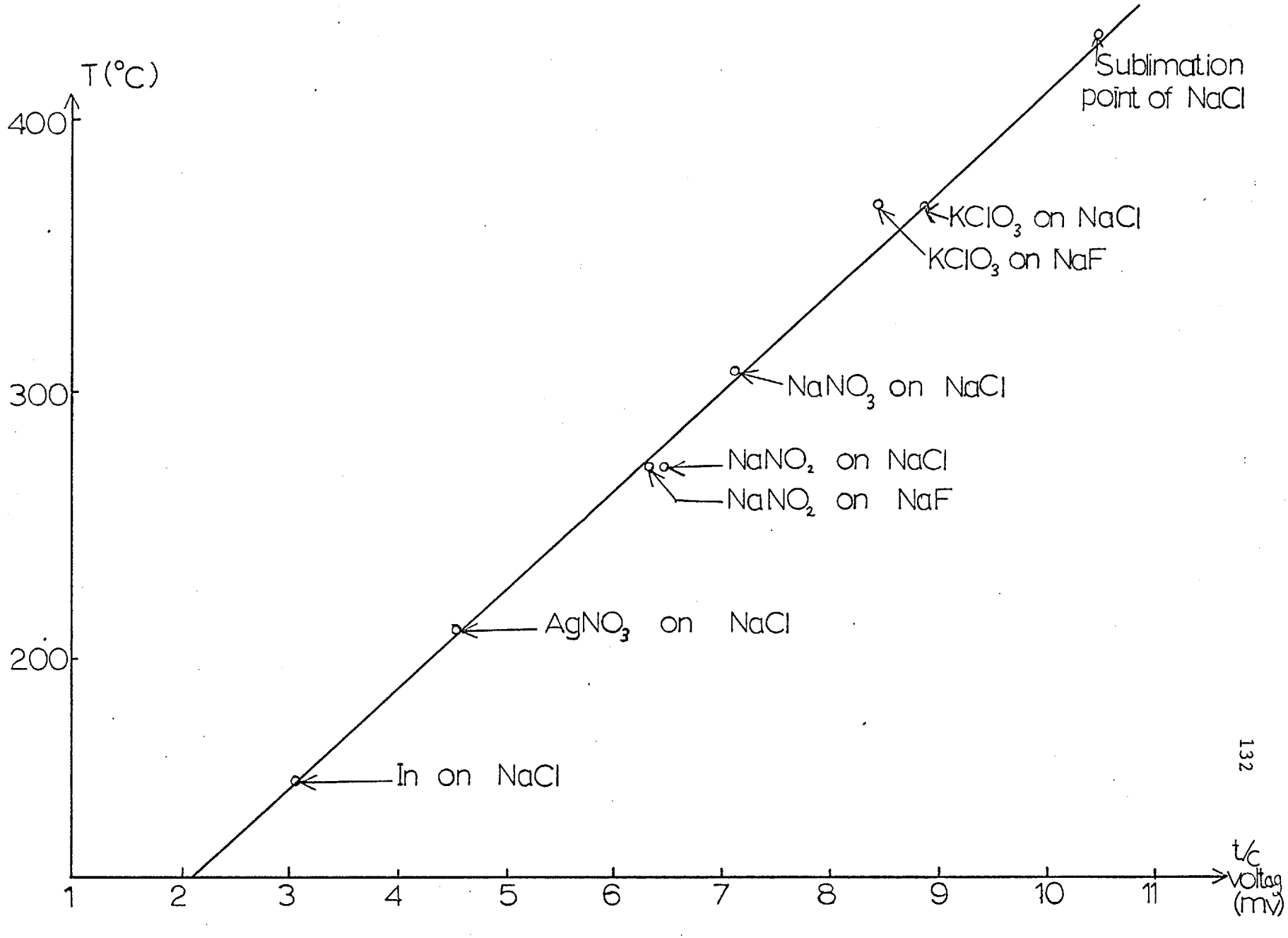

Figure 4.2 Calibration curve for the substrate temperature

(a) (b)

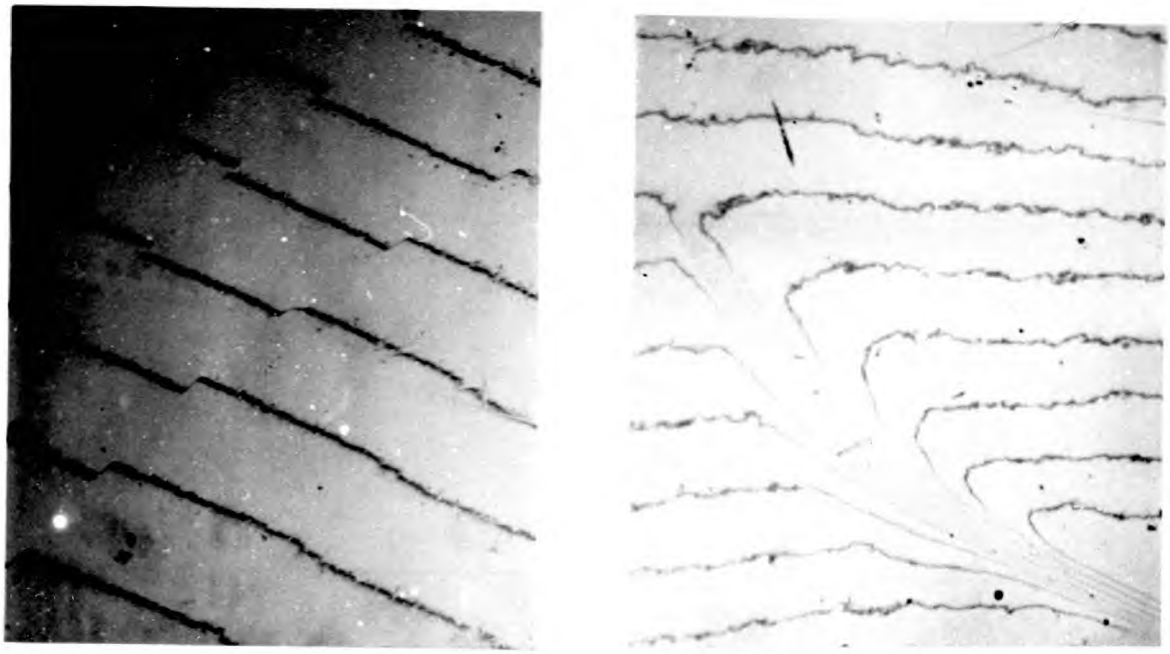

Figure 4.3 Multiple beam interference patterns of (a) cleaved and (b) polished NaCl substrates

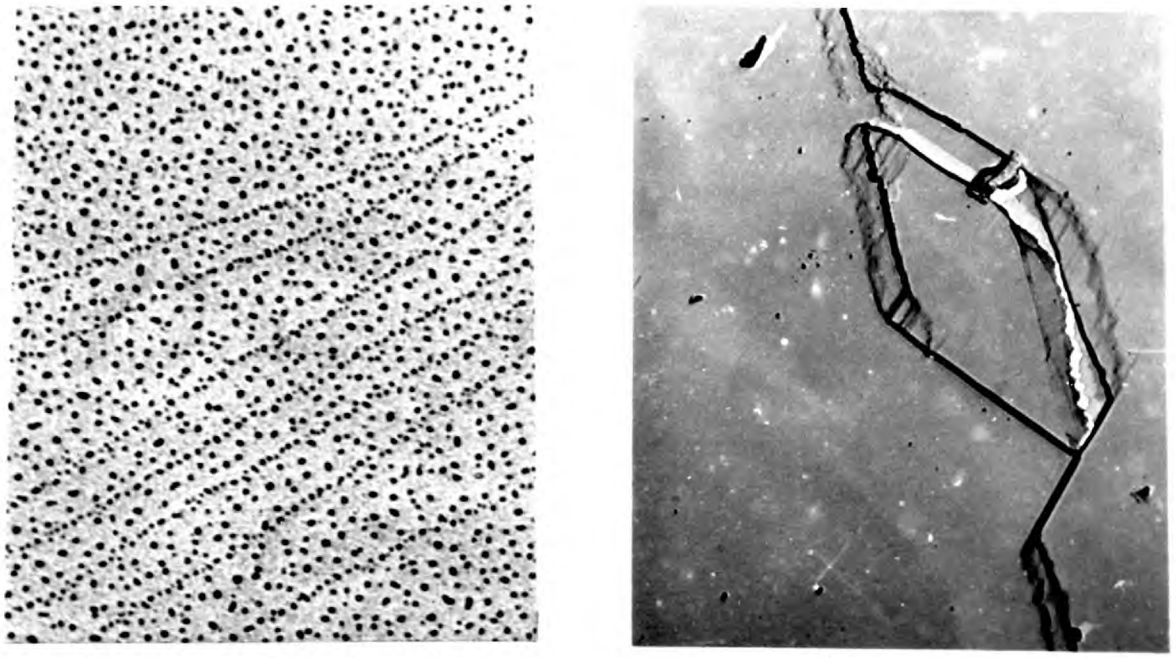

(a) (b)

Figure 4.4 (a) Cleavage steps on NaCl decorated with gold (x 200000)
(b) Pt-C replica of cleaved NaCl (x 8000)

(a)

(b)

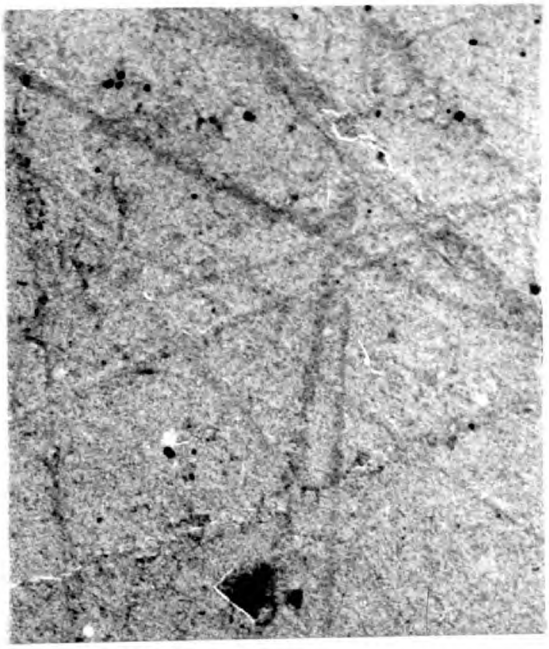

(c)

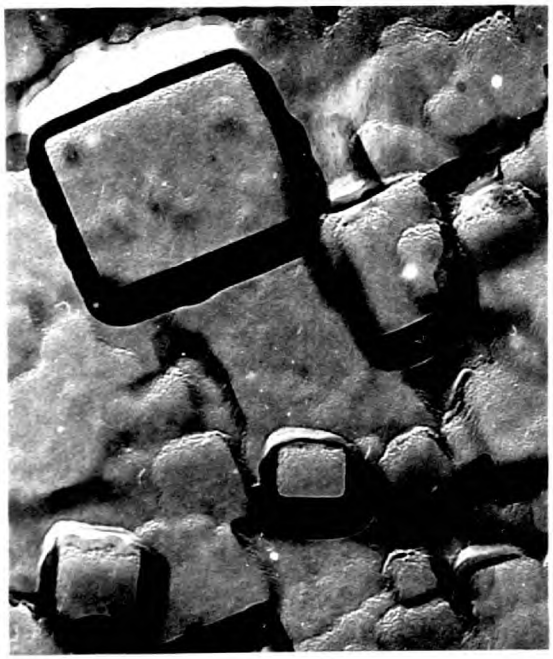

(d)

Figure 4.5 (a) Pt-C replica of polished substrate (x 36000)

(b) Electron micrograph of film grown on polished substrate (x 5000)

(c) Pt-C replica of crystallites on polished NaCl (x 80000)

(d) Pt-C replica of poorly-polished NaCl (x 23000)

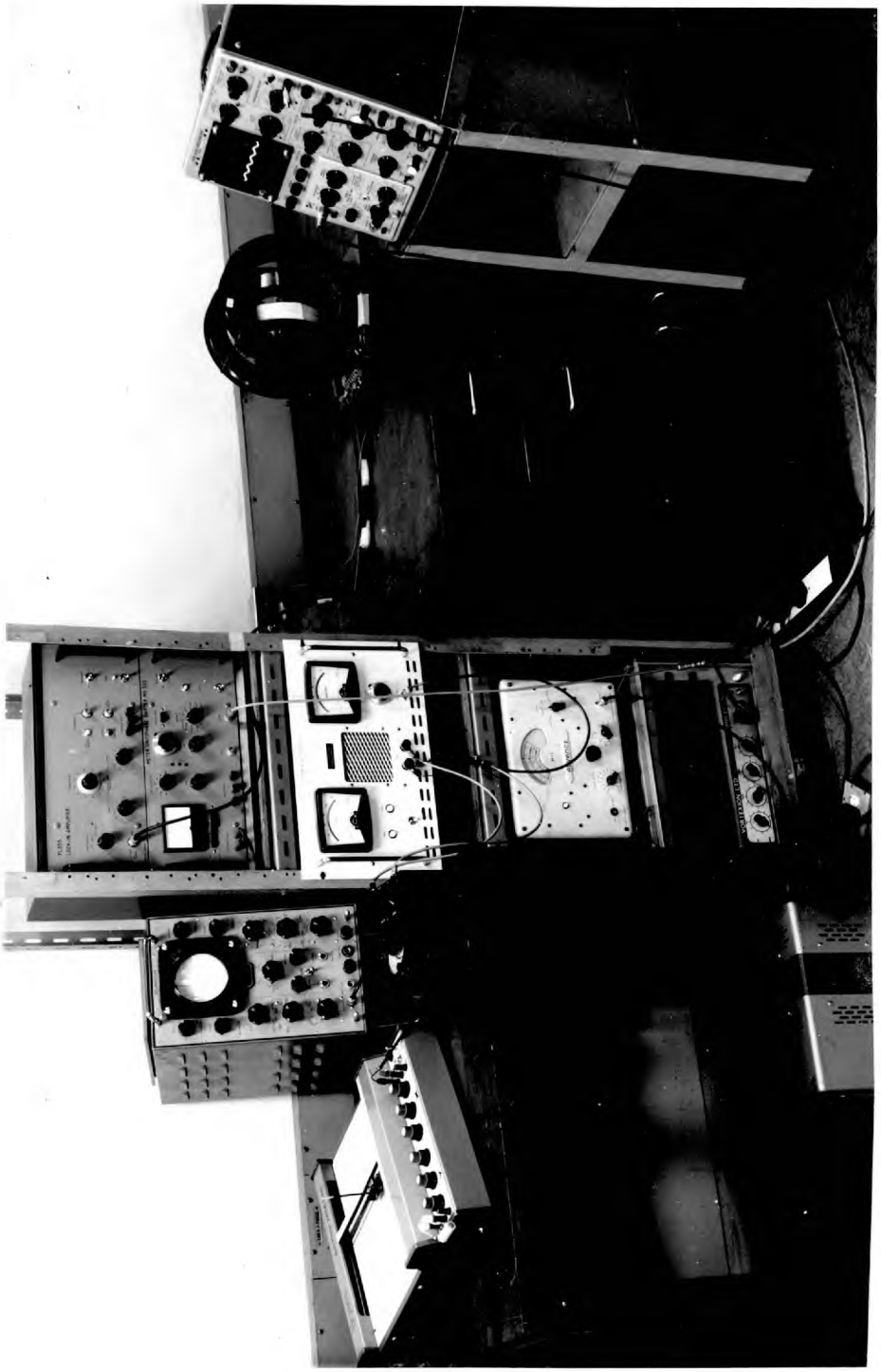

Figure 4.6.a Photograph of the bias susceptibility apparatus

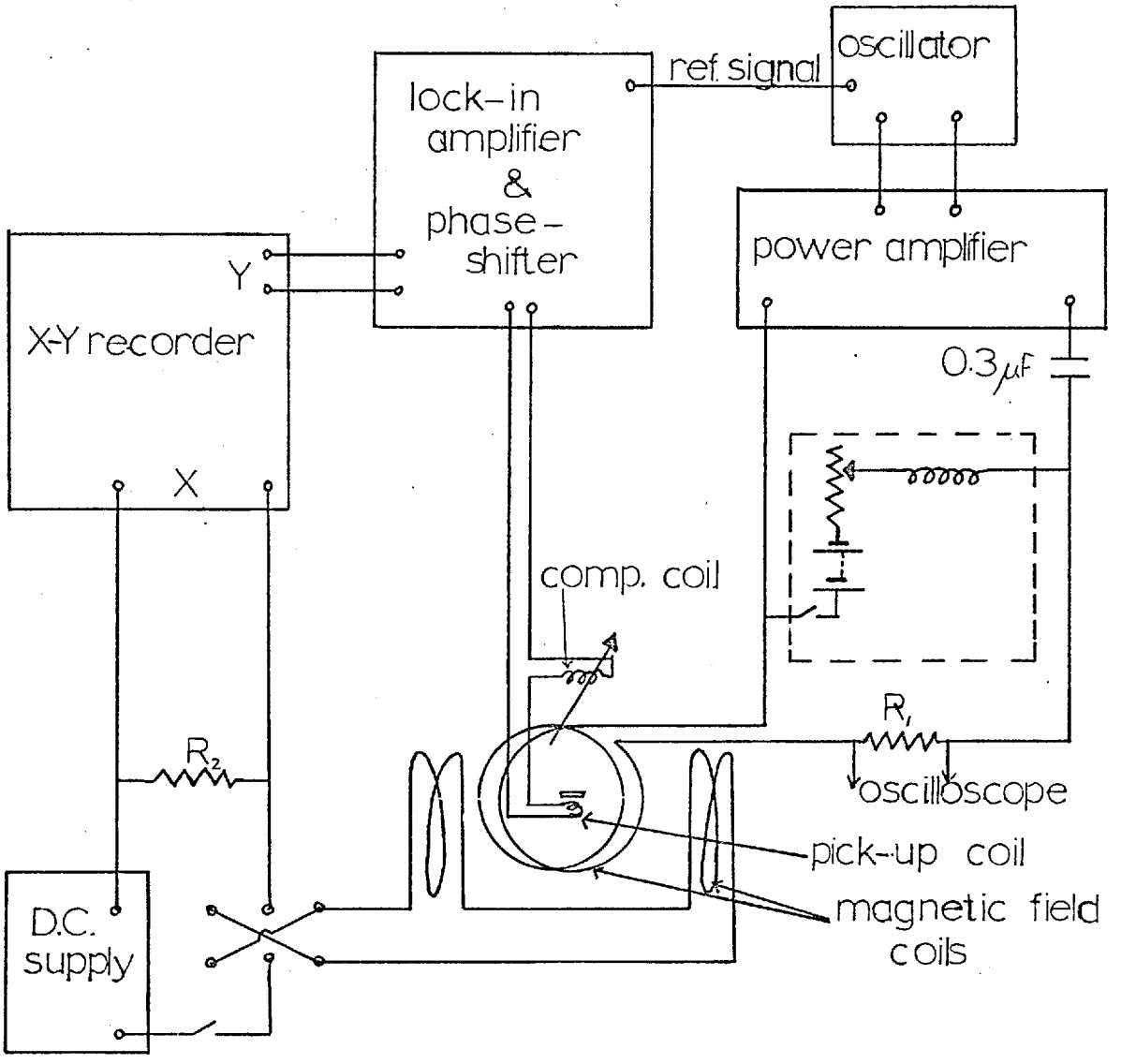

Figure 4.6.b Block diagram of the susceptibility apparatus

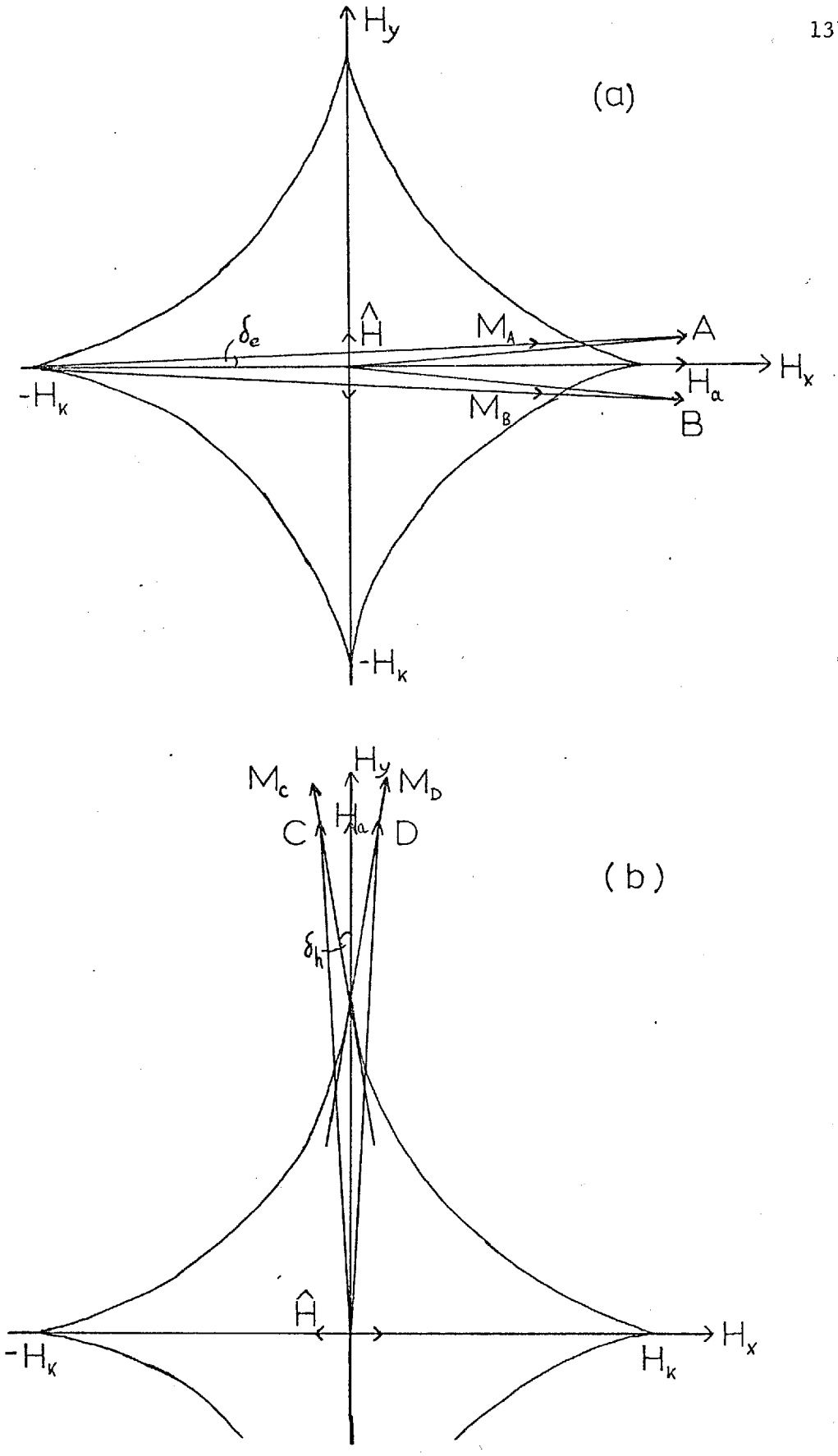

Figure 4.7 The field configurations for the susceptibility curves in (a) the easy and (b) the hard directions

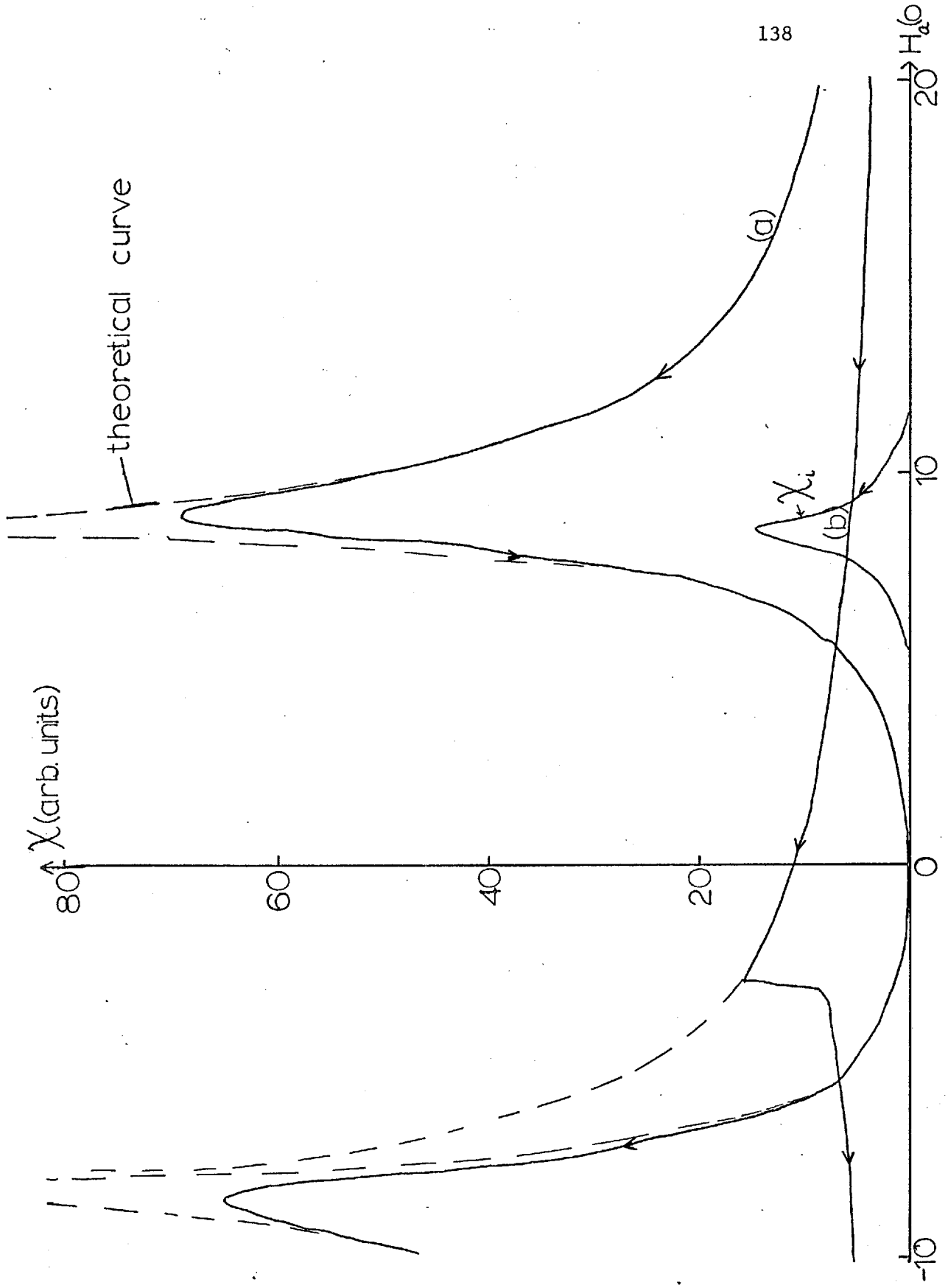

Figure 4.8 The transverse susceptibility and the losses (χ_i) plotted as a function of the bias field for a uniaxial film in (a) the hard and (b) the easy direction

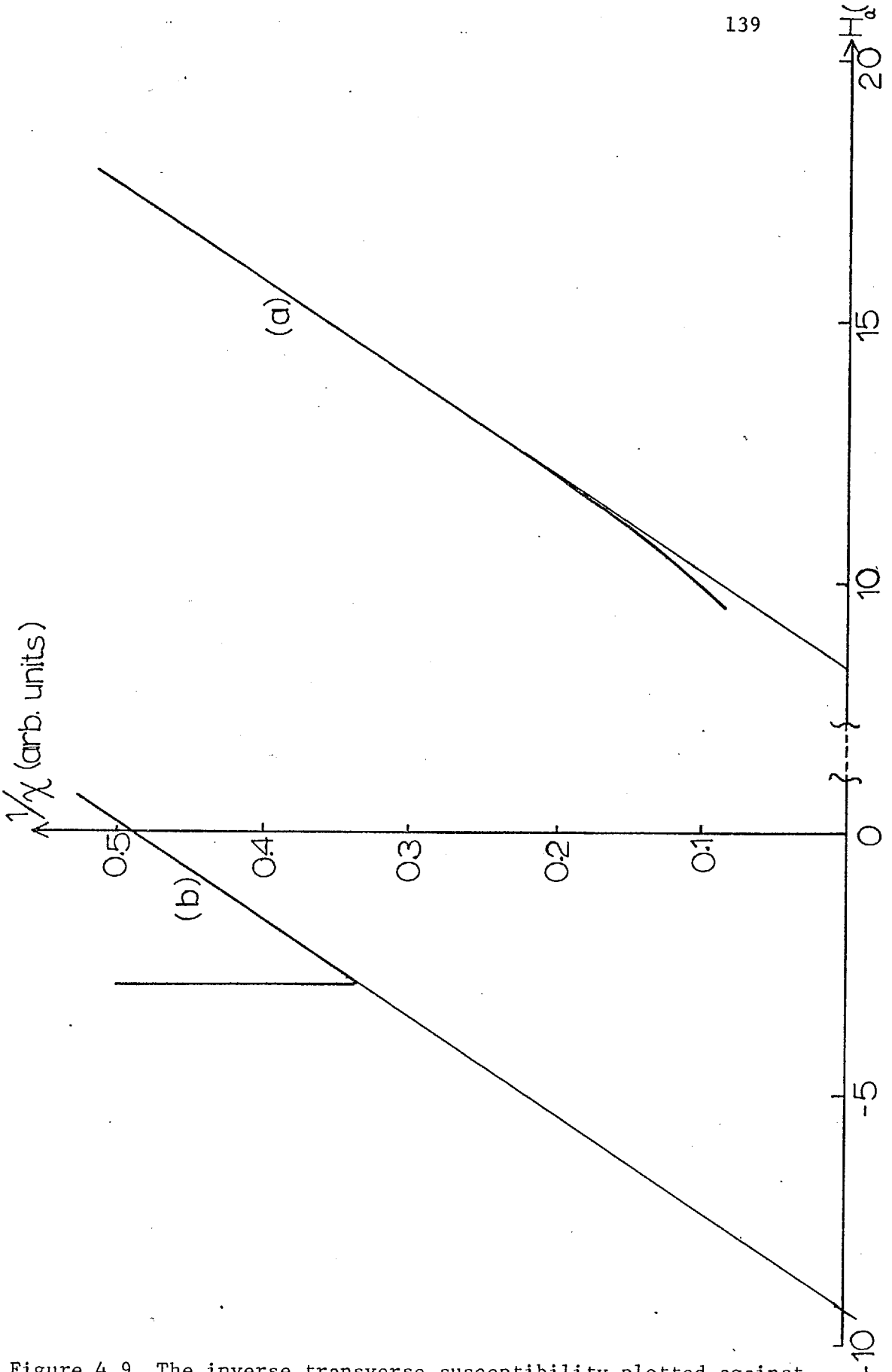

Figure 4.9 The inverse transverse susceptibility plotted against the bias field for the same film as in figure 4.8

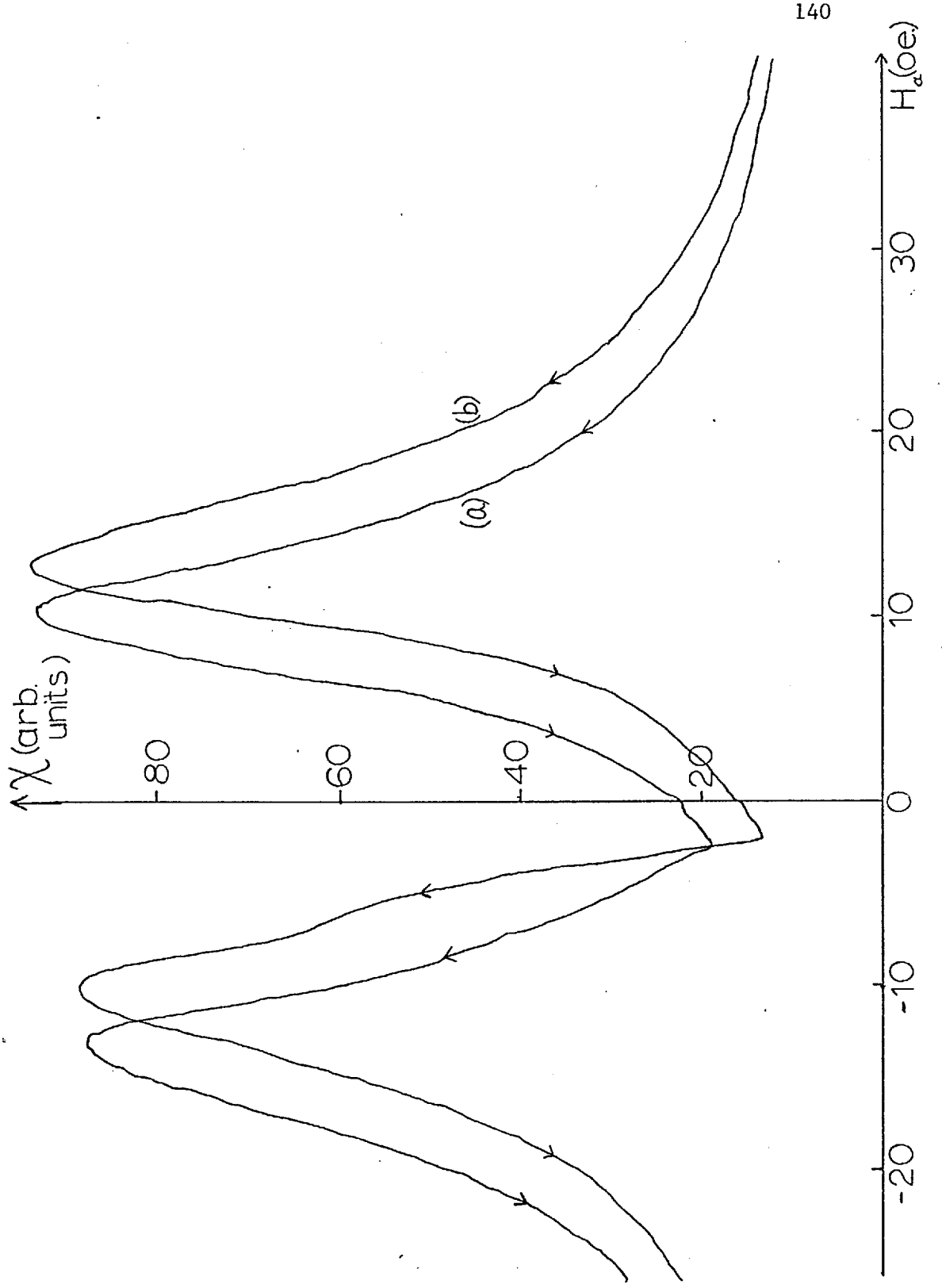

Figure 4.10 The susceptibility curves for a single-crystal film prepared on NaCl. (a) uniaxial easy and (b) uniaxial hard direction

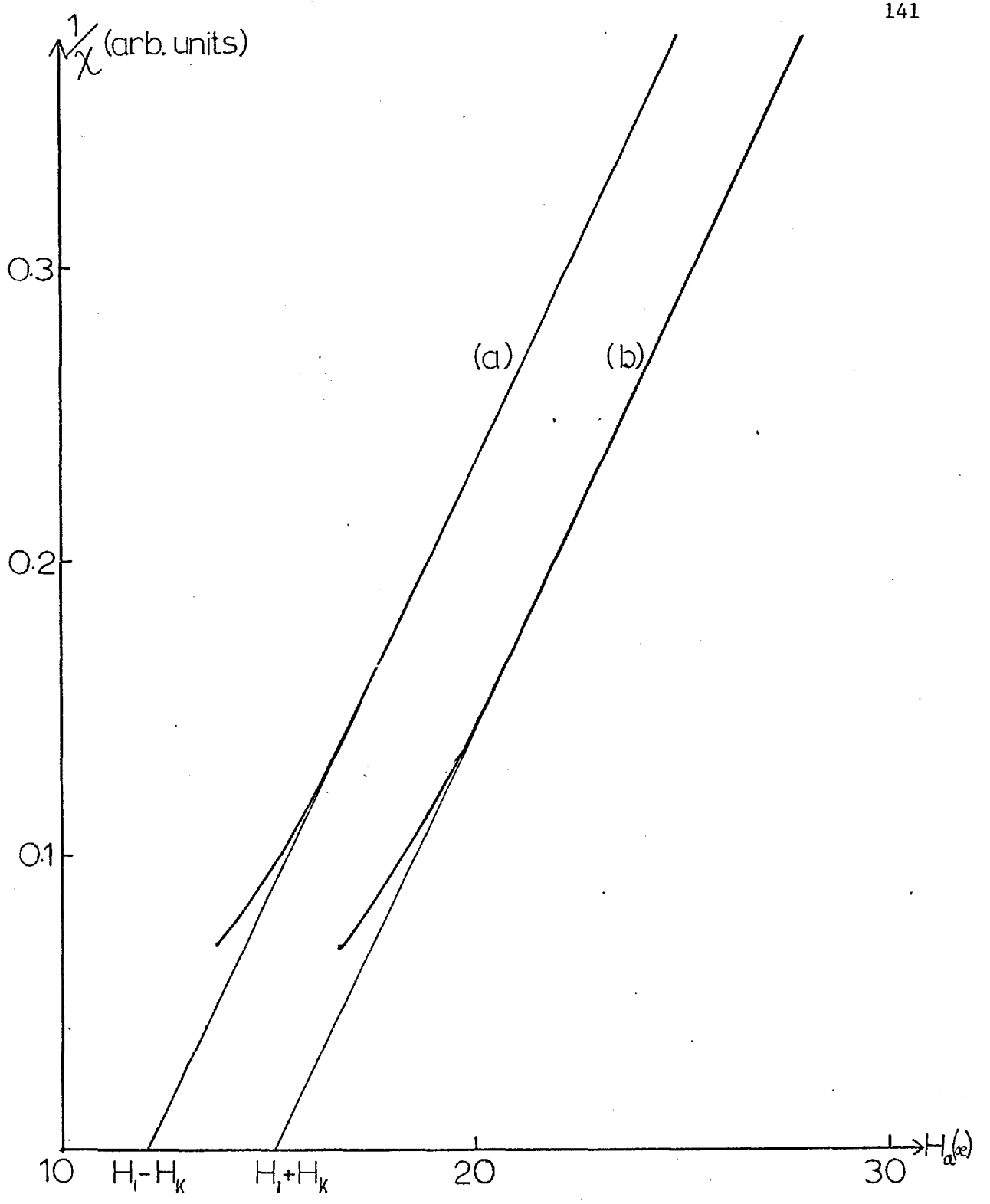

Figure 4.11 The inverse susceptibility curves for the same film as in figure 4.10

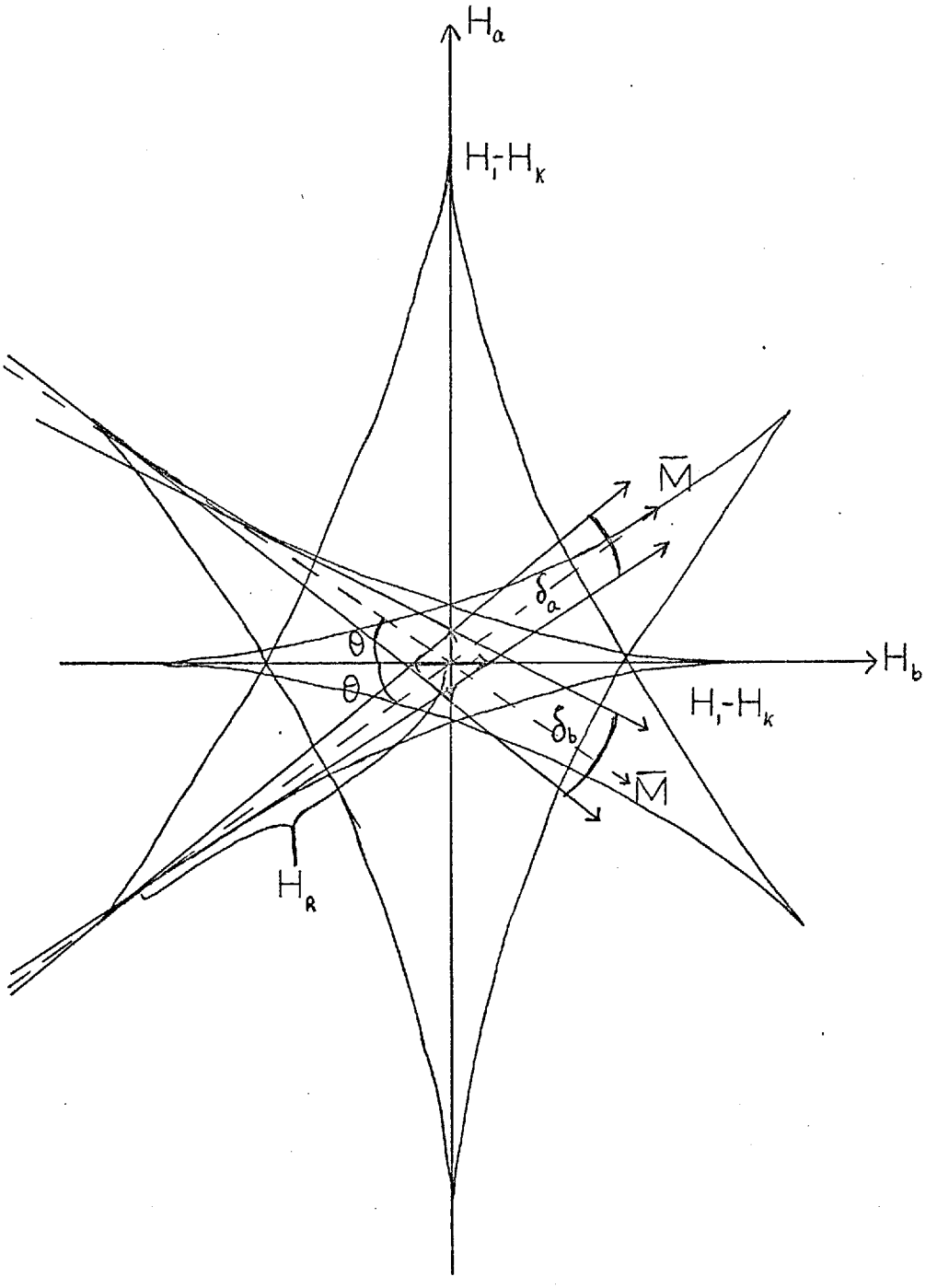

Figure 4.12 Diagram for the calculation of the zero-field susceptibilities

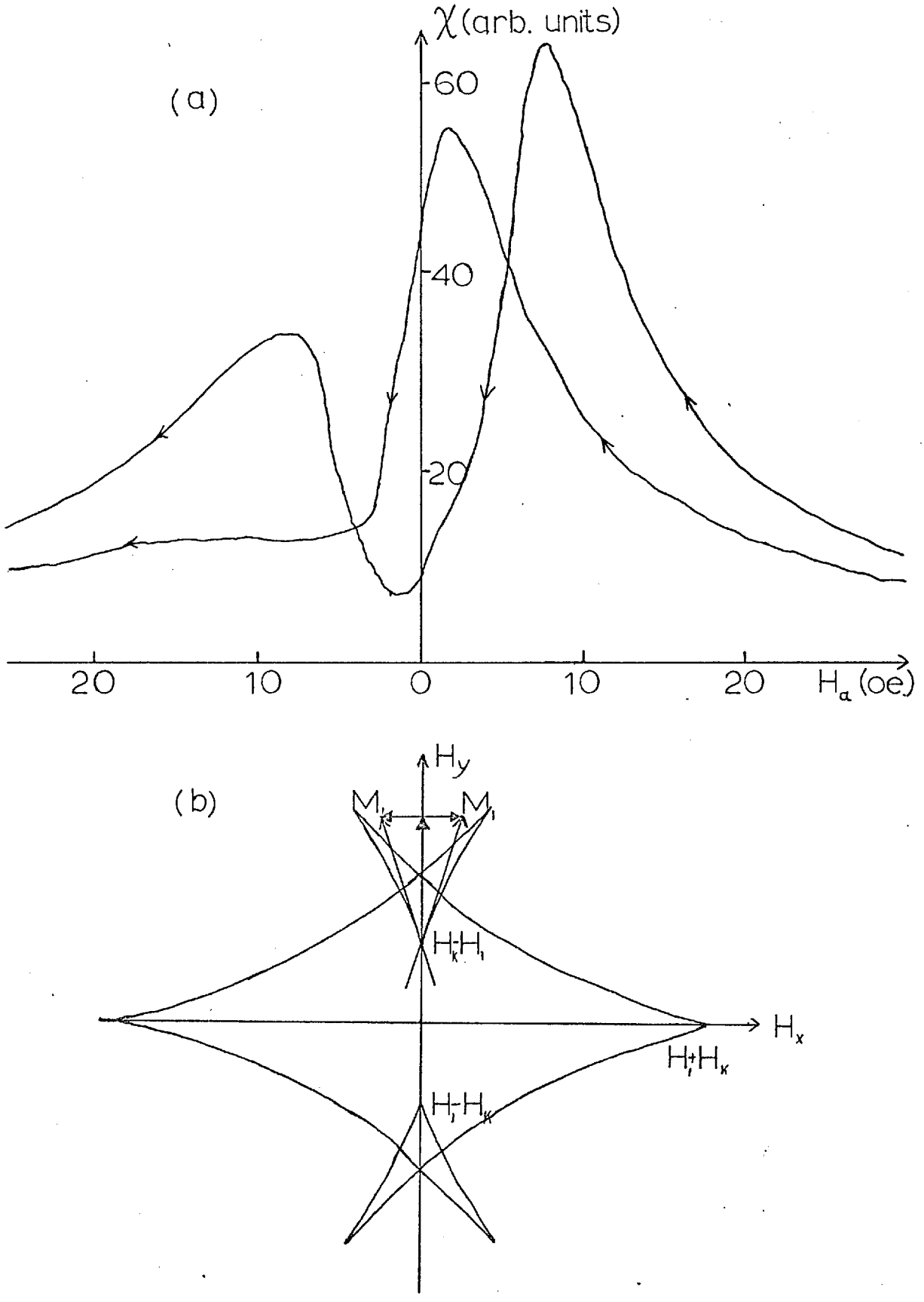

Figure 4.13 Susceptibility curves and biaxial astroid for a film with $H_1 < H_k$

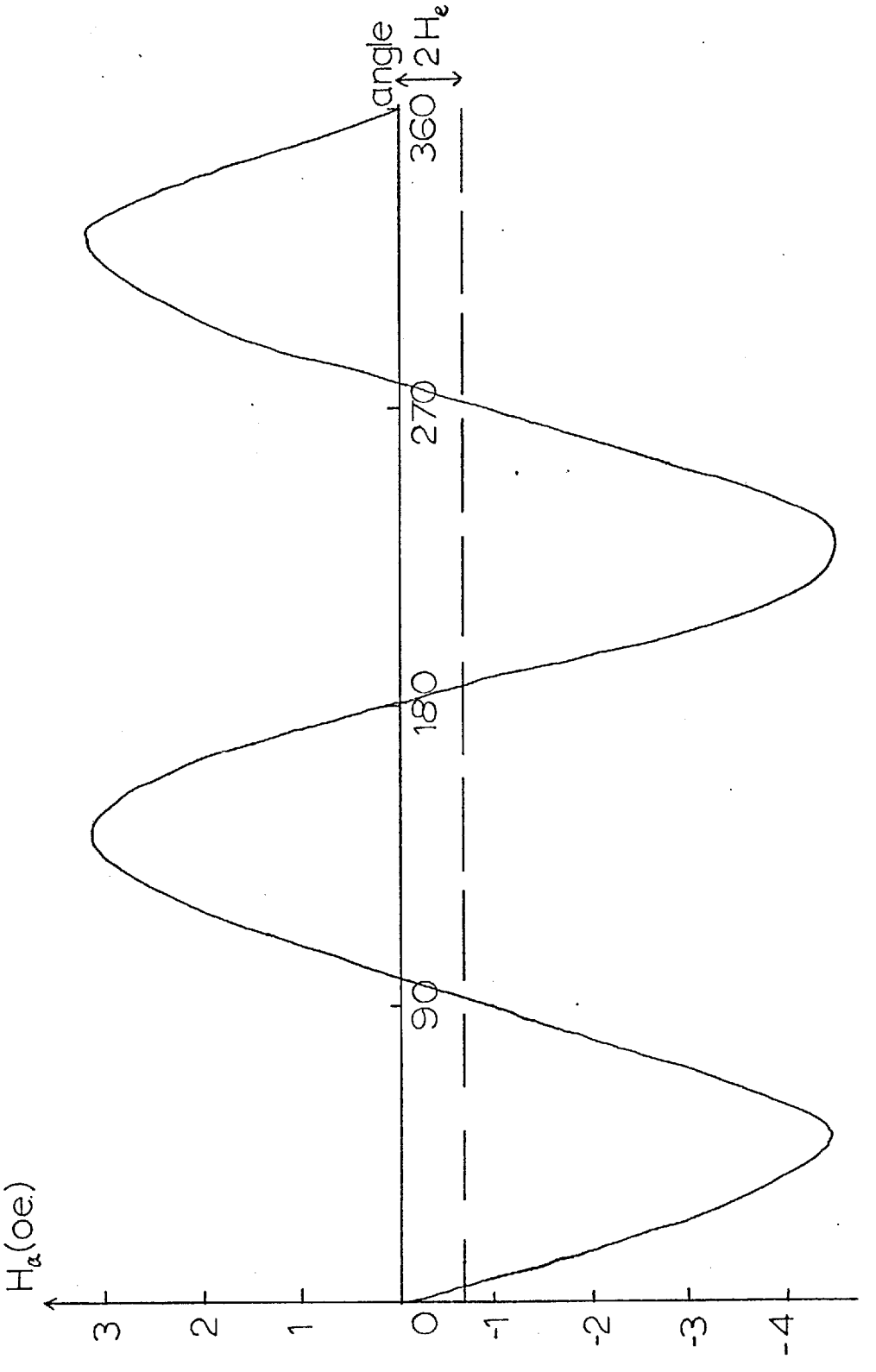

Figure 4.14 Low-field torque curve of a uniaxial film

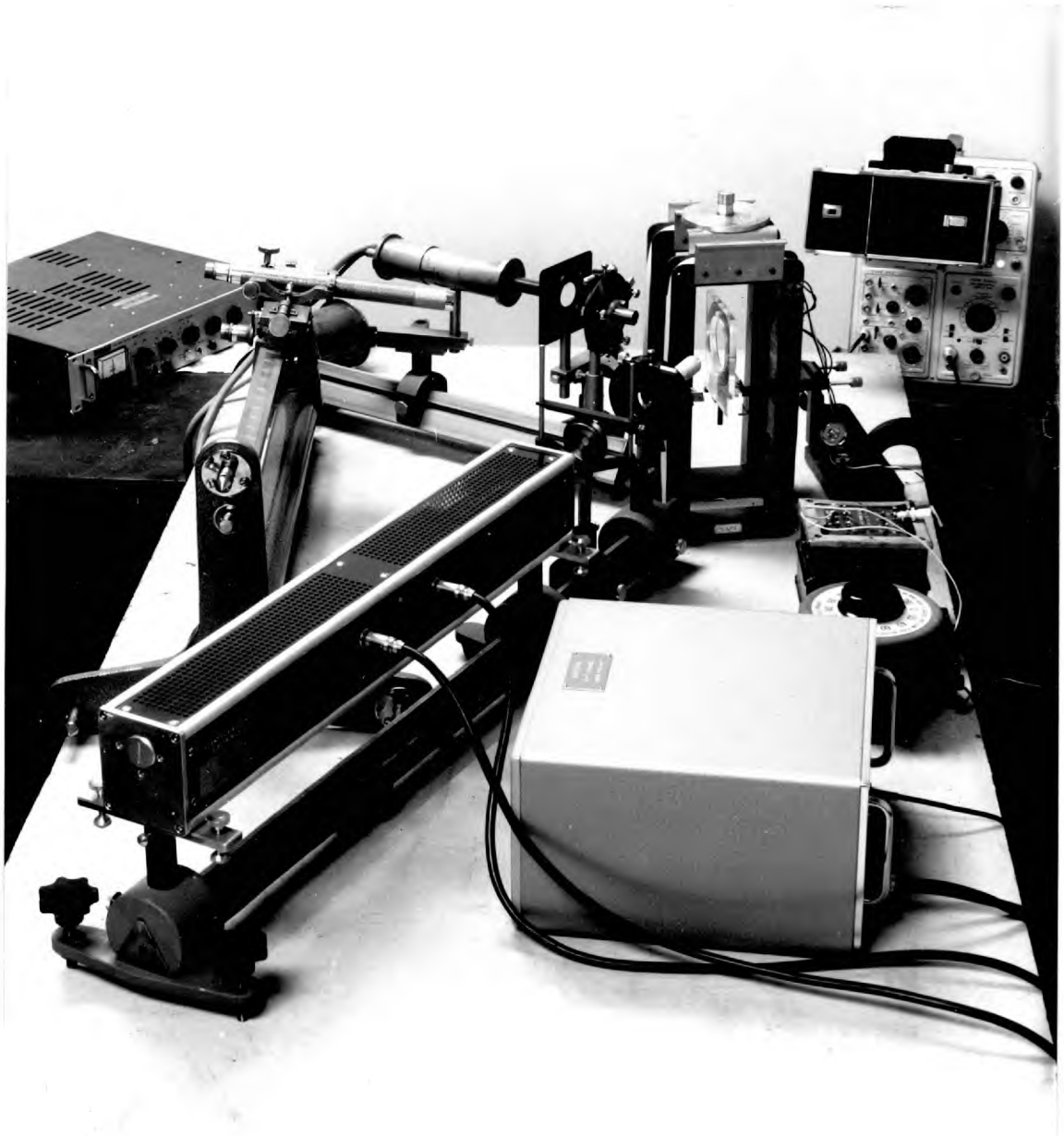

Figure 4.15 Photograph of the Kerr apparatus

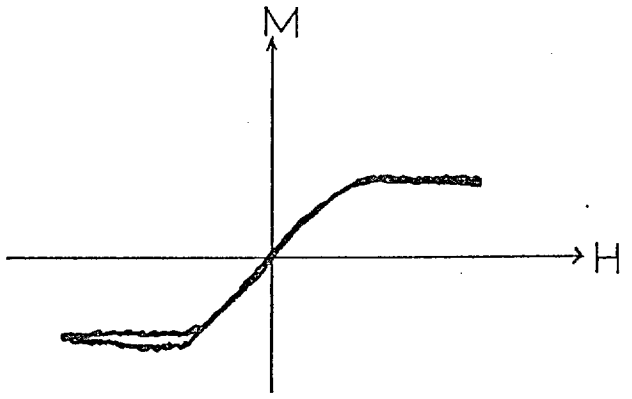

(a) Uniaxial hard axis

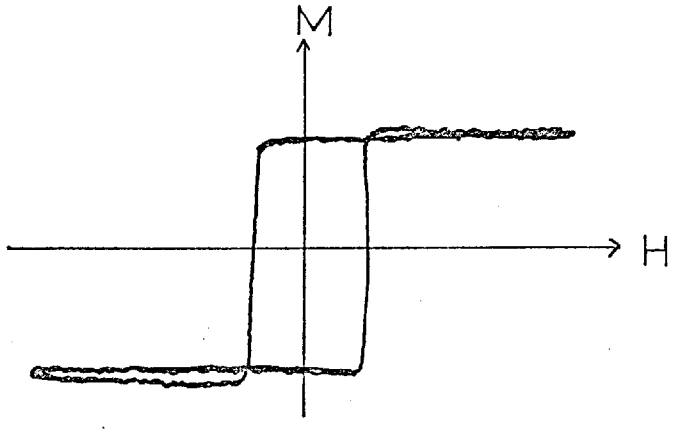

(b) Uniaxial easy axis

Figure 4.16 Traces of the hysteresis loops from the Kerr Effect

CHAPTER 5

Crystallographic Structure of the Films

In chapter 4 it was shown that the susceptibility curves can be used to determine the presence of both biaxial and uniaxial anisotropies. It is important to correlate these magnetic properties with the crystallographic structure of the films. The main variant is the films' crystallographic orientation which may be directly observed in the electron microscope by means of their diffraction patterns.

For the magnetic measurements in the following chapters two main approaches were used to control the film properties: firstly, the effect of the substrate temperature on the films and secondly, the effect of the nature of the substrate (both the material and preparation of the substrate).

In this chapter the effects of these parameters on the film structure are discussed and an attempt is made to explain them qualitatively. No attempt was made to verify these explanations by further experiments.

5.1. The Effect of the Substrate Temperature

The electron micrographs and diffraction patterns of eight films prepared on NaCl at various substrate temperatures are shown in figure 5.1. As the substrate temperature is increased several general observations can be made:

(1) There is an increase in crystallite size;

(2) The imperfections grow in size and decrease in number;

(3) The diffraction pattern changes from a ring pattern (figure 5.1(i)) into a spot pattern (figure 5.1(vii));

(4) Once the ring pattern has disappeared the spot pattern has satellite spots around most of the main spots, which gradually disappear as the temperature is increased further. These satellite spots are caused by the phenomena of twinning and double diffraction and will be dealt with in more detail later.

The diffraction patterns can be divided into five types: (a) the ring pattern, as in figure 5.1(i); (b) ring pattern + spots of smaller intensity, as in figure 5.1(ii); (c) spot pattern + rings of smaller intensity, as in figure 5.1(iv); (d) spot pattern + twin spots, as in figure 5.1(v); (e) spot pattern, as in figure 5.1(vii). These types of diffraction patterns are found to have an approximately linear dependence on the substrate temperature.

The four observations mentioned above can be explained as the direct result of higher substrate temperatures as follows: at higher substrate temperatures the adatoms and islands on the substrate will possess more thermal energy and, therefore, higher mobility. This means that they will show more liquid-like behaviour and so will allow re-orientation of islands when coalescing. Taking this to the limit, it can be said that the higher the substrate temperature the more perfect is the single-crystal film. The upper limit, however, will be governed by re-evaporation of the material from the substrate. As T_s increases the accommodation coefficient of the material on the substrate decreases, as will the associated sticking coefficient. Eventually, a temperature

will be reached when these coefficients are zero and so no film will be produced. For NaCl, sublimation of the substrate occurs before this temperature is reached. The thermal etching which ensues causes the films to have a milky appearance when the surface roughness produced is on the optical scale ($\sim$ 5000 Å). Higher substrate temperatures can be used on other alkali halides such as NaF, LiF resulting in better single-crystal films (S.16).

At lower magnifications long striations are observed on the better single-crystal films. These are termed 'bending or extinction contours' and can stretch over several millimetres. They result from the bending of the specimen so that the contrast is due to the varying angle of incidence between the electron beam and the film. Theoretically one expects a series of fringes around the extinction contour, which can be observed for thin specimens (H.18). For thicker films the fringes are not generally resolved due to the anomalous absorption effects caused by inelastic scattering. This results in the extinction contours appearing as single broad bands. The extinction contours are not usually continuous over large-angle grain boundaries (T.8) and so the lengths of the extinction contours give an indication of how perfect a single-crystal the film is.

At intermediate temperatures the smooth changeover from (100) ring to (100) spot patterns is interrupted by the appearance of spurious spots. It was found that large areas had hexagonal orientations correspondong to (111). As the temperature was increased further these extra spots disappeared. Whatever the mode of growth of epitaxial

films it is generally conceded that the formation of the initial islands is most important. The atomistic nucleation theory of Rhodin and Walton (R.5) can be used to explain these extra spots. In their theory the nucleation rate contains a term known as the critical nucleus size which is of extreme importance in epitaxy. It is defined as the smallest number of atoms which, when grouped in a cluster, has a greater probability of growth than decay on the adsorption of another atom. At high supersaturations the critical size will be a single atom, so a pair should grow rather than split into two atoms. Thus for a metal deposit on NaCl at room temperature the critical nucleus is likely to be a single atom and the stable pairs of atoms can attach to the substrate in any random direction giving polycrystalline films. However, as pointed out by Gillet (G.5) for NaCl the pairs will preferentially align in the [110] directions as this provides favourable sites over large distances. Therefore, we expect a predominantly (100) orientation.

As the substrate temperature is increased whilst maintaining a constant incident rate the supersaturation decreases and eventually a supersaturation will be reached where there is an equal probability of growth and decay for a pair. The critical nucleus is now a pair and islands will grow when they contain a minimum of three atoms. Following a similar argument to that of Walton et al (W.8), the most stable configuration containing three atoms will be an equilateral triangle. This produces a film with the (111) plane parallel to the substrate. The growth rate of this configuration will be affected by the energetically unfavourable sites which have to be occupied by the third atom.

If the supersaturation is decreased further there comes a point where a group of three atoms has an equal probability of growth and decay. The critical nucleus now becomes the two adjacent sides of a square so that the most stable cluster will be a square. Since this cluster has many energetically favourable sites for a face-centred cubic metal on a cubic substrate the nucleation rate is expected to be far higher for this configuration than for the (111). Thus, although the films at intermediate temperatures will contain some (111) regions they should be predominantly (100). The orientation which is favoured is governed by two conditions: (a) the critical nucleus leading to one orientation is more strongly adsorbed than any other orientation, which is mainly the case for f.c.c. metals on cubic substrates; (b) the critical nucleus which leads to another orientation is adsorbed strongly but subsequent growth requires the addition of atoms in unfavourable positions, so that this orientation nucleates but is unable to grow.

A slightly different, three-dimensional, explanation has been proposed by Gillet et al (G.5). At high supersaturations they observed in electron micrographs both triangular and square islands for gold on NaCl. They propose that both these nuclei are present at high supersaturations but due to its larger size the square has a lower growth rate so this gives a predominantly hexagonal orientation. When the film becomes purely (100) it is suggested that the supersaturation has decreased sufficiently to provide a stable island containing five atoms in the form of a pyramid with a square base. This is preferential to a pyramid with a triangular base if the binding energy of the metal atom to three others is less than the adsorption energy of the atom on the substrate.

Both explanations seem acceptable although only Walton et al (W.8) obtain good quantitative agreement. It would seem that the explanation of Gillet et al (G.5) is applicable at a later stage in the growth, after the critical nuclei are deposited. The rectangular pyramid proposed by Gillet must be the stage after the square for three-dimensional growth. This shape has four (111) planes on its surface enabling a model for the observed twinning to be visualised.

5.1.1. Twinning and Double Diffraction. Once the main (100) pattern has been established, there exists around each main spot a group of four symmetrically placed satellite spots, which disappear at higher temperatures. These result from microtwins, which are small regions having a new and special orientation with respect to the matrix. The twin orientation is obtained by rotating the matrix orientation by 180° about a particular crystal direction known as the twin axis. For most f.c.c. metals these twin axes are usually the four [111] directions. Since these twins are a new orientation the composite diffraction pattern should contain two separate patterns.

As mentioned previously, for f.c.c. metals the twin axes are [111] but due to the shape transform of the film the new pattern lies ~~usually lying~~ in the diffraction pattern or reciprocal lattice plane. For this case the construction of the generated twin points is simply a reflection of the main spots in the twin axis. This gives the impression of the satellite spots mentioned earlier. In figure 5.2. the constructed twin spots are shown by the full circles.

The Miller indices of the reciprocal lattice twinned spots may be calculated fairly simply for the case where the twin axis lies in the

reciprocal lattice plane (pg 141, reference H.20). The satellite spots were first explained as twin spots for permalloy by Burbank and Heidenreich (B.17) who deduced the origin of the twins as a relief mechanism occurring at the boundaries of growing nuclei to reduce the strain energies.

Comparing the diffraction pattern of an actual twinned film (figure 5.1(v)) with the predicted one, figure 5.2. shows a discrepancy in the number of satellite spots. Double diffraction is the phenomenon which produces four satellite spots around each main spot. As its name suggests, double diffraction occurs when a diffracted beam acts as an incident beam for another region and is diffracted a second time. The resulting composite diffraction pattern is a superposition of the two, the second pattern being produced by a translation of the first pattern until the first diffracted beam becomes the new origin. This is the explanation of the occasional appearance of so-called 'forbidden' reflections, i.e. diffraction spots which should be inherently absent when the structure factor is zero.

Due to the symmetry of the diffraction pattern of cubic materials, double diffraction should result solely in an increase in the intensity of existing spots. For a twinned region, however, it results in the appearance of the other twinned spots shown in figure 5.2. as the open circles. It has been shown by Pashley et al (P.7) that the double diffraction of the twins can only occur in the vicinity of twin boundaries and is not a property of the boundary itself. Since films possess a large number of relatively small-sized twins, double diffraction is nearly always present to produce the four satellite spots.

Several other irrational spots (such as the forbidden (110) spots) have been observed in (001) permalloy films by Alessandrini (A.6). They can be explained in terms of the double diffraction of twinned regions. From Alessandrini's work, these irrational spots depend on the presence of (111) orientations which are created during an annealing process and are not generally present in evaporated films.

5.2. The Effect of Various Substrates

Three different alkali-halide substrates were used, all cleaving in the [100] directions. Films prepared on the sodium fluoride (a) and lithium fluoride (b) substrates at various substrate temperatures are shown in figure 5.3. A comparison of these films with those produced on sodium chloride at various temperatures can be made from figures 5.1. and 5.3.

The polycrystalline films prepared on NaF and LiF appeared very similar in the electron microscope to those prepared on NaCl. This is because the effects of the various physical properties of the substrates have been masked by the lack of mobility of the adatoms causing the polycrystallinity.

At higher substrate temperatures the films on NaF and LiF again looked very similar when prepared under similar conditions (T_s, pressure etc.). The films prepared on NaCl did, however, appear to have a slightly higher defect density than those on NaF and LiF, as can be seen by comparing figures 5.1(vii) and 5.3(a)(T_s = 340°C). In fact, at about 330°C the defect densities for films grown on NaCl and NaF are $\simeq 1.5 \times 10^{10}/cm^2$ and $\simeq 7 \times 10^{9}/cm^2$ respectively.

The main differences produced by the substrates can be seen by comparing the diffraction patterns. Generally speaking, the films grown on NaF and LiF possess a higher degree of orientation (for approximately the same substrate temperature) than films grown on NaCl. One possible explanation for this is an increase in the binding energy between the deposit and the substrate causing the (100) sites to be preferred even more than the (111). This means that the intermediate, mixed, diffraction pattern will occupy a smaller temperature range leading to an effective lowering of the epitaxial temperature.

The binding energy quoted above will be affected by surface impurities and since NaCl is so soluble in water any water-vapour attack from the ambient atmosphere would tend to smooth out the cleavage steps initially and so reduce the number of nucleation sites. The surface could also be more effectively cleaned for the NaF and LiF substrates since a higher bake-out temperature could be used.

Another important point which may contribute to the improved epitaxy is the difference in sublimation points of the alkali halides. The rock-salt, having a relatively low one ($\sim 420^{\circ}C$) will have a fairly significant evaporation rate at high deposition temperatures. This has the effect of mixing with the film giving the milky appearance mentioned previously. Thus, to avoid this, the substrate temperature has to be kept down to about $330^{\circ}C$ whereas for NaF and LiF the maximum is much higher, enabling increased mobility of the adatoms to improve the epitaxy. Even below $330^{\circ}C$ the vapour pressure of NaCl is higher than those of LiF and NaF, hence more gets into the film.

5.3. The Effect of Various Preparations of NaCl

The various methods of preparation were described briefly in section 4.2. and their effect on the magnetic properties, especially the polishing, ~~especially~~, is discussed in section 6.5. This section deals with the effects visible in the electron microscope.

5.3.1. Polished Substrates. The most obvious feature of the 'polished substrate' films is the scratches transmitted from the substrate into the film. These are shown in the electron micrograph of a 'polished' film in figure 4.5.b. and the Pt-C replica of the substrate (figure 4.5.a). The polishing of the substrate also produced films with a better degree of orientation In figure 5.4. two films prepared in the same evaporation are shown. Film (a) was grown on a cleaved substrate whilst film (b) was grown on a polished substrate. The polished film has a better orientation showing less twinning and less spread of orientation. Single-crystal 'polished' films usually showed a faint ring pattern near the centre of the spot pattern. The origin of this was thought first to be due to some of the polishing material remaining on the substrate surface and possibly undergoing some chemical transformation during the evaporation. This was dismissed after a calculation was made of the possible diffraction patterns from the polishing compound. It is now proposed that this ring pattern originates from misoriented material deposited along scratches in the substrate.

A possible explanation of the improved orientation is that the polishing process has, by producing inclusions, dislocations etc., increased the infra-red absorption coefficient of the NaCl. The two

substrates would then be at different temperatures for the same evaporation. This explanation appears to be supported by the micrographs in figure 5.4. The polished film has a smaller defect density and the stacking faults present are well oriented along two perpendicular directions, indicating very good orientation. Both of these points can be explained by a higher substrate temperature.

5.3.2. Etched Substrates. The electron micrographs and diffraction patterns of two films prepared in the same evaporation are shown in figure 5.5. The etched substrate (b) has produced a film with a far better orientation although the defect density is higher. These two observations do not tally with an increase in the substrate temperature.

It is proposed that the etching has produced a large number of preferential nucleation sites which are crystallographically orientated. This will greatly improve the epitaxy while the crystallite size and defect density as determined mainly by the substrate temperature will remain about the same.

It has been shown by Sella and Trillat (S.17) that thermal etching introduces substantial micro-relief causing many defects to be introduced in films grown on this type of substrate. If the etching used produces the same roughness as the thermal etching then the increased defect density can be explained as the result of the growing together of these non-planar regions.

(i) $T_s = 130^{\circ}C$

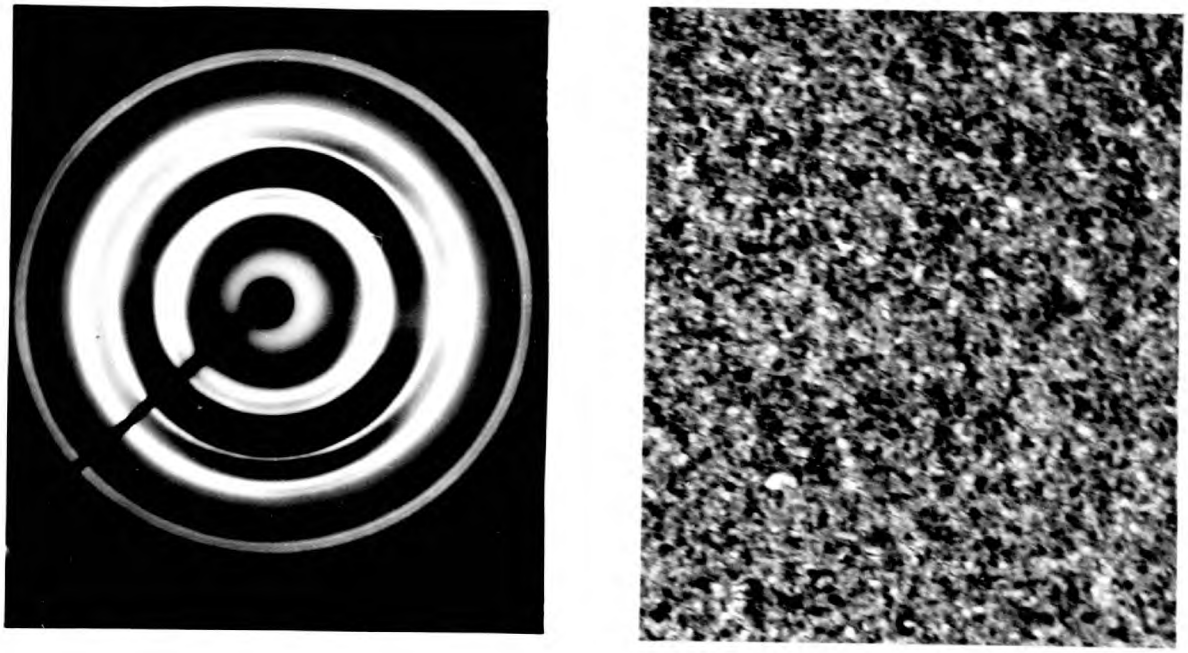

(ii) $T_s = 160^{\circ}C$

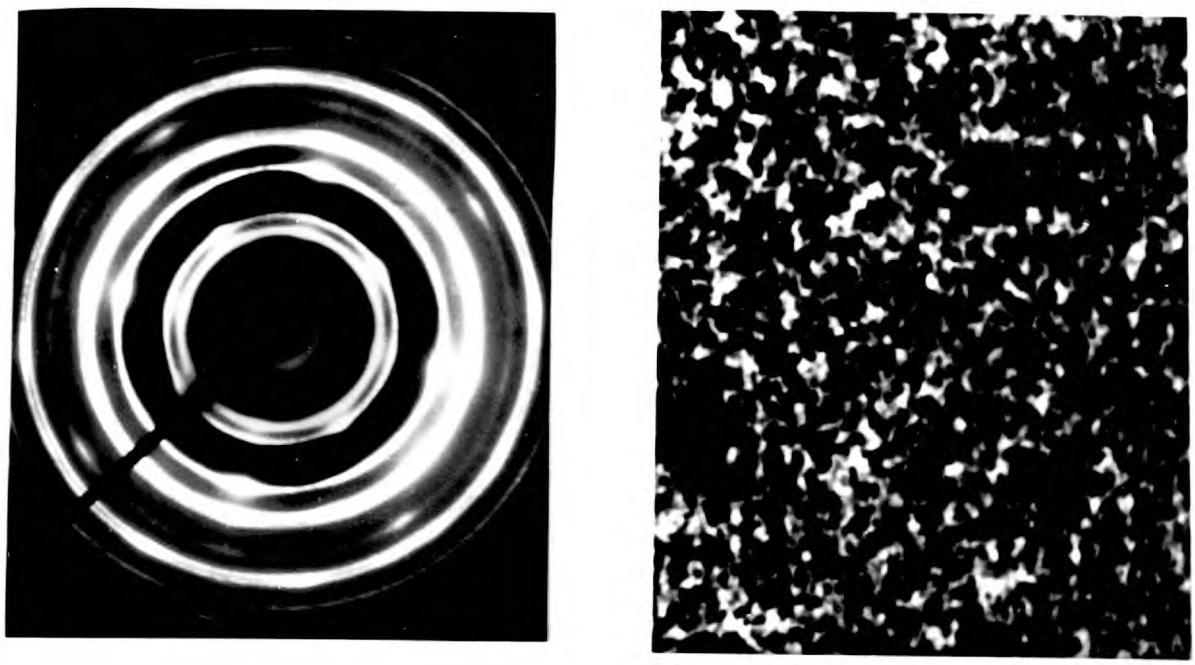

Figure 5.1 Electron micrographs (x 100000) and diffraction patterns of films grown on cleaved NaCl at various temperatures

(iii) $T_s = 220^{\circ}C$

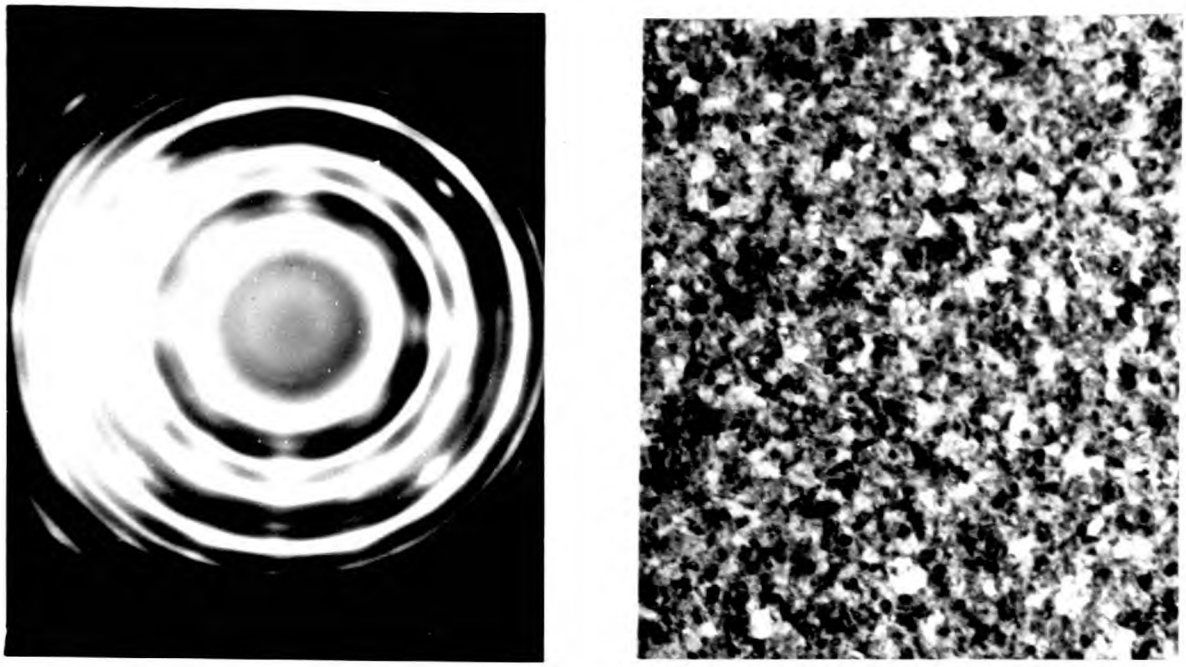

(iv) $T_s = 240^{\circ}C$

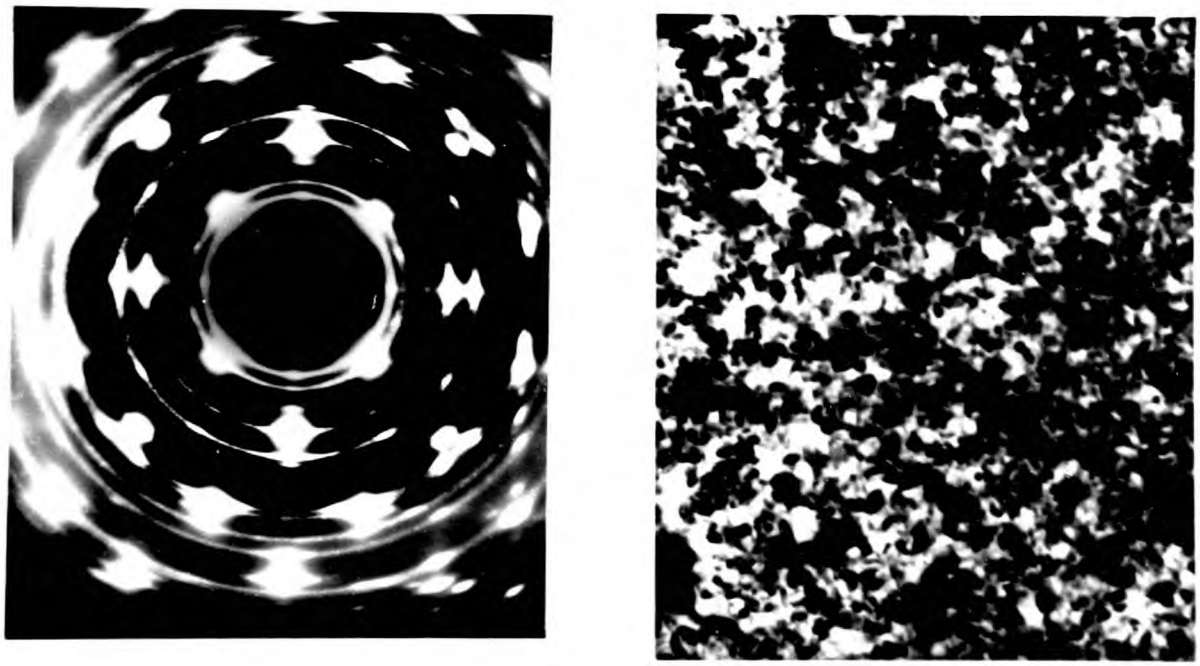

Figure 5.1 (continued)

(v) T_s = 280°C

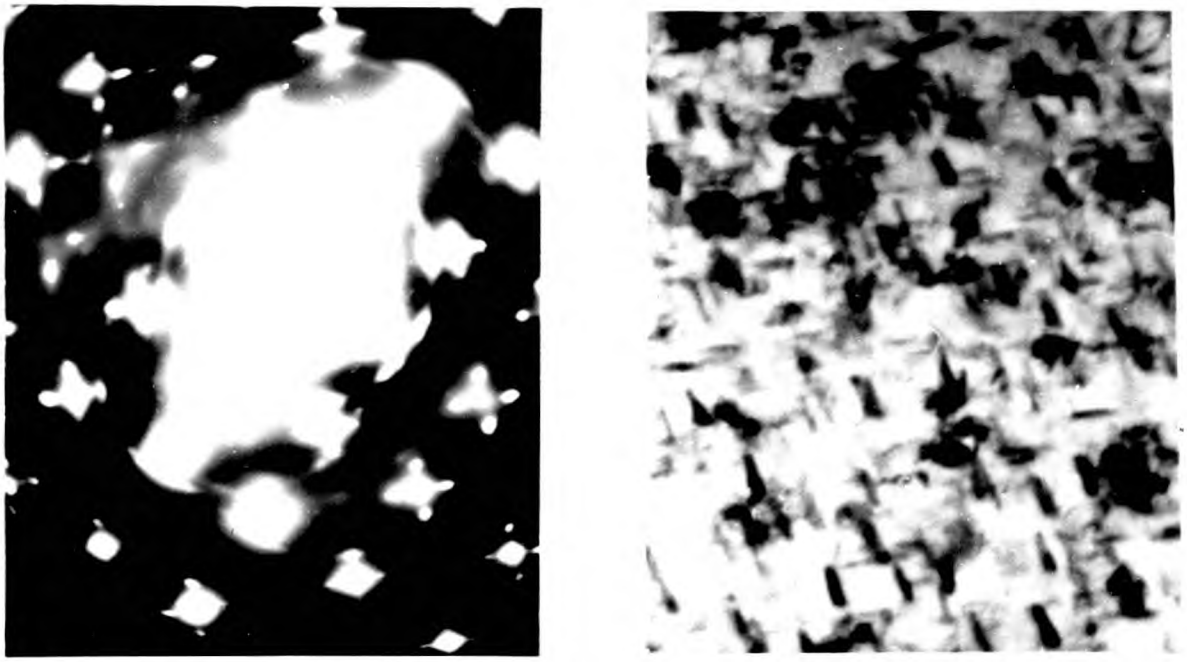

(vi) T_s = 290°C

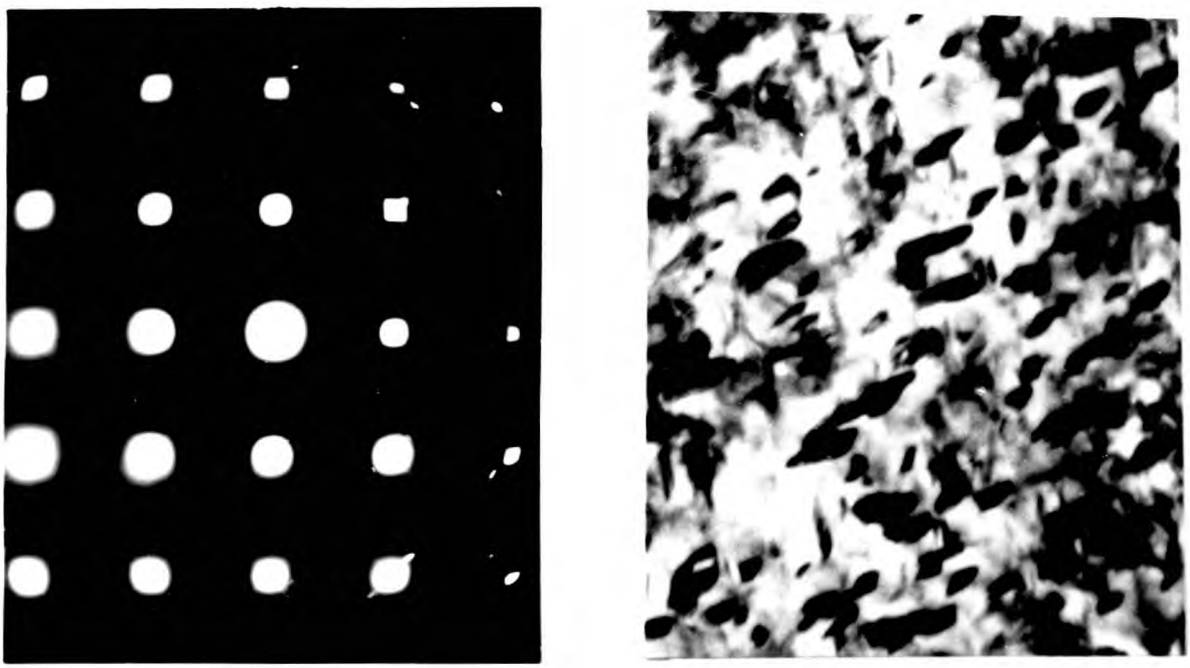

Figure 5.1 (continued)

(vii) $T_s = 320^{\circ}C$

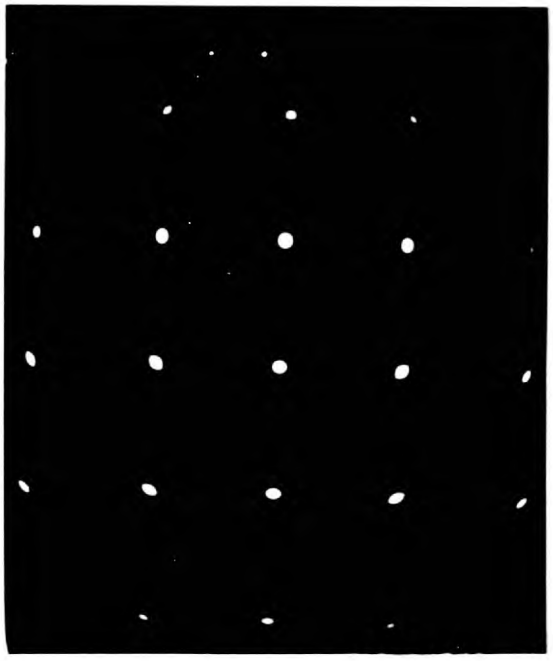

(viii) $T_s = 340^{\circ}C$

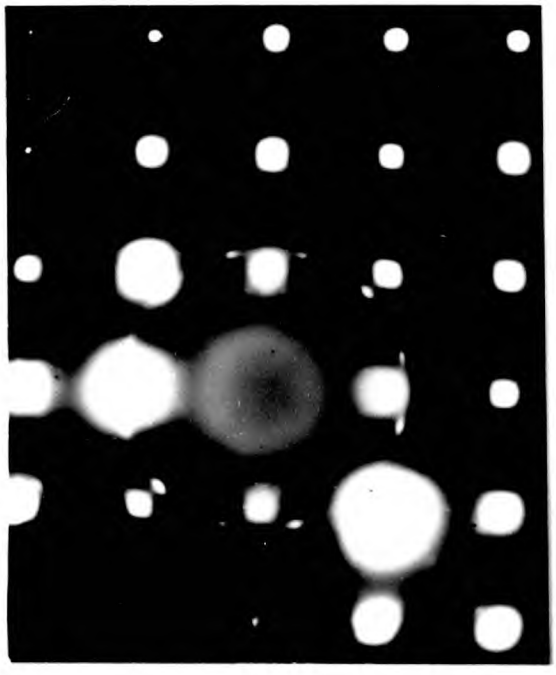

Figure 5.1 (continued)

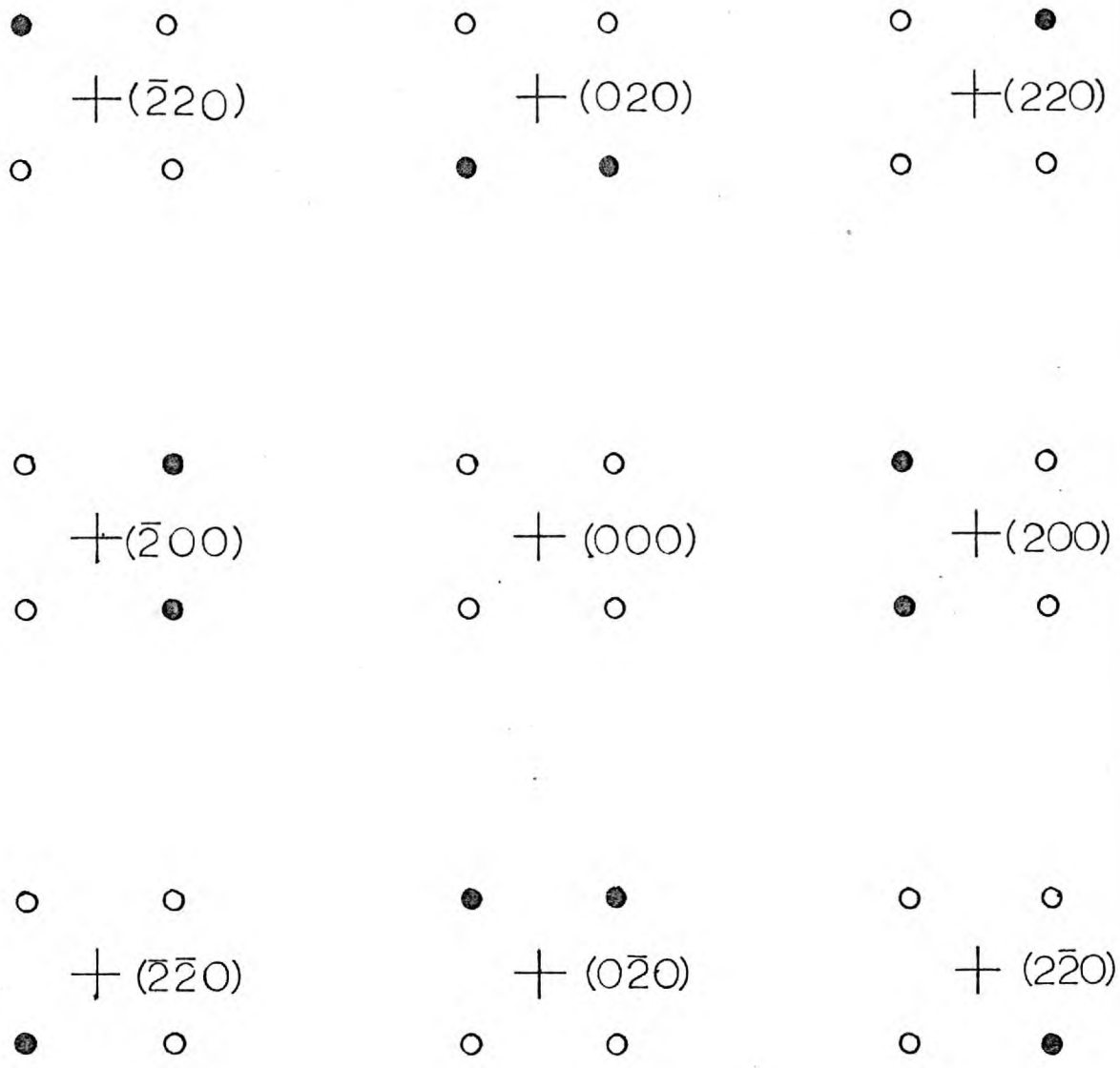

Figure 5.2 Composite diffraction pattern of an f.c.c. metal

+ Main spots

● Primary twin spots

○ Double diffraction of twin spots

(a) NaF $T_s = 230^{\circ}C$

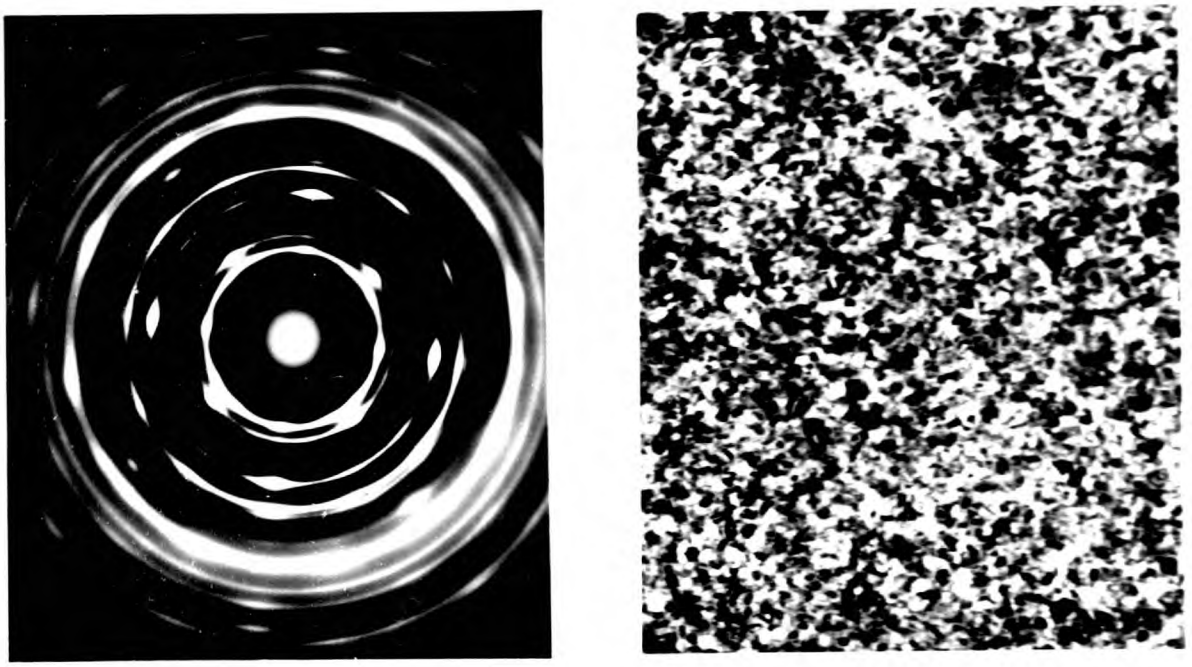

(b) LiF $T_s = 225^{\circ}C$

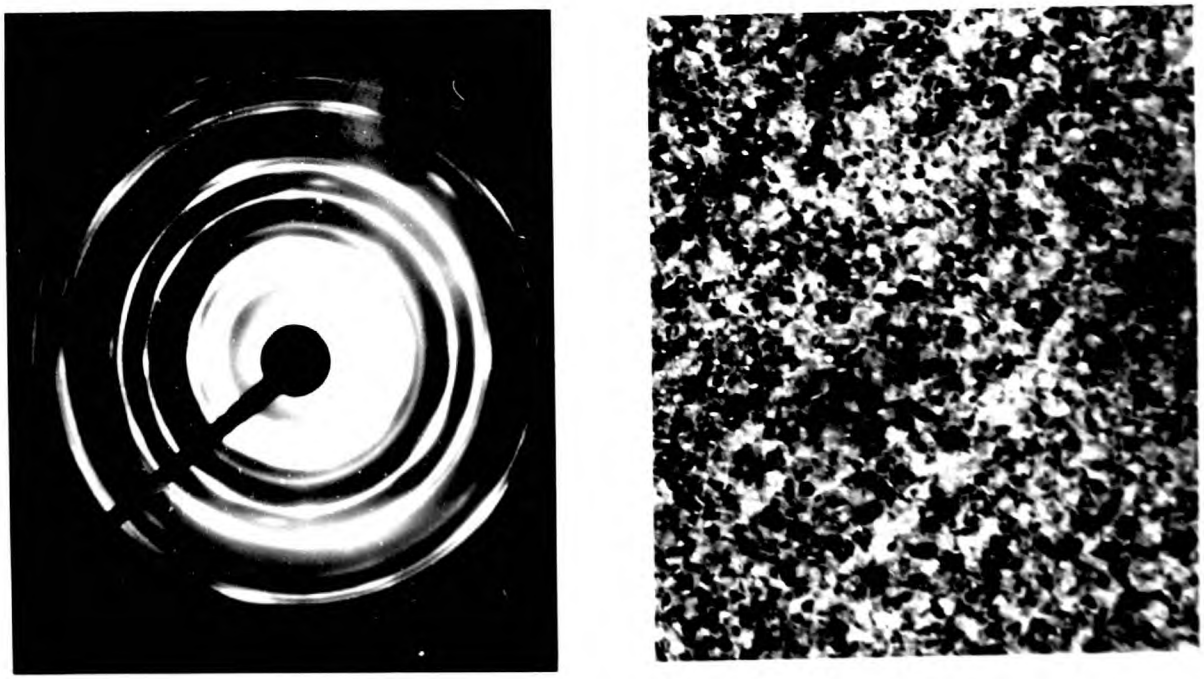

Figure 5.3 Electron micrographs (x 100000) and diffraction patterns of films grown on (a) NaF and (b) LiF at various temperatures

(a) NaF $T_s = 260^{\circ}C$

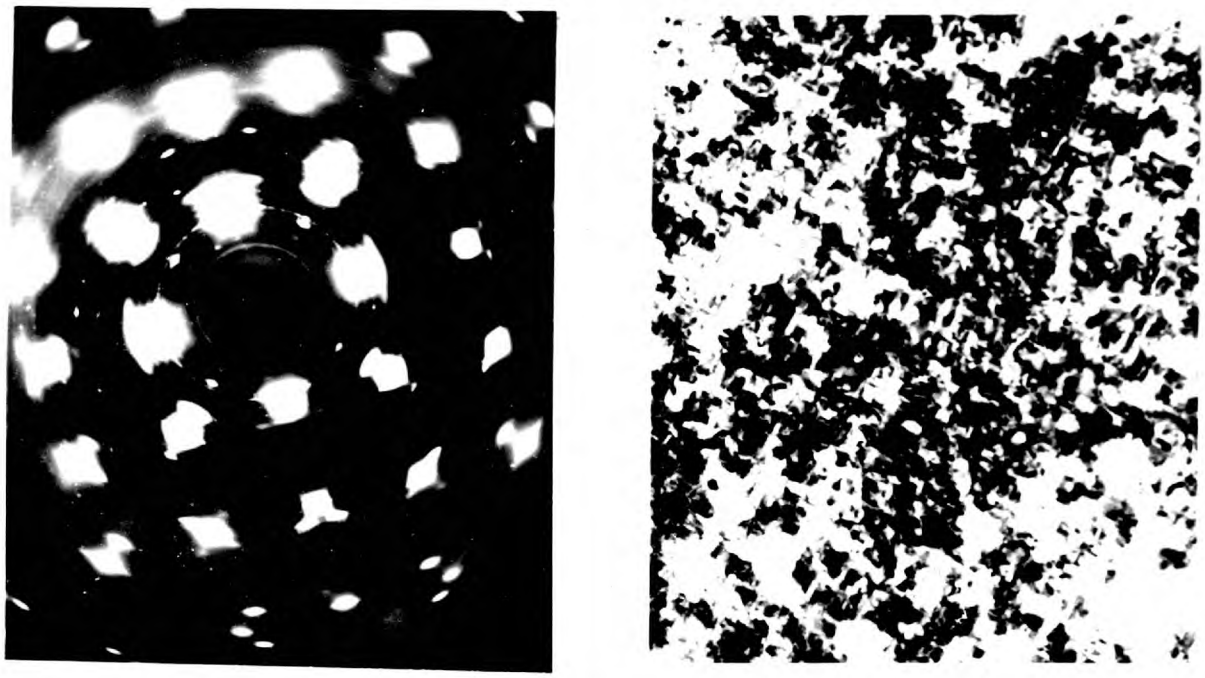

(b) LiF $T_s = 260^{\circ}C$

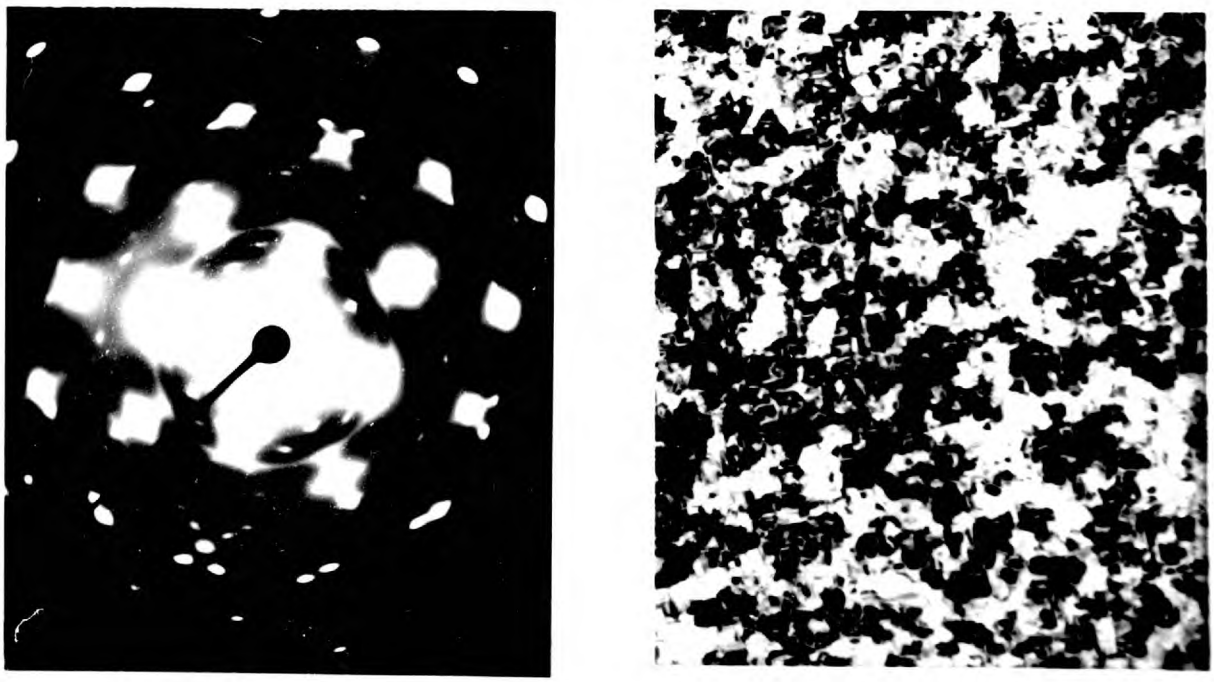

Figure 5.3 (continued)

(a) NaF $T_s = 340^{\circ}C$

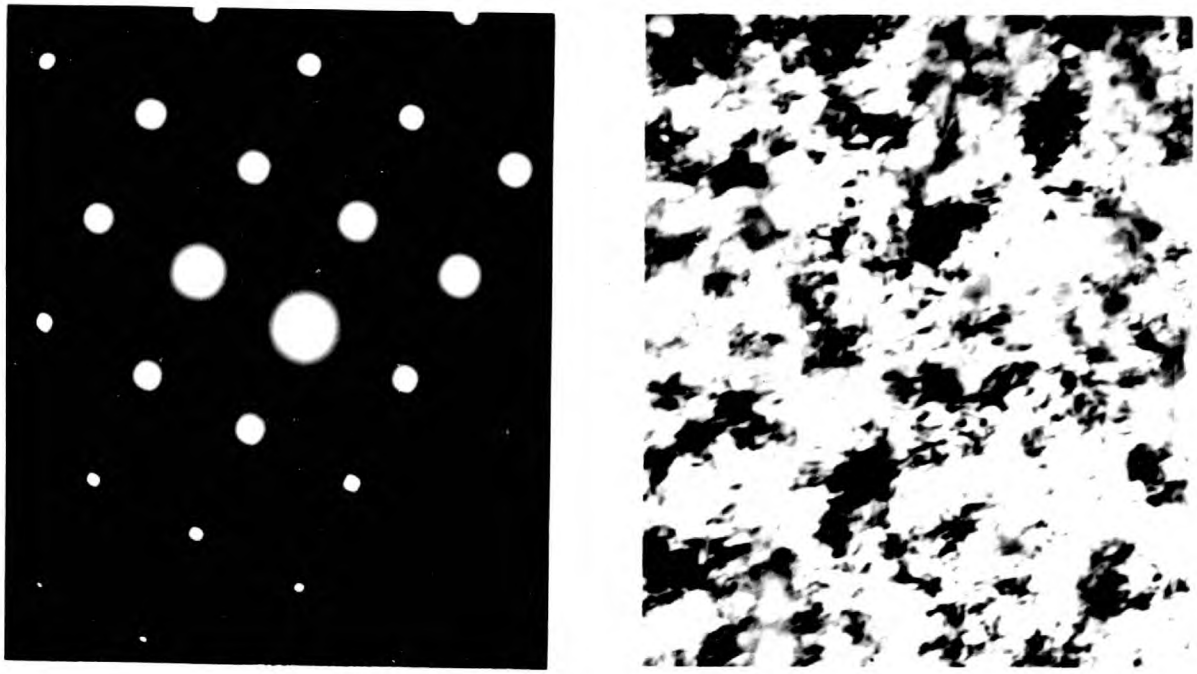

(b) LiF $T_s = 270^{\circ}C$

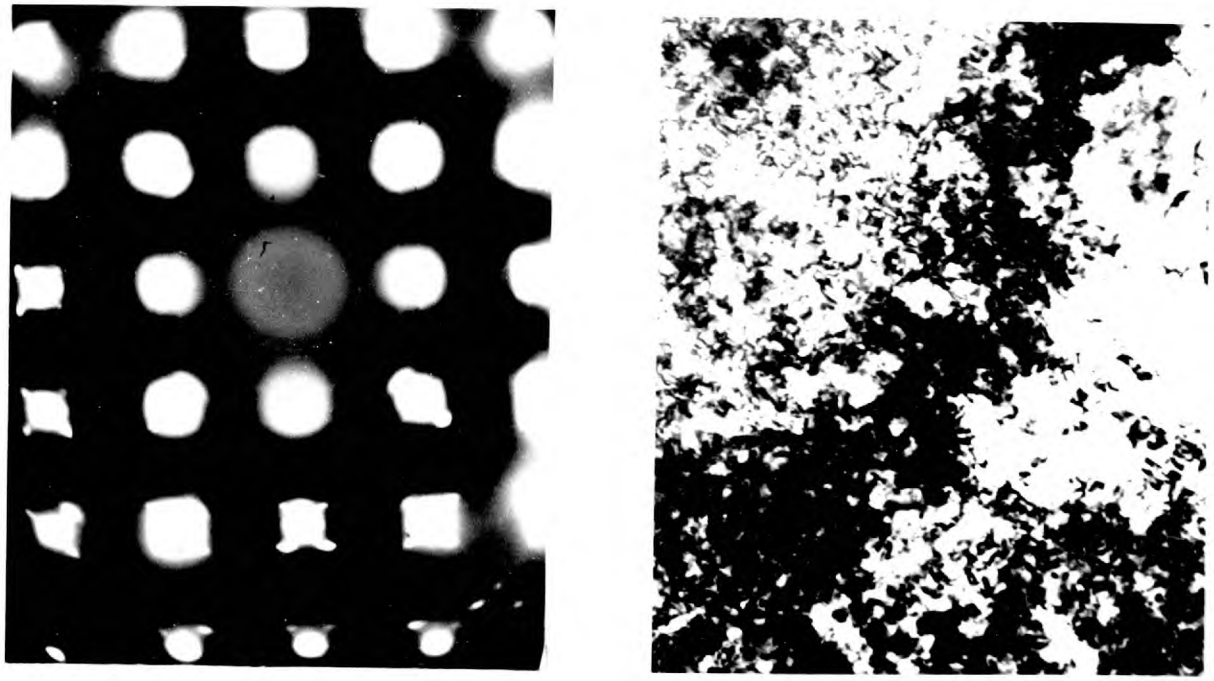

Figure 5.3 (continued)

(a) Cleaved NaCl

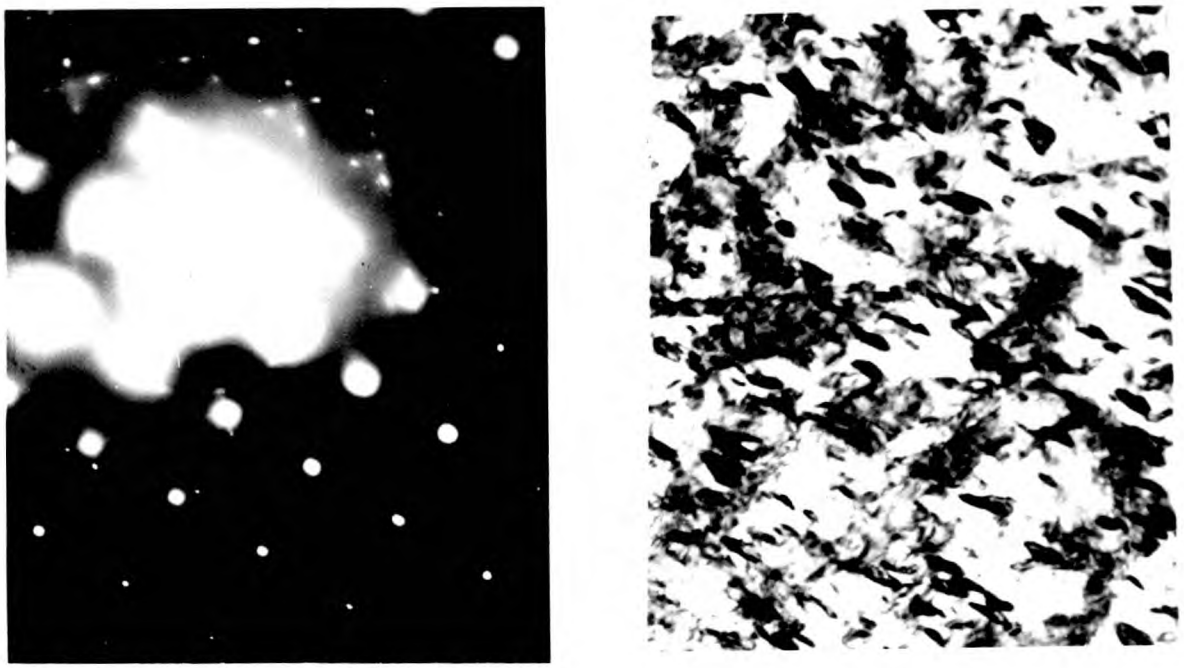

(b) Polished NaCl

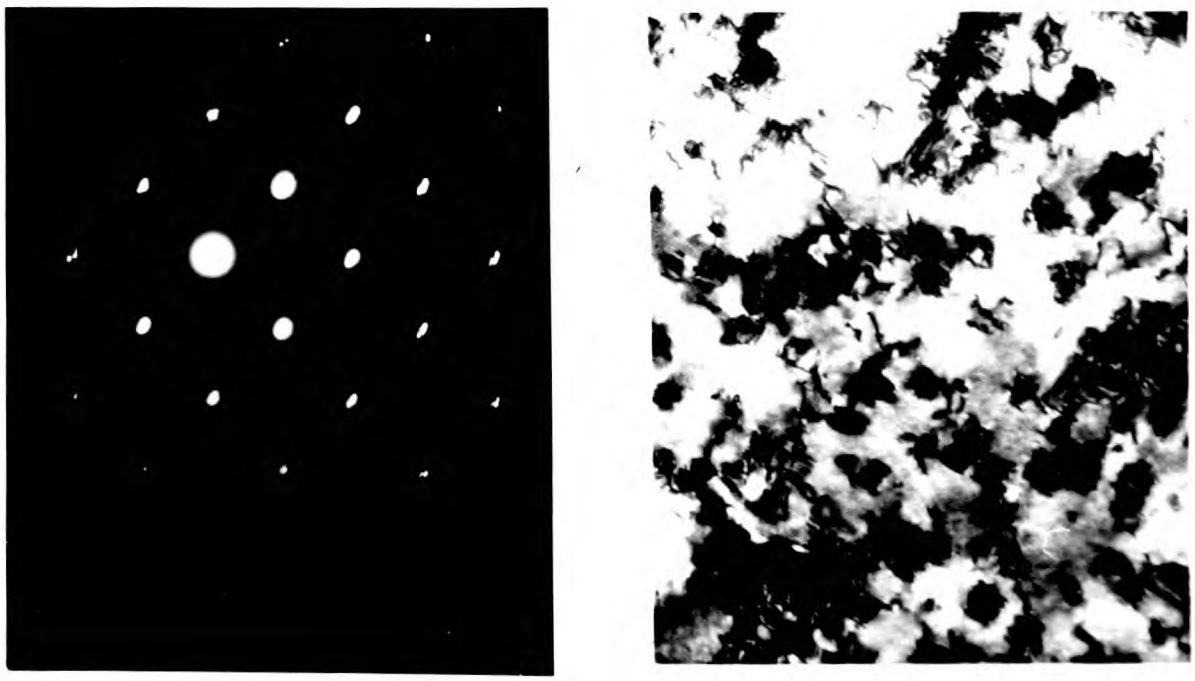

Figure 5.4 Comparison of electron micrographs (x 100000) and diffraction patterns of films grown in the same evaporation on (a) cleaved NaCl and (b) polished NaCl (T_s = 230°C)

(a) Cleaved NaCl

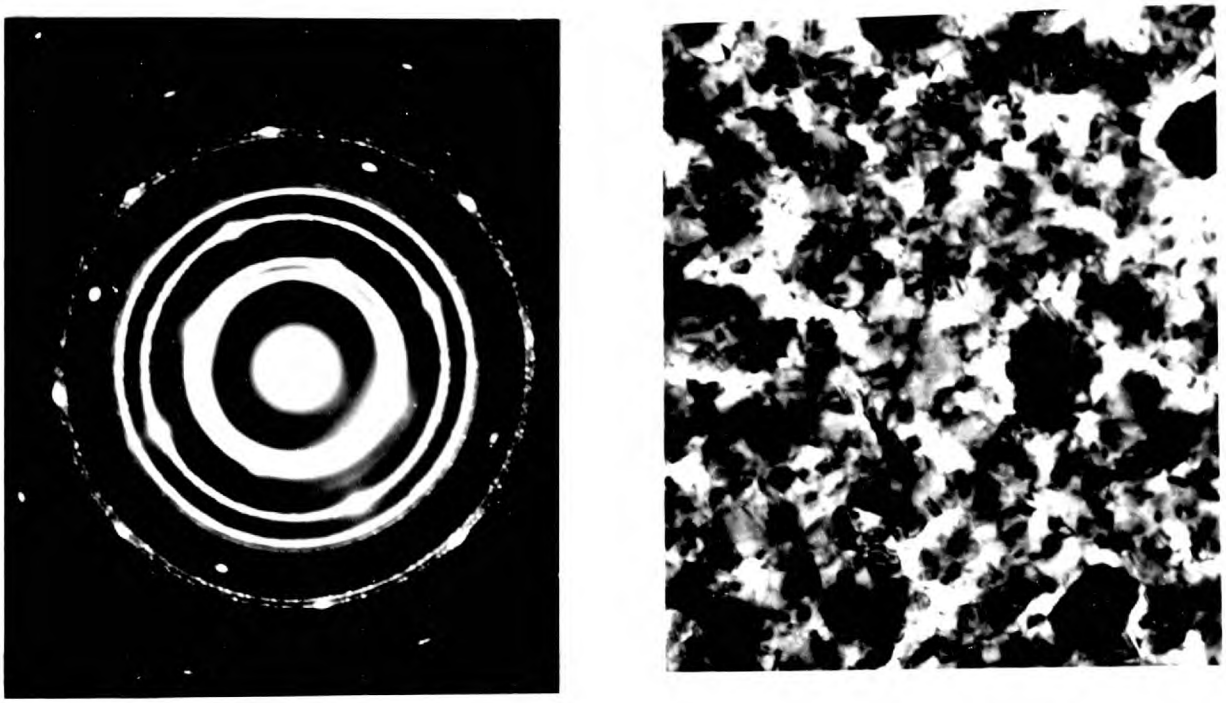

(b) Etched NaCl

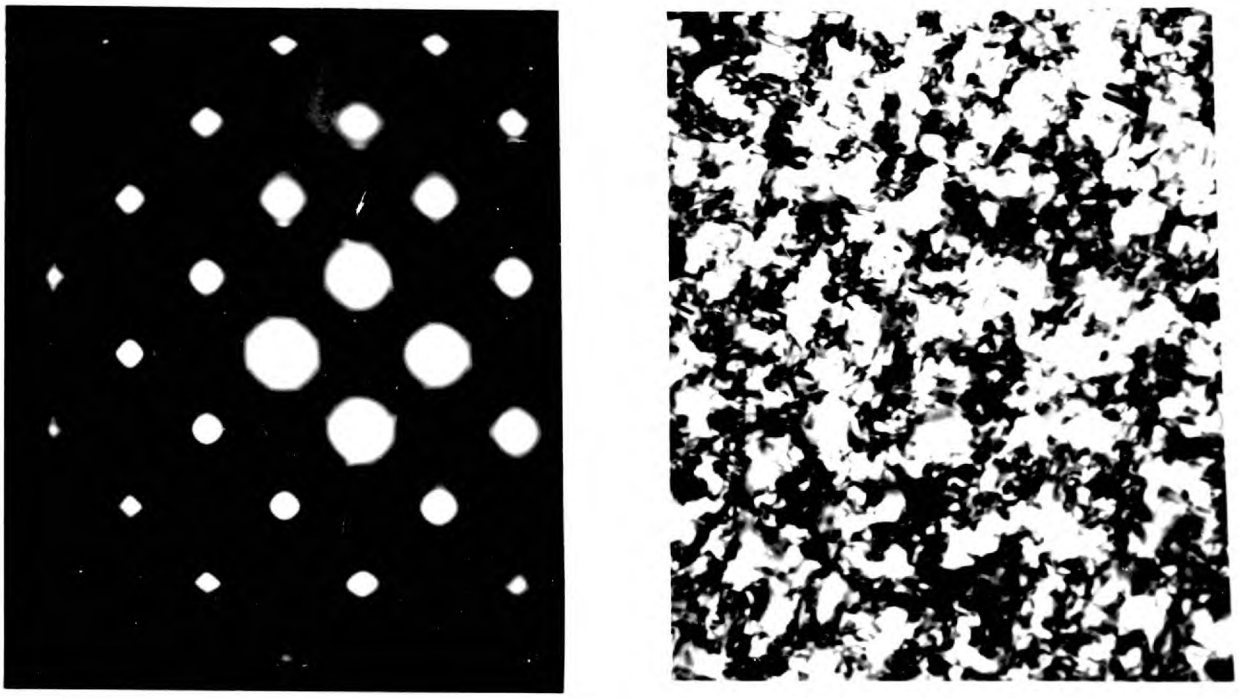

Figure 5.5 Comparison of electron micrographs (x 100000) and diffraction patterns of films prepared in the same evaporation on (a) cleaved NaCl and (b) etched NaCl (T_s = 300°C)

CHAPTER 6

Magnetic Properties: (A) Derived from the Susceptibility Curves

In this chapter we are concerned with the variation of magnetic properties, derived from the susceptibility curves, with the film properties. The film properties under consideration are dependent on the temperature of the substrate during evaporation, the substrate material and the preparation of the substrate. This chapter relates the magnetic properties directly to these variables mentioned above.

6.1. Introduction

The susceptibility as a function of the applied-bias field has been obtained as described in section 4.3. From these curves several parameters can be determined: (i) the separation parallel to the bias field of the susceptibility curves in the uniaxial easy and hard directions is equal to $2H_k$ so that the uniaxial anisotropy constant may be found; (ii) the field values for the inverse susceptibility curves at theoretically infinite susceptibility in the two biaxial hard directions enable both H_1 and H_k to be measured and hence both the uniaxial and biaxial anisotropy constants may be determined for single-crystal films with this specific anisotropy orientation (i.e. uniaxial and biaxial hard axes parallel); (iii) for the uniaxial films the coercive force, H_c, may be easily measured; (iv) for each film, $\frac{\chi_p}{\chi_o}$ and $H_p - H_k$ can be compared directly with ripple theory predictions for uniaxial films. χ_p is the peak susceptibility in a field H_p and χ_o is the normalising susceptibility

in an effective field of H_k. For the biaxial films the effective anisotropy field must be used, $(H_1 \pm H_k)$ in both instances, and then a similar comparison is possible.

All the films prepared on cleaved substrates showed very similar behaviour, apart from the actual magnitudes of the measured fields. The films prepared on etched substrates behaved in the same manner as those on cleaved substrates and so both results are considered together. However, the polished substrates produced films showing certain anomalies which will be discussed separately in the final section.

6.2. The Variation of the Uniaxial Anisotropy with the Substrate Temperature during Evaporation

The two main types of investigation into the origins of the induced anisotropy in thin films are: first, the variation of H_k or K_u with one property of the film, such as the substrate temperature or composition of a well-known alloy system (Ni-Fe), the other properties being kept constant; second, using the activation energies, the various contributions to H_k from annealing experiments are determined.

We are concerned here with the variation of H_k with the substrate temperature. The variation of H_k with T_s for the permalloy films grown on the single crystal substrates of sodium chloride, sodium and lithium fluoride is shown in figure 6.1. These films do not all have identical properties and it is presumably the composition variation which causes the large scatter in H_k values, although the films on NaCl may be affected by inhomogeneous film-to-substrate bonding caused by the affinity between NaCl and water vapour in the ambient atmosphere. This effect

should be small since the stress contribution for these compositions is small.

All of the previously-reported work on the temperature dependence of H_k has been for films grown on glass for which the crystallographic orientation remains virtually unchanged. Care has to be taken when comparing previous H_k values at various temperatures since certain abnormalities in this curve are obtained if H_k is measured by the hysteresis-loop method. Feldtkeller (F.13) has shown that as the substrate temperature is increased beyond about 350°C the coercive force increases suddenly. This influences the hysteresis loop in such a way that the anisotropy field as measured from the hard-direction loop also increases sharply. When H_k is measured using the susceptibility method or torque methods this increase is absent and the general monotonic decrease continues as predicted by theory (P.8). A systematic study of H_k for various Ni-Fe alloy films on glass at various substrate temperatures has been performed by Wilts (W.9). The substrate temperature was monitored very carefully and this data seems to be representative of previous work on this substrate. On figure 6.1. the temperature variation of H_k for a polycrystalline film on glass has been plotted for an 80/20 NiFe film, the values being inferred from H_k versus composition curves at various substrate temperatures. Also on figure 6.1. are shown the values obtained by Feldtkeller (F.13) using the susceptibility method for an 81/19 NiFe film, also on glass.

It can be seen that the anisotropy field starts at a higher value and drops much more rapidly than the values for films prepared on glass.

This must be connected with the change in crystallographic orientation, since the values for the various substrates lie on a similar curve when plotted against the degree of orientation as indicated by the type of diffraction pattern as shown in figure 6.2 and chapter 5. The results for films on sodium and lithium fluoride substrates in figure 6.1. show the smallest scatter as can be seen from the lines through the experimental points.

As the variation of uniaxial anisotropy with composition and temperature is in good agreement with the theoretical models of directional ordering and constraint release machanisms we must investigate the possible changes which might occur in these models when applied to single crystals.

6.2.1. Contribution from Constraint Energy. This will be small since the average magnetostriction, λ_s for 80/20 NiFe, is small. West (W.6) calculated the constraint energy per unit volume (e_λ) for a cubic crystal as:

$$e_\lambda = -\left[\frac{B_1 B_1'}{C_{11}' - C_{12}'}\right]\sum_{i=1}^{3} \alpha_i^2 \beta_i^2 - \frac{B_2 B_2'}{C_{44}'}\left(\alpha_1\alpha_2\beta_1\beta_2 + \alpha_2\alpha_3\beta_2\beta_3 + \alpha_3\alpha_1\beta_3\beta_1\right)$$

where β_i are the direction cosines of the magnetisation at temperature T' and α_i those at temperature T. B_1, B_2 are the magnetoelastic coupling constants at T^oC and C_{ij}' the cubic elastic constants at T'^oC.

For a polycrystal this energy term is averaged over all angles $\alpha_i \beta_i$ and gives:

$$K_u = -\frac{9}{10}\left[(C_{11} - C_{12})\,\lambda_{100}\,\lambda'_{100} + 3C_{44}\,\lambda_{111}\,\lambda'_{111}\right]$$

For an 80/20 NiFe film deposited at room temperature when the constraint temperature $T' = T_s = T$, the measuring temperature, K_u has the value of 45 erg/cc implying an anisotropy field of 0.09 oe.

For the case of a perfect single crystal with the field applied along the [100] direction during deposition the contribution to the anisotropy is:

$$K_u = -\frac{9}{4}(C_{11} - C_{12})\ \lambda_{100}\ \lambda'_{100}$$

equivalent to an anisotropy field of 0.08 oe for an 80/20 NiFe film.

It can be concluded from this that although there is a difference between the single crystal and polycrystal induced anisotropy, this effect is negligible for an 80/20 NiFe film as the magnetostriction constants are so small.

6.2.2. Contribution from Directional Ordering. This mechanism is well understood for bulk alloys and has had a lot of success in thin films. It originates from a hypothetical term:

$$e_j = w \cos^2 \phi_j$$

in the energy of a pair of nearest-neighbour 'A' atoms in an alloy AB. In this expression j is an index specifying the orientation of the AA bond under consideration, w is a temperature-dependent coefficient which disappears above the Curie temperature and ϕ_j is the angle between the spontaneous magnetisation M_s and the bond 'j'. Affixing a prime to the quantities at the substrate temperature T' during evaporation, the total energy per unit volume due to pair ordering at a temperature T is given by Sclonzewski (S.4) as:

$$e = \sum_j n_j e_j \propto \sum_j w \cos^2 \phi_j \exp(-e'_j/kT') \propto \sum_j \left[1 - \frac{w' \cos^2 \phi'_j}{kT'}\right] w \cos^2 \phi_j$$

n_j being the number of AA bonds with orientation specified by 'j'. $\frac{w'}{kT'}$ is typically of the order of 10^{-3} so that only the first term in the expansion need be considered.

For a polycrystal with all the bonds isotropically distributed the anisotropic term in e is equivalent to an anisotropy constant of $-\frac{ww'}{kT'}$.

With a single crystal these bonds will not be isotropically oriented so that the direction of the field during deposition is important and it could lead to different anisotropy energies. It is assumed that the magnetisation lies parallel to the field applied during deposition so that ϕ' is the angle between H and the AA bond. If only nearest-neighbour pairs are considered there will be six pairs for the f.c.c. structure, as shown in figure 6.3. The orientations of the distinguishable pairs relative to the central atom (0,0,0) are the atoms:

A_1, $(\frac{a}{2}, 0, \pm\frac{a}{2})$; A_2, $(\pm\frac{a}{2}, \frac{a}{2}, 0)$; A_3, $(0, \frac{a}{2}, \pm\frac{a}{2})$.

With the field during deposition in the [100] direction and M lying parallel to [100] the energy takes the form:

$$e_{100} \propto \left[\frac{w}{2} - \frac{ww'}{kT'}\right]$$

When M is in the [010] direction the energy due to directional ordering is:

$$e_{010} \propto \left[\frac{w}{2} - \frac{ww'}{2kT'}\right]$$

This is equivalent to a uniaxial anisotropy constant:

$$K_{100} = -\frac{1}{2}\frac{ww'}{kT'}$$

When the deposition field is along [110] the energies with M lying parallel to [110] and $[1\bar{1}0]$ are:

$$e_{110} \propto \left[c - \frac{5}{4}\frac{ww'}{kT'}\right] \quad \text{and} \quad e_{1\bar{1}0} \propto \left[c - \frac{5}{32}\frac{ww'}{kT'}\right]$$

where c is a position-independent constant. These equations imply a uniaxial anisotropy constant:

$$K_{110} = -\frac{35}{32}\frac{ww'}{kT'}$$

With the deposition field along the [111] direction all the bonds are at the same angle to [111] so that there is no induced uniaxial anisotropy.

Thus for a perfect single crystal with the field during deposition applied along [100], the induced uniaxial anisotropy is half the polycrystalline value. From figure 6.1 we see that at the highest substrate temperatures the anisotropy field is 1.7 ± 0.5 oe compared with the polycrystalline value of Wilts' (W.9) of about 3 oe which is in good agreement with the theoretical prediction.

The room temperature evaporations produce films which are polycrystalline but all the crystallites have (100) planes parallel to the (100) substrate face. The theoretical polycrystalline value as determined by Sclonzewski (S.4) takes all possible orientations into the averaging process and will therefore contain some contributions from crystallites with the [111] direction parallel to the applied field. The room-temperature films on single-crystal substrates will have crystallites in which the applied field lies between [100] and [110] in the (001) plane. The uniaxial anisotropy constant of these films will be an average of K_{100} and K_{110}. Hence the anisotropy field for polycrystalline films prepared on single-crystal substrates should be higher than for films grown on glass or any amorphous substrate. This is observed experimentally as shown in figure 6.1.

From this it can be concluded that the temperature variation of the anisotropy field for films grown on single-crystal substrates cannot be quantitatively described as the temperature dependence of the crystallite orientation is not known. However, the general shape of the graph has been shown to possess a sharper drop than for polycrystalline films. Also, the residual anisotropy field of good single-crystal films has been shown to be approximately equal to the theoretical value of half the polycrystalline value.

This directional ordering can apply to iron pairs in Ni-Fe alloys, vacancies and defects, but it does not apply to interstitials. A further difference in the anisotropy constant between single-crystal films and polycrystalline films is concerned with the diffusion of imperfections along grain boundaries. This follows from the fact that for epitaxial films, grain misorientations will be smaller and so the effect of grain boundaries will be much more localised. Consequently, the amount of diffusion will be reduced as will the contribution to the anisotropy field.

6.3. The Effect of Stress on the Biaxial Anisotropy Constant

A comparison of the magnetocrystalline anisotropies of the single-crystal NiFe films shows large discrepancies amongst themselves and also with bulk data (B.18). The most likely origin of this has been presumed to be due to 'isotropic' stresses in the film caused by differential thermal expansion between the film and the substrate (F.14, T.9). (The term 'isotropic' not being strictly valid since the thermal expansion

will not be completely isotropic but very little data has been recorded on the expansion coefficients of NiFe and so the thermal expansion will be assumed isotropic.)

Several other suggestions have been made as to the origin of the discrepancy between film and bulk values of K_1, such as the lattice misfit between film and substrate (C.16) or the orientation of voids and imperfections (T.10). Good agreement has been obtained for nickel films grown on NaCl (F.14) and LiF (S.16) using the thermal expansion argument.

An isotropic stress, σ, produces a biaxial anisotropy $K_{1\sigma}$ given by:

$$K_{1\sigma} = \sigma(\tfrac{2}{3} h_4 - 2h_3)$$

where h_3 and h_4 are the third and fourth order magnetostriction constants. Assuming the discrepancy between film and bulk anisotropy, ΔK, is due to the thermal expansion mechanism, we can derive an isotropic stress. This in turn will be associated with a strain, ε, which can be obtained using classical elasticity theory, remembering that $\sigma_x = \sigma_y = \sigma$ and $\sigma_z = 0$. It can easily be shown that: $\sigma = \dfrac{\varepsilon}{S_{11} + S_{12}}$ where S_{ij} are the elastic compliances. These can be expressed in terms of the elastic modulii (c_{ij}) ie:

$$S_{11} = \frac{C_{11} + C_{12}}{(C_{11} - C_{12})(C_{11} + 2C_{12})} \quad \text{and} \quad S_{12} = \frac{-C_{12}}{(C_{11} - C_{12})(C_{11} + 2C_{12})}$$

If $\dfrac{\Delta l}{l}$ is the expansion coefficient and ΔT the temperature range over which the film is bonded to the substrate during cooling, then the strain produced is given by:

$$\varepsilon = \left[\left(\frac{\Delta l}{l}\right)_{NiFe} - \left(\frac{\Delta l}{l}\right)_{substrate}\right]\Delta T$$

The constraint temperature, T_c, is defined as the temperature at which the film bonds to the substrate and may be determined from:

$$T_c - T_o = \frac{(S_{11} + S_{12})\ \Delta K}{\left[\left(\frac{\Delta l}{l}\right)_{NiFe} - \left(\frac{\Delta l}{l}\right)_{sub}\right]\left(\frac{2}{3} h_4 - 2h_3\right)}$$

$$= \frac{C_{11}\ \Delta K}{(C_{11} - C_{12})(C_{11} + 2C_{12})\left[\left(\frac{\Delta l}{l}\right)_{NiFe} - \left(\frac{\Delta l}{l}\right)_{sub}\right]\left(\frac{2}{3} h_4 - 2h_3\right)} \qquad (6.1)$$

where T_o is the measuring temperature.

It is necessary to use the expansion coefficient applicable to the temperature range ΔT which must be done by trial and error. However, the errors involved in h_3 and h_4 are over 100% so that the loss of accuracy in neglecting this effect is unimportant. For the temperature range 0 - 200°C the expansion coefficients are given below:

80/20 NiFe: $13 \times 10^{-6}\ ^{o}C^{-1}$ (B.19); LiF: $41 \times 10^{-6}\ ^{o}C^{-1}$ (C.17)

NaF: $36 \times 10^{-6}\ ^{o}C^{-1}$ (A.4) NaCl: $44 \times 10^{-6}\ ^{o}C^{-1}$ (C.17).

The values of the magnetostrictive constants h_3 and h_4 for NiFe alloys near the permalloy composition have been determined only by Bozorth and Hamming (B.20) for a 78% NiFe alloy in both quenched and slowly-cooled conditions. During film production the iron and nickel atoms will be arriving randomly at the substrate and so the compositional ordering will be negligible (apart from iron pair ordering) for room temperature depositions. At higher temperatures this is not so obvious but due to the high rate of cooling ($\sim 10^3$ °C/hr) the films will possess very little compositional ordering. It was therefore decided that the values for the quenched alloy would be more appropriate. The values for 80% and 82% NiFe alloys were obtained using a linear interpolation between 78% Ni and 100% Ni and are given in table 6.1.

Table 6.1 (reference B.20)

Composition (%Ni)	h_3 ($\times 10^{-6}$)	h_4 ($\times 10^{-6}$)
78	-0.3 ± 0.8	1.1 ± 1.4
100	-2.8 ± 3.1	-7.5 ± 5.2
80	-0.6	0.3
82	-0.33	-0.5

There is also very little data on the elastic constants of NiFe alloys and following West (W.6) a linear interpolation of the results of Alers et al (A.7) for 30% NiFe and 100% Ni has been used to determine the elastic constants of 80% and 82% NiFe as shown in table 6.2.

Table 6.2 (reference A.7)

Composition (%Ni)	$C_{11} \times 10^{-12}$	$C_{12} \times 10^{-12}$	$C_{44} \times 10^{-12}$
30	1.480	0.896	1.131
100	2.508	1.500	1.235
80	2.10	1.33	1.20
82	2.14	1.35	1.21

The bulk value of K_1 for 80/20 NiFe (and 82%) was taken from Bozorth and Walker (B.18) to be -3×10^3 erg/cc. The various substrates are compared by using three films (one on each substrate) with very similar physical properties (T_s, composition, thickness).

The film grown on LiF used for comparison with bulk was produced on a substrate held at 330°C and was 800 Å thick and contained 80% nickel.

The biaxial anisotropy field was measured as 27 oe, implying a magneto-crystalline anisotropy constant $= -13.5 \times 10^3$ erg/cc

$$\therefore T_c - 20 = \frac{4.08 \times 10^{-7} \ (-10.5 \times 10^3)}{-28 \times 10^{-6}} = 154^\circ C \quad \text{i.e. } T_c \simeq 175^\circ C.$$

In table 6.3 the constraint temperature and isotropic stresses in the films on the various substrates are shown together with their 'physical' properties.

Table 6.3

Substrate	T_s(°C)	Composition (%Ni)	Thickness Å	K_1(x10^3) erg/cc	T_c(°C)	σ(x10^9) dyne/cm^2
LiF	330	80	800	-13.5	175	-7.5
NaF	340	82	800	- 6.8	110	-3.6
NaCl	330	80	~700	- 5.5	55	-1.3

To determine whether the thermal expansion origin of ΔK is feasible the constraint temperature (T_c) and isotropic stress (σ) in the film must be compared with previous values to see if they are acceptable.

Very little work has been done on the calculation of the constraint temperatures for films on single-crystal substrates. In fact, the author could only find the values due to Secemski (S.16) which were 190°C for nickel films on lithium fluoride and 195°C on sodium chloride. The agreement with the lithium fluoride substrate is extremely good, considering the large errors involved in interpolating the film constants from bulk data; also the substrate temperature used by Secemski was higher. The disagreement in the case of the sodium chloride substrate could be

due to several factors. An obvious reason is connected with the solubility of NaCl in water. It is thought that the large scatter of H_1 values for single-crystal films grown on NaCl is caused by the small microdissolution of the substrate producing uneven local bonding and so decreasing the average constraint temperature. This appears to be borne out by the change in T_c with the solubility of the substrate in water (tables 6.3 and 4.2). There is a general decrease in T_c and an increase in the insolubility.

Another reason for these discrepancies is that only one film on each substrate has been considered and this may not be an average film, although the scatter of data for films on NaF and LiF is far less than that on NaCl.

As regards the isotropic stress in films, a great deal of work has been concerned with Ni and NiFe alloys on glass or mica but very little with alkali halide substrates. (Glass and mica make suitable substrates since the distortion caused by the isotropic stress can easily be measured by interference techniques (H.19).)

In table 6.4 overleaf are listed some of the experimental results obtained by various workers.

A comparison of stresses in table 6.4 shows confusion as to whether the stress is compressive or tensile. Measurements of the perpendicular anisotropy of NiFe films grown on rocksalt (K.7) require an isotropic tension in the film of about 2×10^{10} dynes/cm^2. In a recent review by Fujiwara and Sugita (F.15) it is stated that this tension is present over the nickel range 55% to 100%. All the results determined from the perpendicular anisotropy measurements disagree with other methods. The

Table 6.4

Substrate	T_s (°C)	Composition (%Ni)	Stress ($\times 10^9$ dyne/cm^2)	Method	Author
(100) LiF	330	80	-7.5	Difference in K_1 between film and bulk	Present work
(100) NaF	340	82	-3.6		"
(100) NaCl	330	80	-1.3		"
(100) LiF	365	100	-10.0		Secemski (S.16)
(110) LiF	400	80	-18.0		*Tokutaka et al (T.9)
Glass	330	81	-1.0	Substrate distortion	Prutton (P.9)
Glass or mica	330	83	-4.0		Weiss & Smith (W.10)
Glass	225	80	+7.0		Spain (S.18)
(100) NaCl	>200	100	-12.0	X-ray	Freedman (F.14)
Mica	300	100	+5.0	Ferromagnetic resonance	Macdonald (M.9)

* The stress is incorrectly quoted as tensile but must be compressive since $K_1 < 0$ for 80/20 NiFe.

origin of this tension and the discrepancy is not at all clear and several possible mechanisms, including imperfection ordering and oxygen diffusion have been proposed.

From table 6.4 the isotropic stresses measured in the films depend both in sign and magnitude on the orientation of the film, the substrate material and the substrate temperature. The sign discrepancy in the case of Spain's value can possibly be explained by the strong substrate temperature dependence of the stress in permalloy films (e.g. Prutton (P.9), Smith and Weiss (W.10)).

It can be said, however, that the calculated stresses are in agreement with previous values. Since the signs of K_1 and $\frac{2}{3} h_4 - 2h_3$ for permalloy are the same as for nickel but smaller in magnitude, by direct comparison with the single-crystal films (F.14, S.16) a compressive stress of smaller magnitude than for nickel should be expected. This is in fact what is observed. The variation in magnitude of the stress with the various substrates can be ascribed to the same origin as the constraint temperature variation, i.e. to the effects of the substrate surface on the substrate-film bond.

6.4. A Comparison of $H_p - H_k$ and χ_p/χ_o with Ripple Theory

It was mentioned in chapter 3 that in films with large relative susceptibilities, (χ_p/χ_o), the field for peak susceptibility, H_p, (in the hard direction) is usually close to H_k, i.e. $H_p - H_k \rightarrow 0$. These films approach the ideal single-domain behaviour predicted by Stoner and Wohlfarth (S.1). This section will be concerned with comparing these

values ($H_p - H_k$, χ_p/χ_o) with the existing ripple theories for uniaxial films and then extending them for biaxial films.

Consider the general form of the susceptibility for a film with a total effective field, H_{eff}, applied (equation 3.11):

$$\chi = M_s/H_{eff}$$

The ripple theories are mainly concerned with evaluating this field and it can usually be written as a sum of the ideal S-W field, $H(\alpha)$, and a ripple field, H_R. In all the theories, H_R can be written as a function of the applied field, usually a power (n).

The peak susceptibility will occur at a field H_p given by:

$$\frac{\partial \chi}{\partial H_a} = 0 \qquad .. \quad .. \quad .. \quad .. \quad .. \quad .. \quad .. \quad .. \quad .. \qquad (6.2)$$

The susceptibility in the easy or hard direction for a general ripple theory may be written as:

$$\chi = \frac{M_s}{\left[H_a \pm H_k + S(H_a \pm H_k)^n\right]} \qquad .. \quad .. \quad .. \quad .. \quad .. \qquad (6.3)$$

where S is a film-dependent constant.

Equations 6.2 and 6.3 give: $H_p \pm H_k = (-\frac{1}{nS})^{\frac{1}{n-1}}$ .. .. (6.4)

This gives a theoretical expression for $H_p \pm H_k$, dependent on each ripple theory, from which the local anisotropy constant can be determined (via S).

Referring back to equation 6.3:

$$\chi = \frac{M_s}{(H_a \pm H_k)\left[1 + S(H_a \pm H_k)^{n-1}\right]} \qquad .. \quad .. \quad .. \quad .. \qquad (6.5)$$

Now at the peak susceptibility, χ_p, $H = H_p$ and using 6.4 in 6.5 we have:

$$\left.\begin{aligned} \frac{\chi_p}{M_s}(H_p \pm H_k) &= \frac{1}{1 - \frac{1}{n}} \\ \text{or} \quad \frac{\chi_p}{\chi_o}(h_p \pm 1) &= \frac{n}{n-1} \end{aligned}\right\} \quad .. \quad .. \quad .. \quad .. \quad .. \quad .. \quad .. \quad (6.6)$$

Therefore from each ripple theory the theoretical dependence of $\frac{\chi_p}{\chi_o}$ on $h_p \pm 1$ can be plotted.

6.4.1. Form of the Ripple Field. There are three basic theories from which we can determine the ripple field. These belong to Feldtkeller (F.9), Harte (H.8) and Hoffmann (H.9) and have been dealt with in chapter 3. The ripple field due to Feldtkeller, equation 3.20, is $\frac{M_s \overline{\theta^2} Df}{\overline{\lambda}}$, the power n depending on the values taken for the mean ripple amplitude and wavelength.

First using the values due to Hoffmann, equations 3.5 and 3.6, for $\overline{\lambda}$ and $\overline{\theta^2}$, we have for the ripple field:

$$H_R = S_{F1}(H_a \pm H_k)^{-\frac{1}{4}} \qquad (\text{i.e. } n = -\tfrac{1}{4}) \quad .. \quad .. \quad .. \quad (6.7)$$

where $S_{F1} = \frac{0.04\ D^{\frac{1}{2}} S^2}{A^{\frac{5}{4}}\ M_s^{\frac{1}{4}}}$

This is the long-wave ripple wavelength. Using Rother's value of $\lambda = 4d$ and $\theta = C\frac{Kd^2}{A}\left(\frac{2A}{M^2 Dd}\right)^{\frac{1}{4}}$ gives a constant ripple field, i.e. n = 0. Leaver et al (L.10) made the assumption that the short-wave ripple wavelength had an amplitude given by Hoffmann's long-wave value (3.6) so:

$$H_R = S_{F2}(H_a \pm H_k)^{-\frac{3}{4}} \qquad (\text{i.e. } n = -\tfrac{3}{4}) \quad .. \quad .. \quad .. \quad (6.8)$$

where $S_{F2} = \frac{0.015\ D^{\frac{1}{2}} S^2}{d\ (AM_s)^{\frac{3}{4}}}$.

Harte's expression for the effective field depends on the scale of the inhomogeneity causing the ripple and has been tabulated in chapter 3. The power (n) of the ripple field is $-\frac{1}{4}$ for the fine-scale inhomogeneity and $-\frac{3}{2}$ for the coarse scale. The constants (Ω_f and Ω_c) can also be found in table 3.2.

Hoffmann (H.10) has extended his theory to evaluate the susceptibility directly: $$\frac{\chi}{\chi_o} = \frac{1}{h_a \pm 1}\left\{1 - \frac{P(\hat{H})}{(h_a \pm 1)^{3/8}} - \frac{Q(\hat{H})}{(h_a \pm 1)^{19/8}}\right\}$$

where $P(\hat{H})$ and $Q(\hat{H})$ are constants dependent on the a.c. measuring field. When either the second or third term dominate we have:

$$\frac{\chi_p}{\chi_o}(h_p - 1) = {}^{3}/_{11} \quad \text{(2nd term)}$$

$$\text{or} \quad {}^{19}/_{27} \quad \text{(3rd term)}.$$

He evaluates the peak field directly as:

$$H_p - H_k = \frac{1}{M_s}\left\{\frac{11}{16}\frac{KdA^{\frac{1}{8}}}{\sqrt{2\pi M_s A}\,(2D)^{\frac{1}{4}}}\right\}^{8/3} \qquad \text{(6.9)}$$

Thus we can compare directly the experimental values of χ_p/χ_o as a function of $(h_p - 1)^{-1}$, (one point per film), with the theoretical slopes predicted by the three theories in a similar manner to Leaver et al (L.10).

6.4.2. Uniaxial Films. The results for these films are shown in figure 6.4. Most points lie between the bounds of the Hoffmann theory in agreement with Leaver et al (L.10) but some points remain outside all the theoretical boundaries. There are three possible reasons for this which are considered below.

Firstly, it may be that the film is no longer a single domain and that the domain splitting caused during the hard axis fall-back has

already begun in certain areas so that the effective field is not accurately described simply by the applied field, anisotropy and ripple fields. An extra stray field acting on the ripple, caused by the free poles on the low-angle ripple walls, must be taken into account in the effective field. If the field at which the susceptibility decreases to 90% of the ideal S-W susceptibility is used instead of H_p in figure 6.4 then most of the films previously lying outside Hoffmann's limits are found to lie within these limits.

Secondly, the transverse susceptibilities used for these determinations may not have been measured exactly in the easy and hard directions. A small angular discrepancy, although not apparent at high fields where the S-W model is applicable, will be severely enhanced near the astroid and will produce an asymmetry in the inverse susceptibility curves near H_k in the hard direction. It is at these points where a slight misorientation produces a non-zero average torque on the magnetisation resulting in a drastic change in the susceptibility. This has been observed for one film lying outside the theoretical lines, even using the field values for 90% susceptibility.

The third possibility is that the films outside the limits do not behave in accordance with the theories. There is no evidence supporting this possibility since the first two explanations can account for all the discrepancies.

From the various theories the local anisotropy constant can be determined using equation 6.4. This is especially relevant for three films, 11NF1, 16NF1 and 45NF1 as the values obtained for these can be compared with those from other sources (chapter 7 and section 6.5). The values obtained are listed in table 6.5.

Table 6.5

Specimen number	$H_p - H_k$ (oe)	Local random anisotropy (erg/cc)				Method for previous value	Bulk value (erg/cc)
		Hoffmann	Harte	Feldtkeller	Previous value		
11NF1	0.88	9.8×10^3	2.3×10^4 fine scale	4.5×10^2 a	1×10^4	Critical loss curve	3×10^3
16NF1	0.32	5.6×10^3	1.0×10^4 fine 4.1×10^4 coarse	1.7×10^2 a	1×10^4	Critical loss curve	3×10^3
45NF1	4.1	1.7×10^4	1.2×10^4 coarse	1.2×10^3 a 8×10^4 b	6.9×10^3	Non-linear effective field	3×10^3

The relevant formula used in the theories of Feldtkeller and Harte is the one for the line nearest to the film in figure 6.4. It should also be noticed that film 45NF1 lies quite close to Harte's coarse-scale ripple line in agreement with the conclusions of section 6.5.

The values obtained for the local anisotropy show general agreement apart from Feldtkeller's values, which are over an order of magnitude lower. If the field-dependent ripple wavelength is used rather than a constant then acceptable values are obtained.

In summary, we can say that the majority of uniaxial films measured lay within the extreme theoretical boundaries in figure 6.4, most being incorporated by Harte's fine and coarse scales and by Hoffmann's two limiting cases. Relatively poor agreement was obtained for Feldtkeller's phenomenological theory both on figure 6.4 and the local anisotropy values. This suggests that the magnetisation direction can only approximately be regarded as sinusoidal. The films which lay outside the limits had either low values of χ_p / χ_o or high values of $H_p - H_k$, both indicating high dispersion and the possibility of domains existing at the peak susceptibility field as mentioned previously.

6.4.3. Biaxial Films. The ripple theories may be extended to single-crystal films as long as the anisotropy field incorporates both the uniaxial and biaxial anisotropies, which for the combination in these films means using $H_a - H_1 \pm H_k$ instead of $H_a \pm H_k$. The peak susceptibility must be normalised with respect to the susceptibility in a field equal to the resultant anisotropy field, $H_1 \pm H_k$. The susceptibility in the uniaxial

easy direction at the field which gives zero inverse susceptibility in the hard direction, is the susceptibility in a field, H_k. The required susceptibilities are then calculated using:

$$\frac{\chi_{p\pm}}{\chi_o} = \frac{H_1 \pm H_k}{H_k} \frac{\chi_p}{\chi_o}$$

the sign depending along which biaxial hard axis the field is applied, positive sign for field along the uniaxial hard axis.

The graphs for the uniaxial easy and hard directions are shown in figures 6.5a and 6.5b.

Again nearly all the points lie within the theoretical limits and those outside can be explained in a similar way as the uniaxial films were. Several negative values for $H_p - (H_1 \pm H_k)$ were obtained especially for films measured in the uniaxial easy direction. They occurred for films having an anisotropy ratio $\frac{H_1}{H_k} < 1$, in which case wall-motion effects may be reducing H_p below the theoretical switching field.

Most of the points lie within the limits of Hoffmann's theory, whereas relatively poor agreement is obtained for the theories of Harte and Feldtkeller. There seems no obvious reason for the poor agreement of biaxial films with Harte's theory.

It can be concluded that the present ripple theories apply equally well to single-crystal and uniaxial films, provided that the resultant anisotropy field is used, and wall-motion effects can be neglected.

6.4.4. Zero-field Susceptibility. In section 4.3.4. the susceptibility in zero field in two adjacent biaxial hard directions was shown to be directly related to the anisotropy ratio K_1/K_u.

The experimental points are shown of the susceptibility ratio $\frac{\chi_e}{\chi_h}$ squared against $(H_1 + H_k)/(H_1 - H_k)$ in figure 6.6. These points should lie on a straight line in accordance with equation 4.3.

As expected for high ratios of $\frac{H_1}{H_k}$, where $\frac{H_1 + H_k}{H_1 - H_k}$ tends to unity, the agreement is fairly good but the relation breaks down for $\frac{H_1}{H_k} < 3$. On a closer inspection, this breakdown is found to be associated with higher values of the susceptibility in the easy direction with the hard-direction susceptibility remaining almost the same from film to film. The higher easy direction susceptibility is strongly indicative of some form of locking or blocking preventing the magnetisation from rotating towards the easy axis. A possible explanation is proposed on the following lines: In the theory of blocking (H.7) the most important parameter is the effective field acting on the magnetisation; as this approaches zero, blocking effects become more important. For effective fields just below zero then the onset of locking is observed where both the ripple and the ripple walls are prevented from moving by the stray fields induced by the non-uniformity of M_s. This situation causes a higher value of M in the field direction than expected from the S-W model and so the susceptibility measured will be larger than predicted by S-W. The ideal S-W effective field in the uniaxial easy direction is $H_1 - H_k$ and as $\frac{H_1}{H_k}$ approaches unity so the field for peak susceptibility, H_p, approaches zero. Hence the zero-field susceptibility will be measured at smaller effective fields, as $\frac{H_1}{H_k} \rightarrow 1$, thus an increase in locking-effects on the zero-field susceptibility is expected resulting in higher values of χ_e / χ_h than predicted.

Alternatively, it can be said that the predicted dependence of $\frac{\chi_e}{\chi_h}$ on H_1 and H_k was derived, for zero field, assuming that the magnetisation was lying in one of the combined easy directions. However, for low anisotropy ratios the combined easy axes will be close to the uniaxial easy direction and so in the 'hard' axis domain splitting the angles between two adjacent domains will be fairly small ($\sim 20^{o}$) in zero field and so the stray fields will affect the magnetisation directions, tending to keep adjacent domains parallel. This results in a breakdown of the theory used for deriving the relation between $\frac{\chi_e}{\chi_h}$ and $\frac{H_1 + H_k}{H_1 - H_k}$.

When the anisotropy ratio $\frac{H_1}{H_k} < 1$ this cannot be applied since the zero-field easy-direction susceptibility will be measured in a positive effective field and the uniaxial easy direction will be an overall easy direction.

6.5. The Magnetic Properties of Films Prepared on Polished Substrates

As was mentioned at the beginning of this chapter, films prepared on polished substrates (loosely referred to as 'polished' films) showed anomalous behaviour in the susceptibility curves. This behaviour was suggestive of very high dispersion and extremely small susceptibilities. It increased with the substrate temperature to such an extent that no low-field measurements could be made on the single-crystal films prepared on these substrates since the flux changes were so small, although electron diffraction patterns showed very good crystallographic orientation. This section is concerned, therefore, in explaining the behaviour of polycrystalline 'polished' films using Harte's ripple theory.

First, however, it must be mentioned why films were prepared on polished substrates. Cleaved single-crystal substrates necessarily possess a large number of cleavage steps on their surfaces which can act as domain-wall nucleation sites. An attempt was made to remove these steps by polishing in a similar manner to Heavens et al (H.16) in the hope of increasing the coercive field. This would result in the film's behaving as a near-ideal single domain, the switching occurring by rotation, which is a faster process. Polishing removes the cleavage steps and replaces them with scratches which are on a far smaller scale and should have a smaller effect on the coercive field. The polishing, however, produces certain anomalies in the switching process which will now be discussed in detail.

The susceptibility curves in the uniaxial easy and hard directions for two such films are shown in figures 6.7 and 6.8. Figure 6.7 applies to a film deposited at room temperature, while for the film in figure 6.8 the deposition temperature was 150°C.

6.5.1. Bias Field along the Easy Direction. Reversal of the magnetisation occurs very gradually with this field configuration and although the films are not inverted (see table 6.6) the susceptibility behaviour is very similar to that of inverted films (compare with figure 5 in reference F.9).

The gradual reversal can be explained in a similar manner as being due to the stray fields produced by the high dispersion. As the field is increased in the reverse direction to saturation the ripple amplitude

increases until the ripple walls become blocked. The ripple is still allowed to rotate within these domains, causing a peak in the susceptibility. The film finally reverses by means of domain-wall movement probably nucleated at imperfections such as scratches as well as the film edge. The wide range of fields over which reversal occurs (see table 6.6 below) is presumably caused by the complicated stray field configuration allowing some regions to switch at lower fields than others.

Table 6.6

Properties of Permalloy Films Prepared on Cleaved and Polished NaCl

Substrate preparation	T_s	H_k (oe)	H_c (oe)	Field range for reversal (oe)	$\frac{\chi_p}{\chi_o}$	$\frac{H_p - H_k}{H_k}$	$\frac{H_c}{H_k}$
NaCl cleaved in air	room temp.	8.1	3.4	$\pm$ 0.3	3.6	0.1	0.4
NaCl cleaved in air	160°C	5.3	1.26	$\pm$ 0.1	6.4	0.06	0.25
NaCl polished with tin oxide	room temp.	22.2	15.8	$\pm$ 2.0	1.0	0.5	0.7
NaCl polished with ceric oxide	room temp.	8.2	5.5	$\pm$ 2.0	0.9	0.5	0.7

6.5.2. Bias Field along the Hard Direction. A comparison of figures 6.7 and 6.8 with the low-dispersion case (figure 4.8) shows both an increase in the width of the curve and a drop in the peak susceptibility. This is more accentuated the higher is the substrate temperature. These changes

indicate a larger spread in the distribution of the local anisotropy fields and/or the local anisotropy easy directions.

As previously mentioned, two indirect measures of the ripple amplitude and the dispersion are χ_p/χ_o and $H_p - H_k$. The values for two 'polished' films of these magnetic constants are shown in table 6.6 with the values for two 'cleaved' films.

The general shape of the curves with the bias field in the hard direction can be explained in terms of ripple hysteresis causing the rotational hysteresis.

The high values of the induced uniaxial anisotropy fields measured are thought to be due to anisotropically oriented lattice defects. This suggestion is based on work done on nickel films grown on similar substrates by Secemski (S.16). He observed anomalously high uniaxial anisotropy constants for films on polished and etched substrates, as compared with cleaved substrates. On annealing these films at 250°C for ten minutes the values dropped to more acceptable values. He concluded that this decrease in K_u was due to the annealing out of mobile lattice defects. These defects were assumed to be caused by the increased number of nucleation sites produced by the polishing, thereby increasing the number of stacking faults which occur when islands coalesce.

All the films prepared on polished substrates exhibited rotatable initial susceptibility (RIS). The effect of this on the susceptibility curve is shown by the dotted line in figure 6.8 for the field in the easy direction after the film had previously been saturated in the hard direction. This type of behaviour was usually, but not invariably, observed in films prepared on cleaved rocksalt. It is thought that

this might be due to the large local stresses (C.11) introduced by the inhomogeneous film-to-substrate bonding. Films prepared on cleaved NaF and LiF, which are almost insoluble in water, did not show RIS. The uneven bonding may have been caused by the dissolution of small areas of the substrate by water vapour from the ambient atmosphere.

6.5.3. The Inverse Susceptibility Curves. These curves are shown in figure 6.9. There are two main differences between these and the corresponding plots for low-dispersion films. The first and most important is that a large and constant internal field is observed parallel to the applied field, which for the film shown is almost equal to H_k (8.2 oe). The second difference is the reduced slope of the line which is connected with the smaller pick-up coil voltages observed in these films. For the film shown, the slope is a factor of 5 smaller than expected and so is very unlikely to be due simply to a compositional change or an increase in the amount of non-magnetic material in the film.

Consider first the possible explanations for the reduction of the susceptibility. As the applied field approaches H_k the ripple amplitude increases and so the component of the magnetisation parallel to the field decreases, reducing the voltage in the pick-up coil. However, for reasonable values of the angular dispersion this can only reduce the signal by 5 - 15%. It would seem, therefore, that there is another factor influencing the pick-up coil voltage, which is considered below.

Films with specifically enhanced dispersion will be locked over wide field ranges and in this state can no longer be treated as single

domains. They may be considered roughly as a series of parallel domains for which the external flux distribution will be different.

A simple calculation was performed to determine whether the change in flux distribution could produce a significant drop in pick-up coil voltage. The two extreme cases, shown in figure 6.10, of a single domain and a locked state with 90° dispersion were taken. Calculating the pick-up flux, ϕ_{sc}, through a search coil of negligible width compared with the domain-wall spacing (ℓ) in the same manner as Oguey (0.2) we have:

$$\phi_{sc} = \left[\phi(o,a) - \phi(o,b)\right] \phi_F$$

where ϕ_F is the flux in the film and $\phi(x,y)$ is the fraction of flux passing outside the point (x,y) (always less than 0.5).

For the single domain:

$$\phi_{sc} = \frac{\phi_F}{\pi} \tan^{-1} \frac{2L(b - a)}{4ab + L^2} \qquad (6.10)$$

For the set of parallel domains with spacing ℓ:

$$\phi_{sc} = \frac{\phi_F}{\pi} \left\{ \tan^{-1} \frac{2\ell(b - a)}{4ab + \ell^2} + \sum_{n=1}^{L/2\ell} \left[\tan^{-1} \frac{4a\ell}{4a^2 + (16n^2 - 1)\ell^2} - \tan^{-1} \frac{4b\ell}{4b^2 + (16n^2 - 1)\ell^2} \right] \right\} \qquad (6.11)$$

The dimensions of the experimental arrangement were as follows: film width, L = 1 cm; search coil width (b - a) = ¾ cm situated ¼ cm from the film (a). This gives for the single domain:

$$\phi_{sc} = 0.2\, \phi_F.$$

With a domain-wall spacing of 1 mm, $\phi_{sc} = 0.16\, \phi_F$. However, as ℓ decreases the number of comparable terms in the summation in equation 6.11 increases, as a result of which the following estimates are very approximate:

for $\ell = 10^{-2}$ cm $\quad \phi_{sc} \simeq 0.1 \phi_F$

and for $\ell = 10^{-4}$ cm $\quad \phi_{sc} \sim 0.03 \phi_F$.

The only conclusion which may be drawn is that it is possible for the flux picked up by a search coil not actually in contact with the film to be reduced by the film's splitting into domains. The decrease will not be as great as calculated for two reasons. First, the finite width of the search coil will increase the flux picked up in case 2 more than case 1, and secondly, the case of 90° dispersion is never actually reached.

The source of the constant internal field will now be examined. The presence of this field could be explained by a biaxial anisotropy constant of $+ 4.0 \times 10^3$ erg/cc.

A low-field torque curve of another film prepared on polished NaCl when Fourier analysed showed a biaxial anisotropy field of 7.3 oe, over half the uniaxial contribution. However, since the signals were low and there were doubts as to whether the film was a single domain a high-field torque curve was taken using the apparatus described in section 4.4.2. The Fourier analysis showed a uniaxial field of 22.6 oe and a biaxial component of about 0.3 oe (the susceptibility value for H_k was 22.2 oe). The origin of this field-dependent biaxial anisotropy is not magnetocrystalline for three reasons: (a) the films are completely polycrystalline with no preferred orientation in the (100) plane; (b) the composition is such that K_1 is negative; (c) the anisotropy changes with measuring field.

The proposal by Prosen et al (P.10) that a biaxial anisotropy could result from substrate scratching was considered but random polishing

should not produce any biaxial anisotropy (P.11). Since sodium chloride cleaves easily along [100] it was thought that the scratches might have some fine structure along [100] directions causing a biaxial shape anisotropy. However, no evidence for this was observed on Pt-C replicas of the polished substrates.

The field dependence of the anisotropy constant suggests that its origin is connected with the coupling of isolated regions as proposed by Torok (T.4) and Yelon (Y.2). In fact a reasonable explanation has been obtained using the calculation of Yelon (Y.2) whereby two interacting uniaxial regions produce a field-dependent biaxial anisotropy. This method of treating short-range interactions between adjacent scratched regions is only a rough approximation since it treats only interactions between pairs of regions. A better approach is to use a properly-constructed ripple theory.

The explanation proposed here to account for the constant internal field is based on the ripple theory of Harte (H.8). In these films the magnetisation is thought to be blocked at high fields (up to about $5H_k$) and so the S-W model is no longer applicable, hence χ^{-1} is no longer proportional to $H_a \pm H_k$. The susceptibility is given by $\chi = \frac{M_s}{H_{eff}}$ where H_{eff} is a hypothetical effective field parallel to the magnetisation. From chapter 3 the effective field can be written in the form:

$$H_{eff} = H(\alpha) + H_R$$

where H_R is the ripple field. The constant internal field referred to above can be explained as being equal to the ripple field in Harte's non-linear case where the ripple field is equal to the intrinsic non-linear

field, Ω, (table 3.2) which is field independent. This has the effect of shifting the inverse susceptibility curves by a field, Ω. In order to check the validity of this explanation the magnitude of Ω must be determined and the range of applied fields over which the approximation is valid should be compared with the range over which the measured inverse susceptibility is proportional to the applied field (figure 6.9).

6.5.4. Comparison between Theory and Experiment. Before evaluating the non-linear field, Ω, we must determine which inhomogeneity scales are applicable. For these films the exchange coupling length (equation 3.16a) is about 10^3 Å whilst the magnetostatic coupling length (equation 3.16b) is about 5×10^5 Å.

In these films on polished substrates there are two possible inhomogeneities. One is the random scratching of the substrate and the other is the individual crystallite. Since films grown on cleaved substrates do not show the same kind of behaviour, the latter source of ripple, if present, must arise from a difference in the mode of growth on polished and cleaved substrates. The dimensions of these inhomogeneities are for the scratches, a characteristic width and separation around 5000 Å while the crystallites are about 100 Å across. From the coupling lengths it can be seen that the crystallite size is less than the exchange length, a situation Harte refers to as fine-scale ripple. The scratch size falls between the two coupling lengths and thus fits into Harte's category of coarse-scale ripple.

In both of these cases it is possible to calculate from Harte's theory the range of field values over which the non-linear approximation

is accurate to a given degree. The details are given in Appendix A.2 and the result is that this approximation should cease to apply at fields, $H_a \pm H_k$, greater than 16 oe. However, the data in figure 6.9 shows that the experimental curves are indistinguishable from straight lines up to a field $H_a \pm H_k$ of about 55 oe. It is clear that the non-linear approximation does not give an acceptable description of the data.

However, when the theoretical expression of H_{eff} is evaluated without any approximations and plotted against $H_a \pm H_k$ (see curves 1 on figure 6.11a and 6.11b) it is found that the plot appears to be very nearly a straight line over quite substantial regions. This raises the possibility of fitting the exact solution of H_{eff} to the data of figure 6.9. It has been done by drawing several different straight-line fits to the exact solutions in figure 6.11 of which lines 5 are examples. The best fit is obtained when the theoretical field range (over which the straight line fits the exact solution to 1%) is the same as the experimental field range (over which the points in figure 6.9 lie on a straight line to the same accuracy). Again, the details are given in Appendix A.2; the result is that a very good fit is obtained with the assumption of a coarse-scale ripple, but not a fine-scale ripple. It is therefore concluded that the susceptibility data can be explained by the effects of scratching produced during polishing. From the intercept of the straight-line approximation 5 in figure 6.11 the intrinsic non-linear effective field Ω can be evaluated by comparison with the experimental curve in figure 6.9. The theoretical formulation of Ω as given in table 3.2. enables the evaluation of K, the local random anisotropy constant, as 6.9×10^3 erg/cc.

6.5.5. Conclusions. It has been shown that the effect of polishing is to produce highly-dispersive magnetic behaviour which can be explained using Harte's theory. The additional dispersion can be ascribed to the scratches introduced during polishing, producing a collection of planar areas with a local root mean square value of anisotropy of 6.9×10^3 erg/cc, separated by non-planar or discontinuous regions.

This highly-dispersed film behaviour manifests itself in the susceptibility curves in several ways: (a) the magnitude of the signal, as compared with a low-dispersion film of similar thickness, decreases appreciably as can be seen from figures 4.8, 6.7 and 6.8, which have the same attenuation for the susceptibility; (b) an 'effective' non-linear field, independent of the applied field is observed; (c) a large amount of rotational hysteresis is observed with the bias field in both the easy and hard directions. (The curves from which measurements were taken were always obtained by decreasing the field from saturation); (d) locking occurs on reduction of a hard direction field with the result that the susceptibility in zero field is appreciable (about 30% of the peak susceptibility); (e) reversal in the easy direction occurs over a wide range of fields due to blocking of the magnetisation ripple and the presence of energy barriers for domain-wall motion at or near the scratches.

Similar work carried out by Doyle et al (D.4) on films electro-deposited on wires emphasises this highly-dispersive behaviour caused by the surface roughness of the substrate.

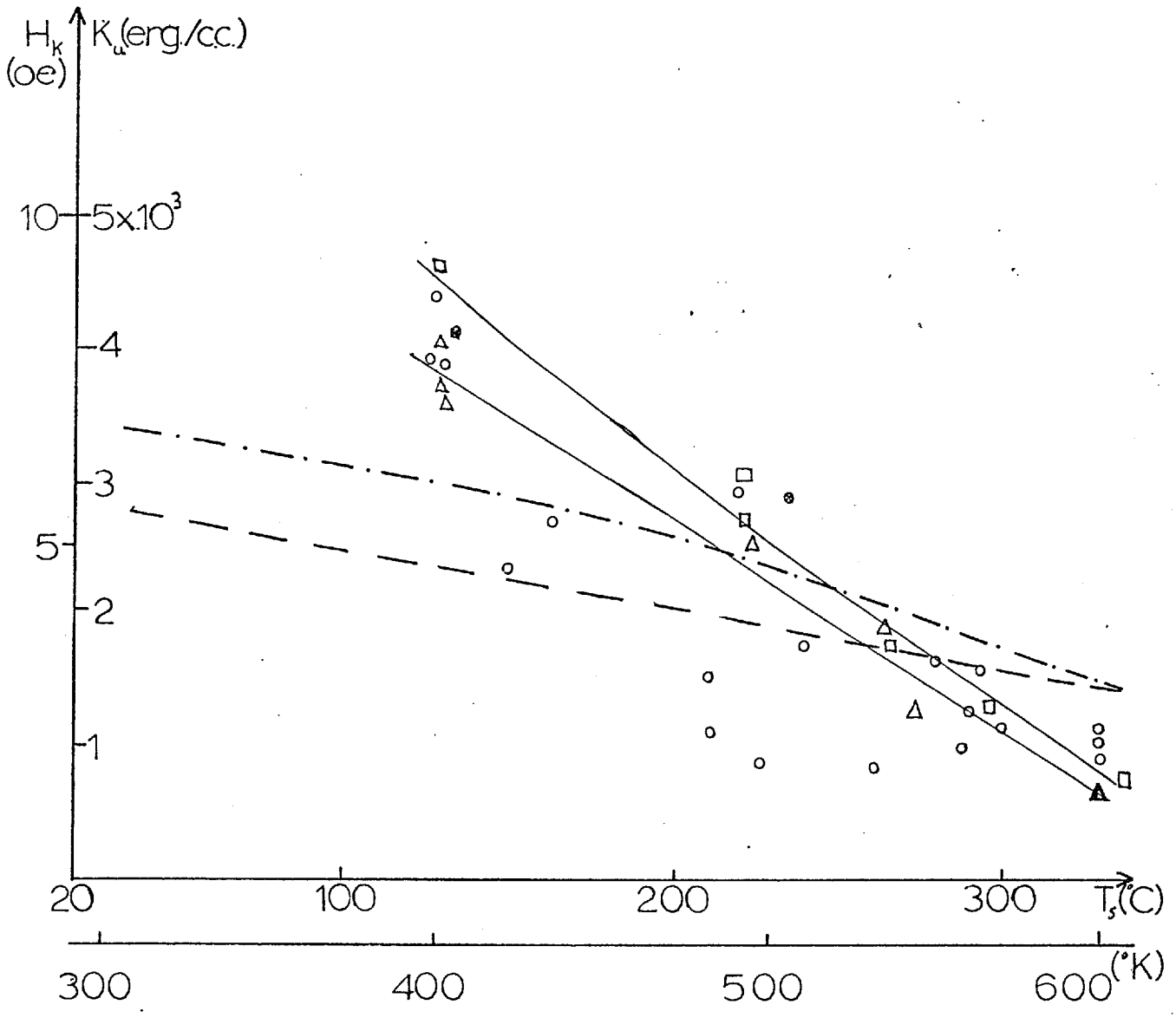

Figure 6.1 The variation of H_k (or K_u) with substrate temperature

□ NaF substrate Δ LiF substrate ○ NaCl substrate

(⊗ etched)

— — — Feldtkeller's results for 81/19 NiFe on glass

—·—·— 80/20 NiFe on glass inferred from the results of Wilts

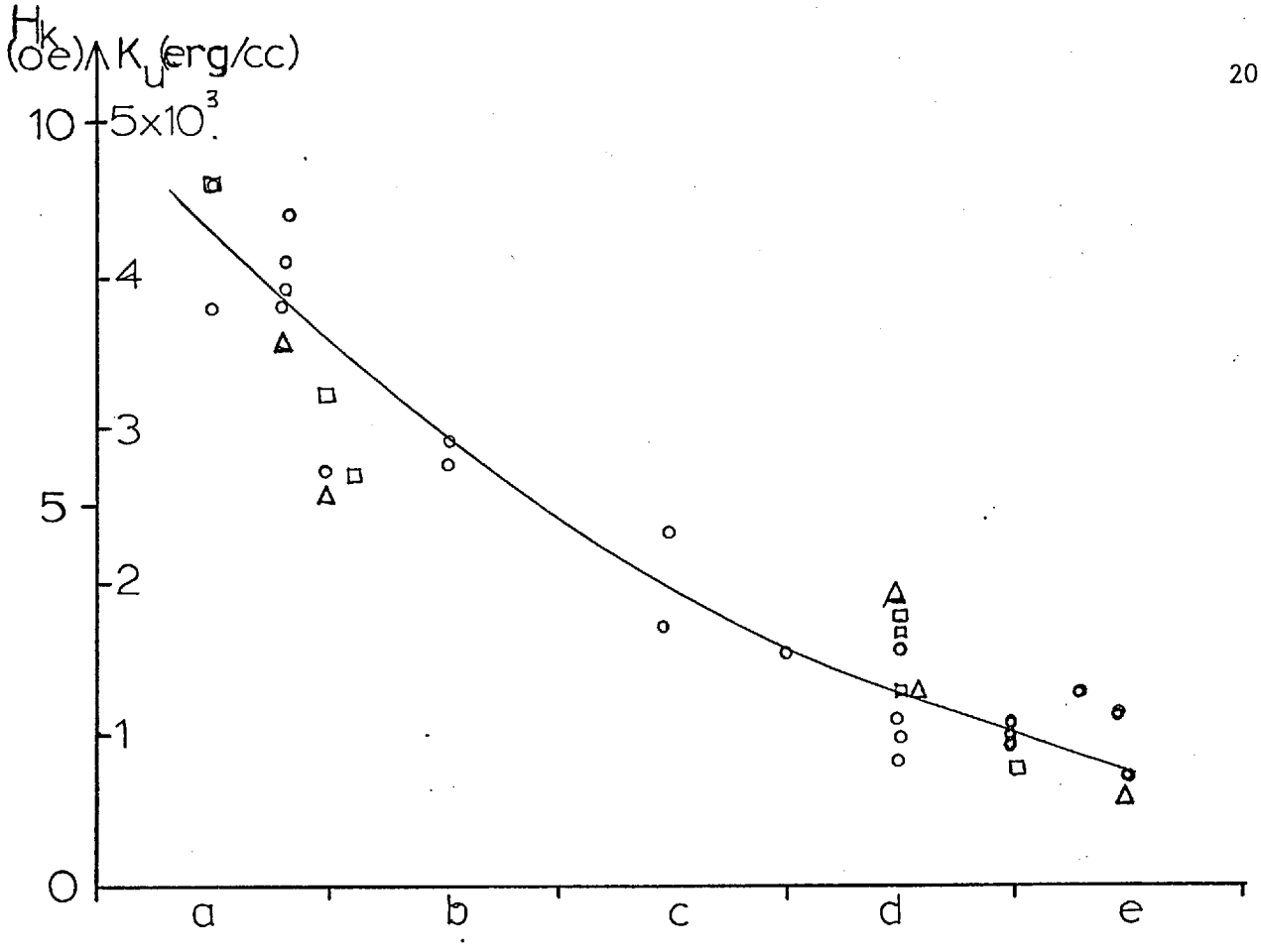

Figure 6.2 The variation of H_k (or K_u) with type of diffraction pattern as outlined on page 148

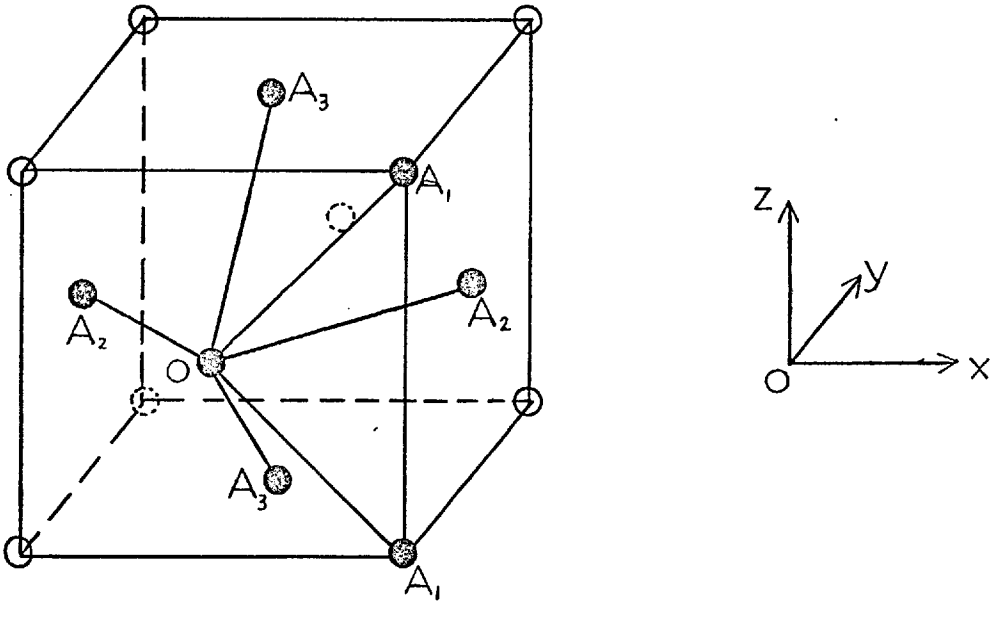

Figure 6.3 Nearest neighbours for an atom O in an f.c.c. metal

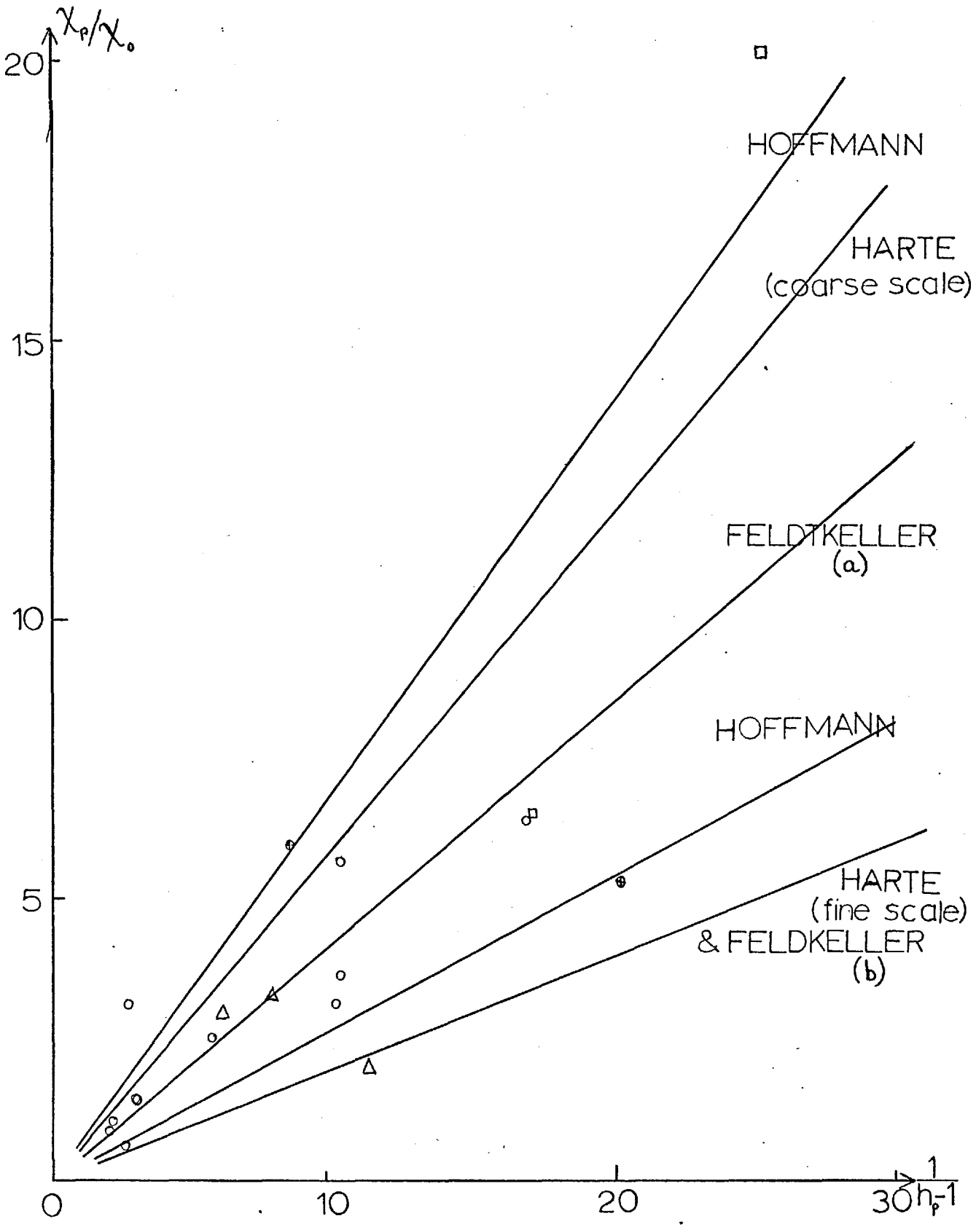

Figure 6.4 Plots of χ_p/χ_o against $1/(h_p - 1)$ for uniaxial films compared with various theories

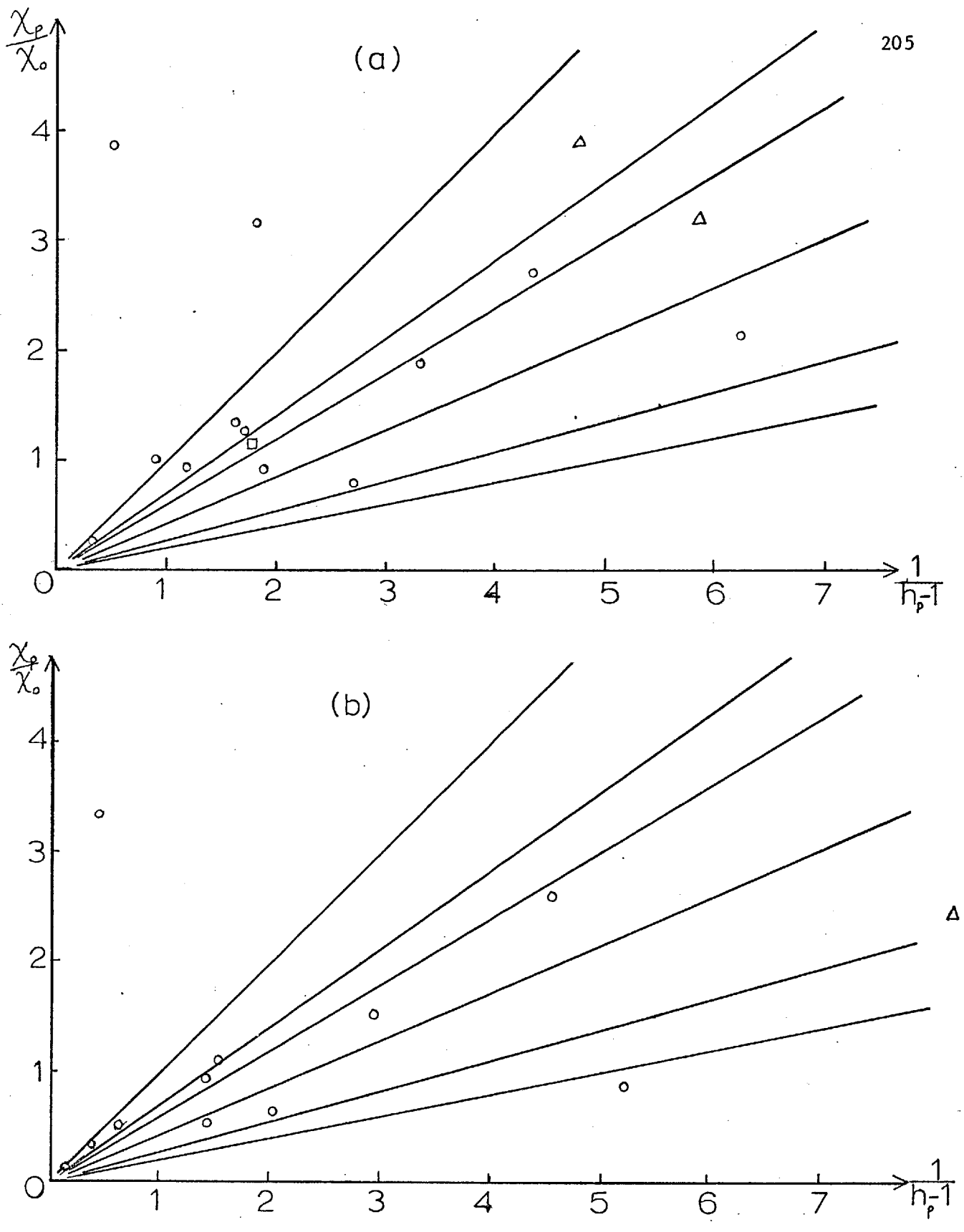

Figure 6.5 Plots of χ_p/χ_o against $1/(h_p - 1)$ for biaxial films in (a) the uniaxial hard and (b) the uniaxial easy directions

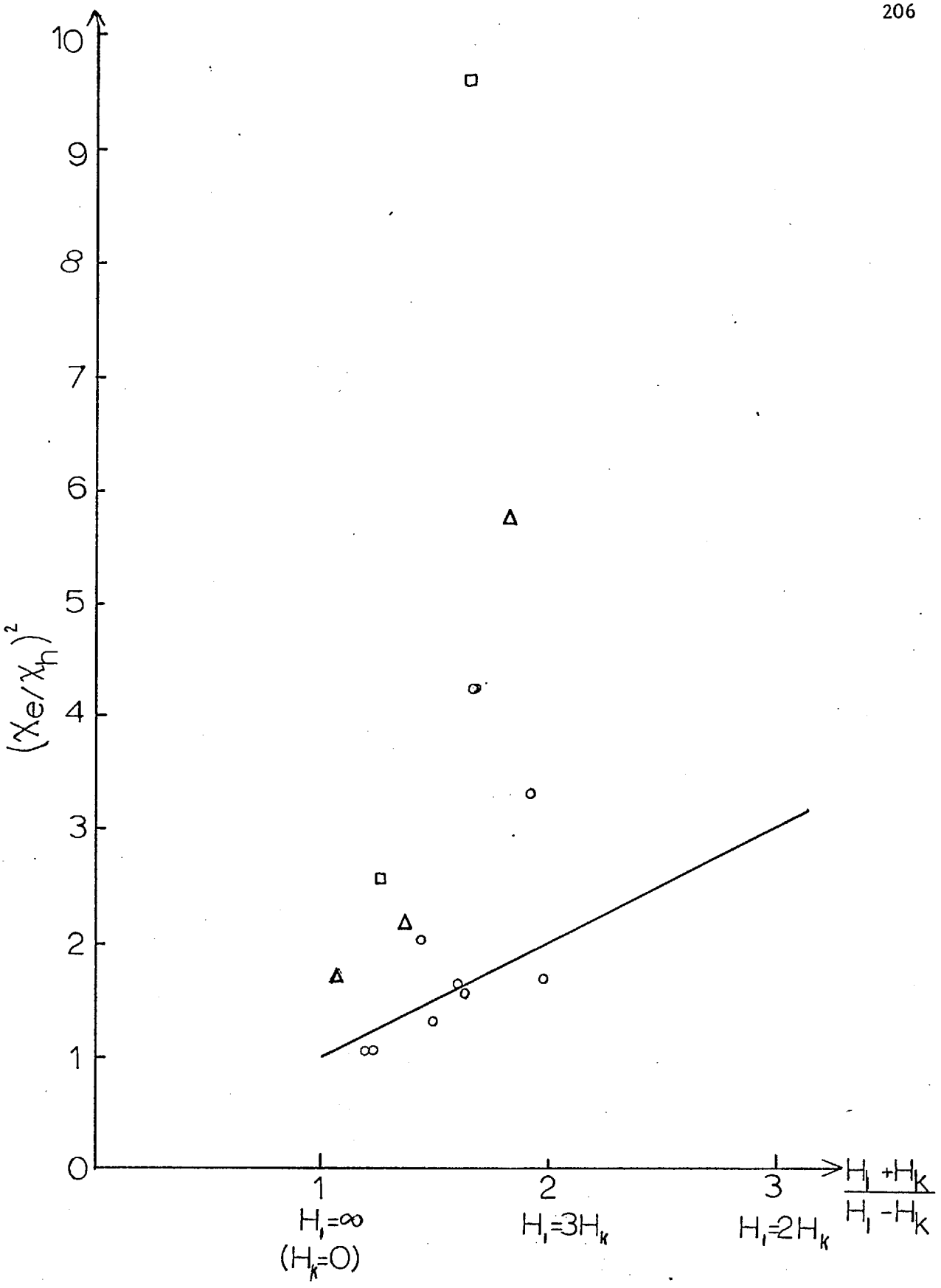

Figure 6.6 A comparison of $(\chi_e/\chi_h)^2$ versus $\frac{H_1 + H_k}{H_1 - H_k}$ with theory for biaxial films

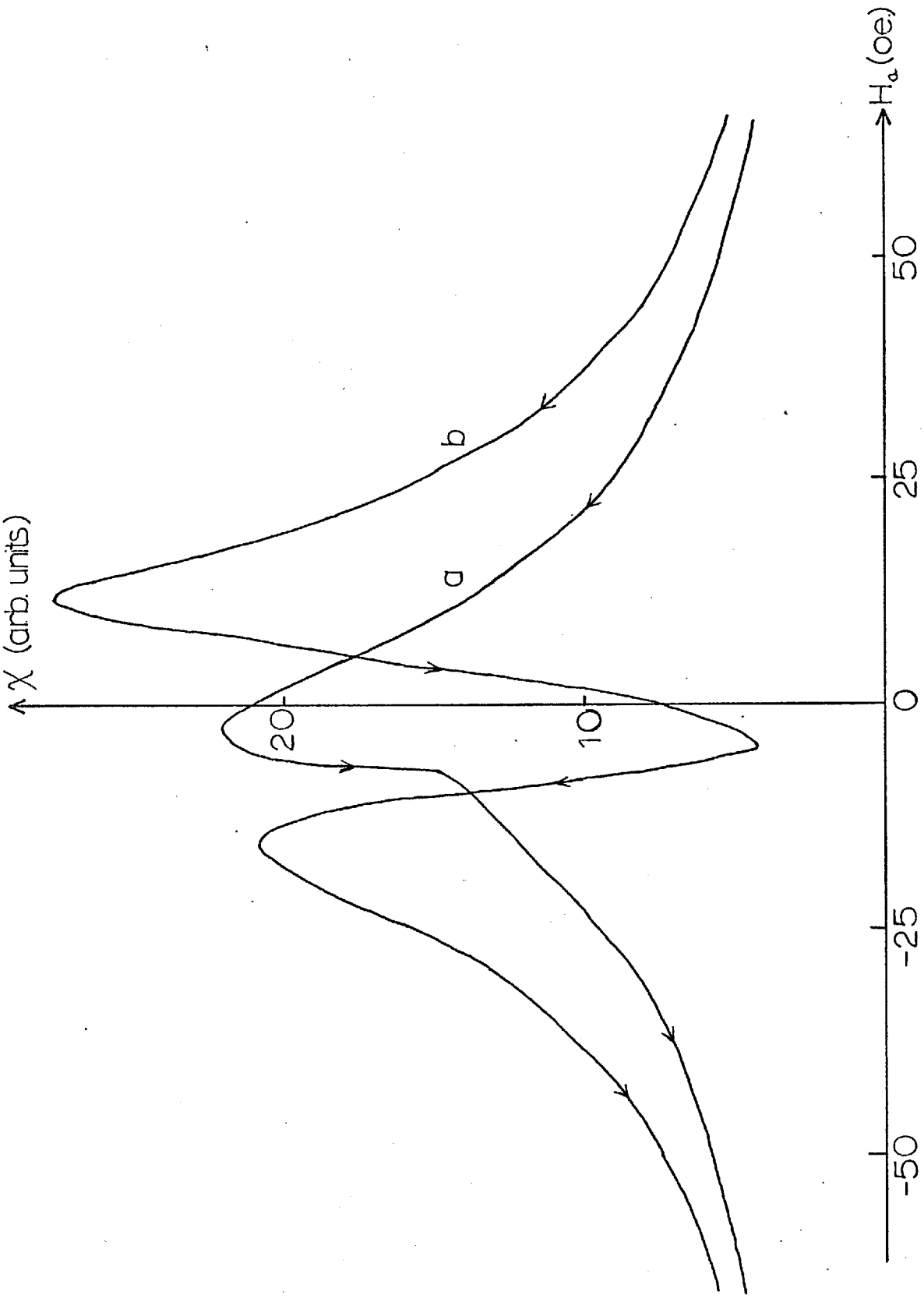

Figure 6.7 The susceptibility curves for a film prepared on a polished substrate at room temperature. (a) easy and (b) hard directions

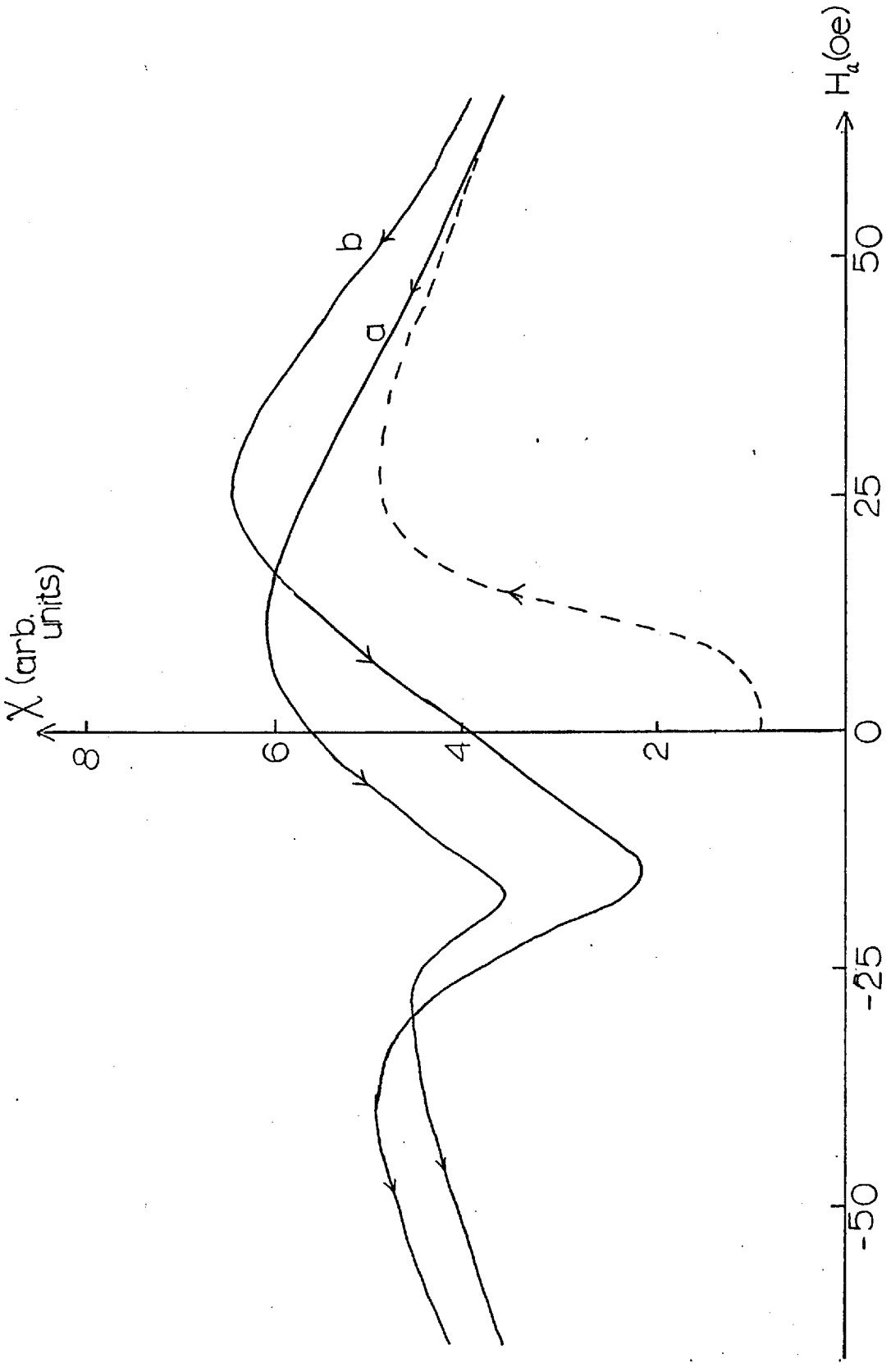

Figure 6.8 The susceptibility curves for a film prepared on polished NaCl at 150°C (a) easy and (b) hard direction

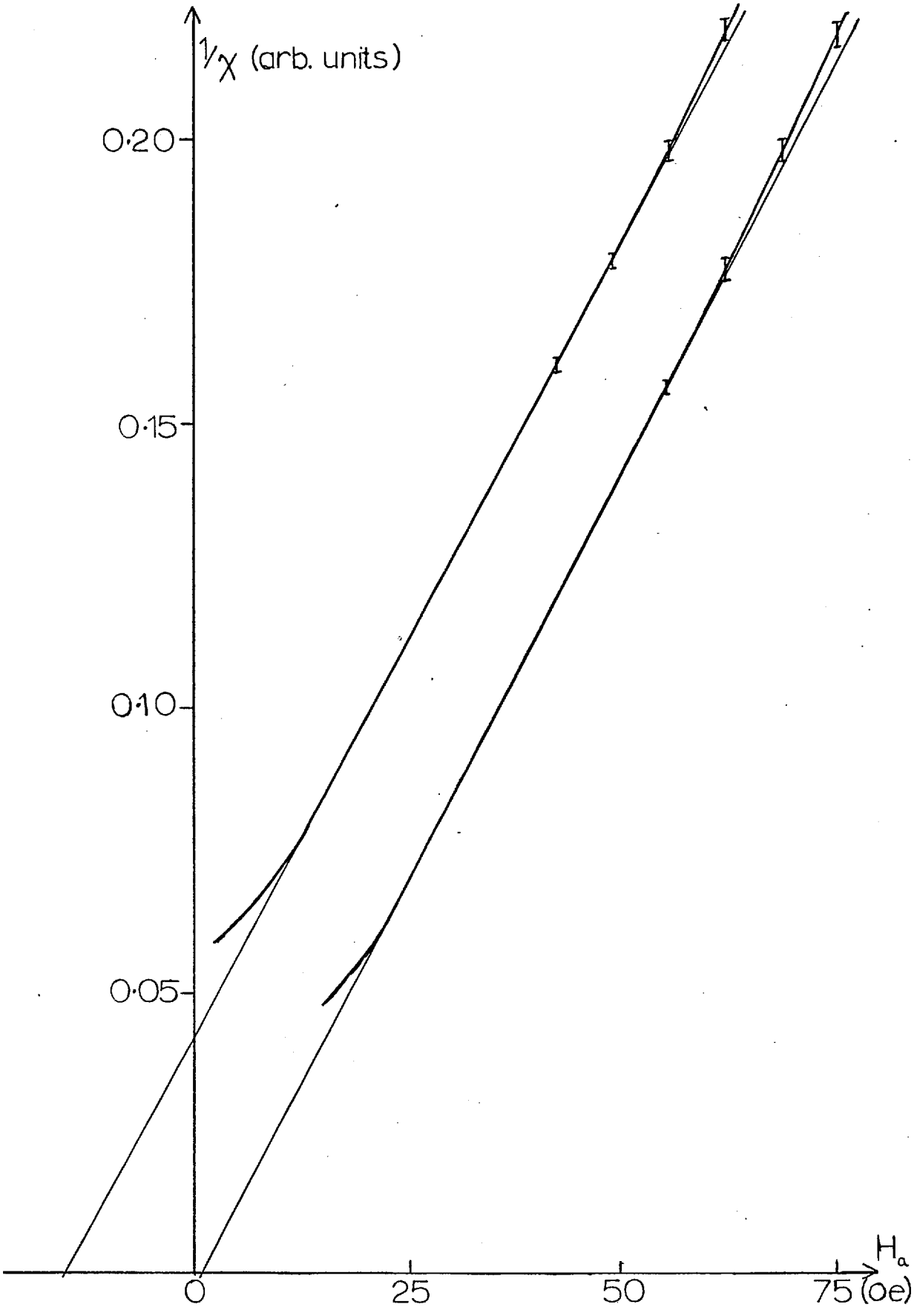

Figure 6.9 The inverse susceptibility curves of a film on a polished substrate

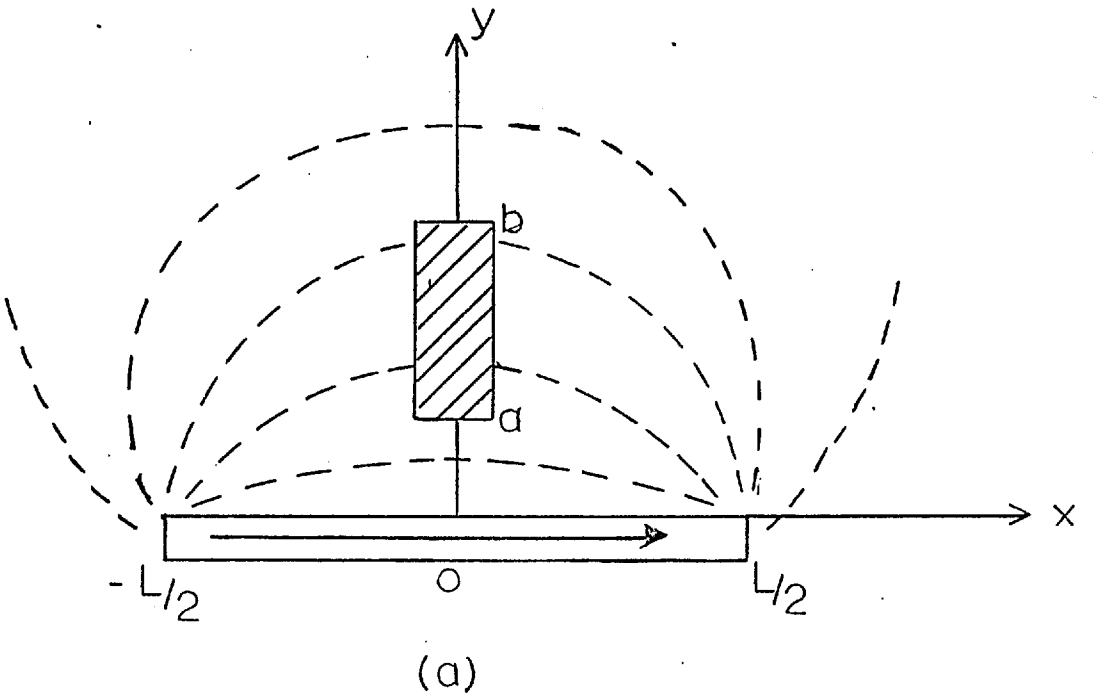

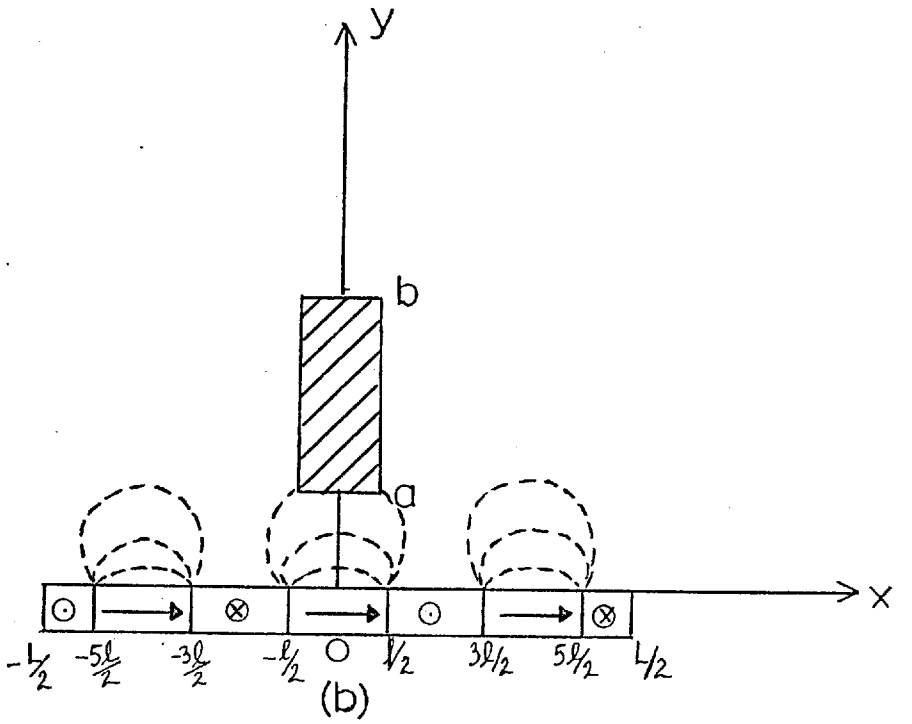

Figure 6.10 The flux distributions for the two extreme cases of
(a) a single domain and
(b) a locked state with 90° dis ersion

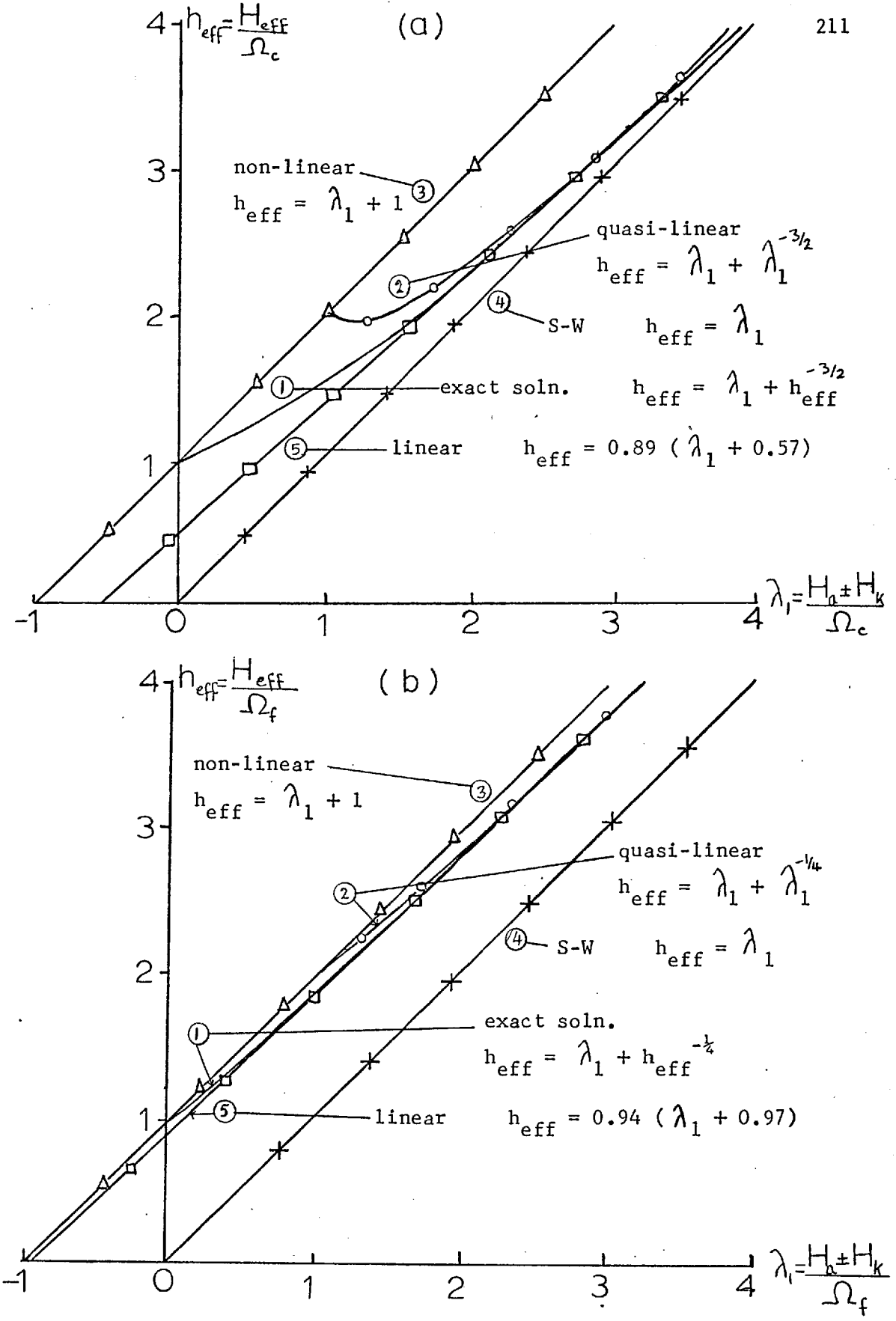

Figure 6.11 The effective field plotted as a function of the applied field ($H_a \pm H_k$) for (a) the coarse scale and (b) the fine scale, in reduced notation

CHAPTER 7

Magnetic Properties: (B) Maximum Loss Curves

In this chapter the peak imaginary susceptibility is measured as a function of the combined a.c. and bias fields. The shape of the resulting curve is discussed in terms of two separate models. First, using Hoffmann's blocking curve and secondly, using a modified wall-motion model.

7.1. Introduction

Since the origin of quadrature flux or imaginary susceptibility has been shown to be ripple hysteresis (H.13) it was thought that by careful measurement of the losses around the hard axis the shape of the blocking curve as postulated by Hoffmann (H.7) could be determined. To enable contributions to the imaginary susceptibility to be made the field vector must cross the blocking curve from the outside (a single-domain state) causing the ripple walls to remain fixed. A further change in the field is then required to reorient the ripple by moving at an angle to the average magnetisation.

The easiest method of achieving this is to superimpose an a.c. field on top of a bias field in the hard direction, the size of the a.c. field governing the portion of the blocking curve under surveillance. This method is limited to small a.c. fields as the signal drops off as the magnetisation approaches the a.c. field direction.

The experimental procedure was to fix a value of the a.c. field using the biased susceptibility apparatus described in section 4.3, and then the bias field was decreased in the hard direction until a peak in the imaginary susceptibility (corresponding to maximum losses) was observed. This was repeated for several values of a.c. field and the field combinations were then plotted in field space. The curve so obtained represents a plot of the maximum losses which, if they correspond solely to irreversible ripple reorientations should be the blocking curve or, because of hysteresis, a curve almost parallel to it.

The imaginary susceptibility was measured by adjusting the reference signal phase to the phase-sensitive detector so that the out-of-phase component of the input signal was amplified. Care has to be taken in setting the phase as all phase shifts in the electronics must be eliminated as was mentioned in section 4.3.1. The variation of the imaginary susceptibility with the bias field for a fixed a.c. field is shown in figure 4.8.

The normalised maximum loss curves are shown in figure 7.1. for two films, 11NF1 and 16NF1, which have widely differing properties (see table 7.1).

Table 7.1

Film	Substrate	H_k (oe)	H_c (oe)	Field range for reversal (oe)	$\frac{\chi_p}{\chi_o}$	$\frac{H_p - H_k}{H_k}$	$\frac{H_c}{H_k}$
11NF1	Cleaved NaCl	8.8	8.6	$\pm$ 1.8	3.1	0.1	0.98
16NF1		5.3	1.26	$\pm$ 0.1	6.4	0.06	0.25

The measurements for the second film were performed at three frequencies (200, 600 and 2000 c/s) (figure 7.2) to eliminate instrumental errors and any relaxation phenomena.

7.2. The Blocking Curve and Ripple Hysteresis

As a field applied in or near the hard axis is decreased from saturation the ripple amplitude increases as the field approaches the astroid. The large stray fields involved cause blocking which prevents the ripple walls from moving but still allows rotation within the domains. The fields at which this occurs have been calculated by Hoffmann and form the blocking curve, figure 7.3. The equation of the blocking curve in parametric form is given by Hoffmann as:

$$h_x = -\cos^3\theta + h_b \cos\theta \pm \frac{Q}{2}\sin\theta \qquad (7.1a)$$

$$h_y = \sin^3\theta + h_b \sin\theta \pm \frac{Q}{2}\cos\theta \qquad (7.1b)$$

where θ is the angle the magnetisation makes with the easy axis and h_b and Q are constants given by:

$$h_b = \frac{1}{AK_u}\left\{\frac{M_s}{4\pi n}\left(\frac{D}{2}\right)^{\frac{1}{2}}(Kd\sigma_1)^2\right\}^{4/5} \qquad (7.2a)$$

$$\text{and} \quad Q = \frac{1}{AK_u}\frac{(Kd\sigma_1)^2}{4\pi n}\left(\frac{3}{2}\right)^{\frac{1}{2}} \qquad (7.2b)$$

where the terms have their usual meaning (Appendix A.1) and $\sigma_1^2 \simeq \frac{1}{2}$, $n \simeq D/d$. Using the following values: $A = 10^{-6}$ erg/cc, $K_u = 3 \times 10^3$ erg/cc, $M_s = 10^3$ gauss, crystallite size $d = 170 \times 10^{-8}$ cm, thickness $D = 450 \times 10^{-8}$ cm and $K = 3 \times 10^4$ erg/cc, values of 0.098 for the normalised blocking field, h_b, and 0.009 for Q were obtained. The effect of the

final terms in equations 7.1a and 7.1b will be negligible with this value of Q near the hard axis.

By fitting the theoretical and experimental curves in the hard direction ($h_x = 0$, $h_y = 1 + h_b$) a value for h_b of 0.022 is obtained which is of the right order. Using this value equation 7.2a predicts a local anisotropy of 1×10^4 erg/cc which can be explained by a stress of 1.0×10^9 dyne/cm^2 using the model due to Doyle and Finnegan (D.3). However, the general shape of the blocking curve in comparison with the actual loss curve shown in figure 7.4 demonstrates very poor agreement as they have opposite curvatures for fields above H_k.

For the field configuration applied here the losses will mainly arise from the freeing of the ripple rather than its blocking. The method by which the losses are thought to arise is shown in figure 7.5. In (i) the field is outside the blocking curve and the ripple is free. Diagram (ii) shows the blocked ripple with the resultant field just touching the blocking curve. Further decrease of the a.c. field rotates the ripple within these domains until the limiting stable case (iii) is reached. Any further increase in field will free the ripple causing a large irreversible change in the magnetisation with an accompanying loss.

If the ripple angle is θ when the film becomes blocked then the transverse component of magnetisation, $M_t = M_s\theta$ and the associated transverse field can be approximated to:

$$H_t \simeq M_t/\chi_t \quad \text{where } \chi_t \text{ is the transverse susceptibility.}$$

Using the approximation due to Feldtkeller (F.6a) for the transverse susceptibility derived assuming motionless ripple walls and a sinusoidal

variation in the ripple amplitude:

$$\chi_t = M_s/(H_a \pm H_k + \frac{M_s D f \theta^2}{\lambda}) \quad .. \quad .. \quad .. \quad .. \quad .. \quad (7.3)$$

where D is the film thickness, λ the ripple wavelength and f a numerical factor depending on both λ and the crystallite size (approximately constant for $\lambda \geq 20$ x crystallite size), thus:

$$H_t = M_s \theta / \chi_t = \theta(H_a \pm H_k + \frac{M_s D f \theta^2}{\lambda})$$

$$\text{or} \quad H_t = H(\alpha)\theta + \frac{M_s D f}{\lambda} \theta^3 \quad .. \quad .. \quad .. \quad .. \quad .. \quad .. \quad (7.4)$$

Therefore if a field H_t is applied perpendicular to the mean magnetisation direction the limiting case will be reached and the ripple will be virtually free. Applying this correction to the blocking curve should give the loci of the fields for maximum loss.

The expression used for deriving a value for λ at the blocking curve was twice the domain spacing in the hard-axis fall-back, given by Hoffmann (H.9) as:

$$\lambda = 2\pi\sqrt{\frac{2A}{M_s H(\alpha)}} = 2.09\ H(\alpha)^{-\frac{1}{2}} \mu m \quad .. \quad .. \quad .. \quad .. \quad (7.5)$$

In determining the ripple amplitude, the dispersion in the thin-film, fine-scale inhomogeneity case of Harte's ripple theory (H.8) was used. For fields near the astroid the intrinsic non-linear effective field is greater than the applied field $(H_a - H_k)$ so that:

$$\theta = \frac{I(\frac{1}{2},\frac{3}{2})^{\frac{1}{2}}}{I(\frac{3}{2},\frac{3}{2})^{3/10}} \left(\frac{4\pi dK}{D}\right)^{2/5} \frac{1}{(4\pi M_s)^{4/5}} \quad .. \quad .. \quad .. \quad .. \quad (7.6)$$

where $I(\frac{1}{2},\frac{3}{2})$ and $I(\frac{3}{2},\frac{3}{2})$ are numerical constants, d is the crystallite diameter, D the film thickness and K the local anisotropy constant.

With $K = 10^4$ erg/cc, $d = 100$ Å, $D = 500$ Å, $M_s = 10^3$ gauss,

$$\theta = 0.03 \text{ radians.}$$

The field correction including these values becomes:

$$H_t = 0.03\, H(\alpha) + 0.0019\, H(\alpha)^{\frac{1}{2}} \quad .. \quad .. \quad .. \quad .. \quad (7.7)$$

Applying this correction for the ripple hysteresis reduces the curvature as shown in figure 7.4 although the curve still remains convex. A further prediction resulting from this explanation is that below an a.c. field of amplitude $2H_t$ no losses should be observed as the blocked ripple is never freed. Since losses were observed below $2H_t$ it follows that there should be more than one contribution to the losses. Careful observation of the amplitude of the imaginary susceptibility as a function of the a.c. field showed a uniform increase with no peak near $2H_t$.

The suggestion that these losses were caused by long-range 'skew' or a dispersion in the blocking fields was dismissed for the following reasons: Since the ripple amplitude at blocking is independent of field it will be constant round the curve, a result of which is that the maximum losses will occur when the largest possible area is blocked. Consequently, the maximum loss curve will be an envelope of all possible blocking curves which enhances the convexity of the blocking curve. This applies even for a Gaussian distribution of blocking fields as can be seen from the sign of d^2h_y/dh_x^2.

It appears that this explanation is inadequate on several counts and so the next approach is concerned with the losses due to wall motion.

7.3. Wall-motion Model

Without any applied a.c. field a reduction in the bias field in the hard direction leads to the production of an equal number of 'oppositely' magnetised domains ('hard-axis fall-back').

The onset of this will occur by the formation of low-angle ripple walls. It is proposed here that the application of an a.c. field will cause small irreversible movements of the ripple walls by 'Barkhausen' jumps. There are at least two possible methods by which the walls can move, as shown in figure 7.6. Case (a) consists of enlargements and diminutions of domains magnetised nearest to the applied field while case (b) consists of movements of ripple walls into and out of unblocked regions. To decide which would be the dominant process we need to compare the energy changes in both cases.

From Middlehoek's thesis (pg 129, M.3) we have for a wall of length l, moving under an applied field H, a distance dx,

$$H = \frac{1}{2M_s}\left[\frac{d\gamma}{dx} + \frac{\gamma}{D}\frac{dD}{dx} + \frac{\gamma}{l}\frac{dl}{dx}\right]$$

where γ is the surface energy density of the wall and D the film thickness. This is calculated from the three coercive-force mechanisms of anisotropy variations, thickness changes and alterations in the wall length respectively. For the small changes involved in these wall movements the thickness variations will be assumed either negligible or the same in both cases.

Middlehoek (M.3) calculates the field required to overcome an anisotropy variation ΔK as $\frac{a}{4}\frac{\Delta K}{M_s d}$ where a is the wall width and d the crystallite size. Suppose that the field required for a wall-length

change, dl, is H_{dl} (according to Middlehoek this will be ~ 0.025 oe) then the fields required to move the walls in the two cases are:

$$(a) \quad H_a = H_T + \frac{a}{4M_s d}\Delta K_a \qquad (7.8a)$$

and $$(b) \quad H_b = H_T + \frac{a}{4M_s d}\Delta K_b + H_{dl} \qquad (7.8b)$$

Now $H_a > H_b$ if: $\Delta K_a - \Delta K_b > \frac{4M_s d}{a} H_{dl}$ i.e. if $\Delta K_a - \Delta K_b > 0$.

For a film to be uniformly blocked throughout at almost the same field the anisotropy field variation will be very small, whereas the anisotropy variations required to produce a mixture of blocked and unblocked regions will be far higher.

$$\therefore \Delta K_a - \Delta K_b < 0.$$

Hence $H_a < H_b$ and so the walls in case (a) will move at a lower field.

This is only a rough calculation and the existence of cleavage steps in the substrate will probably produce easy nucleation sites for reverse domains making the mechanism (b) a distinct possibility.

To check if one type of wall motion predominated, visual observations using the Bitter technique (B.3) were made on a similar film grown on LiF. LiF was chosen because it possesses cleavage steps but does not dissolve in the colloid, as did NaCl and NaF.

The experimental field configuration used in the loss measurements could not be reproduced exactly as only one field could be applied at once. However, the following photographs indicate that both types of wall motion occur. Figures 7.7a and 7.7b show the film after saturation in the hard direction and secondly with a small field (1.2 oe) in the easy direction.

However, in both cases we will be concerned with the movement of low-angle walls and the fields at which these movements occur. Due to energy considerations this film should possess low-angle walls of the Néel type (figure 1.5b). Thus if the losses do occur because of irreversible wall perturbations then they should occur at or near the coercive fields for Néel walls.

Neglecting thickness variations and wall-length changes Middlehoek has shown that for domains magnetised at an angle ϕ to the easy axis the coercive force is given by:

$$H_c = \frac{C_N \gamma_N(180^\circ)}{2M_s} \frac{(1 - \sin\phi)^2}{\cos\phi} \quad .. \quad .. \quad .. \quad .. \quad .. \quad (7.9)$$

Films of thicknesses used in these experiments will have cross-tie walls for angles $(\phi) < 20^\circ$ and the coercive force is given by:

$$H_c = \frac{C_B \gamma_B(180^\circ)}{2M_s} \cos\phi \quad .. \quad .. \quad .. \quad .. \quad .. \quad .. \quad (7.10)$$

where $\gamma_N(180^\circ)$, $\gamma_B(180^\circ)$ are the surface energies of the Néel and Bloch or cross-tie walls, C_B and C_N being constants.

These curves are shown in figure 7.8a superimposed on the maximum loss curves plotted with the constants

$$\frac{C_N \gamma_N(180^\circ)}{2M_s} = \frac{C_B \gamma_B(180^\circ)}{2M_s} = H_k \text{ and } H_y = H_k \sin\phi.$$

These values for the constants were chosen since good quantitative agreement has been obtained by Il'icheva et al (I.2) using these values. The approximation $\sin\phi = H_y/H_k$ is fairly accurate for small values of H_x (or H_y).

As can be seen from the graph the curvatures of the theoretical and experimental curves are in agreement. The loss curve of film 11NF1 lies in closer agreement with the wall-motion model although it increases faster as the magnetisation approaches the hard axis. The second loss curve, for film 16NF1, lies parallel over a wider field range, and a vertical displacement of the theoretical curve would give extremely good agreement as shown in figure 7.8b.

This is justified by combining this model with Hoffmann's blocking curve. It has been assumed that walls are only present for fields $< H_k$, but when the film becomes blocked there exist low-angle walls which may be moved by the a.c. field. If this is the case then the equation for the field for wall motion will be:

$$H_y = (1 + h_b)\, H_k \sin\phi$$

$$H_x = H_k \frac{(1 - \sin\phi)^2}{\cos\phi} \qquad \text{(7.11)}$$

In figure 7.8b a value of 0.022 was used for h_b for 16NF1 as in figure 7.4.

The relatively poor agreement for film 11NF1 is explained by one of the shortcomings of this wall-motion explanation. In Middlehoek's original derivation of the theoretical coercive force he neglected to take into account the magnetostatic interactions produced by the non-180° domain walls. Now the magnetostatic-free poles induced on the domain walls will give rise to an energy density of $\underline{M}_s$.grad U where U is the magnetostatic potential.

The magnetostatic potential consists of two terms, a surface term which is negligible for Néel walls, and a volume term which is only important for small domains. The volume term for long needle-shaped domains can be approximated by line dipoles on each side of the domain wall and if the wall separation is comparable with the domain-wall width then this term will be large. For films 500 Å thick the Néel wall width is about 400 Å, so for the domain separation to be comparable with the wall width there should be a density of $\sim 10^5$ walls per cm.

A convenient method of determining this density is by comparing the experimental hard direction hysteresis loop with those predicted by Middlehoek (pg 120, M.3) for various domain-wall separations. The local hard-axis loop for film 16NF1 is shown in figure 4.16a obtained by using the Kerr effect as described in chapter 4. The magnetisation intersects its saturation value at a field of 5.7 oe. By comparing this with the susceptibility-method determination of H_k (5.3 oe) a wall density of about 8 walls/cm is derived. From this it appears that the magnetostatic interactions for film 16NF1 are negligible and so Middlehoek's formula is applicable. However, for film 11NF1 the hard-direction loop was very open and the loop properties varied substantially across the film, which made it impossible to estimate the wall density. It must be fairly high since this film has high dispersion, as may be deduced from its properties (table 7.1) so that we cannot expect Middlehoek's formula to agree.

7.4. Conclusions

It appears that the losses which contribute to the imaginary susceptibility, as determined using the transverse biased susceptibility

apparatus, originate in small irreversible wall movements rather than ripple hysteresis. The low-angle ripple walls, of the Néel type, produced during the blocking process are moved in small discreet jumps by the superimposed a.c. field.

Previous explanations of these losses by Feldtkeller (F.6b) have been based on ripple hysteresis and irreversible reorientations. The difference between small jumps of very low-angle walls (ripple walls) and irreversible-ripple reorientations is very slight. As can be seen from the Lorentz micrographs in Feldtkeller's papers it is very difficult to distinguish between the two. The predicted fields at which these losses occur will depend solely on the model used. Feldtkeller (F.6b) derives the losses by ripple hysteresis for fields just outside the astroid using a method developed by Preisach (P.12) and Néel (N.6). They were considering hysteresis losses by wall motion in the Rayleigh region (small magnetisation changes). The difference between this treatment and that of Feldtkeller seems to be just nomenclature.

The conclusions that can be drawn are therefore that the loss curves measured here can be explained using a wall-motion model even though the actual losses may be caused by ripple reorientations.

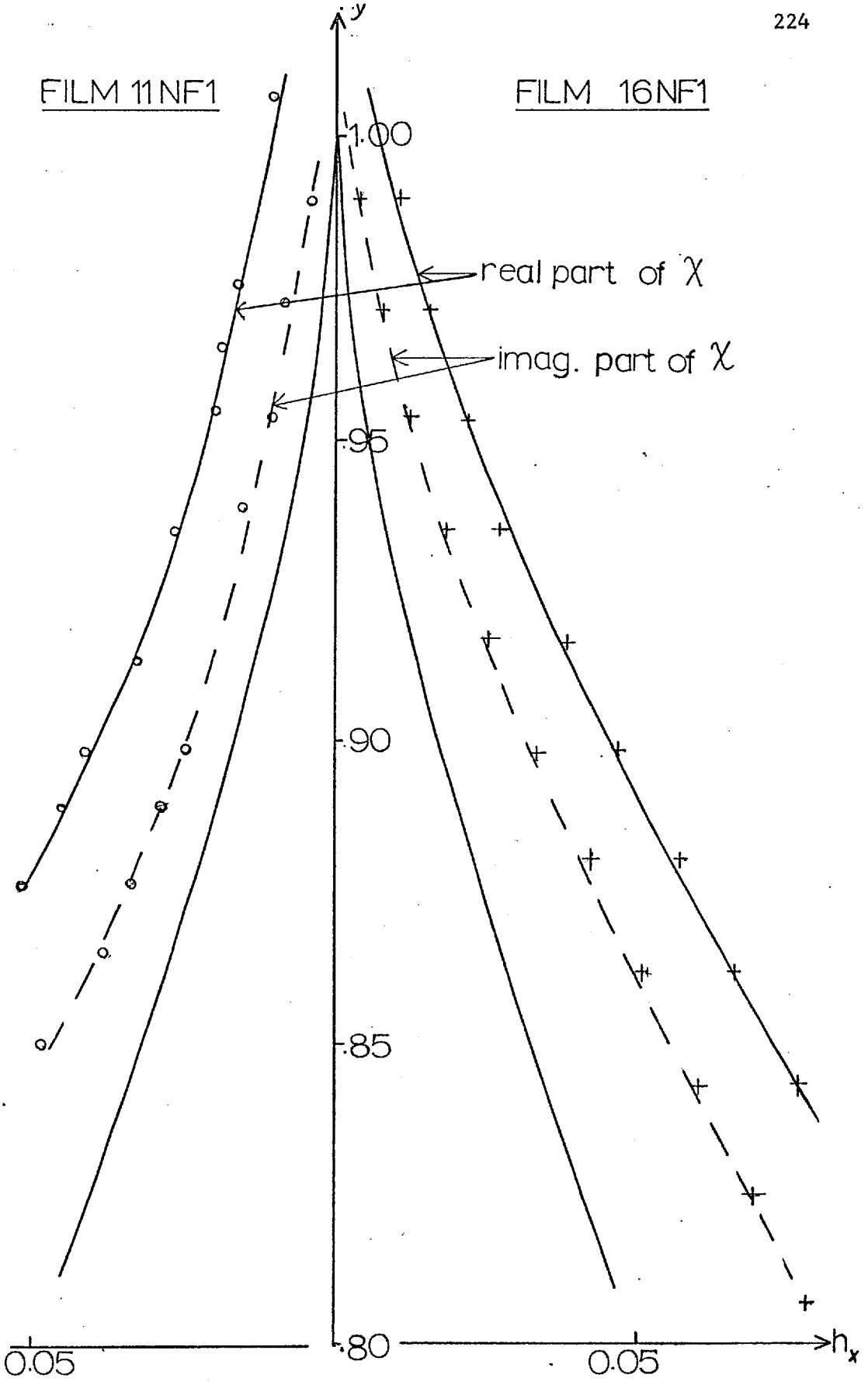

Figure 7.1 Plots of the bias field (h_y) against the a.c. 'tickle' field (h_x) for maxima in the real and imaginary parts of the susceptibility for two films

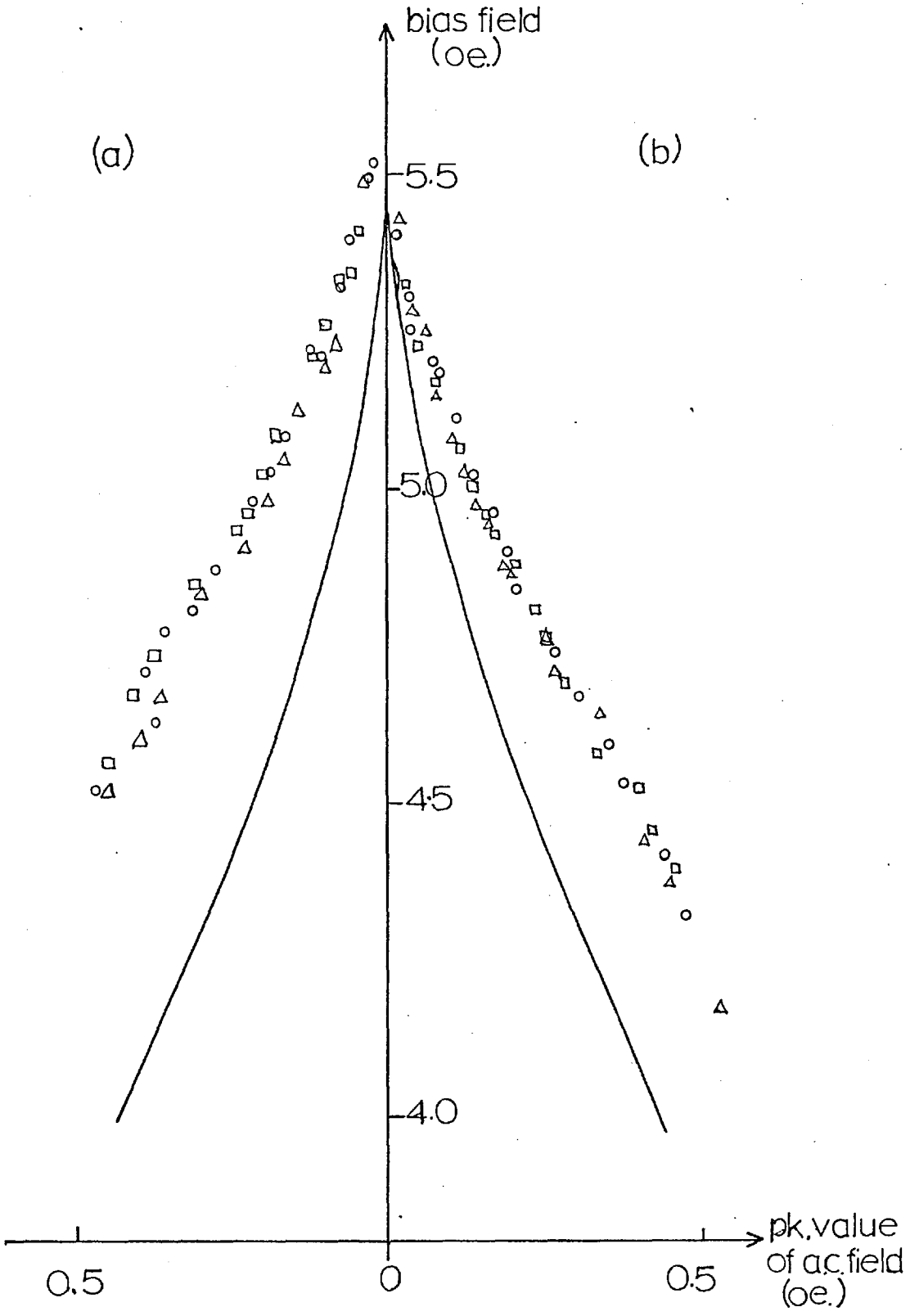

Figure 7.2 Locus of fields for peak values of (a) the real and (b) the imaginary susceptibility at various a.c. field frequencies

(□ 200 c/s, Δ 600 c/s, o 2000 c/s)

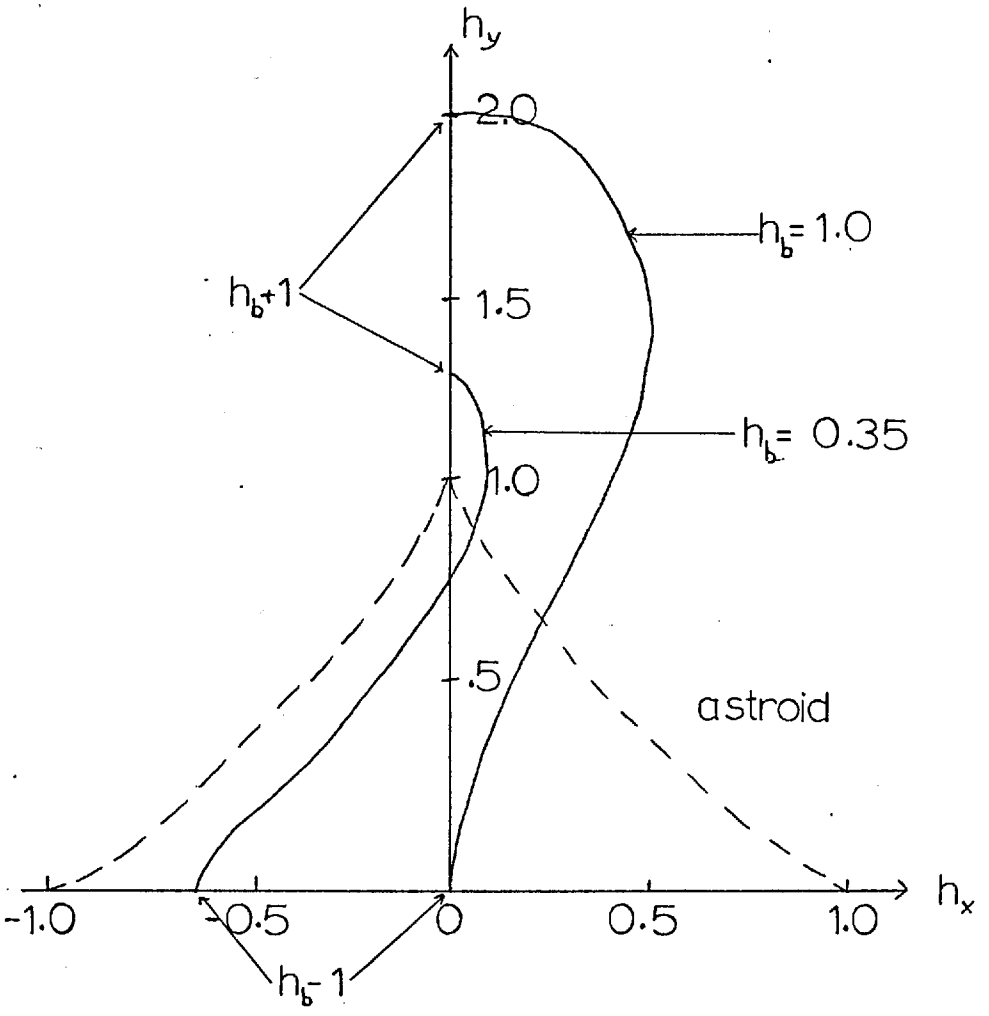

Figure 7.3 Theoretical blocking curve for the two cases where the blocking field h_b = 1.0 and 0.35

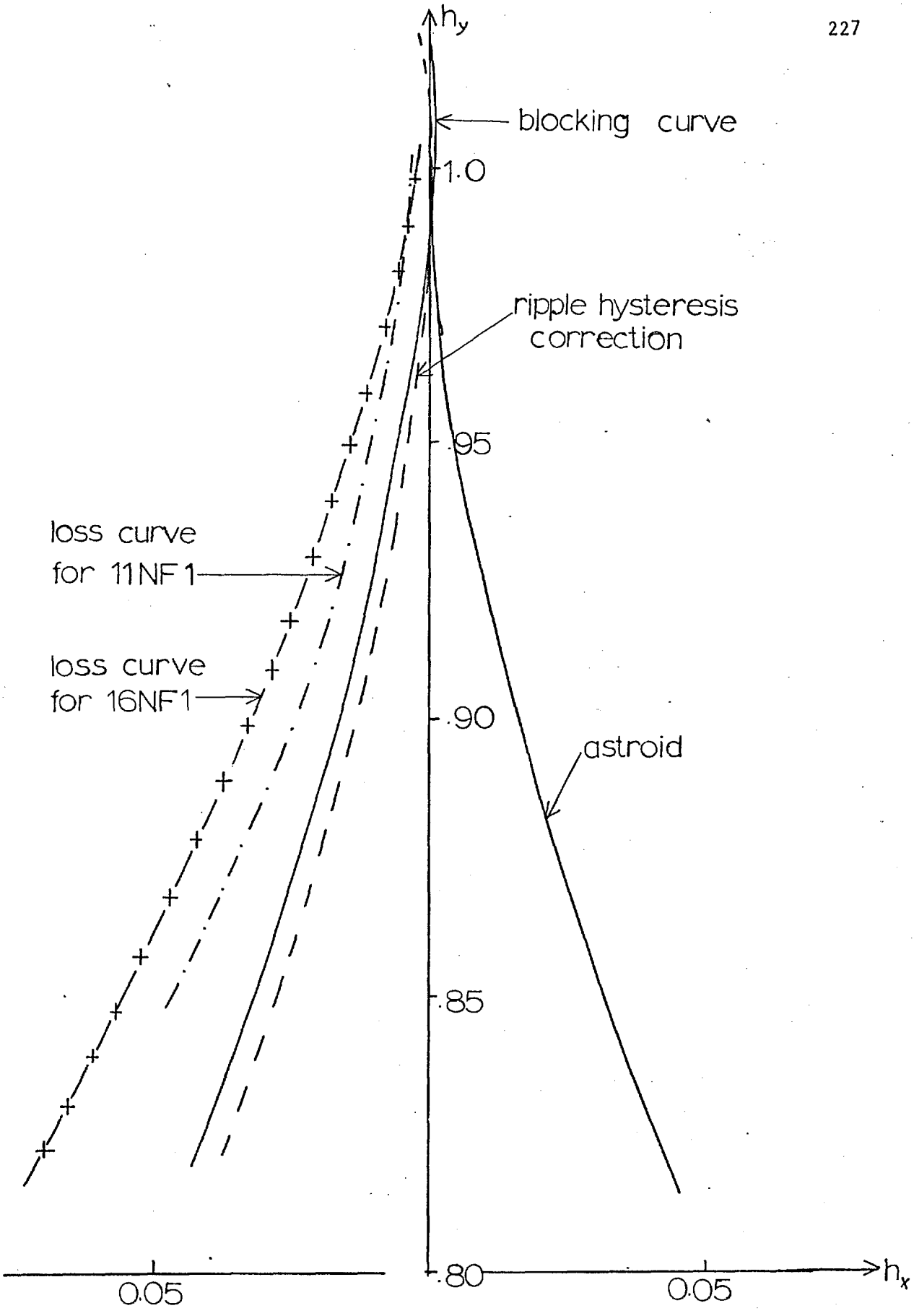

Figure 7.4 Comparison of the loss curves with the blocking curve, with and without ripple hysteresis correction

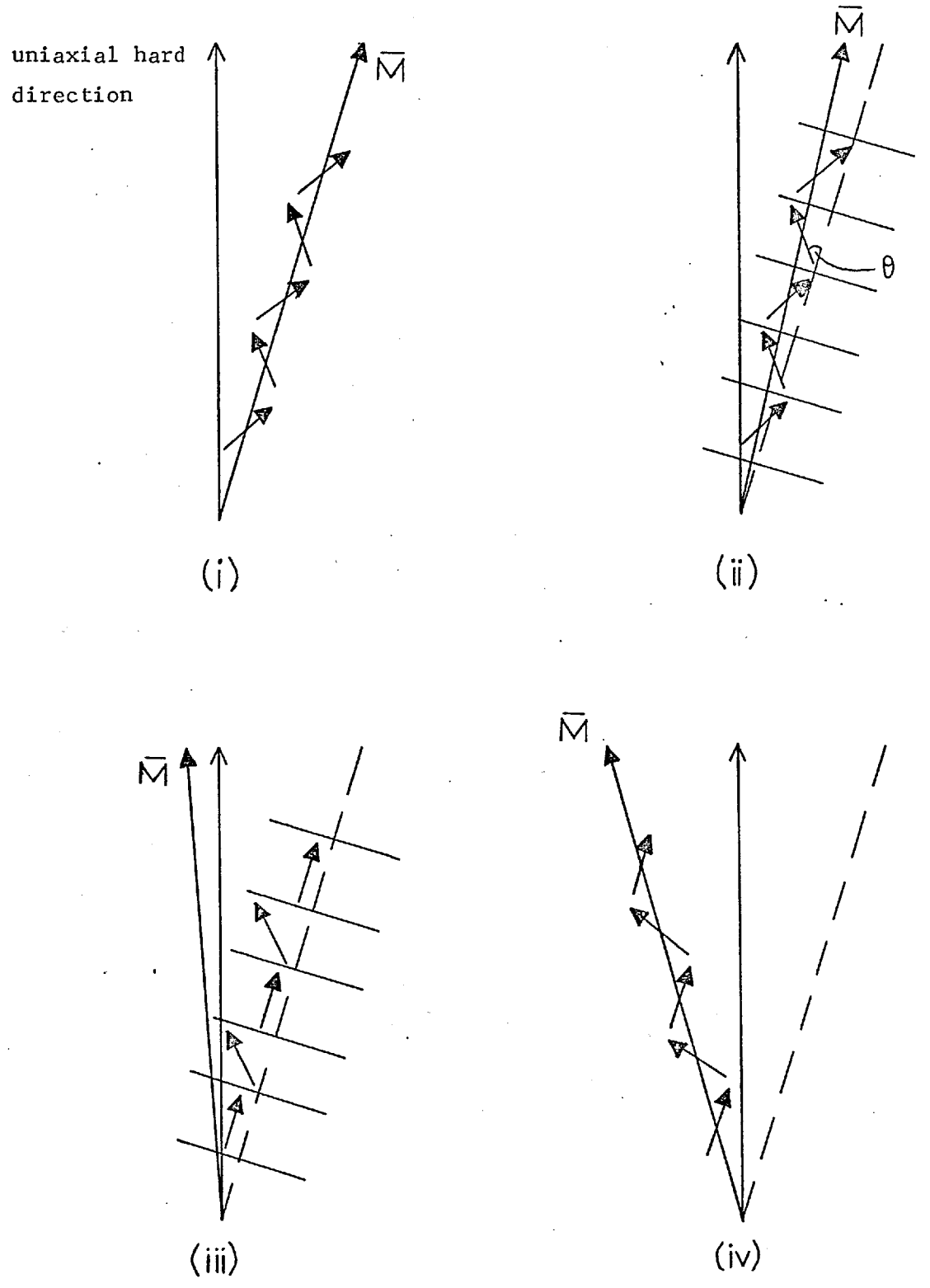

Figure 7.5 Model for ripple hysteresis

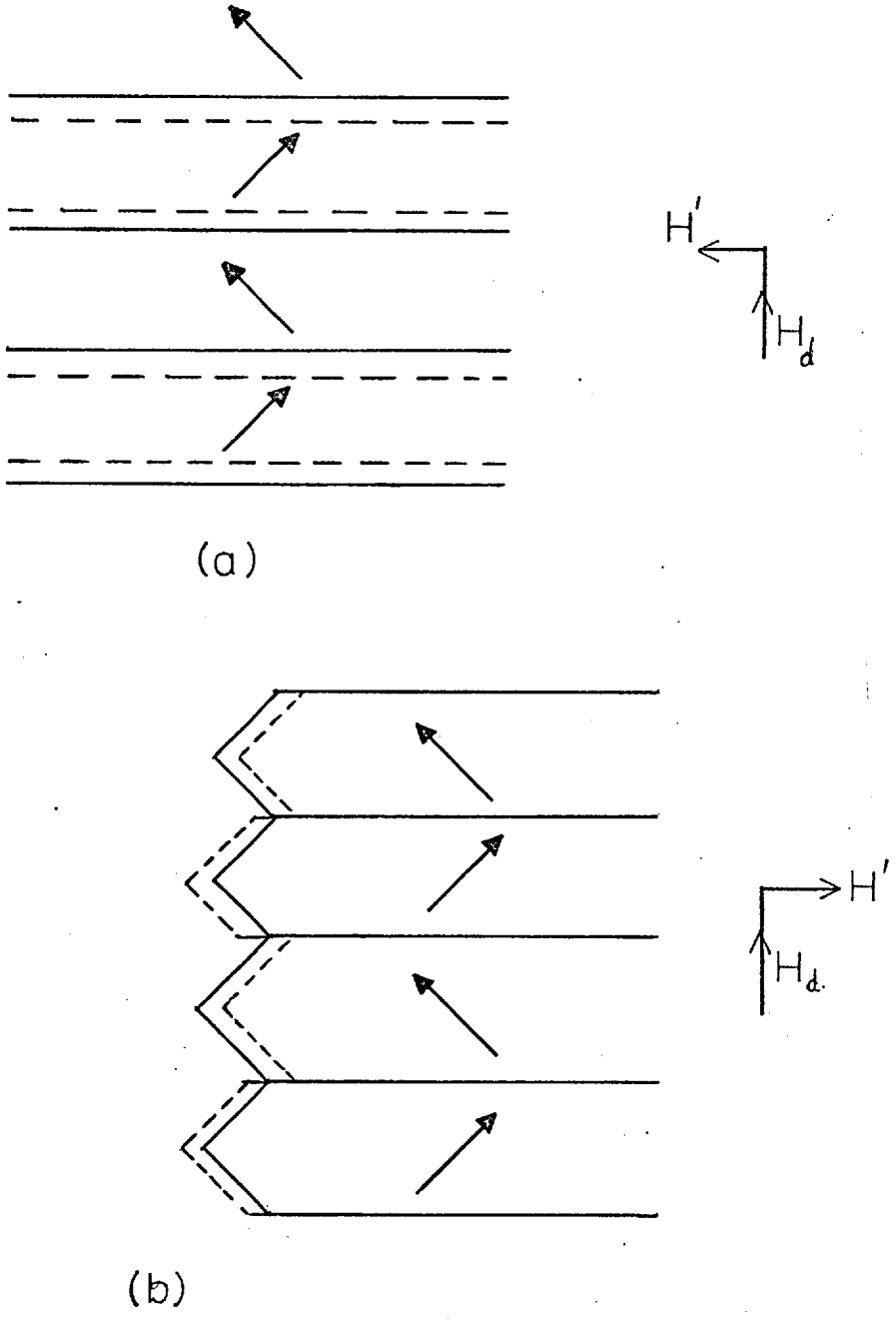

Figure 7.6 Model for two types of wall motion

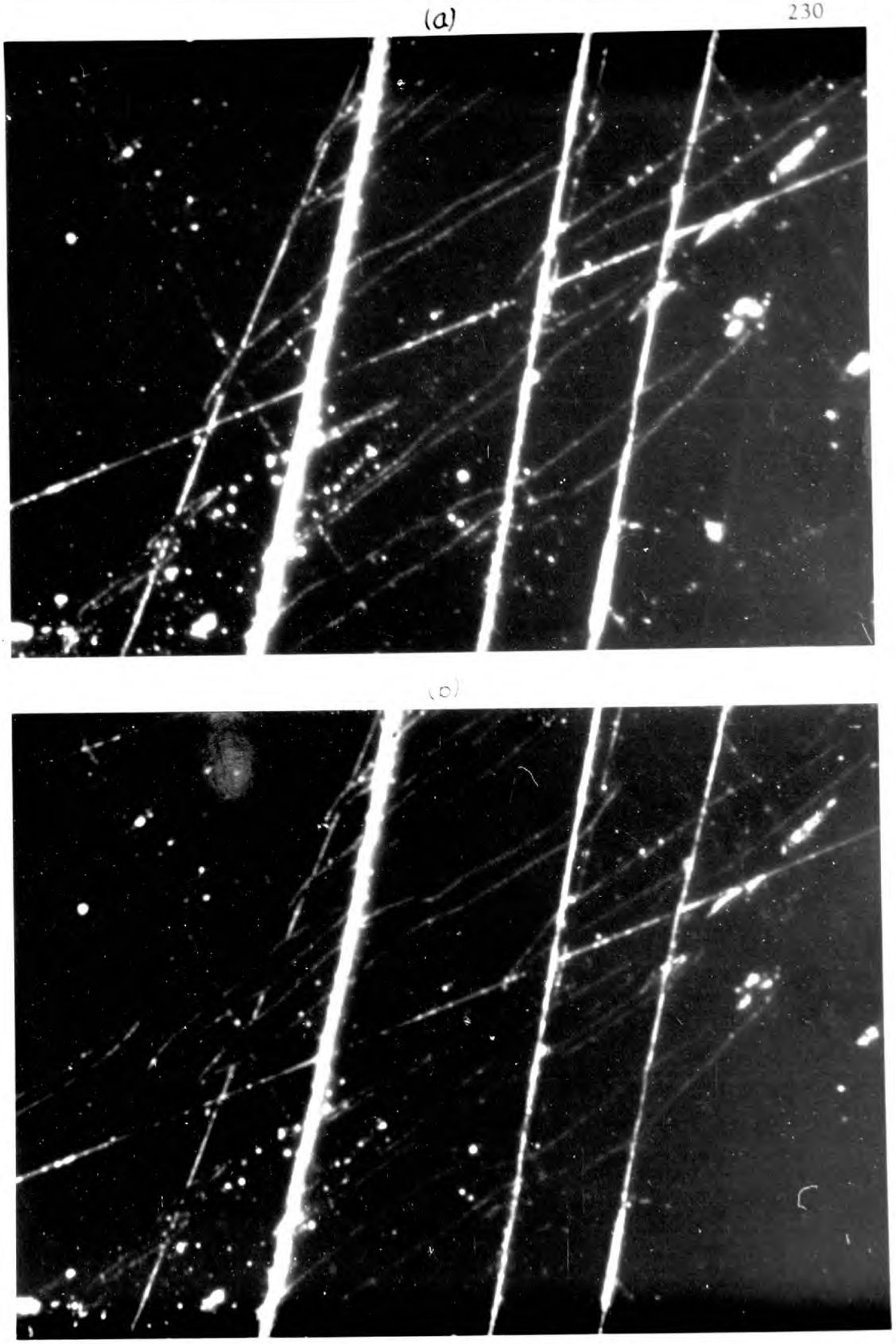

Figure 7.7 Bitter patterns of film grown on LiF with
(a) zero field after saturation in hard direction and
(b) a field of 1.2 oe in easy direction

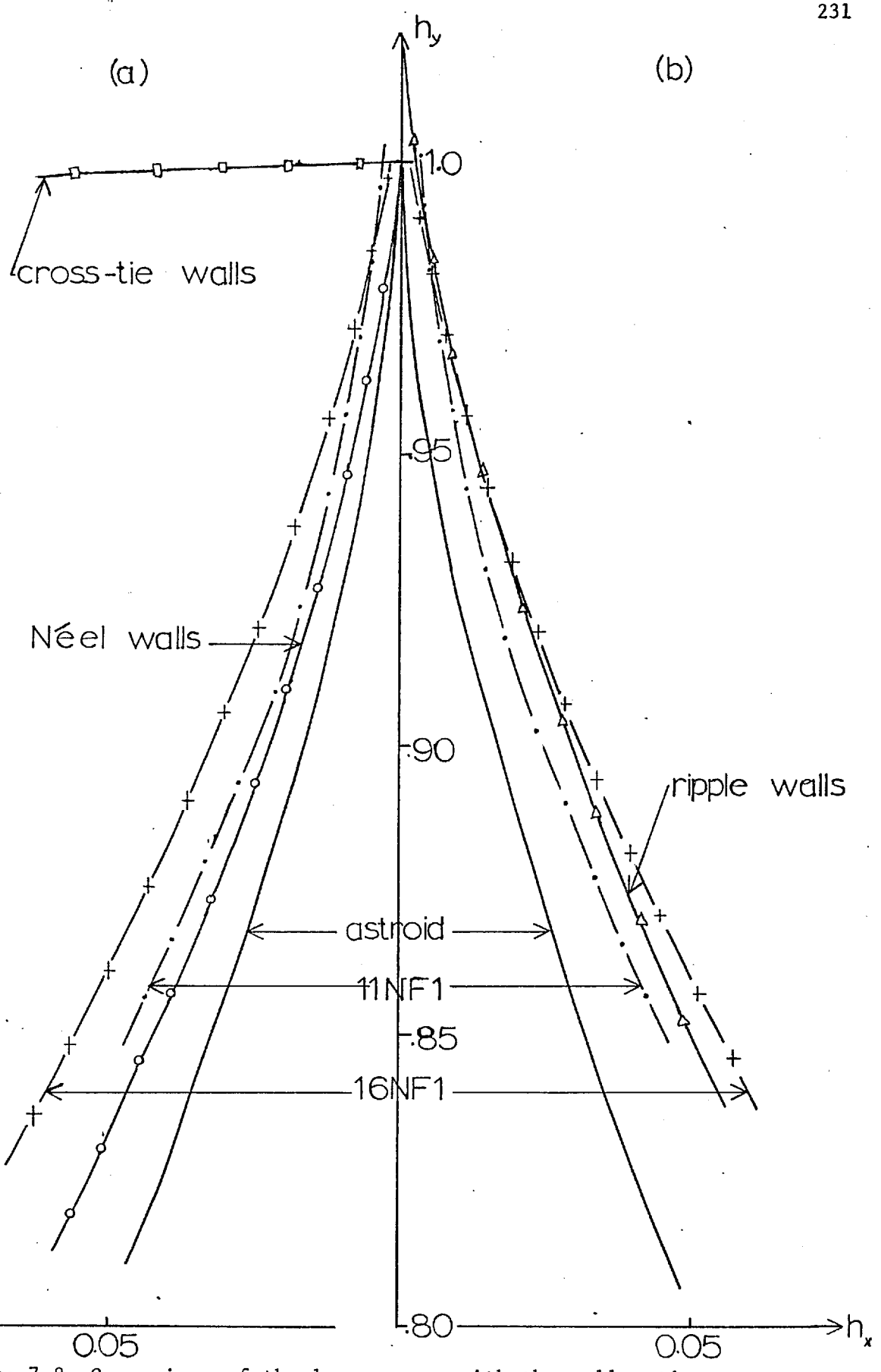

Figure 7.8 Comparison of the loss curves with the wall-motion curve for Neel walls and ripple walls

CHAPTER 8

Magnetic Properties: (C) Hysteresis Loops

This chapter is concerned with the hysteresis loops of some of the more perfect single-crystal films. With a biaxial anisotropy one expects two switches, corresponding to 90^{o} jumps (figure 2.4), rather than the single 180^{o} switch observed in the uniaxial easy-direction hysteresis loops. For a field applied in an intermediate direction these 90^{o} jumps should occur at different fields producing a metastable state where the magnetisation is almost perpendicular to the applied field. Pugh (P.6) suggested that this could be used as a store whereby the film is kept in this metastable state by a constant bias field and the application of a small positive or negative field causes a 90^{o} switch into one of the two binary states.

8.1. Introduction

Due to the difficulty encountered in producing well-orientated single-crystal films only a few authors (D.5, L.12, Y.1) have investigated their switching properties. They all found that the agreement between their films and the rotational model of Stoner and Wohlfarth was poor at low fields but good at high fields. An important point which was neglected in this previous work was the presence and effect of the uniaxial anisotropy. All the films prepared in this work exhibited a uniaxial component down to 10% of the biaxial anisotropy, its size depending to a large extent on the substrate temperature during the evaporation

(figure 6.1). It was found that this component could not be ignored in the energy calculations, in particular those for the switching curve. In fact a uniaxial component of about 10% produces theoretical hysteresis loops containing double steps for 31^{o} around the uniaxial and biaxial hard axis and 14^{o} around the uniaxial easy axis, rather than 22.5^{o} for a pure biaxial anisotropy. It can be seen, therefore, that the uniaxial component must not be neglected.

8.2. Comparison between the Theoretical and Experimental Loops

The film for which a detailed analysis was performed was epitaxially grown on sodium fluoride. It had biaxial and uniaxial anisotropy fields of 13.6 oe and 1.52 oe respectively as measured from their susceptibility curves (chapter 4). This corresponds to anisotropy constants of 6.7×10^{3} and 7.4×10^{2} erg/cc. The hysteresis loops were obtained using the longitudinal Kerr effect over 0.8 mm^{2} areas. The two biaxial hard-axis loops, corresponding to the uniaxial easy and hard directions, are shown in figure 8.1, together with the loops at 45^{o} to this direction, loosely referred to as the biaxial easy axes. A series of loops for this film at various angles to the uniaxial hard direction are shown in figure 8.3. (The slight opening observed in the loop at 15^{o} is due to a slight misalignment of the analyser to emphasise the steps.)

8.2.1. The Stoner-Wohlfarth Rotation Model.

The film being considered has a ratio of anisotropies, b_1, equal to 9 and the associated rotation switching curve is calculated by finding the field conditions for an

inflexion point in the energy (as in section 2.4). The curve is shown in figure 8.2, being very similar to the pure biaxial case only the easy axes are 3^{o} further away from the uniaxial hard axis. The aligned hysteresis loops, calculated as for the pure biaxial anisotropy, can be compared directly with the experimental loops by changing from the reduced values of the switching curve to the actual values for this film (multiplied by H_k = 1.52 oe). The agreement is exceptionally good (figure 8.3) except near the 'biaxial easy' axis. This is very like the case of uniaxial anisotropy films. The explanation of reversal in the easy direction by 180^{o} wall motion could again solve this problem.

A similar comparison of loops for a single-crystal cobalt film grown on MgO by Doyle (D.5) showed poor agreement with the coherent rotation model and fairly good agreement with a wall-motion model originated by Kondorsky (K.8).

8.2.2. The Kondorsky Wall-motion Model. This model is based on the assumption that only non-coherent rotation is allowed, which implies that the anisotropy field is very much greater than the critical field for wall motion. When the component of the applied field perpendicular to the bisector of the initial and final direction of the magnetisation is equal to a certain critical field, determined by the film structure, the film switches.

Doyle extended this model to the case of biaxial anisotropy by allowing 90^{o} wall motion rather than 180^{o} wall motion as in the uniaxial case. There will then be two steps in the hysteresis loop at intermediate

angles. These two steps occur at the same field in the easy and hard directions producing one, 180^{o}, switch. Referring to diagram 8.4 we see that the switching fields are given by the components H_w and H'_w

where: for the switch M_1 to M_2 $H_w = -\frac{H_o}{\cos(\alpha - 132^{o})}$ and for M_2 to M_3 $H'_w = -\frac{H_o}{\cos(222^{o} - \alpha)}$ H_o being the critical field and the negative sign indicating the direction of H relative to M_1.

To find the critical field, H_o, the switching field in the 'biaxial easy direction' was fitted with the theoretical value. Using this value of H_o the resulting loops are plotted together with the experimental loops in figure 8.5. For a pure non-coherent rotation model there are only discontinuous changes so that the magnetisation remains constant except at these changes.

8.3. Discussion

A comparison of the two models with the experimental loops shows that the actual values using the S-W theory, assuming only the biaxial and uniaxial anisotropy fields, agree extremely closely. Furthermore, the correct number of 90^{o} switches or double steps are observed and the change in remanence also agrees with the coherent rotation model. However, near the 'biaxial easy' axis the film switches before the predicted fields for rotation are reached. The switch is very sudden and not gradual like the previous switches, indicating that this is due to wall motion. A gradual switch points to rotation of a film possessing a finite amount of dispersion.

Thus the film under observation behaves in an identical way with a good uniaxial film in that the coherent rotation model of Stoner and Wohlfarth may be extended to the biaxial anisotropy case and predicts the correct switching modes except near the 'biaxial easy' axis where the film is switched by the motion of 180° domain walls.

There are several possible reasons why these results conflict with the work of Doyle (D.5). The main ones are: first, the uniaxial anisotropy cannot be neglected; secondly, this work is concerned with the behaviour of small areas whereas Doyle's measurements were over the whole film; finally, these films may have had improved epitaxy due to the electron bombardment during production.

The extra, intermediate states corresponding to a switch through approximately 90° were never observed for films prepared on single-crystal sodium chloride in agreement with the work of Yelon et al (Y.1). Several films prepared on lithium fluoride were tried and these showed some intermediate states but the relatively large uniaxial anisotropy prevented them from being as successful as the films grown on sodium fluoride.

8.4. Anomalous Hysteresis Loops

Occasionally a loop was observed with a double switch on one side only, as shown in figure 8.6d. On decreasing the field to an extremely critical value both double switches could be observed (figure 8.6b). Comparing figures 8.6b and 8.6c it can be seen that a small increase in field prevents the 90° switch, suggesting some form of locking. This may be caused by an area adjacent to the one under observation switching

through 90^{o} and so producing stray fields which could cause locking in the observed area until a further increase in the field causes another 90^{o} switch in this area, thus removing the stray fields and allowing the region being measured to switch through 180^{o}. A non-symmetrical distribution of these areas which cause locking can account for the non-appearance of this effect in the opposite direction.

If there were a large number of these regions, randomly distributed throughout the film, then the double switches would be obliterated and the hysteresis loops would be similar to those observed for films on NaCl. If this explanation is correct then NaCl should possess a large number of these areas whereas NaF and LiF should have only a few. This suggests that the cause of these areas is possibly connected with the substrate solubility. Sodium chloride dissolves easily in water and so the film-to-substrate bonding may be extremely uneven due to local dissolution of the substrate near film discontinuities by water vapour in the ambient atmosphere. This produces regions which are not bonded to the substrate and so will contain different stresses and consequently different magnetic properties to those parts of the film still bonded to the substrate. Since NaF and LiF only dissolve very slightly in water these areas should be few and far between, therefore having very little effect on the overall properties.

In conclusion, it seems that the disappearance of 90^{o} switches by coherent rotation in films prepared on NaCl could be explained by a large number of unequal stress areas producing local stray fields which prevent 90^{o} switching of adjacent areas by locking. This then allows

only 180^{o} switching, probably by wall motion or possibly by partial rotation as suggested by Yelon et al (Y.1). However, for films prepared on NaF and LiF the stresses in the film are thought to be fairly uniform and so the local stray fields will be small, allowing these 90^{o} switches to be observed.

uniaxial and biaxial
hard axis

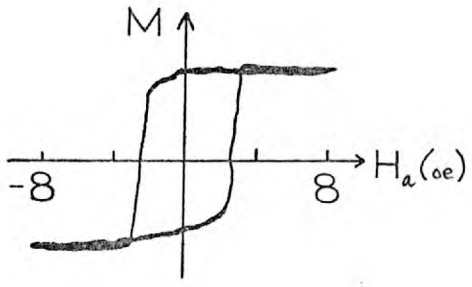

'biaxial easy' axis

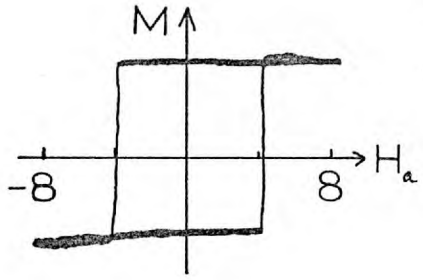

uniaxial easy and
biaxial hard axis

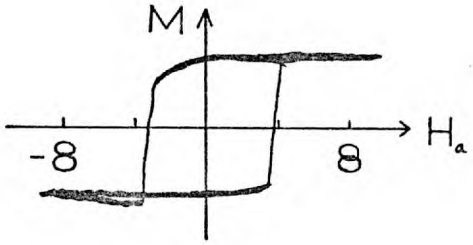

'biaxial easy' axis

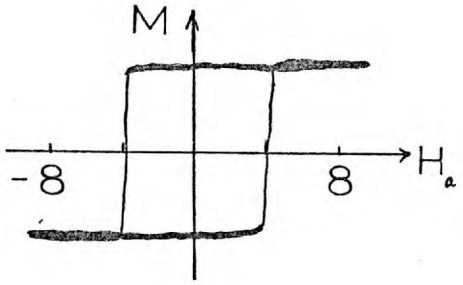

Figure 8.1 Traces of the hysteresis loops of a film on NaF in the biaxial easy and hard axes

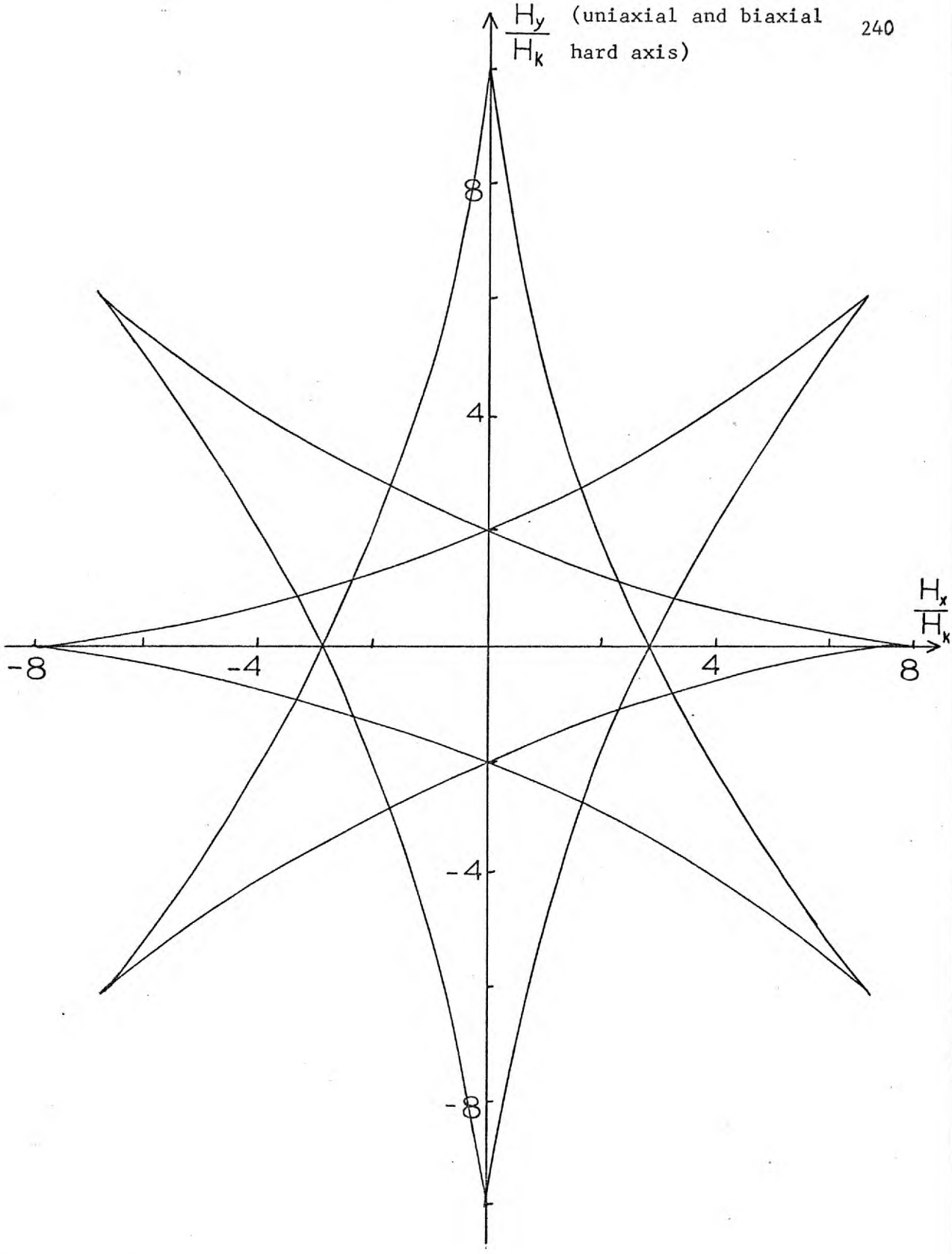

Figure 8.2 The switching threshold curve for a film with a ratio of anisotropies $b_1 = H_1/H_k = 9$

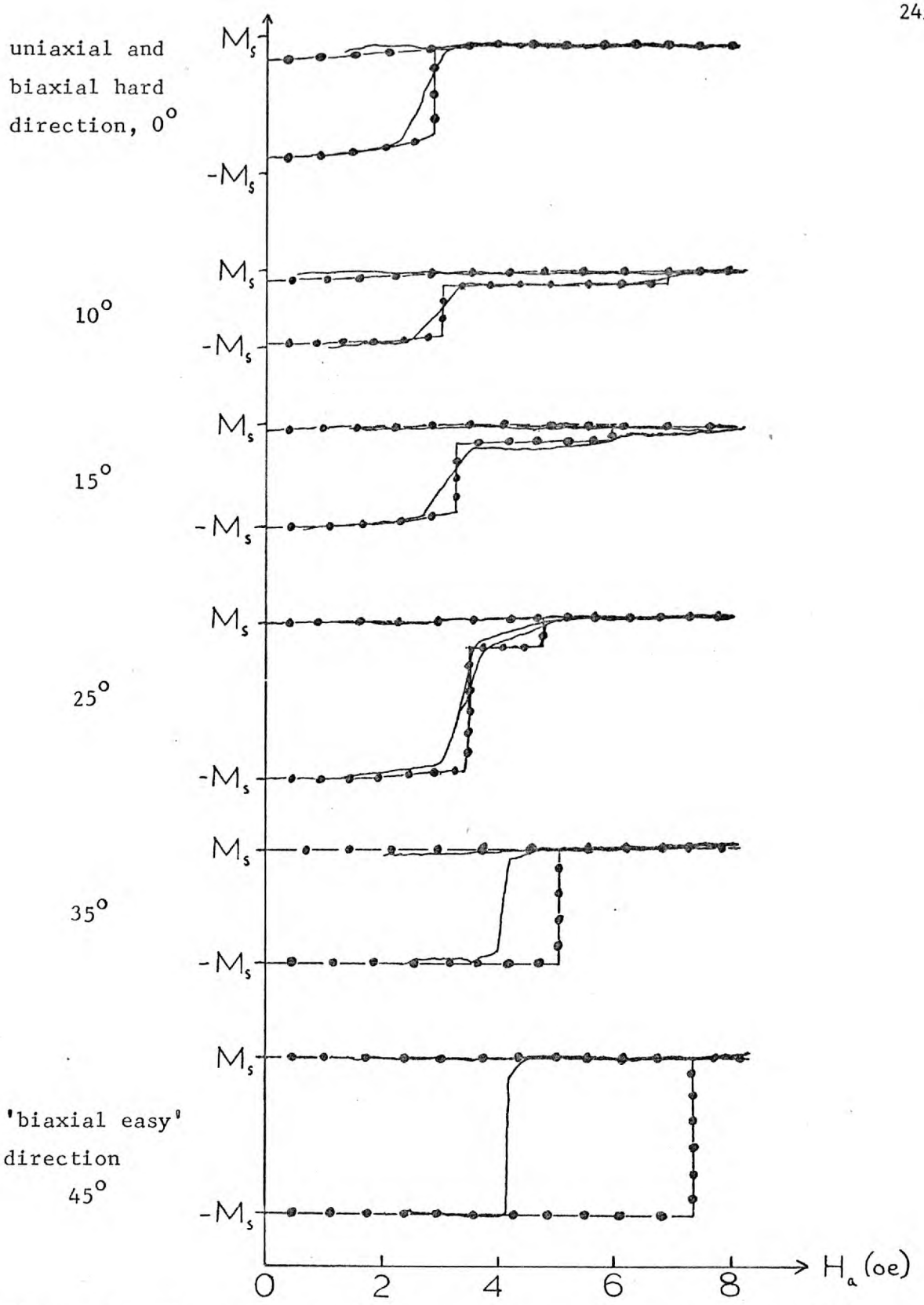

Figure 8.3 The experimental hysteresis loops (———) for the field applied at various angles to 100 and the theoretical loops of the S-W model (-o-o-o-)

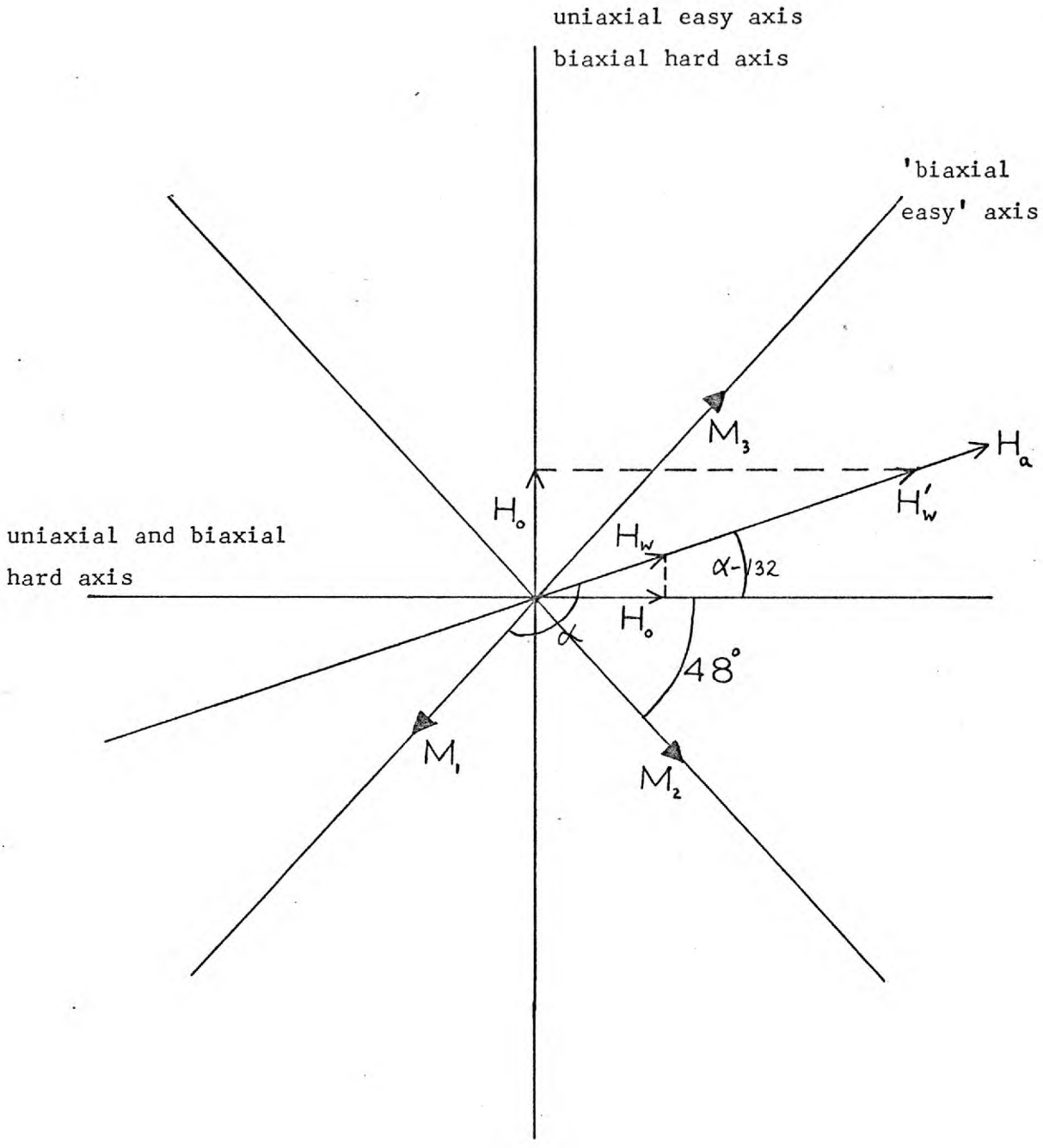

Figure 8.4 Kondorsky's wall-motion model for biaxial anisotropy

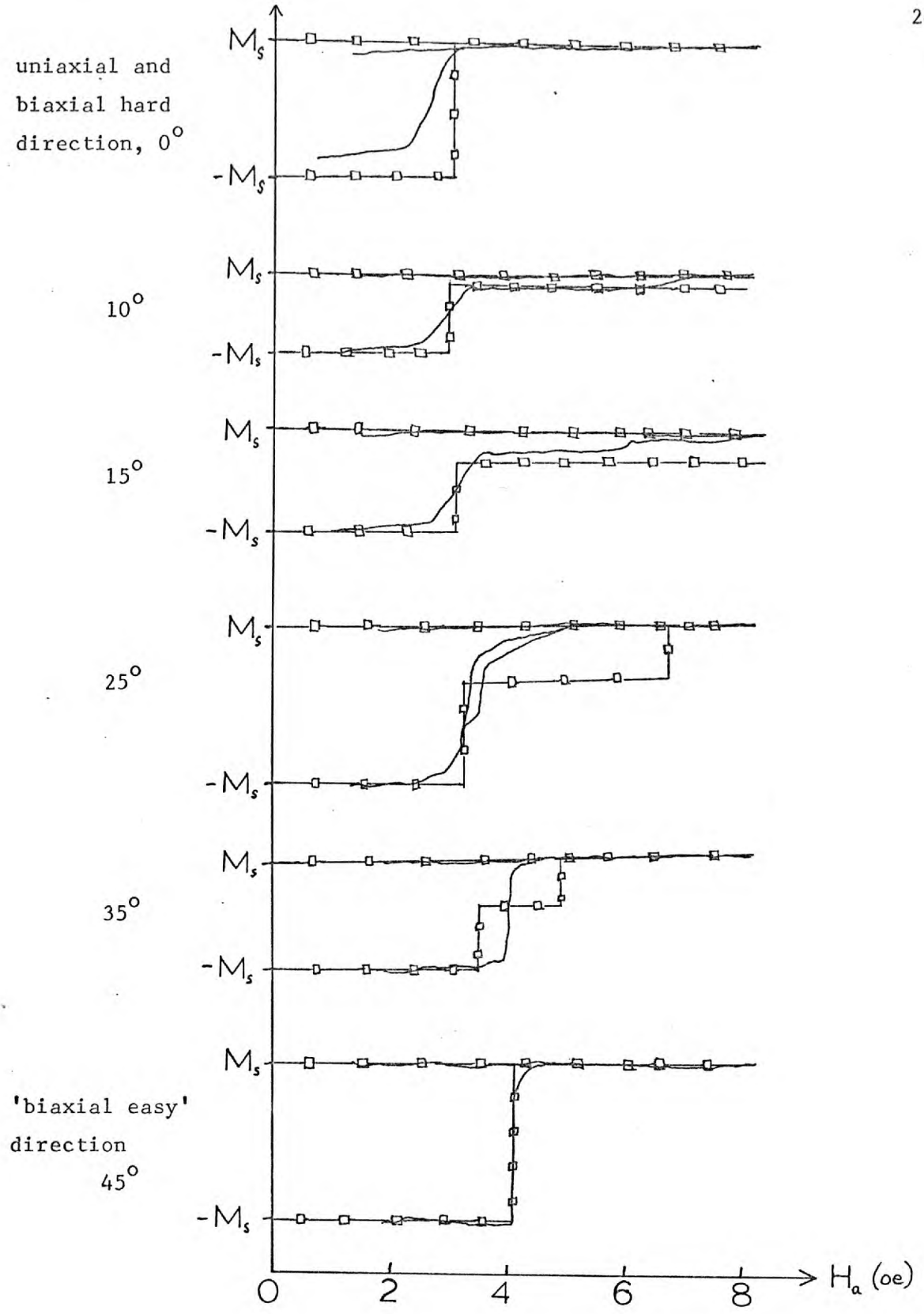

Figure 8.5 The experimental hysteresis loops (——) for the field at various angles to 100 compared with the theoretical loops of the Kondorsky model (-□—□-)

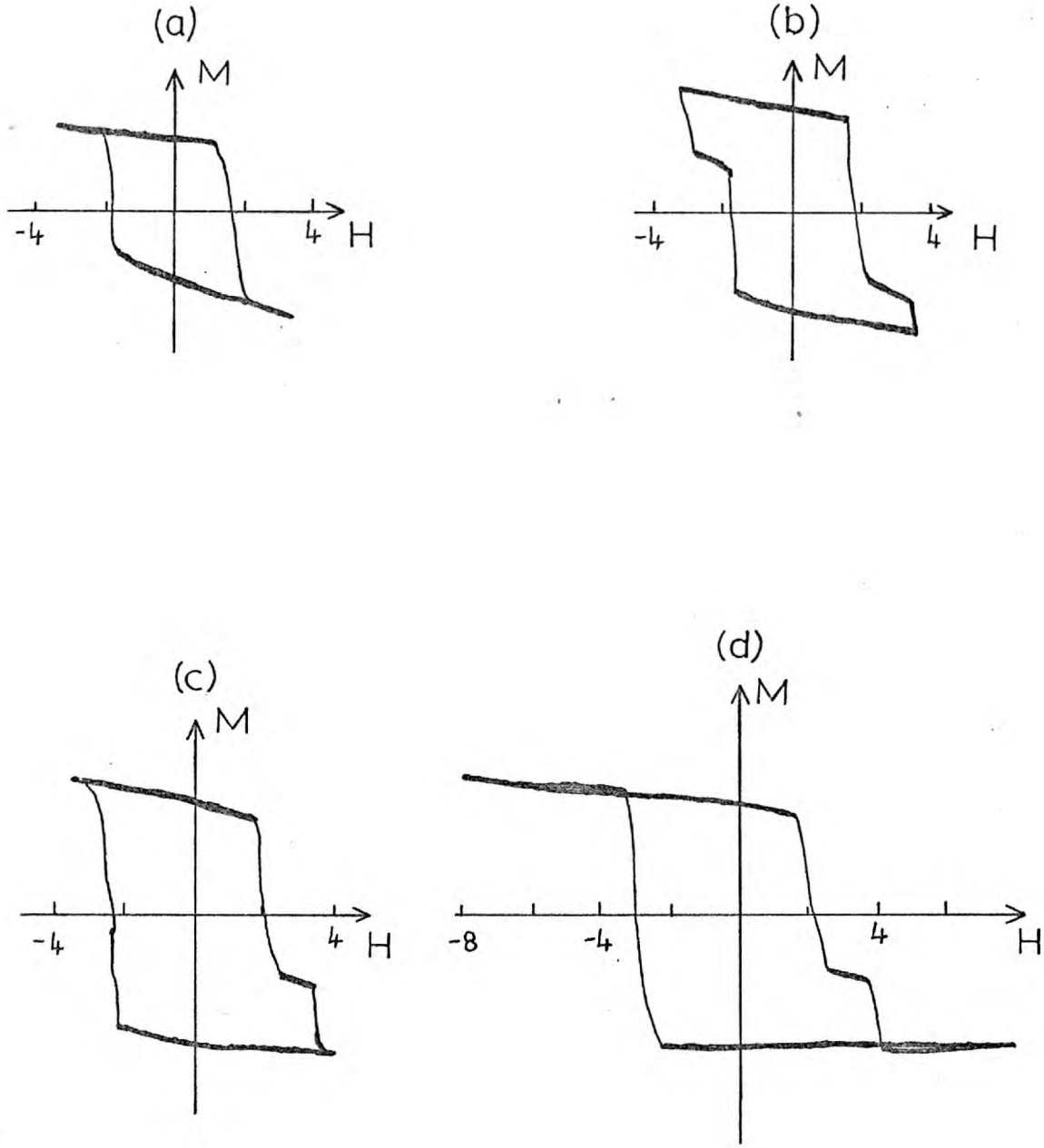

Figure 8.6 Series of anomalous hysteresis loops for increasing applied fields

SUMMARY

The aim of this section is to correlate the research outlined in the preceding chapters and in particular to connect the magnetic and crystallographic results. It was previously mentioned (section 1.3) that the aim of this work was to study the effects on the magnetisation ripple of the various degrees of orientation of the film. This entailed the production of single-crystal films. Sodium chloride was the substrate used as this had the advantage of being the most common, and hence the cheapest.

The orientation was altered by changing the substrate temperature for each successive evaporation. The changes in the uniaxial and biaxial anisotropy constants (measured using the susceptibility apparatus) with substrate temperature have been explained as the direct result of the effect of the change in the degree of orientation on the directional ordering contribution.

Ripple effects have been measured rather indirectly by comparing $H_p - H_k$ versus χ_p / χ_o for each polycrystalline film against the predictions of the various theories. All the films were incorporated by the two limiting cases of both Hoffmann's and Harte's theories. This treatment was then extended to biaxial anisotropy and applied to the single-crystal films, in both biaxial hard axes (corresponding to the uniaxial easy and hard axes). Again, good agreement in both directions was obtained, but for films with low values of H_1/H_k the uniaxial easy

direction produced poor agreement. This was explained as being due to wall-motion effects.

The biggest disadvantage encountered using NaCl was the large scatter of values of K_u and K_1 at similar substrate temperatures. This is thought to be due to the ease with which NaCl dissolves in water so that microdissolution occurs near film discontinuities, affecting the stress in the film and also the constraint temperature. Another possible cause which may affect the magnetic properties is the low sublimation point of NaCl which could also affect the epitaxy. It was decided to use other alkali halide substrates with slightly different physical properties. The two other substrates used were LiF and NaF, both cleaving in the [100] direction.

Films prepared on NaF and LiF were far superior both crystallographically and magnetically:

(i) The films had lower defect densities and a smaller spread in orientation for similar evaporations at elevated temperatures (>250°C), but these differences were much less at lower temperatures.

Magnetic properties were fairly similar to films on NaCl at the lower temperatures but they deviated widely at higher temperatures.

(ii) The single-crystal hysteresis loops showed extremely good agreement with the single domain theory for films grown on NaF, but films on NaCl did not even show a double step in the hysteresis loops. Observation of certain films on NaF and LiF with double steps on only one side of the loop enabled an explanation to be proposed for the lack of double steps for films on NaCl. It is thought that the solubility of

NaCl caused varying properties in adjacent regions and large local stray fields, preventing pure rotation.

(iii) The magnetocrystalline anisotropy constant had higher values for the NaF and LiF substrates than for NaCl but all three were higher than bulk values. This was explained as being due to an isotropic stress caused by differential thermal expansion between the film and substrate. The stresses and constraint temperatures were higher for NaF and LiF, which was attributed to a better surface and no microdissolution.

A large amount of previous work had been concerned with methods of improving epitaxy by electron bombardment, vacuum cleaving, etc. In this work several other preparations of the NaCl were tried with the same aim. The NaCl substrates were both etched and polished, resulting in improved epitaxy in both cases, although the etched substrates produced films with increased defect densities. The polishing, besides improving the epitaxy, removed the cleavage steps, replacing them with far smaller scratches. Although the polished substrates provided better epitaxy the magnetic properties were drastically affected by the scratches, producing coarse-scale ripple and interaction fields. The anomalous susceptibility curves of these films were successfully explained using Harte's ripple theory. The 'etched films' with improved epitaxy had very similar magnetic properties to the films on cleaved NaCl.

The only direct ripple measurements performed were concerned with the loss mechanisms, as explained in chapter 7, whereby the biased susceptibility apparatus was used for plotting the loci of the maximum

imaginary susceptibility in field space. The resulting curve was expected to correspond to Hoffmann's blocking curve. However, even allowing for a certain degree of ripple hysteresis the agreement was very poor. By considering the losses to arise by irreversible ripple wall motions the loss curves can be described fairly accurately using the coercive field calculations of Middlehoek (M.3) for films which have negligible interactions between ripple walls. Although the theoretical treatments of ripple reorientations and ripple wall movements are distinguishable, in the actual experimental observations of Feldtkeller (F.6.b) it is virtually impossible to distinguish between the two.

APPENDIX 1

Glossary

A	exchange constant
b_1	ratio of anisotropies (K_1/K_u)
B	magnetic induction
d	crystallite diameter
D	film thickness
$h = H/H_k$	reduced field
$\hat{H}$	peak a.c. field in susceptibility apparatus
$H(\alpha)$	Stoner-Wohlfarth single-domain field
H_a	applied field
H_b	blocking field
H_c	coercive field
H_e	earth's field
H_{eff}	total effective field
H_k	uniaxial anisotropy field $(2K_u/M_s)$
H_p	value of applied field for peak susceptibility
H_s	stray field
H_1	biaxial anisotropy field $(2K_1/M_s)$
K	local anisotropy constant
K_1	first-order magnetocrystalline anisotropy constant
L	torque exerted on film by the field $(\partial E_k/\partial\theta)$
M_s	saturation magnetisation

P	pressure (torr)
T_s	substrate temperature (^{o}C)
U	magnetostatic potential
α_{90}	'angular dispersion'
δ	magnetisation dispersion
λ	ripple wavelength
λ_{hkl}	magnetostriction constant in the [hkl] direction
λ_s	average magnetostriction constant
μ	permeability
Φ	magnetic flux
$\chi(\chi_t)$	real transverse susceptibility
χ_i	imaginary susceptibility
χ_i'	incremental susceptibility (real part)
χ_o	transverse susceptibility in a field H_k $(M_s^2/2K_u)$
χ_p	peak value of transverse susceptibility
Ω	non-linear intrinsic field (Harte's theory)

APPENDIX 2

In chapter 6 the inverse susceptibility curves were compared with the theoretical predictions of Harte (H.8). In figure 6.11 the theoretical values of H_{eff} are plotted against the applied field, $H_a \pm H_k$, both axes being normalised with respect to a field Ω. The coarse-scale ripple in figure 6.11.a the normalising field, Ω_c, is given by:

$$\Omega_c = \left[\frac{K^4 \pi L}{4RM_s^3} \left\{ I(\tfrac{3}{2},\tfrac{3}{2}) \right\}^2 \right]^{1/5} = 1.22 \times 10^{-2} K^{4/5} \text{ oe} \quad .. \quad .. \quad (A.2.1)$$

where the exchange constant $A = 1 \times 10^{-6}$ erg/cm^3, $M_s = 10^3$ gauss, the film thickness $2L = 10^3$ Å and the inhomogeneity scale, R, $= 5 \times 10^3$ Å. K is the r.m.s. value of the local anisotropy and $I(\frac{3}{2},\frac{3}{2})$ is a constant, equal to 1.854. The case of the fine-scale ripple is covered in figure 6.11.b in which the normalising field, Ω_f, is given by:

$$\Omega_f = \frac{M_s}{2A} \left[\frac{(RK)^4 \pi L \left\{ I(\tfrac{3}{2},\tfrac{3}{2}) \right\}^2}{4\pi M_s} \right]^{2/5} = 3.56 \times 10^{-7} K^{8/5} \text{ oe} \quad .. \quad .. \quad (A.2.2)$$

The symbols have the same meaning and R has been put equal to 10^2 Å.

It is important to note that the intercept of line 3 on the H_a axis in figure 6.11 is Ω_c or Ω_f. The validity of the non-linear approximation can now be checked. From the intercept in figure 6.9 a value for Ω was determined and then the field range over which the approximate solution agreed to within 10% with the correct solution was calculated. In the cases of both fine and coarse-scale ripple the upper limit of agreement occurred at a field, $H_a \pm H_k$, of 16 oe, which is well below the point at which the experimental curves begin to deviate from linearity.

It is obvious from figure 6.11 that the non-linear approximation is in any case a rather poor fit to the correct solution, having a markedly different slope.

The method finally used for fitting the data in figure 6.9 to the correct solution was described in the text but essentially involved approximating the correct solution with the straight line 5. From the intercept of this line on the $(H_a \pm H_k)$ axis the value of Ω was determined and the field range over which this approximation gave 1% accuracy was then calculated and compared with the experimental range as follows.

The experimental points agree with the straight line in figure 6.9 to within 1% over a range of $H_a \pm H_k$ of 19 ± 3 oe to 57 ± 8 oe. The errors quoted mainly arise from small discrepancies between the two lines, possibly caused by some anisotropy in the film's structure, or in the case of the lower limit, by the onset of wall motion. For the same accuracy the ranges calculated for two suitable lines in figure 6.11 are 23 to 50 oe for the coarse scale and 13.5 to 135 oe for the fine scale. The former figures fit very closely with the experimental range, but the latter give far too wide a range. Moreover, the choice of a different straight line in figure 6.11.b which reduces the upper limit also reduces the lower one.

Since the value of Ω_c is directly related to K it is possible to determine the latter after finding the best fit and using equation A.2.1. For the polished film in figure 6.9, K is calculated as 6.9×10^3 erg/cm^3.

APPENDIX 3

Publication

The following paper was published during the course of these studies on the magnetic properties of films prepared on polished NaCl substrates:

'The effect of surface roughness on the susceptibility of thin permalloy films'

R. J. Fairholme & K. D. Leaver

British J. Appl. Phys. Series 2 Vol. 2 pg 1267-77 (1969)

REFERENCES

A.1. Anderson, J. C. 'The use of thin films in physical investigations' Academic Press (1966)

A.2. Aharoni, A. J. Appl. Phys. 37 pg 3271-9 (1966)

Aharoni, A. J. Appl. Phys. 38 pg 3196-9 (1967)

A.3. Aharoni, A. J. Appl. Phys. 39 pg 861-2 (1968)

A.4. 'The American Handbook of Physics' McGraw-Hill (1963)

A.5. Aubert, G. J. Appl. Phys. 39 pg 504-10 (1968)

A.6. Alessandrini, E. I. J. Appl. Phys. 37 pg 4811-5 (1966)

A.7. Alers, G. A., Neighbours, J. R. & Sato, H. J. Phys. Chem. Solids 13 pg 40-55 (1960)

B.1. Bassett, G. A. Phil. Mag. 3 pg 1042-5 (1958)

B.2. Blois, M. S. J. Appl. Phys. 26 pg 975-80 (1955)

B.3. Bitter, F. Phys. Rev. 38 pg 1903-5 (1931)

B.4. Bloch, F. Z. Phys. 74 pg 295-335 (1932)

B.5. Barnett, M. E. & Nixon, W. C. J. Sci. Inst. 44 pg 893-8 (1967)

B.6. Banbury, J. R. & Nixon, W. C. J. Sci. Inst. 44 pg 889-93 (1967)

B.7. Birss, R. R. Adv. in Phys. 8 pg 252-91 (1959)

B.8. Bloch, F. Z. Phys. 61 pg 206-19 (1930)

B.9. Bean, C. P. & Livingston, J. D. J. Appl. Phys. 30S pg 120-9 (1959)

B.10. Barkhausen, H. Phys. Zeits. 20 pg 401-3 (1919)

B.11. Berkowitz, A. E. & Greiner, J. H. J. Appl. Phys. 36 pg 3330-41 (1965)

B.12. Baltz, A. & Doyle, W. D. J. Appl. Phys. 35 pg 1814-8 (1964)

B.13. Brown, W. F. J. Appl. Phys. 40 pg 1214-5 (1969)

B.14. Baltz, A. Proc. Int. Conf. Mag. & Mag. Mat. (Nottingham) pg 845-6 (1964)

B.15. Beck, A. H. W. 'Thermionic Valves' C.U.P. (1953)

B.16. Beam, W. R. & Siegle, W. T. Rev. Sci. Inst. 36 pg 641-3 (1965)

B.17. Burbank, R. D. & Heidenreich, R. D. Phil. Mag. 5 pg 373-82 (1960)

B.18. Bozorth, R. M. & Walker, J. G. Phys. Rev. 89 pg 624-8 (1953)

B.19. Bozorth, R. M. 'Ferromagnetism' Van Nostrand (1951)

B.20. Bozorth, R. M. & Hamming, R. W. Phys. Rev. 89 pg 865-9 (1953)

C.1. Crittenden, E. C., Hudimac, A. A., Strough, R. I. Rev. Sci. Inst. 22 pg 872-7 (1951)

C.2. Crittenden, E. C. & Hoffmann, R. W. Rev. Mod. Phys. 25 pg 310-5 (1953)

C.3. Carey, R. & Isaac, E. D. 'Magnetic Domains' Eng. Univ. Press (1966)

C.4. Craik, D. J. & Tebble, R. W. 'Ferromagnetism & Ferromagnetic Domains' North Holland Series (1965)

C.5. Craik, D. J. & Griffiths, P. M. Brit. J. Appl. Phys. 9 pg 279-82 (1958)

C.6. Cohen, M. S. IEEE Trans. Magnetics MAG-4 pg 48-50 (1968)

C.7. Corciovei, A. IEEE Trans. Magnetics MAG-4 pg 6-11 (1968)

C.8. Corciovei, A. Czech J. Phys. 10 pg 568-78 (1960)

Corciovei, A. Czech J. Phys. 10 pg 917-26 (1960)

C.9. Corciovei, A. J. Phys. Chem. Solids 26 pg 1939-47 (1965)

C.10. Chikazumi, S. 'Physics of Magnetism' Wiley (1964)

C.11. Cohen, M. S. J. Appl. Phys. 33 pg 2968-80 (1962)

C.12. Crowther, T. S. J. Appl. Phys. 34 pg 580-7 (1963)

C.13. Cohen, M. S. Chapter 10, 'Thin Film Phenomena' ed K. L. Chopra McGraw-Hill (1969)

C.14. Chambers, A. & Prutton, M. Thin Solid Films 1 pg 235-9 (1967)

C.15. Castaing, R. & Descamps, J. J. Phys. Rad. 16 pg 304-17 (1955)

C.16. Chikazumi, S. J. Appl. Phys. 32S pg 81-2 (1961)

C.17. Coombes, L. S., Ballard, S. S., McCarthy, K. A. J. Opt. Soc. Am. 41 pg 215-22 (1951)

D.1. Dietze, H. D. & Thomas, H. Z. Phys. 163 pg 523-34 (1961)

D.2. Döring, W. Z. Naturforschg. 16a pg 1146-52 (1961)

D.3. Doyle, W. D. & Finnegan, W. F. J. Appl. Phys. 39 pg 3355-64 (1968)

D.4. Doyle, W. D., Josephs, R. M. & Baltz, A. J. Appl. Phys. 40 pg 1172-81 (1969)

D.5. Doyle, W. D. IEEE Trans. Magnetics MAG-2 pg 68-73 (1966)

E.1. Edel'man, I. S. Bull. Acad. Sci. USSR (Phys. Ser.) 30 pg 93-5 (1965)

E.2. Ennos, A. E. Brit. J. Appl. Phys. 4 pg 101-6 (1953)

E.3. Ennos, A. E. Brit. J. Appl. Phys. 5 pg 27-31 (1954)

F.1. Frenkel, J. & Dorfman, J. Nature 126 pg 274-5 (1930)

F.2. Feldtkeller, E. & Fuchs, E. Z. Ang. Phys. 18 pg 1-4 (1964)

F.3. Fowler, C. A. & Fryer, E. M. Phys. Rev. 94 pg 52-56 (1954)

Fowler, C. A. & Fryer, E. M. Phys. Rev. 104 pg 552-3 (1956)

F.4. Fuller, H. W., Hale, M. E. & Rubinstein, H. J. Appl. Phys. 30 pg 789-91 (1959)

F.5. Feldtkeller, E. Naturwiss 48 pg 474-5 (1961)

F.6.a. Feldtkeller, E. J. Appl. Phys. 34 pg 2646-52 (1963)

b. Feldtkeller, E. Proc. Conf. Mag. & Mag. Mat. (Nottingham) pg 837-42 (1964)

F.7. Flanders, P. J., Prutton, M. & Doyle, W. D. J. Appl. Phys. 34 pg 1075-6 (1963)

F.8. Fujii, T., Uchiyama, S., Yamada, E. & Sakaki, Y. Jap. J. Appl. Phys. 6 pg 1-7 (1967)

F.9. Feldtkeller, E. Zeit. Phys. 176 pg 510-24 (1963)

F.10. Fujii, T., Uchiyama, S., Tsunashima, S. & Sakaki, Y. Proc. Intermag. (1969)

F.11. Fisher, R. D. & Haber, H. E. Appl. Phys. Letters 2 pg 11-12 (1963)

F.12. Frenkel, J. Z. Phys. 26 pg 117-38 (1924)

F.13. Feldtkeller, E. Appl. Phys. Letters 7 pg 9-11 (1963)

F.14. Freedman, J. F. J. Appl. Phys. 33 pg 1148-50 (1962)

F.15. Fujiwara, H. & Sugita, Y. IEEE Trans. Mag. MAG-4 pg 22-5 (1968)

G.1. Garrood, J. R. Proc. Phys. Soc. 79 pg 1252-62 (1962)

G.2. Green, A. & Thomas, B. W. J. J. Sci. Inst. 43 pg 399-401 (1966)

G.3. Glass, S. J. & Klein, M. J. Phys. Rev. 109 pg 288-91 (1958)

G.4. Gradmann, U. & Müller, J. Phys. Stat. Sol. 27 pg 313-24 (1968)

G.5. Gillet, E. & Gillet, M. Compt. Rend. Acad. Sci. 262 pg 359-62 (1966)

H.1. Hirth, J. P., Hruska, S. J. & Pound, G. M. pg 9 'Single Crystal Films' ed M. H. Francombe and H. Sato Pergamon Press (1964)

H.2. Halpern, V. Brit. J. Appl. Phys. 18 pg 163-173 (1967)

H.3. Huber, E. E., Smith, D. O. & Goodenough, J. B. J. Appl. Phys. 29 pg 294-5 (1958)

H.4. Heisenberg, W. Z. Phys. 49 pg 619-36 (1938)

H.5. Huber, E. E. & Smith, D. O. J. Appl. Phys. 30S pg 267-9 (1959)

H.6. Hoffmann, H. Phys. Kondens. Materie 2 pg 32-52 (1964)

H.7. Hoffmann, H. IEEE Trans. Magnetics MAG-2 pg 566-70 (1966)

H.8. Harte, K. H. J. Appl. Phys. 39 pg 1503-24 (1968)

H.9. Hoffmann, H. IEEE Trans. Magnetics MAG-4 pg 32-8 (1968)

H.10. Hoffmann, H. Phys. Stat. Sol. 7 pg 383-98 (1964)

H.11. Hoffmann, H. Z. Angew. Phys. 18 pg 499-502 (1965)

H.12. Hoffmann, H. J. Appl. Phys. 35 pg 1790-8 (1964)

H.13. Harte, K. J., Cohen, M. S., Weiss, G. P. & Smith, D. O. Phys. Stat. Sol. 15 pg 225-31 (1966)

H.14. Hoffmann, H. Phys. Stat. Sol. 7 pg 89-104 (1964)

H.15. Hutchins, G. A. 'Symposium on the Electron Microscope' pg 390-404 ed T. D. McKinley, K. F. J. Heinrich, D. B. Wittry (1964)

H.16. Heavens, O. S., Miller, R. F., Moss, G. L. & Anderson, J. C. Proc. Phys. Soc. 78 pg 33-7 (1961)

H.17. Hoffmann, H. Phys. Stat. Sol. 5 pg 187-202 (1964)

H.18. Hashimoto, H., Howie, A. & Whelan, M. J. Proc. Roy. Soc. 269A pg 80-103 (1962)

H.19. Hoffmann, R. W. & Crittenden, E. C. Phys. Rev. 78 pg 349 (1950)

H.20. Hirsch, P. B., Howie, A., Nicholson, P. B., Pashley, D. W. & Whelan, M. J. 'Electron Microscopy of Thin Crystals' Butterworth (1965)

I.1. Ignatchenko, V. A. Soviet Phys.,J.E.T.P. 13 pg 863 (1961)

I.2. Il'icheva, E. N., Kanavina, N. G. & Shishkov, A. G. Bull Aced Sci. USSR (Phys. Ser.) 30 pg 106-110 (1966)

J.1. Jacobs, M. H., Pashley, D. W. & Stowell, M. J. Phil. Mag. 13 pg 129-156 (1966)

J.2. Jones, G. A. Brit. J. Appl. Phys. 15 pg 857-8 (1964)

J.3. Joenk, R. J. IBM Research Rep. RC-1281 (1964)

J.4. Jamieson, J. A., McFee, R. H., Plass, G. N., Grube, R. H. & Richards, R. G. 'Infra-red Physics and Engineering' McGraw-Hill (1963)

K.1. Kittel, C. Phys. Rev. 70 pg 965-71 (1946)

K.2. Kayser, W. IEEE Trans. Magnetics MAG-3 pg 141-57 (1967)

K.3. Kittel, C. Rev. Mod. Phys. 21 pg 541-83 (1949)

K.4. Klein, M. J. & Smith, R. S. Phys. Rev. 81 pg 378-80 (1951)

K.5. Kriessman, C. J., Belson, H. S. & Edelman, F. H. J. Appl. Phys. 30S pg 262-3 (1959)

K.6. Kirenskii, L. V., Pyn'ko, V. G., Surkov, N. I. Bull. Acad. Sci. USSR (Phys. Ser.) 29 pg 96-9 (1965)

K.7. Koikeda, T. & Chikazumi, S. J. Phys. Soc. Jap. 20 pg 878-9 (1965)

21 pg 399 (1966)

K.8. Kondorsky, E. J. Physics (USSR) 2 pg 161-181 (1940)

L.1. Lewis, B. & Campbell, D. S. J. Vac. Science & Tech. 4 pg 209-18 (1967)

L.2. Leick, W. Annalen Phys. Chem. 58 pg 641-715 (1896)

L.3. Lambeck, M. IEEE Trans.Magnetics MAG-4 pg 51-4 (1968)

L.4. Lissberger, P. H. J. Opt. Soc. Am. 51 pg 948-966 (1961)

L.5. Lo, D. S., Olson, A. L., Olson, C. D., Oredson, H. N., Simon, W. J. & Torok, E. J. J. Appl. Phys. 38 pg 1344-46 (1967)

L.6. Lee, E. W. Rep. Prog. Phys. 18 pg 184-229 (1955)

L.7. Lo, D. S. & Hanson, M. M. J. Appl. Phys. 38 pg 1342-3 (1967)

L.8. Lommel, J. M. & Graham, C. D. J. Appl. Phys. 33 pg 1160-1 (1962)

L.9. Leaver, K. D. Thin Solid Films 2 pg 149-72 (1968)

L.10. Leaver, K. D., Prutton, M. & West, F. G. Phys. Stat. Sol. 15 pg 267-76 (1966)

L.11. Leaver, K. D. J. Appl. Phys. 39 pg 1151-2 (1968)

L.12. Lo, D. S. & Torok, E. J. Proc. Intermag. pg 2.1.1.-2.1.4. (1965)

M.1. Middlehoek, S. J. Appl. Phys. 34 pg 1054-59 (1963)

M.2. Methfessel, S., Middlehoek, S. & Thomas, H. IBM J. Res. & Dev. 4 pg 96-106 (1960)

M.3. Middlehoek, S. Ph.D. Thesis, Univ. of Amsterdam (1961)

M.4. Mayer, L. J. Appl. Phys. 28 pg 975-83 (1957)

M.5. Methfessel, S., Middlehoek, S. & Thomas, H. J. Appl. Phys. 32S pg 294-5 (1961)

M.6. Methfessel, S., Middlehoek, S. & Thomas, H. J. Appl. Phys. 32 pg 1959-63 (1961)

M.7. Middlehoek, S. IBM J.Res. & Dev. 6 pg 394-406 (1962)

M.8. Maksymowicz, L. & Maksymowicz, A. Acta. Phys. Pol. 28 pg 833-9 (1965)

M.9. Macdonald, J. R. Phys. Rev. 106 pg 890-2 (1957)

N.1. Néel, L. Compt. Rend. 241 pg 533-6 (1955)

N.2. Néel, L. J. Phys. Rad. 15 pg 225-39 (1954)

N.3. Neugebauer, C. A. Phys. Rev. 116 pg 1441-6 (1959)

Neugebauer, C. A. Z. Angew Phys. 14 pg 182-5 (1962)

N.4. Néel, L. J. Phys. Rad. 17 pg 250-5 (1956)

N.5. Nix, W. D. & Huggins, R. A. Phys. Rev. 135A pg 401-7 (1964)

N.6. Néel, L. Cah. Phys. 12 pg 1 (1942)

O.1. Oredson, H. N. & Torok, E. J. J. Appl. Phys. 36 pg 950-1 (1965)

O.2. Oguey, H. J. Rev. Sci. Inst. 31 pg 701-9 (1960)

P.1. Pashley, D. W. Phil. Mag. 4 pg 324-35 (1959)

P.2. Prutton, M. 'Thin Ferromagnetic Films' Butterworth (1964)

P.3. Prutton, M. Phil. Mag. 4 pg 1063-7 (1959)

P.4. Prutton, M. Brit. J. Appl. Phys. 11 pg 335-8 (1960)

P.5. Prosen, R. J., Holmen, J. O. & Gran, B. E. J. Appl. Phys. 32S pg 91-2 (1961)

P.6. Pugh, E. W. IEEE Trans. Comm. & Elec. 83 pg 544-8 (1964)

P.7. Pashley, D. W. & Stowell, M. J. Phil. Mag. 8 pg 1605-32 (1963)

P.8. Prutton, M. & Bradley, E. M. Proc. Phys. Soc. 75 pg 557-74 (1960)

P.9. Prutton, M. Nature 193 pg 565-6 (1963)

P.10. Prosen, R. J., Gran, B. E., Kivel, J., Searle, C. W. & Morrish, A. H. J. Appl. Phys. 34 pg 1147-8 (1963)

P.11. Prosen, R. J., Gondo, Y. & Gran, B. E. J. Appl. Phys. 35 pg 826-7 (1964)

P.12. Preisach, F. Z. Phys. 94 pg 277-302 (1935)

R.1. Robinson, G. J. Phys. Soc. Jap. 17 (B.1) pg 558-62 (1962)

R.2. Rother, H. Zeit. Phys. 168 pg 42-54, 148-154, 283-291 (1962)

R.3. Roth, M. Phys. Stat. Sol. 14 pg 115-20 (1966)

R.4. Rother, H. Zeit. Phys. 179 pg 229-43 (1964)

R.5. Rhodin, T. N. & Walton, D. pg 31 'Single-Crystal Films' ed M. H. Francombe & H. Sato Pergamon (1964)

S.1. Stoner, E. C. & Wohlfarth, E. P. Phil. Trans. Roy. Soc. A240 pg 599-642 (1948)

S.2. Suzuki, T., Wilts, C. H. & Patton, C. E. J. Appl. Phys. 39 pg 1983-6 (1968)

S.3. Stowell, M. J., Law, T. J. Phys. Stat. Sol. 16 pg 479-85 (1966)

S.4. Sclonzewski, J. IEEE Trans. Magnetics MAG-4 pg 15-19 (1968)

S.5. Smith, D. O. & Weiss, G. P. J. Appl. Phys. 36 pg 962-3 (1965)

Smith, D. O., Weiss, G. P. & Harte, K. J. J. Appl. Phys. 37 pg 1464-5 (1966)

S.6. Shtrikman, S. & Treves, D. J. Appl. Phys. 31S pg 72-3 (1960)

S.7. Smith, D. O. J. Appl. Phys. 32S pg 70-80 (1961)

S.8. Smith, D. O. & Harte, K. J. J. Appl. Phys. 33 pg 1399-1413 (1962)

S.9. Smith, D. O., Huber, E. E., Cohen, M. S. & Weiss, G. P. J. Appl. Phys. 31S pg 295-7 (1960)

S.10. Sato, H., Toth, R. S. & Astrue, R. W. J. Appl. Phys. 34 pg 1062-4 (1963)

S.11. Sato, H., Toth, R. S. & Astrue, R. W. pg 395 'Single Crystal Films' ed M. H. Francombe & H. Sato Pergamon Press (1964)

S.12. Suzuki, T. & Wilts, C. H. J. Appl. Phys. 39 pg 1151-3 (1968)

S.13. Smith, D. O., Cohen, M. S., Weiss, G. P. J. Appl. Phys. 32 pg 1755-62 (1960)

S.14. Stirland, D. J. Appl. Phys. Letters 8 pg 326-8 (1966)

S.15. Spangenburg, K. R. 'Vacuum Tubes' McGraw-Hill (1948)

S.16. Secemski, E. Ph.D. Thesis, London Univ. (1969)

S.17. Sella, C. & Trillat, J. J. pg 201 'Single Crystal Films' ed M. H. Francombe & H. Sato Pergamon Press (1964)

S.18. Spain, R. J. Appl. Phys. Letters 6 pg 8-9 (1965)

T.1. Taniguchi, S. Sci. Rep. Res. Inst. Tohuku Univ. A7 pg 269-81 (1955)

T.2. Torok, E. J., Oredson, H. N. & Olson, A. L. J. Appl. Phys. 35 pg 3469-81 (1964)

T.3. Tsukahara, S. & Kawakatsu, H. J. Phys. Soc. Japan 21 pg 313-25 (1966)

T.4. Torok, E. J. J. Appl. Phys. 36 pg 952-60 (1965)

T.5. Tsukahara, S. J. Jap. Phys. Soc. 23 pg 189-204 (1967)

T.6. Tolansky, S. 'Multiple Beam Interferometry' O.U.P. (1948)

T.7. Torok, E. J., White, R. A., Hunt, A. J. & Oredson, H. N. J. Appl. Phys. 33 pg 3037-41 (1962)

T.8. Thomas, G. 'Transmission Electron Microscopy of Metals' Wiley (1962)

T.9. Tokutaka, H. & Maejima, R. J. Phys. Soc. Jap. 20 pg 632-3 (1963)

T.10. Takahashi, M., Watanobe, D., Kono, T. & Ogawa, S. J. Phys. Soc. Jap. 17 (B.1) pg 554-7 (1962)

U.1. Uchiyama, S., Fujii, T., Masuda, M. & Sakaki, Y. Jap. J. Appl. Phys. 6 pg 512-51 (1967)

V.1. Valenta, L. Czech. J. Phys. 7 pg 127-51 (1957)

Valenta, L. Bull. Acad. Sci. USSR (Phys. Ser.) 21 pg 879-885 (1957)

W.1. Walton, D. J. Chem. Phys. 37 pg 2182-8 (1962)

W.2. Weiss, P. J. Phys. 6 pg 661-90 (1907)

W.3. Wohlleben, D. J. Appl. Phys. 38 pg 3341-52 (1967)

W.4. Wade, R. H. Phil. Mag. 10 pg 49-67 (1964)

W.5. Wilts, C. H. & Humphrey, F. B. J. Appl. Phys. 39 pg 1191-6 (1968)

W.6. West, F. G. J. Appl. Phys. 35 pg 1827-40 (1964)

W.7. Wilts, C. H. J. Appl. Phys. 35 pg 2097-101 (1964)

W.8. Walton, D., Rhodin, T. N. & Rollins, R. W. J. Chem. Phys. 38 pg 2698-704 (1963)

W.9. Wilts, C. H. Proc. Int. Symp. on Basic Problems in Thin Films (Clausthall) pg 422-8 (1965)

W.10. Weiss, G. P. & Smith, D. O. J. Appl. Phys. 33 pg 1166-7 (1962)

Y.1. Yelon, A., Voegeli, O. & Pugh, E. W. J. Appl. Phys. 36 pg 101-8 (1965)

Y.2. Yelon, A. J. Appl. Phys. 38 pg 325-7 (1967)